Dissertation zur Erlangung des Doktorgrades der Fakultät für Chemie und Pharmazie der Ludwig-Maximilians-Universität München

In-vitro modeling and nanoparticulate targeting of EMT in breast cancer

Lorenz Isert

aus Den Haag, Niederlande

2023

Erklärung

Diese Dissertation wurde im Sinne von §7 der Promotionsordnung vom 28. November 2011 von Frau Prof. Dr. Olivia M. Merkel betreut.

Eidesstattliche Versicherung

Diese Dissertation wurde selbstständig und ohne unerlaubte Hilfe erarbeitet.

München, 05.04.2023

(Lorenz Isert)

Dissertation eingereicht am: 05.04.2023

1.Gutachter: Prof. Dr. Oliva Merkel

2.Gutachter: Prof. Dr. Stefan Zahler

Mündliche Prüfung am: 25.05.2023

To my family.

Acknowledgement

First of all, I want to express my gratitude to Prof. Dr. Olivia Merkel for the opportunity to work on this interdisciplinary, highly relevant and also challenging topic. I strongly appreciate your scientific support, your guidance throughout my work and your valuable advice which contributed to my scientific development over the last years. In fact, I am grateful to look back of now over 7 years of productive collaboration since I have started in your lab at Wayne State University in Detroit as scientific intern as part of my "Praktisches Jahr". I very much enjoyed working in your groups, not least because of the unique working atmosphere with numerous social events!

I also want to thank Prof. Dr. Winter and Prof. Dr. Frieß for all the scientific discussions and valuable input during the "Donnerstagsseminar" and their contributions to this great working atmosphere at the Techno-Lehrstuhl.

I also want to thank Dr. Aditi Mehta and also Dr. Friederike Adams for their supervision and guidance in the last years as well as for their repeated scientific input. Especially, I want to thank Aditi for introducing me into the principle methodologies and scientific approaches of biological research which were fundamentally important for me to develop as scientist. I am very thankful for your support and coordination of the project but even more for becoming a friend and for the discussions we had in "Haus K" enjoying Munich's best Espresso Doppio Macchiato together with our team and snacking some sweets.

Likewise, I want to deeply thank the whole team of AK Merkel, in particular my lab-mates Natascha and Rima as well as the rest of the initial team including Bettina, Tobi and later Christina, Domizia and Christoph. You have been a great technical, scientific and social support in all PhD-related and non-related topics. Whenever "shit" happened, I knew I could count on you, that we would gather to find solutions. I am happy we became friends and fellow sufferers along our PhDs and I am hoping to stay with you in contact in the long-term.

Furthermore, I want thank the electrospinning team from the Department of Cardiac Surgery of the LMU. I highly appreciated the pleasant and supportive collaboration with Dr. Nikolaus Thierfelder, Maximilian Grab and Benedikt Freystetter. The start of the collaboration and the scientific input from your team was a milestone for my project without which I could not have made the same progress. The easy and uncomplicated access to your devices as well as the fruitful discussions with Max and Bene gave me the felling to be a "quasi-member" of your team. Thank you all!

I am also very thankful to Prof. Dr. Stefan Zahler and his team, who gave me the opportunity to conduct a major part of my imaging work in their confocal and AFM labs. The valuable conceptual ideas and scientific input by Prof. Zahler are strongly appreciated. In particular, I have to thank Mehak Passi! You have been a great collaborator and your support depicts an invaluable contribution to my research. Thank you!

Furthermore, I want to thank Dr. Andreas Roidl, Bianca Köhler and Altea Olivia for the collaboration and support in cell culture-related questions and exchange of cell lines for my project. Likewise, I thank Dr. Christoph Müller for his help with the GC-MS measurements and Prof. Dr. Vollmar and her team for the access to their labs and instruments. I further want to thank Christian Minke for his help with the SEM images.

Additionally, I have to thank Prof. Dr. Don C. Lamb and his team for their scientific input and collaboration. Especially, I want to thank Irene Gialdini for her huge contribution during our collaboration. The effort, counsel and time she invested in our project were invaluable for me and I am really glad to have made your acquaintance, Irene.

Moreover, I want to thank all colleagues of the AK Merkel, AK Winter and AK Frieß to become more than just colleagues. I am very happy that I can call many of you my friends! All the hiking and skiing trips, the evenings at the soccer and beach volleyball field and the beers thereafter made the PhD-time a wonderful experience which I don't want to miss. Special thanks go to Ute, Natascha, Fabi and Dennis. Thank you, for your support and friendship, your encouraging words when I was struggling and all the endless discussions about science, the sense of life and above.

My deepest gratitude goes to my family, my parents, my grandma and my brothers, who always supported me in all decisions I made throughout my life. Thank you for your love, your sheer endless patience and for being a 24/7-place of counsel and safety

Table of content

Chapter IX

Aim of the thesis

Tumors are referred to as wounds that never heal. A constantly inflamed environment drives essential alterations on the cellular and acellular level, disturbing tissue homeostasis whilst sustaining tumor progression. Accordingly, tumor cells may enlist the Epithelial-to-Mesenchymal-Transition (EMT) as pro-metastatic cellular differentiation program, which is triggered by biochemical and biophysical cues received from the inflammatory tumor microenvironment. Since EMT is thought to promote several steps of the metastatic cascade, identification of strategies on how to pharmaceutically interfere with EMT are particularly meaningful.

However, to study and successfully inhibit EMT, *in vitro* designs are required that bio-mimic the *in vivo* situation. The present thesis relates to the development of an *in vitro* model respecting topographical peculiarities of the diseased tissue of the mammary gland. As such, **tumor-associated collagen signatures (TACS),** i.e. differentially orientated stromal collagen fibril-bundles that surround primary tumors of the mammary gland, were identified in the past to contribute to tumor progression. These collagen fibers are thought to function as adhesion and migration substrates for cancer cells once they have succeeded to reach the stromal compartment. Cancer cells may exploit TACS as "migratory highways" that facilitate transmigration through the extracellular matrix of the stroma. Additionally, confinements by the fibrous matrix display a mechanical trigger which may initiate malignant alterations of the cellular phenotype. Here, electrospinning was applied as bio-engineering approach in order to reconstruct the unique architectural features of TACS. The aim was to reproducibly create a submicron fiber-matrix that can be transferred to cell culture. Ideally, these bio-mimetic cell-culture substrates allow for common *in vitro* assays and methods to study cellular interference with and behavior on a TACS-like scaffold. In particular, investigations concerning the role of EMT and the cellular EMT-phenotype during breast cancer cell migration in the context of such a biophysically altered environment are of interest, since efficient migration with the aid of TACS ultimately favors metastasis. In other words, the question whether a distinct degree of cellular EMT-phenotypic characteristics is required to enable migration along the fibers, was addressed. If so, therapeutic interventions that inhibit the transition towards a mesenchymal or restore an epithelial phenotype have the potential to prevent cancer metastasis by locally restricting migration. Studying phenotypic and biophysical properties of cells within the advanced *in vitro* model may consequently help to identify new interrelations between cancer cells, EMT and the tumor microenvironment. Thereby, novel molecular targets for the design and clinical application of drug candidates combating breast cancer in the future can hopefully be detected.

Lipid or polymeric nanoparticles comprise the ability to stably encapsulate nucleic acids as pharmaceutical active payload. Only in recent years, mRNA- and siRNA-based medicines were successfully approved and are now available as therapeutics to prevent or treat infectious or orphan diseases. RNA interference may be especially relevant for the treatment of cancerous diseases as tumors are most often accompanied by up- or dysregulated proteins that are drivers of the malignant

state. This thesis aims to formulate a nanoparticulate delivery vehicle that specifically targets EMT-phenotypic breast cancer cells. Such phenotypes are of particular threat to patients because they lack a therapeutic treatment option. This "undruggable" nature can be potentially circumvented by applying nanoparticles that pilot EMT-specific cell surface receptors. The transmembrane protein **CD44** was elucidated as promising candidate, as its overexpression is linked to cancer malignancy and EMT. Here, the dual-functional role of **hyaluronic acid (HA)** as (1) **targeting moiety** of HA-modified polyelectrolyte complexes, short polyplexes, and (2) **stealth molecule** to improve polyplex stability *in vitro* and *in vivo,* is being investigated. As part of identifying an appropriate formulation, different strategies how to non-covalently immobilize HA on the particle surface are being tested.

In summary, the underlying work aims to design a breast cancer-relevant *in vitro* model comprising topographical cues to influence the cancer cell's phenotype similar to what cells experience *in vivo*. Findings from the model will ideally be adopted and transferred for the formulation development of siRNA-containing nanoparticles to be specifically internalized by EMT-phenotypic breast cancer cells via HA-coatings. Effective delivery should ideally inhibit EMT or enable the reversion of the mesenchymal phenotype once an ideal siRNA candidate is identified. In a proof-of-concept experiment, nanoparticles are finally applied to the TACS-like in vitro model and potential pharmacological effects of selected siRNA molecules are evaluated.

Chapter I introduces the reader into (patho-) physiological and histological aspects of the mammary gland, the regulatory network of EMT, the design of advanced cancer-relevant *in vitro* models and the formulation of nanoparticles, in particular for therapeutic siRNA delivery.

In **Chapter II** a cell-line based EMT-model is developed. Four breast cancer cell lines of different malignancy are categorized regarding their EMT-phenotype. Simultaneously, soluble and solid factors reflecting the inflammatory tumor microenvironment are included and tested for their EMT-induction capacity in the respective cell lines.

GASC1 and KDM6b are epigenetic molecules, which exert a regulatory function on EMT via their enzymatic activity on histone marks. **Chapter III** examines their contribution in the EMT-model established in Chapter II. Their potential as therapeutic targets interfering with EMT is discussed.

In **Chapter IV** electrospun nanofibers are introduced as 3-D cell culture model to mimic tumor-associated collagen signatures as are found in the diseased tissue of the mammary gland. Following the notion of **Chapter II**, EMT-phenotype and EMT-phenotypic changes including cellular biomechanics, triggered by the fiber topography, are monitored and compared to EMT-induction of growth factors.

As part of **Chapter V**, HA-coated polyplexes are tested as siRNA-delivery vehicles to target CD44-overexpressing breast cancer cells. The physico-chemical properties of the nanoparticles are correlated

with their stability in harsh environments as well as with their uptake efficiency *in vitro*. In particular, the role of different CD44 isoforms on cellular uptake is analyzed.

Chapter VI briefly presents the use of the TACS-like *in vitro* model as cell culture transfection platform for the delivery of siRNA. In a proof-of-concept experiment, polyplex uptake similarly as described in Chapter V is studied.

In **Chapter VII**, a more complex, triblock copolymeric delivery system is introduced. By co-encapsulation of fluorescent quantum dots and fluorescently-labeled siRNA, a FRET-based theranostic strategy is established. The ability of this approach to characterize assembly, stability and disassembly of polyplexes *in vitro* is presented.

Chapter VIII finally comprises a summary of the results and suggestions for future experiments using EMT in breast cancer including possible pharmacological approaches.

Chapter I

General introduction

1 The mammary gland: From development to malignancy

1.1 Development and structure of the tissue of the mammary gland

The development of the tissue of the mammary gland is a unique and complex process that roughly runs through four distinct phases (**Figure 1)**. During embryogenesis, a rudimental gland is established which enters a quiescent stage after birth. It is not before puberty where, under the influence of ovarian hormones, remarkable morphogenetic changes occur. Due to proliferation and swelling of cells at the terminal end buds of the rudimental gland a multilayered epithelium (Cap and Bud cells) is formed whereas the ductal structures undergo successive cycles of elongation and branching to eventually expand into a tree-like bi-layered epithelium with hollow ducts and lobules. This elaborate network of branched ducts is embedded in the adipocyte-rich mammary fat pad.

Under endocrine and paracrine stimuli lobulo-alveolar buds are formed during pregnancy as a result of massive remodeling including further ductal branching and proliferation. During lactation, luminal cells differentiate into milk-producing secretory alveoli. At this stage only, the tissue of the mammary gland fulfils its functional evolutionary role. Finally, as part of the involution, post-lactational apoptosis removes 80 % of the epithelium to rebuild a pattering that resembles the structures of the virgin gland.[1, 2]

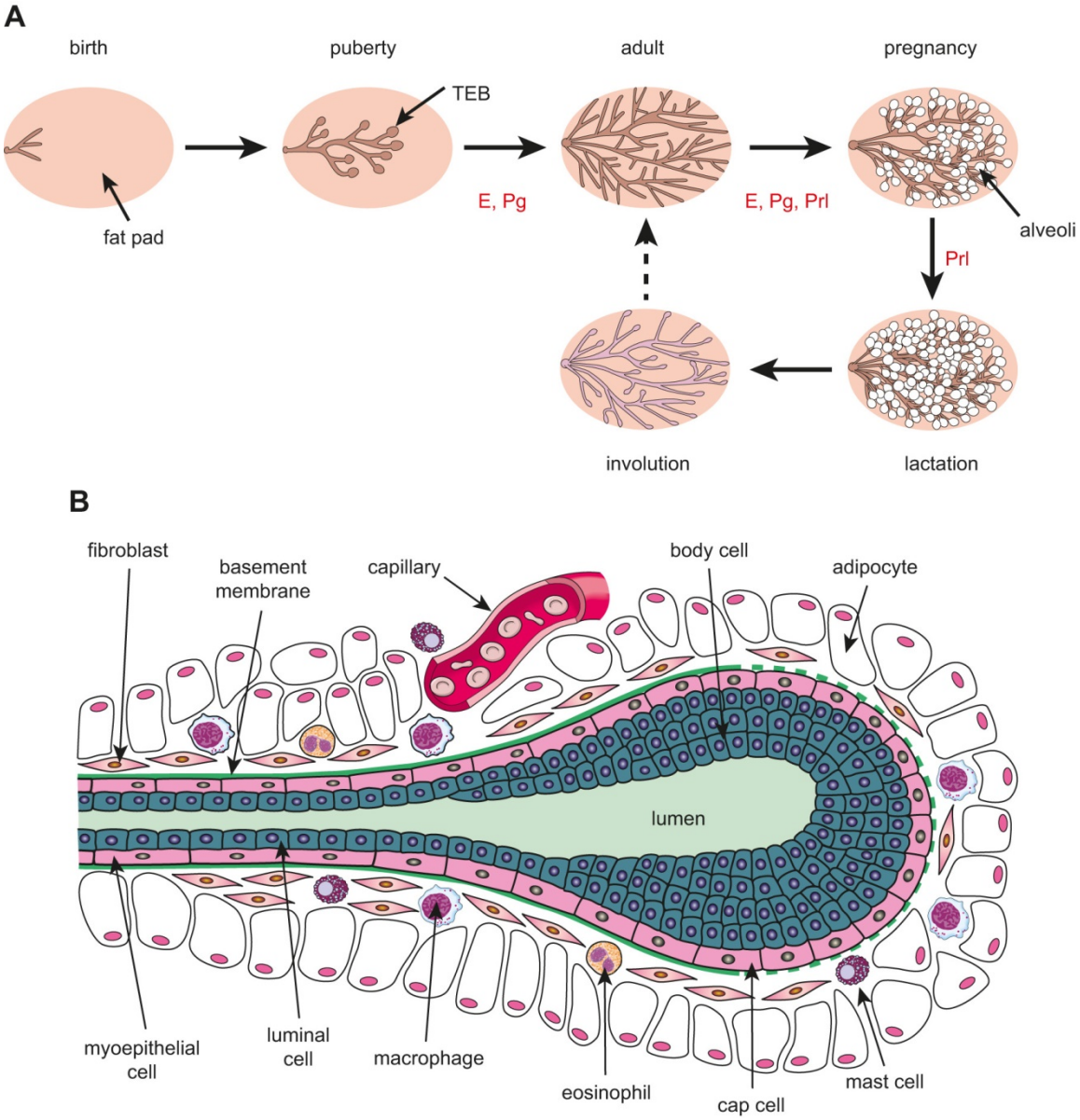

Figure 1. *Illustration displaying the development (**A**) and histology (**B**) of the mammary duct network.[3]*

The epithelium itself consists of an inner layer of luminal epithelial cells and an outer layer of basal myoepithelial cells (**Figure 1**). About two decades ago it was shown that 1 out of 50 basal cells are provided with multipotency. These mammary stem cells (MaSC) are capable of differentiating towards either luminal or basal progenitors.[4] Whereas the luminal epithelial layers' functional role is mainly restricted to developing into lactiferous ducts, the functionality of myoepithelial cells is more complex. Besides coordinating differentiation, proliferation, polarization and migration of adjacent luminal cells, myoepithelial cells produce the basement membrane (BM) which unsheathes the epithelium, separating epithelial from stromal compartment. Moreover, the contractile competence of the myoepithelial layer is required for the transport of milk towards the nipple of a breast-feeding woman.[5]

The BM, as physical barrier between the epithelial and stromal compartment comprises a thin but dense layer (= 0.2 µm) consisting of collagen IV, laminin and proteoglycans. Its extracellular matrix (ECM) is distinct from the one of the stromal compartment that predominantly harbors fibrillar collagen I, hyaluronic acid and fibronectin.[6] Both, BM and stromal ECM provide the cells with adhesion substrates, physical support, and spatial orientation contributing to ductal and lobular morphogenesis. Together with the cellular fraction of the stroma including fibroblast, vascular endothelial cells and immune cells they regulate tissue homeostasis. Notably, the immune microenvironment plays a pivotal role in tissue homeostasis and morphogenesis. Stromal, tissue-resident macrophages engage with MaSC in close proximity to the epithelium to support their regenerative capacity. Epithelial, ductal macrophages are thought to actively participate in apoptosis and phagocytosis occurring during involution. Cytokines and enzymes secreted from eosinophils and mast cells contribute to (patho-) physiological development processes. Additionally, cells of the adaptive immune system, such as Th1 cells, participate in tissue homeostasis.[7]

1.2 Cellular stress response, DNA damage and risk factors

Eukaryote cells feature evolutionary conserved instructions such as the cellular stress response (CSR) allowing them to sense stress damage and providing solutions how to cope with it. Within a tissue, endogenous cellular stresses, including reactive oxygen species (ROS), DNA-replication and endoplasmic reticulum stress, may synergize with environmental and exogenous stresses (e.g. hypoxia, starvation, hyper-osmosis) to disturb tissue homeostasis. Once a damage threshold is reached, CSR pathways are activated with the goal to minimize overall stress load. One of the first responses is the attenuation of cellular growth and proliferation which can reduce replication stress and thereby prevents mutagenesis. Activating cell-cycle checkpoints helps to maintain and monitor cellular integrity. Moreover, as a consequence of nutritional deprivation, cellular ATP levels decrease with a concomitant accumulation of misfolded proteins in the endoplasmic reticulum. Cells can respond via upregulating anti-oxidative factors and inducing heat shock proteins that function as chaperons to refold proteins.[8] To summarize, cells are capable of defusing a high stress load that occurs on a daily basis by using the CSR. However, once the delicate equilibrium between net cell growth and cell death rates, i.e. homeostasis, is impaired, cancer can arise.

Regarding the tissue of the mammary gland, environmental factors such as chronic inflammations and high levels of steroid hormones depict major stressors that may lead to cellular accumulation of DNA-damage and eventually mutagenesis.[7] A high risk factor to develop post-menopausal breast cancer is obesity [9] being considered as a state of chronic inflammation entailing tissue infiltration of macrophages. Pro-inflammatory mediators, upregulated in these macrophages increase the levels of released ROS species that cause DNA damage. Obesity is further associated with upregulation of aromatase levels leading to an increase in the production and circulation of estrogens. Their

proliferative effects, induced by the binding to the estrogen receptor alpha (ERα) with subsequent translocation into the nucleus to function as transcription factor, elevate the likelihood of DNA damage to occur. Besides the action of soluble factors linked to obesity, altered mechanical properties of the adipose tissue affect homeostasis. Obesity shows the risk to develop mammary interstitial fibrosis which in turn increases the stiffness of the ECM. The altered mechano-signaling ultimately perturbs the function of tumor suppressor molecules, impairing the repair of DNA double-strand breaks.[7]

The physiological menstrual and reproductive cycle comprises massive remodeling of the mammary gland as well as pronounced fluctuations of ovarian hormones. It can therefore be considered as stressor, possibly inducing malignant changes of the mammary epithelium.[2] It was shown that due to symmetric self-renewing cell divisions, the number of hormone insensitive MaSC expands during pregnancy and lactation. This increased pool of stem cells increases the short-term risk of developing hormone-insensitive cancers. Instead, after involution, the amount MaSC decreases and their self-renewing capacity is compromised reducing the long-term risk of establishing cancer. On the other hand, advanced maternal age for the first pregnancy and lack of breast-feeding are other pregnancy-related factors to increase the risk of developing breast cancer.[10] As described above, estrogen can be considered a promotor of malignant transformations. This is in particular relevant, as during the menstrual cycle an imbalance between estrogen and progesterone occurs, which due to its repetitive nature continuously increases the risk of defective DNA repair and of mutations, potentially leading to pre-malignant and malignant transformations. Additionally, estrogen amplifies mutagenic signals as it stimulates the secretory function of stromal cells that in turn may stimulate aberrant epithelial cells.[10]

Besides the latter risk factors and well-known lifestyle risk factors such as excessive alcohol consumption and smoking, as well as genetic predisposition decisively determines the probability to develop breast cancer. About 10 % of all breast cancer patients were shown to possess a hereditary predisposition and are associated with a family history.[10, 11] Mutations in master regulators of DNA repair and cell-cycle such as BRCA1/2, TP53 and PTEN entail loss of function of the encoded proteins leading to an impaired CSR.

1.3 The classification of breast cancer

Female breast cancer (BC) has become the largest cancer disease worldwide with a prevalence of 2.3 million new cases in 2020 with numbers rising, predominantly in the western high income countries. In 7 % of cases, patient will suffer from a lethal outcome with a higher incidence in low-to-middle income countries. [10, 12]. Briefly, the disease progresses along epithelial proliferations, benign neoplasms, *in situ* carcinomas to finally invasive and metastatic breast cancer.[13]

Malignant transformations arising within the epithelium of the mammary gland are, by definition, adenocarcinomas. Breast cancer is a heterogeneous disease on the molecular level, comprising local-regional and metastatic patterns. Pathologists further assess histological tumor type and grade as they provide complementary information to estimate prognosis and to decide over the therapeutic intervention. Morphologically, BC can be divided into 19 major histotypes including invasive (ductal) breast cancer of "no special type", invasive lobular carcinomas and other carcinomas of "special type" which can be further sub-divided. The tumor grade, defined by the degree of differentiation and proliferation activity, is an indicator of the cancers' aggressiveness.[14]

In order to make treatment decision, clinicians currently use a surrogate classification system, which is based on the intrinsic subtype nomenclature defined by Perou and Sorli.[10, 15, 16] Accordingly, histological and molecular features allow the differentiation into five subtypes. Estrogen receptor (ER) and/or progesterone receptor (PR) expressing tumors are considered hormone receptor-positive breast cancers. Depending on the proliferative state and histological properties, they can be further divided into Luminal A-like (strongly ER/PR-positive, 60-70 %) and Luminal B-like $HER2^{negative}$(10-20%) breast cancers. Luminal B-like cancers with amplified HER2 (ERBB2) gene are noted as Luminal B-like $HER2^{positive}$ tumors. Indeed, the HER2 gene is over-amplified in up to 15 % of all BCs, and aberrant activation of the receptor tyrosine-kinase encoded by this gene is linked to increased proliferation, cell survival and metastasis. Cancers that lack hormone receptor expression but exhibit HER2-amplification are recognized as HER2-enriched. Finally, tumors that lack ER-, PR- and HER2-expression are termed triple-negative breast cancer (TNBC, 10-15 %) and exhibit a basal-like gene expression profile.

1.4 From In-situ to invasive breast cancer

The exact mechanism by which breast cancer is initiated is mostly unknown. Likewise, consensus on how *in situ* carcinomas transit to invasive breast cancers (IBC) remains to be reached, and several theoretical models try to describe its underlying biology (**Figure 2**). Among *in situ* carcinomas, 80 % are classified as ductal carcinoma *in situ* (DCIS) which depict about 25 % of all diagnosed BC cases. DCIS is considered as a non-obligatory precursor of IBC. If untreated, 40 % of lesions will emerge into an invasive phenotype.[17] DCIS is defined as premalignant proliferation of neoplastic luminal cells within the ducto-lobular system of the mammary gland being still under the confinement of an intact basement membrane.[18] Contrarily, IBCs display an absence of an intact myoepithelial layer and/or BM including stromal infiltration of malignant epithelial cells.

Hence, accumulation of different genetic aberrations could have allowed luminal epithelial cancer cells to degrade the ECM of the BM followed by stromal invasion (= "Barrier invasion"-model). On the other hand, progenitors of basal myoepithelial cells could have acquired (epi-) genetic alterations affecting their differentiation process. Less differentiated myoepithelial cells are no longer capable of producing adequate amounts of BM-ECM impairing BM integrity (= "Barrier-failure"-model).[5] The healthy myoepithelial layer establishes a physical barrier and is further thought to exert a tumor suppressive effect in a paracrine manner. Secreted proteins such as Maspin could inhibit invasiveness and help to prevent DCIS-to-IBC transition.[17] Alternatively, genetic aberration of MaSC could explain both scenarios.

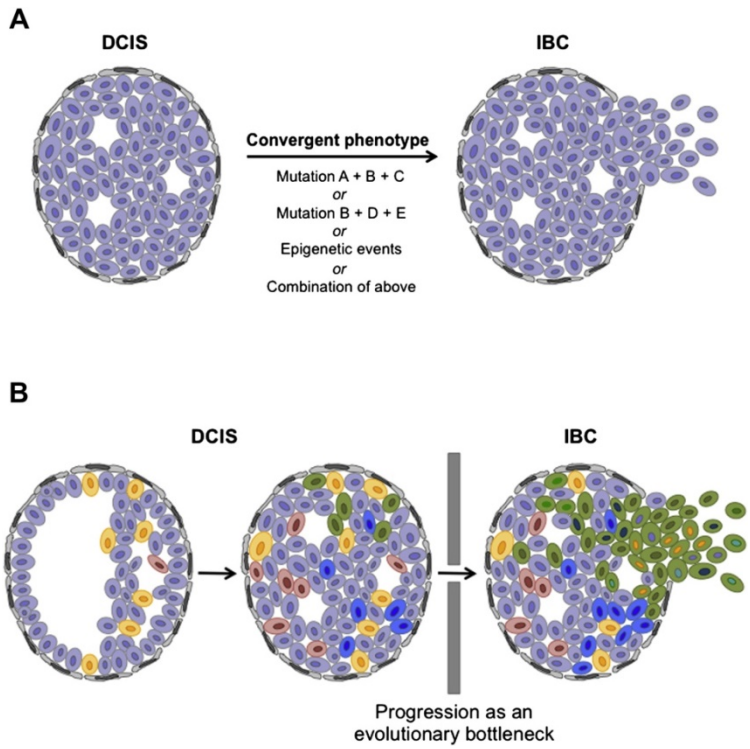

Figure 2. *From DCIS to IBC. (**A**) Convergent phenotype model (**B**) Evolutionary bottleneck model. [17]*

Certainly, the healthy epithelium and (pre-) malignant, transformed epithelial cells (e.g. DCIS) are genetically different due to acquired mutations. However, on the transcriptome level, studies have revealed a high degree of similarity between pre-invasive lesions and invasive breast cancer of the same histological grade. It was not possible to robustly discriminate between DCIS and IBC based on the gene expression signature. Moreover, it was found that DCISs already show a molecular heterogeneity which is mostly congruent with the mosaic observed in IBCs.[17, 19] Thus, the importance of genetic alterations for tumor progression is still under debate, giving rise to distinct evolutionary models (**Figure 2**). Possibly, as proposed by the "convergent phenotype-model", several combinations of somatic aberrations within DCIS are required to become invasive. Different ducts acquire different aberrations, but finally the different DCIS-genotypes lead to the same IBC phenotype. Alternatively, as described by the "evolutionary bottleneck-model", DCIS cells accumulate somatic alterations besides the driver mutations of the neoplastic progenitor, leading to heterogeneous lesions with distinct subclones. Finally, proprietary mutations of one subpopulation help to overcome an evolutionary bottleneck, e.g. by degradation of the BM, and cells become invasive. Still, it is also plausible that multiple clones are able of escaping the ducts and eventually invade into the stroma, which is referred to as "multiclonal invasion-model".[17, 18]

Epigenetic alterations between DCIS and IBC are thought to contribute to the invasive phenotype and may explain the lack of genetic differences. The chromatin states i.e., the accessibility of genes for transcription, are epigenetically controlled, emphasizing their general potential to contribute to tumor progression. For instance, global hypomethylation of oncogenes can be related to their transcriptional activity leading to chromosomal instability, whereas focal hypermethylation of tumor suppressor genes entail gene repression and impaired DNA-repair.[10, 17]

Moreover, the tumor microenvironment and the stromal compartment have been shown to drive tumor progression. The inflammatory environment entails tissue remodeling that is initiated due to infiltration of immune cells. But also paracrine activity of aberrant epithelial cancer cells plays a decisive role for tumors to become invasive.[5, 20-23] Prolonged paracrine stimulation of stromal cells with cytokines or growth factors can cause epigenetic changes. As a consequence, matrix metalloproteinases (MMPs), enzymes that initiate tissue remodeling and are capable of degrading the BM, are upregulated in stromal cells.[5] Indeed, epigenetic alterations of the secretome of stromal cells are possibly activating oncoproteins within the epithelial layer. Moreover, cancer-associated fibroblasts (CAFs) drive the selection of genetically abnormal epithelial cells that later become invasive. Likewise, CAFs enhance the mutation rate of adjacent epithelial cells as they release ROS and increase cancer cell metabolism.[24] The spectrum of the secretome of such activated stromal cells, besides soluble factors, includes the massive deposition of collagen I and other stromal ECM components. As a consequence, tissue density increases, altering the overall mechanical landscape and

ultimately mechano-signaling of cancer cells, which is presumably another driver for tumor progression, from DCIS to IBC.[25-27].

Even though a lot of recent data underlines the similarities between the transcriptome of DCIS and IBC, Knudsen *et al.* showed, by analyzing micro-dissected DCISs and IBCs, that gene signatures representative for the Epithelial-to-Mesenchymal transition (EMT) were enriched in IBCs. The authors concluded that the transcriptional reprogramming towards the invasive EMT phenotype, occurring in the epithelium, may be considered a general difference between DCIS and IBC.[28] Indeed, features such as diminished numbers of cell-cell contacts, increased secretion of ECM degrading enzymes as well as enhanced migratory capacity which are comprised within the EMT program, are theoretically advantageous for neoplastic DCIS cells to transit towards a stroma-infiltrating IBC. Accordingly, transformed cells are capable of detaching from the epithelial entity once they have degraded the BM to eventually invade the stroma of the mammary gland.

2. The Epithelial-to-Mesenchymal transition (EMT)

2.1 The basics of EMT and tumor progression

The Epithelial-to-Mesenchymal transition (EMT) or plasticity (EMP) is a reversible and non-binary trans-differentiation program of epithelial (E) cells. Cells loosen up their cell-cell junctions to acquire a motile state where they gain mesenchymal (M) features at the expenses of epithelial molecular characteristics. Besides abandoning their apico-basal polarity whilst adapting an elongated, spindle-like morphology, the motile state features other pro-invasive factors such as an altered protease-rich secretome and modified cell-substrate adhesion complexes. The reversal of this process during which mesenchymal cells (re-) transform into an epithelial phenotype is called the Mesenchymal-to-Epithelial transition (MET). However, cells not necessarily undergo a full transition but develop intermediate or hybrid E/M or M/E phenotypes. In many patho-physiological scenarios, the cycle of EMT-MET serves as operational mode of cellular plasticity to trans-locate epithelial cells within a specific region of a tissue or even throughout the body during formation of metastases.[29-33] In regard to the biological context, EMT has been categorized into three types.[34]

Type I is associated with many events of embryo formation and organ development. For instance, at the earliest stages of embryogenesis, trophoectoderm cells are required to undergo EMT as it facilitates the invasion of the endometrium and the subsequent proper anchoring of the placenta, which is necessary to establish functional nutrient and gas exchange. Other examples for the participation of EMT type I are gastrulation and neural crest formation.

In the second type of EMT, the differentiation mostly gives rise to a partial-EMT phenotype (E/M) where cells retain some cell-cell junctions, but due to mesenchymal acquisitions are more motile and are able to translocate as a collective. Type II EMT, which is associated with local inflammation, is thought to play a crucial role during wound healing and tissue regeneration as well as, in case of aberrant inflammatory signaling, organ fibrosis.[34] As part of wound re-epithelialization, epidermal keratinocytes at the margin of a lesion build a migratory zone. By undergoing a partial EMT, induced by inflammatory cytokines, cells connectively migrate towards the center of the wound. Proliferating keratinocytes distal from the injury possibly contribute to the movement by exerting proliferative pressure.[35] Simultaneously, it is also thought, that myofibroblasts arising via EMT from resident epithelial cells in close proximity to the wound take part in the wound healing process as they synthesize ECM components and contract the wound bed, enabling approximation of the injured edges.[36]

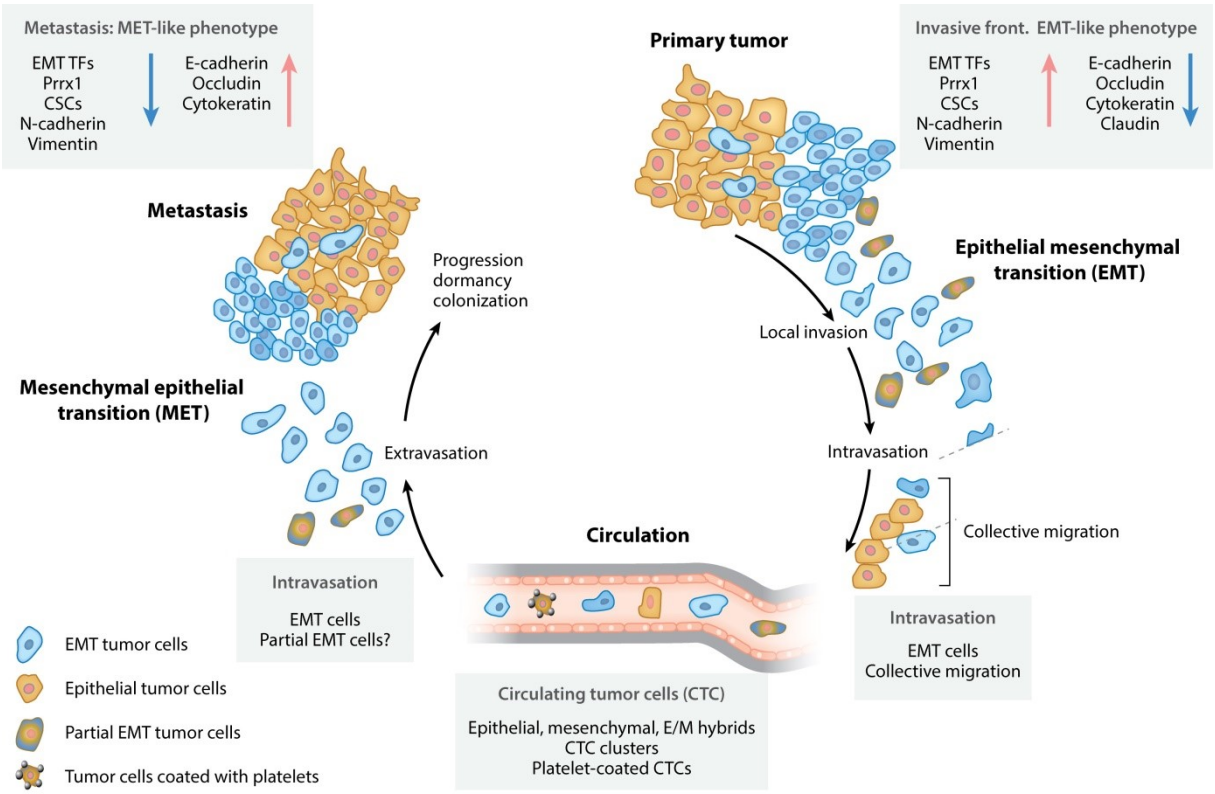

Figure 3. *Schematic scenario of the contribution of EMT and MET during the course of metastasis.[37]*

Finally, EMT of type III is thought to contribute to invasion and metastasis of neoplastic cells (**Figure 3**). Type III EMT may play a central role during tumor progression as the contribution of the EMT-MET cycle is generating the final, life-threatening manifestations of cancer i.e., metastasis. During the

course of metastasis, cellular plasticity as provided by the EMT/EMP program, permits spatio-temporal cellular adaption to differently demanding micro-environmental conditions.[30, 38-42]

Starting with *in situ* carcinomas of epithelial nature, the partial acquisition of mesenchymal properties as a result of prolonged inflammatory stimuli allows cells to tackle the basement membrane, constituting a major mechanical hurdle. As the BM is degraded by the activity of MMPs or other ECM-degrading enzymes, E/M or fully mesenchymal phenotypes may take advantage of the BM failure and penetrate into the surrounding stroma to initiate the subsequent step of metastasis, namely invasion. It is yet to be fully elucidated, whether single mesenchymal cells that have undergone a complete EMT or rather partially transformed E/M hybrids that constitute a multicellular entity, including intact cell-cell junctions of epithelial cells, are the prevailing phenotype at this stage.

The mesenchymal migrating cells undergo massive cytoskeletal re-organization to establish this highly invasive phenotype. Actin-rich protrusions at the leading edge of the cells are sensing the environment to adjust cell mechanics in order to navigate through the tiny pores of the ECM-enriched, dense tumor microenvironment. Simultaneously, locally elevated activity of proteases within protrusions, called invadopodia, is thought to be necessary to pave the way towards the vascular or lymphatic vessels. Protease activity can generate pores or widen existing pores further, supporting the transmigration process. Additionally, as ECM is degraded, latent cytokines and growth factors immobilized within the now degraded ECM are released, which could feed and maintain the (partial) mesenchymal phenotype. Moreover, once mesenchymal cells face major confinements spatially restricting migration, the Mesenchymal-to-Amoeboid transition (MAT) allows for migration in absence of proteolytic ECM breakdown. “Amoeboidness” is currently believed to be an additional phenotype within the universe of EMT introducing further cellular plasticity, compliance and survival advantage in many types of cancers.[43]

With regards to collective migration, it is now believed that helper cells perforate the stromal compartment by their proteolytic activity. Alternatively, based on a front-rear cell organization of the collective entity, partially mesenchymal leader cells may guide the collective as they exert pulling forces on the rear. Those leader cells may either be of epithelial origin (EMT) or of stromal nature. Indeed, CAFs remodel the ECM to form tracks mediating cancer cell migration as well as mechanically pull on collectively migrating cells to direct the migration process.[44] As a collective entity, in contrast to single cells, intercellular signals provide survival cues promoting its invasive capacity and a higher resistance to clinical treatments.[45] In addition, such cell clusters, after successful intravasation into the blood stream, form circulating tumor cells (CTCs) which are more apoptosis-resistant and display an enhanced tumor-initiating potential than their single moving, mesenchymal CTC-counterpart.[46]

CTCs that have survived within the circulation can potentially colonize distant organs to give rise to secondary tumors. Cancer cells indeed receive signals from the matrix of distal organs to direct their metastasis.[47] After attaching to the walls of blood vessels through the participation of adhesion molecule on the cancer cell surface, cells need to leave the endothelium again to finally build metastatic foci. The mesenchymal phenotype is advantageous for both the disruption of endothelial junctions and the invasion into the foreign ECM. The reversion *via* MET, generating an epithelial phenotype, allows for the proliferative expansion of the tumor mass at the secondary side. This explains why distal secondary tumors have histopathological similarities with the primary tumor.

2.2 Induction and regulatory network of EMT

The regulation of the EMT program is highly complex and varies depending on the biological context. The process comprises EMT-inducers, EMT-regulators, and EMT-effectors.[48] Up- or downregulation of expression and/or activity of the EMT-regulator and EMT-effector genes are indicative of the transition or its reversal (**Figure 3 and 4**).

Generally, EMT-inducers function as upstream ligands that bind extracellularly exposed receptors to stimulate intracellular kinase cascades, promoting alterations of gene transcription. Prominent EMT-inducers are mainly soluble factors such as cytokines and growth factors, including TGF-β, TNF-α, EGF, PDGF, NF-κB, Wnt and many more. Similarly, receptors binding to solid components of the stroma i.e. the ECM, such as integrins or Discoidin-domain receptors (DDR) will, after ligand binding, intracellularly initiate transcriptional changes *via* focal adhesion complexes.[49] Their functionality is often linked to the mechanical properties of the microenvironment, where extracellular mechanics are transduced *via* receptor interaction into intracellular signals. These mechanoreceptors may crucially participate in the EMT-induction of breast cancer cells regarding the massive, desmoplastic alterations of the ECM that occur during tumor progression. Moreover, environmental conditions entailing distinct metabolic parameters can trigger EMT-like changes in cancer cells. For instance, hypoxia-induced factors promote the overexpression of the transcription factor SOX9, which impedes the ubiquitination and thereby degradation of SNAIL, a central transcription factor of EMT.[50] Likewise, extracellular acidosis resulting from glycolytic metabolism supports EMT-like changes.[51, 52]

EMT-regulators i.e., activated transcription factors (TFs) stimulated by upstream EMT-inducers, are of fundamental importance during the trans-differentiation as they drive and sustain the phenotypic changes. In most of the cases, their action suppresses epithelial-related genes and/or enhances mesenchymal transcription. TFs such as SNAIL, SLUG, ZEB1 and ZEB2 exert their EMT-regulatory function by directly binding to the promoter region of epithelial genes and consequently preventing their transcription, whereas other TFs such as TWIST repress the epithelial phenotype indirectly. Notably, the central role of TFs is further emphasized as initiation of one of the latter TFs often simultaneously induces the transcriptional activation/repression of multiple EMT-effector proteins

responsible for cell-cell or cell-ECM interaction, cytoskeletal restructuring and increased mobility. Regulation is further operated by epigenetic regulatory mechanisms such as histone or DNA modifications and RNA interference (RNAi) by microRNAs (miRNAs). Depending on its target, miRNAs can work as an epigenetic tool to either suppress/activate EMT-related transcription factors or directly inhibit EMT-effectors. The miRNA-200 family, for instance, is known to directly bind to EMT-related transcription factors ZEB 1 and ZEB 2, leading to their degradation which concomitantly maintains an epithelial or reverts a mesenchymal (MET) phenotype. However, once miRNA-200 is inhibited, ZEB1/2 promotes mesenchymal properties. Such reciprocal repression loops are characteristic for epigenetic regulation of the EMT process via miRNAs and are also described for regulatory networks comprising SNAIL and TWIST.[48] The generation of transcriptionally active or repressive histone marks that are catalyzed by enzymes such as histone methyltransferases/demethylases or histone acetyltransferases/deacetylases (HATs/HDACs) depict another principle of epigenetic regulation of EMT. These covalent modifications on the lysine residues of nucleosome subunits determine DNA-packaging within chromatin, dictating transcriptional activity or repression of genes. Densely packed regions i.e., heterochromatin are transcriptionally inactive whereas less dense euchromatin refers to higher transcriptional activity. Epigenetic enzymes that catalyze these histone modifications co-opt with or are activated by EMT-TFs to repress epithelial genes or enhance mesenchymal gene transcription. However, the mentioned epigenetic contribution is only functional in the short-term. In contrast, DNA-methylations allow progenies over the course of multiple successive cell divisions to exhibit mesenchymal features that can in turn support their ability to invade or disseminate. For instance, methylation at the CpG dinucleotides near promoters of epithelial genes allows for stable gene silencing and thereby can contribute to a mesenchymal phenotype in the long-term.[38]

Finally, EMT-effectors are functional and structural proteins that can also be considered as biomarkers for the EMT process. During the course of EMT, proteins that establish cell-cell junctions such as tight junctions, adherens junctions, desmosomes and hemi-desmosomes are abrogated. At the same time, mesenchymal proteins are upregulated, enabling the restructuring of the cytoskeletal network towards a pro-invasive, spindle-like phenotype. Additionally, the secreted ECM of epithelial cells includes laminin which constitutes the BM-integrity, whereas mesenchymal cells produce BM-degrading enzymes such as MMPs **(Figure 4**). Monitoring these representative markers enables researches to estimate the EMT phenotype. Cells that express both, epithelial and mesenchymal proteins are considered as partial EMT or E/M hybrids. In the past two decades, expression levels of E-cadherin (epithelial) and vimentin (mesenchymal) have been frequently measured in order to estimate the underlying EMT-state, probably also because both proteins exhibit “counter-proteins” which are representative for the opposing phenotype.

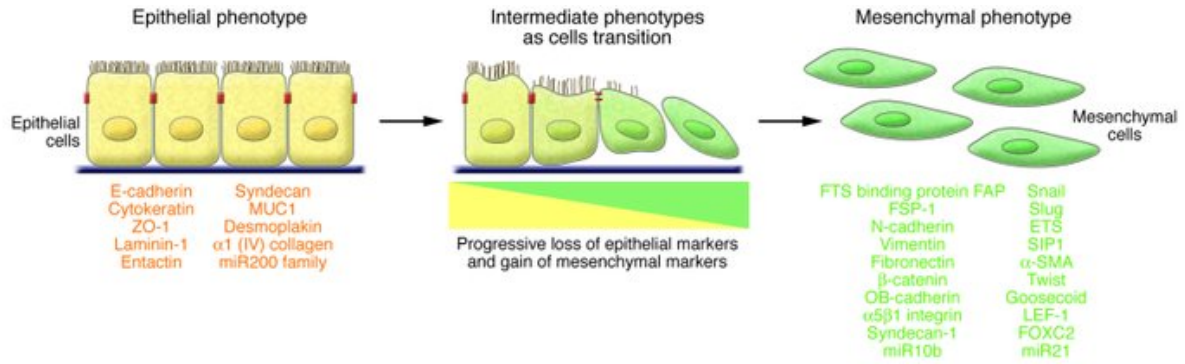

Figure 4. *Biomarkers of the epithelial and mesenchymal phenotype.[34]*

The extracellular domain of the epithelial E-cadherin participates in the establishment of adherence junctions and maintains the mechanical integrity of the epithelial layer. Upon EMT-induction E-cadherin is replaced by the neural N-cadherin, a process known as “cadherin switching”. The destabilization of E-cadherin releases intracellularly-bound β-catenin to function as a transcriptional activator for cell proliferation, whilst adherens junctions, a physical interconnection between neighboring cells, are dissolved. Instead, N-cadherin produces weaker cell-cell junctions and enhances cellular motility also by interacting with multiple growth factor receptor signaling pathways that can induce cell growth and metastasis.[49, 53] Likewise, expression of intermediate filaments changes upon the cytoskeletal re-structuring that is part of EMT. Vimentin, phenotypic of the mesenchymal type replaces cytokeratins in epithelial cells. Cytokeratins span a supportive network ranging from the cell membrane to the nucleus and associate with desmosomes. Desmosomes physically link the cytokeratin network of adjacent cells contributing to the morphology, integrity and mechanical resistance to stress of the whole epithelial entity. Additionally, cytokeratins support the correct localization of E-cadherin in adherens junction underlining their importance for the epithelial phenotype. Contrarily, the structurally similar vimentin-network absorbs localized, mechanical stress on the single-cell level and disperses it over the whole cell. It forms a hyper-elastic network that ensures cell viability even during the migration and invasion of mesenchymal cells through a confined and compressive environment, such as is found in the diseased tissue of the mammary gland. Moreover, vimentin orchestrates with actin and microtubules during directed migration, which, together with its load-bearing function, emphasizes its central role to favor migration and invasion during cancer progression.[54]

2.3 Clinical importance of EMT for breast cancer

Among the different intrinsic subtypes of breast cancer, basal-like phenotypes display a triple-negative phenotype in about 80% of cases and are thus of particular threat to patients.[55] Current causative therapies targeting either the hormone sensitivity of ER-expressing cancers *via* estrogen receptor modulator Tamoxifen (or aromatase inhibitors) or the overexpression of receptor tyrosine kinase HER2 with the monoclonal antibody Trastuzumab, fail to be effective for TNBCs. Studies showed that the basal-like phenotype holds a certain proclivity for distant metastasis to characteristic tissues such as the lung and the brain.[10] Researches proposed, that the underlying genetic context of basal-like breast cancer favors EMT/EMP-initiation giving rise to highly aggressive and characteristically metastasizing tumors.[56] Indeed, EMT-specific markers have been repeatedly linked to TNBCs *in vitro* as well as *in vivo.* Their identification could thus be clinically implemented in the prognostic and diagnostic monitoring of breast cancer.[57-59] The E/M plasticity may equip cancer cells with an adequate tool-set to promote tumor progression including the transitioning from a DCIS to an IBC. On the one hand, as described in Section1.4, EMT-like changes favor the degradation of the BM and the subsequent dissemination of cancer cells from the primary tumor to invade the stromal compartment. On the other hand, EMT presumably confers stem cell-like properties to a small subpopulation of $CD44^{high}/CD24^{low}$ breast cancer cells promoting their self-renewal capacity which is advantageous to initiate a tumor at a secondary side.[60] Such EMT-driven cancer stem cells (CSCs) convert into a quiescent or very slowly replicating state which is resistant to standard cancer therapy. Thus, EMT does not only encourage tumor progression but also mediates drug resistance which may lead to disease recurrence. The contribution of the EMT phenotype is, however, dependent on the various stages of the EMT continuum (*e.g.* intermediate E/M or fully mesenchymal phenotype) which are differentially important for migration, invasion, metastasis and chemoresistance.[61]

Taken together, EMT-related molecular targets are promising candidates for drug development, as their impact on the malignancy of the otherwise “undruggable” nature of the basal-like phenotype is multifactorial. Hence, aiming for EMT-inhibition in breast cancer may enable to hit tumors at different stages of progression thereby improving the patient’s prognosis and health outcome.

3. In-vitro models in cancer research

3.1 From conventional 2-D culture to 3-D environments

It has been mandatory over the last 80 years to pass animal-based trials evaluating the safety and efficacy profile of new drug candidates to get clearance by the Food and Drug administration (FDA) for clinical research studies. In December 2022, the US president Joe Biden signed legislation, however, no longer requiring animal experiments in this respect. Non-animal models such as 3-dimensional "organ chips" and/or computer modeling may also be used to substantiate preclinical studies.

This marks a fundamental change in drug research. It not only helps saving many animal lives but also significantly accelerates drug development due to the high-throughput character of the techniques now being authorized. This progress has been made possible by the design and development of highly complex 3-D cell culture models such as organoids, starting from simple cell line based 2-D models about 50 years ago.

The simplicity, cost-effectiveness and high-throughput character of 2-D cell culture either using isolated primary cells or well-established cancer cell lines has enabled groundbreaking insights into developmental and disease biology as well as mode-of-action studies of drugs in the past. However, 2-D cultures are not suitable to reflect *in vivo* growth conditions. Neither growth substrates nor cell-cell arrangements within 2-D cell cultures depict a good approximation of the (patho-) physiological archetype. Cellular attachment to plastic culture dishes impairs cellular polarization, alters morphology and gene expression, abandons diverse phenotypes and even affects cell division. Intercellular adhesions only occur within the horizontal plane not respecting the 3-D architecture and multi-cellularity of *in vivo* tissue. As a consequence, organization of the structures inside the cell, secretion and cell signaling are crucially affected.[62] Moreover, it should be noted that in order to study invasion and metastasis, 2-D migration assays fail to respect the proteolytic and spatially-confined character of the latter processes. Regarding cancer progression, the aberrant proliferation of cancer cells leads to mechanical compression of cells as well as a shortage of nutrients and oxygen at the core of the growing tumor depicting another biologically relevant shortcoming of conventional 2-D cell culture.[63]

Instead, 3-D cell cultures can re-establish the physiological cell-cell and cell-ECM interactions thereby mimicking tissue peculiarities as found *in vivo*. Furthermore, they partially materialize the complexity of a tissue, including compartmentalization into the epithelial-stromal compartment and physical properties of the ECM. For instance, spheroids i.e., self-assembled 3-D cell clusters, of normal mammary epithelial cells embedded into a BM-mimicking gel resulted in the formation of acinar structures similar to those that are found in the ductal-lobular network of the mammary gland.

Contrary, malignant breast cancer cells formed disorganized colonies and maintained their invasive phenotype, a distinction which cannot be detected in common 2-D cell culture.[63] It is widely acknowledged that cancer spheroids embedded in ECM-mimicking gels, in comparison to 2-D cultures, change their chromatin structure, and consequently their gene expression towards a gene expression profile resembling *in vivo* tumors. Notably, the physico-chemical properties (*e.g.* stiffness) of such ECM-like substrates seem to determine these alterations.[23] Moreover, the tissue-relevant functionality of 3-D cell culture models is particularly relevant for drug-screening purposes. Metabolic activity of drug-converting enzymes is compromised within a few days once transferring primary cells to 2-D monolayers, which may lead to an incorrect interpretation of the toxicity profile *in vitro*. Likewise, cellular morphology and spatial arrangement of cell surface receptors, which are often targets of tumor medicine, are different from 3-D set-ups. This is thought to explain the increased susceptibility to some drugs in two dimensional culture systems when compared to 3-D set-ups. Furthermore, the effectiveness and efficiency of some drugs depend on the cell-cycle phase. Whereas in 2-D cultures most cells reside in the same phase, cell-cycle phases vary in three dimensional cultures. For example, hypoxia-induced G0-phase arrest conferred enhanced drug resistance of cancer cells growing as spheroids.[63-65] Thus, 2-D studies on new drug candidates may overestimate their therapeutic potential.

Overall, the improved *in vitro-in vivo* correlation of 3-D cell culture set-ups contribute to a deeper understanding of developmental and cancer biology. It will also help to enhance the efficiency of clinical trials investigating new drug candidates.

3.2 State-of-the-art in-vitro approaches to model the tumor microenvironment

To allow for a solid prediction of cancer cell behavior and therapeutic efficacy of new drug candidates *in vivo,* it is necessary to provide an environment *in vitro* that accounts for the complexity of the TME. This may include the arrangement of cancer cells and the adjacent stromal compartment, the stiffness and topography of the ECM within the stromal compartments or the paracrine communication between cancer and stromal cells. Depending on the particular stage being investigated (*e.g.* invasion, intravasation), it may be required to customize the respective model accordingly (*e.g.* vascular system, systemic circulation). In the following, current three-dimensional approaches for mimicking the tumor microenvironment will be introduced.

Hydrogel-based approaches are one the most applied techniques to model the TME. Hydrogels present a highly tunable system made either of ECM components such as collagen, fibrin and hyaluronic acid or synthetic polymers such as poly(ethylene)glycol. In general, they are liquid at 4° C but once temperature is raised or cross-linking agents are added polymerization starts, and a network-like matrix is obtained. By concomitantly adding cell types of choice, the latter are incorporated within the hydrogel. Within the gel, the cells self-organize and remodel the matrix once it has solidified. The ease

of tailoring the mechanical properties of hydrogels allows for studying the influence matrix composition and biomechanical properties exert on cells. Synthetic hydrogels offer a higher reproducibility with less batch to batch variations and more precise fine-tuning of the matrix's visco-elastic properties, whereas ECM-based hydrogels are structurally more similar to a native matrix.[66, 67]

Organotypics, as derivative of hydrogels, make use of the latter to compartmentalize different cell types and to study their bidirectional crosstalk, ultimately improving tissue mimicry. Briefly, cancer cells are placed on top of a hydrogel which is laden with other tissue-specific cells types. Such a set-up enables, for instance, the study of communication between epithelial cancer cells and cancer-associated fibroblasts (CAFs) or macrophages, which are normally situated in the adjacent stroma, and to show how they enhance cancer cell invasion.[66, 68]

Micro- and nanofabrication technologies allow for the fabrication of endless micropatterns, complex topographies and curvatures to design fibrous or hard scaffolds on the basis of the native ECM. Both, synthetic (*e.g.* PCL) and naturally occurring polymers (*e.g.* alginate, collagen) can be applied to technologies such as 3-D bioprinting, photolithography or electrospinning. It is possible to design 2.5 to 3-dimensional cues in order to preserve a differentiated, tissue-specific phenotype, rendering such approaches particularly useful for tissue regenerative purposes. Scaffold stiffness, porosity and topography can be easily tuned and synergize with a huge variety in design options. The fibrous and/or porous nature of the scaffolds confines single cells or cell clusters to trigger biological responses such as cell-adhesion, migration, proliferation and differentiation.[63, 67, 69, 70] For instance, it was shown that the proliferation of TNBC cell lines seeded on an electrospun PCL scaffold was enhanced and the cellular phenotype accumulated in CSC-like properties, which emphasize the scaffold's power to mimic the ECM of the cancer stem cell niche.[71]

Spheroids offer an environment more akin to the tumor, with self-established nutrient and hypoxic gradients introducing dimensions that cannot be experienced within conventional 2D culture. Spheroids consist either of one single cell type or as multicellular assembly. Using ultra-low attachment plates or hanging drop cell culture techniques allows cells to establish cell-cell junctions and to proliferate as one single entity. The growing spheroid develops a hypoxic and nutrient-deprived core similar to the *in vivo* conditions. By embedding spheroids into hydrogels, they can be upgraded to organotypics, which permits to investigate the influence of the ECM on a growing tumor or its communication with stromal cells. However, not every cell line is capable of forming spheroids and cultures thereof persist for a short term only.[66, 67]

Organoids or tumoroids, unlike spheroids, are not formed with differentiated cells but self-assemble from stem cells that maintain pathological, genetic and heterogeneous features of the host tumor. Thereby, multicellular structures can be produced that highly resemble the cellular organization of the

host tissue whilst retaining tissue-specific functionalities, including intestinal crypts, renal tubuloids and mammary ducts. Moreover, they can be passaged and cryopreserved similar to conventional cell lines, thus possibly allowing for the replacement of the latter in the future. They constitute “organ”- or “body-on-a-chip” devices that combine organoids with microfluidic devices used for the establishing personalized medicine. Similar to spheroids, they can be further placed into a hydrogel scaffold to become organotypics.[66, 69]

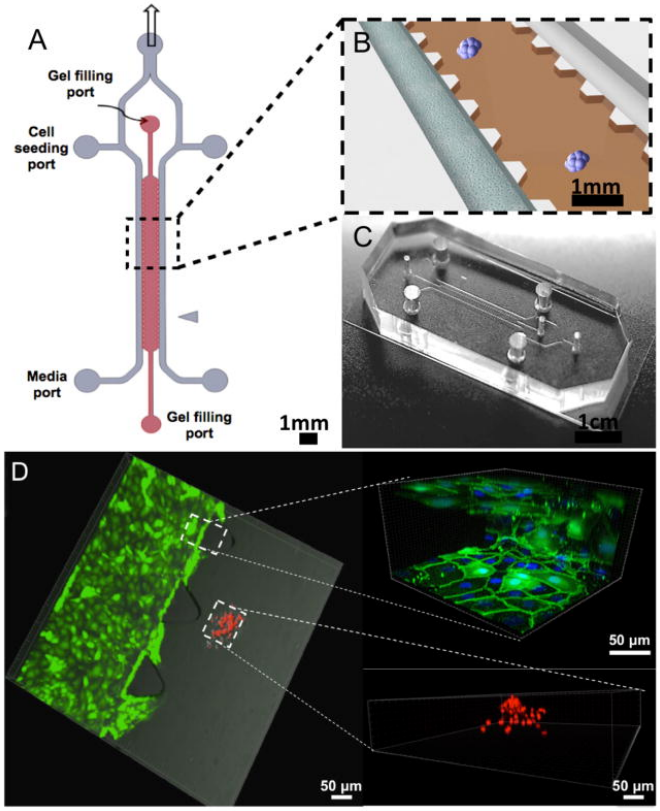

Figure 5. *Microfluidic set-up for co-culture of endothelial monolayer with cancer spheroids.[72] Schematic illustration of the set-up (**A**) and the co-culture (**B**). (**C**) Image of the microfluidic device. (**D**) Confocal image (z-stack) showing the co-culture of the endothelial monolayer (green) with cancer spheroids (red).*

Finally, microfluidics provide the unique advantage to introduce fluid flow, which is a key limitation of other 3-D models (**Figure 5)**. The hollow channels of microfluidic devices are ideal to study the tumor vasculature and processes such as intra- and extravasation in real-time. Different cell types can be included, either perfused or incorporated in a separate compartment. Perfusion enables constant supply of oxygen and nutrients as well as removal of metabolic waste. Further, it allows studying the impact of shear forces and interstitial fluid pressure *e.g.* cues endothelial cells experience from the

blood circulation. Ultimately, any of the above mentioned technologies can be combined with microfluidic devices to introduce a higher level of complexity and tumor mimicry conferring triggers from the ECM as well as cancer-associated stromal cells.[66, 67]

3.3 In-vitro models to study EMT in breast cancer

Tissue peculiarities of the mammary gland which have to be considered for the design of an *in vitro* model mostly rely on the micro-environmental conditions that vary along the different stages of tumor progression. In this section, ways to how bio-mimic tissue organization at different tumor stages and study the possible role of EMT are shortly introduced.

As regards DCIS, one ideally has to account for an intact collagen IV-enriched basement membrane decorated with a layer of myoepithelial cells bearing the neoplastic cells of interest on top. Here, the contribution of EMT-like changes may be the matter of research since the plasticity program confers properties that enable premalignant cells to overcome the physical barrier represented by the BM (see Section 1.4 and 2.3). The BM could be readily imitated by the use of hydrogels to establish organotypic models. Likewise, at a later stage, for invasive breast cancers it is necessary to invade and transmigrate through a densely-packed stromal compartment which comprises, besides stromal cells, biochemically and topographically distinct ECM *i.e.,* fibril-forming collagen I. Here, fibrous scaffolds and/or hydrogels are ideal candidates to bio-mimic the microenvironment of the stromal compartment. Indeed, unique micro-architectural features, so-called tumor-associate collagen signatures (TACS), have been described during tumor progression within the mammary gland and are thought to facilitate invasion and metastasis.[6] Furthermore, despite these BC-specific topographical characteristic, one may include the input the mechanically altered landscape of the stromal compartment exerts on both, DCIS and IBCs. Hence, it may be required for the design of an *in vitro* model to include stiffness gradients and unique visco-elastic properties of the ECM that are described for the different stages of tumor progression to reveal the role of EMT in this context.[73] Finally, for cancer cells to enter or leave the vascular system, EMT-like changes may support transendothelial migration.[74] To study the latter, microfluidic set-ups might be a good choice and introducing a separate compartment loaded with a distinct ECM permits to simulate the final step of metastasis *i.e.,* relocation of cancer cells to a secondary side.

Walter *et al.*[75] tried to answer the question how defects of the BM would affect cellular phenotype of the human mammary epithelial cell line MCF10A. They created a multi-layered gel substrate by first synthesizing a collagen I gel placed on top of a soft poly(acrylamide) gel. There above, a layer of collagen IV was deposited where cells were grown until maximum confluency. Interestingly, manually introducing a physical defect into the collagen IV layer induced an EMT-phenotype at its margin which persisted and invaded into the underlying collagen I matrix. They concluded that the physical rupture of the BM induced the EMT phenotype *via* mechano-signaling. MMP9-driven degradation of

rupture-exposed collagen IV was postulated to be the underlying mechanism for the induction of EMT. Therefore, defects of the BM potentially arising from wounds or incisions may initiate EMT *in vivo* and commence the stromal invasion of cancer cells.

Interleukin-6 (IL-6) is known to promote EMT-like changes in breast cancer cells *via* the JAK/STAT3 signaling cascade including upregulation of TWIST, SNAIL, MMP9 and vimentin.[76] By using a triple-co-culture system comprising a DCIS-spheroid-forming pre-invasive mammary epithelial cell line embedded into a collagen I matrix, it was demonstrated, how the presence of myoepithelial cells can reduce CAF-induced invasion of DCIS into the collagen gel. Accordingly, CAF-DCIS co-cultures showed elevated levels of secreted IL-6, entailing enhanced matrix degradation and invasion of the DCIS. However, this effect was attenuated in the triple-co-culture which presumably relies on reduced secretion of IL-6 as a result of myoepithelial suppression.[77]

Saha *et al.*[78] introduced various breast cancer cell lines to an electrospun fibrous matrix in order to study the cell behavior and the influence of topographies on the cellular phenotype. Indeed, cells dispersed within the fibrous scaffold and aligned with the fiber orientation adopting a more mesenchymal phenotype. They found that morphological elongations of cancer cells were accompanied by an increased secretion of TGF-β1, which subsequently induced EMT in an autocrine manner. Correspondingly, genes that are affected by TGF-β1-signalling were upregulated including the transcription factor SNAIL.

Lastly, Aref *et al.*[72] used a microfluidic system to evaluate the efficacy of drug candidates that interfere with signal transduction pathways implicated in the EMT process. Tumor cell spheroids, incorporated in a 3-D hydrogel, were co-cultivated in close proximity to an endothelial monolayer using a 2-channeled microfluidic system (**Figure 5**). Solely culturing the A549 spheroids in the hydrogel was insufficient to yield an invasive phenotype within 36 h. Once in co-culture with endothelial HUVEC cells, a partial EMT-phenotype developed showing decreased levels of E-cadherin but increased levels of vimentin and cells started to disperse and invade into the matrix. To screen for the efficacy of targeted inhibitors of EMT-relevant signaling molecules the latter were applied in the inlet of the endothelial channel. The inhibitors, including drugs interfering with EGFR and TGF-βR activation, reversed the dissociation of the compact tumor spheroids being in paracrine crosstalk with the endothelial monolayer. Even though this study did not address EMT in breast cancer but in lung cancer, it shows how microfluidic devices can be exploited to study therapeutic interventions regarding EMT in a high-throughput fashion.

3.4 The principles of electrospinning to design fibrous matrices

The use of electrospinning for biomedical purposes has a long history. Its various applications in other related fields is based on the comparatively ease of producing non-woven fiber mats in the micron and submicron scale. Electrospinning can be applied to synthetic and natural polymers, which, together with the aforementioned dimension of the fibers, holds great promise for the design of advanced, ECM-mimicking *in vitro* models. However, it is a very intricate process that requires a lot of optimization to tune physical and visco-elastic properties of the resulting scaffold.[79, 80]

Electrospinning relies on an electrified viscous fluid jet that is carried through the air within an electric field towards a collector of different electric potential. The cost-effective set-up (**Figure 6**) comprises a syringe equipped with a thin, conductive nozzle (≙ electrode), a syringe pump including a tubing system for the transport of a polymeric solution towards the nozzle, a high-voltage supply (5-30 kV) connected to the nozzle and a grounded or oppositely-charged collector (≙ counter electrode) placed perpendicularly to the outlet of the nozzle in 10-30 cm distance. Both, vertical, from "top-to-bottom", or horizontal set-ups of the electrode pair are feasible. Once the polymer solution, advancing at a constant flow rate, enters the conductive nozzle, charge is injected. Due to tensile forces of the solution, a droplet is formed at the outlet of the nozzle. As voltage and with it the electric field strength is increased, tensile forces compete with attractive electrostatic forces. Once they balance out, the pendant drop is elongated, changing its shape from a rounded meniscus to a cone, the so-called "Taylor cone". As voltage is further increased, a polymer jet emits at the tip of the cone and is laterally accelerated, in a straight line, towards the oppositely charged collector. However, within the electric field, the emitting jet is subjected to diverse physical phenomena leading to whipping instabilities. further stretching the jet. The polymeric jet starts to spiral as result of the progressive solvent evaporation and increase in surface charge density whilst approaching the collector. Finally, the elongated, ideally completely solidified fibers randomly deposit on the collector's surface.[81, 82]

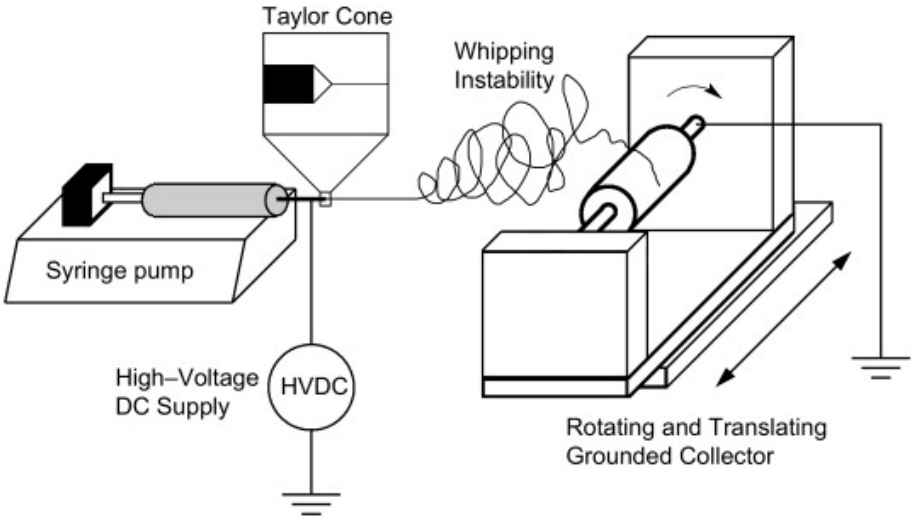

Figure 6. *Basic electrospinning set-up with a rotating collector.[83]*

Researchers have developed a vast set of options to design the physical parameters of the resulting fiber-mesh. For instance, with the choice of the collector, one can easily adjust the relative orientation of the fibers. In its simplest form i.e., the plate collector, randomly coiled fibers are produced due to the bending instabilities. These can be attenuated by introducing an additional magnetic field or by tuning the shape and the strength of the electric field, allowing to align and parallelize the depositing fibers. Likewise, strongly aligned fibers in a parallel orientation are obtained using a rotating collector such as a cylinder or a drum. The whipping instabilities still remain but fibers to get in contact with the rotating collector, spool around it and parallelize. The degree of alignment and pore size of the fibers can be tuned by the rotating speed and the width of a disk vs. cylinder collector. Further, structuring or pattering the collector depicts another measure to fine-tune the scaffold's porosity or architecture.[81, 84]

More complex fiber designs can be achieved by using more than one spinneret *i.e.*, nozzles arranged at different angles relative to the collector. Moreover, using two concentrically aligned nozzles enables to produce core-shell nanofibers with compartmentalization of two materials in a process called coaxial electrospinning, an approach often used to encapsulate drugs into a polymeric shell for the design of controlled drug delivery systems.[79, 80]

Furthermore, the physical and chemical properties of the chosen polymer as well as the polymeric solution affect the outcome of the spinning process. To permit for a constant spinning of the fibers, sufficient entanglements of the polymer molecules are required. The latter depends on the concentration of the polymer solution and the molecular weight of the polymer. Further, conductivity and viscosity of the polymeric solution are crucial for the success of the spinning process as they determine restrictive and attractive forces. In case of strong intermolecular association of a polymer

leading to high viscosities at low concentrations, it may be necessary to blend two different molecular weight species of the same polymer to facilitate the spinning process.[79, 80, 85]

Comprehensive reviews describe many more parameters to be considered during the spinning process such as flow rate, vapor pressure, humidity of the spinning chamber and the applied voltage strength.[82, 86, 87]

Finally, to establish electrospun scaffolds for cell culture purposes, several factors have to be addressed. First, if the chosen polymers are water soluble post-electrospinning, the scaffold will not persist in cell culture medium. Therefore, chemical crosslinking agents such as glutaraldehyde or genipin can be applied in order to retain its topographical features in culture to bio-mimic the native ECM.[80, 88] Second, the fiber dimension and pore size are crucial elements governing to what extent cells will interact with the scaffold. Cells experience microfibers that are within the size-range similar to cells rather as 2.5-dimensional substrates, whereas nanofibrous scaffolds allow for a more complex, 3-D interaction due to higher surface area and elevated number of binding sides. However, small pore sizes may impede cellular infiltration independent of fiber diameter, leading to rather two dimensional cues.[79] Third, some synthetic, hydrophobic polymers (*e.g.* poly(caprolacton)) besides having ideal viscoelastic properties, do not promote cell attachment. Consequently, ECM-coatings with collagen or pre- or post-spinning functionalization of the polymer (*e.g.* RGD-binding motive) are required to design biologically functional scaffolds.[89, 90] Although electrospinning is a relative old technology it is not outdated and researches highly appreciated the sheer endlessly adjustable screws to fine-tuning of the design for various biomedical and biotechnological applications.

4. Nanoparticulate siRNA delivery

4.1 RNA interference (RNAi)

The approval of ONPATTRO® (Patisiran) for the treatment of hereditary transthyretin amyloidosis in 2018, brought the first ever commercial RNAi-based therapeutic to the market, launching a completely new class of medicine. In the following years, driven by the potential to theoretically silence any chosen gene with a known sequence, Givosiran (2019), Lumasiran (2020), Inclisiran (2021) and Vuttisiran (2022) were approved by the FDA, and six other small interfering RNA (siRNA)-based therapeutics are currently being evaluated in clinical trials.[91] However, it took about 20 years from the discovery of RNAi as a regulatory mechanism of eukaryotic cells to control gene expression until its application as therapeutic agent.

Briefly, double-stranded RNA (dsRNA) engages with the cytoplasmic helicase/RNase-like III Dicer, which dissects 21-28 nucleotides-long pieces from dsRNA to produce so-called siRNA. The latter, together with a cluster of essential proteins, is subsequently incorporated into the RNA-induced silencing complex (RISC). There within, the siRNA is split into two single RNA strands recognized as sense and antisense. The antisense strand is capable of binding a homologous messenger RNA (mRNA) sequence, which is in the following cleaved by the enzymatic activity of RISC. Thereby, the translation towards the mRNA-specific protein is impeded causing the "silencing" or downregulation of the underlying gene.[92] Similarly, micro RNAs (miRNAs), other short RNA molecules to enable RNAi, are also processed by Dicer and enter the RISC entity. However, because of secondary structures such as interspaced mismatches and hairpin structures within the miRNA sequence, they are only partially complementary to mRNAs, explaining their more intricate functionality. Besides mRNA cleavage, miRNAs can induce mRNA degradation or simply translational repression. As a consequence, instead of specifically targeting one single mRNA as do siRNAs, miRNA's regulatory network is able to modify the expression of multiple mRNAs at the same time.[93]

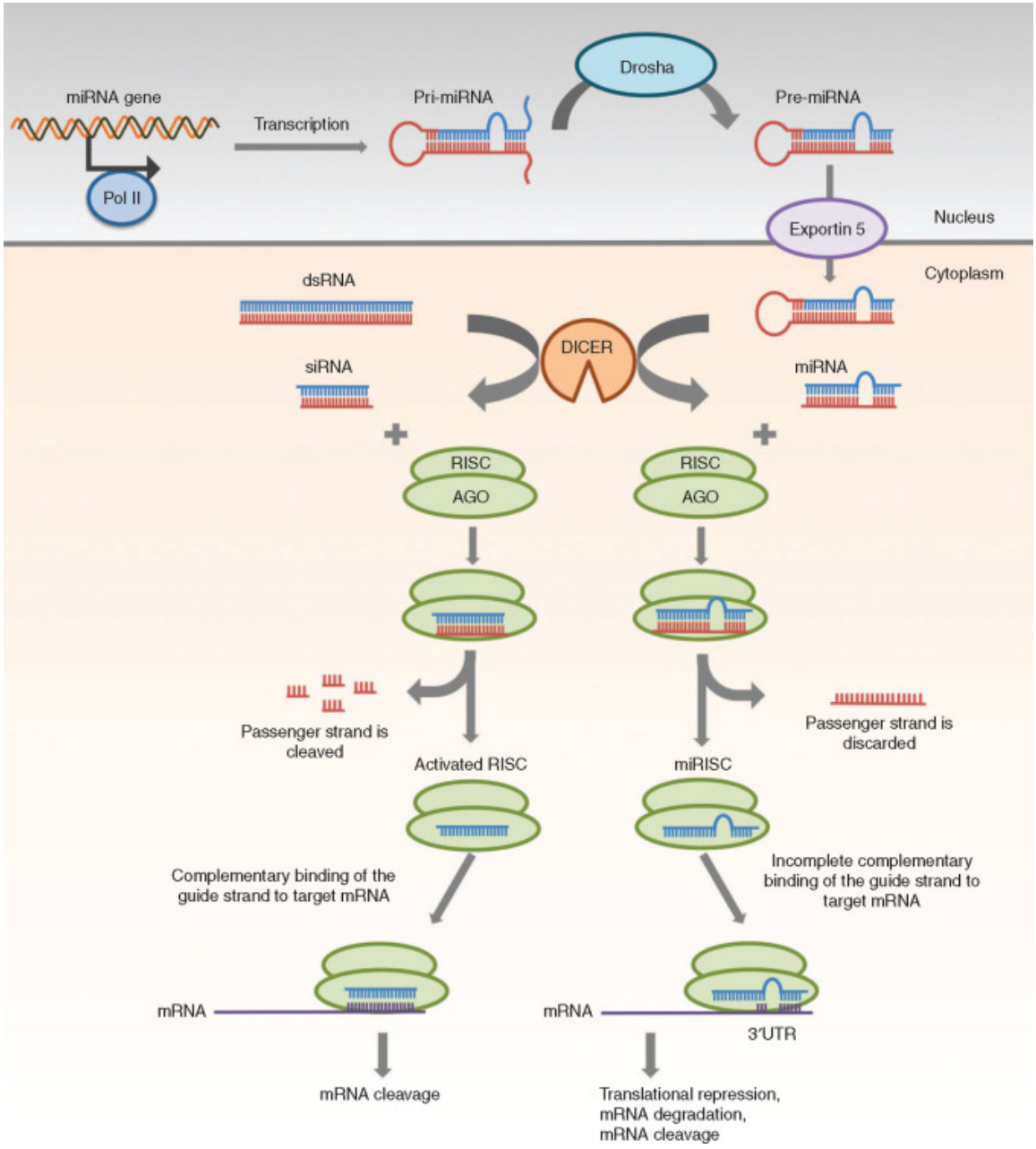

Figure 7. *Mode of action of siRNA and miRNA to induce RNA interference.[93]*

Synthetic siRNA-based antisense strategies exploiting the endogenous RNA silencing machinery are particularly useful (I) as they achieve high selectivity based on Watson-Crick base pairing and (II) offer the possibility to suppress any disease-related gene. It may be even feasible to target disease-specific alleles that are distinct from the normal allele by only one or few nucleotide substitutions allowing for targeting dominant mutants as occurs for some oncogenes.[94] With regard to its therapeutic deployment, the physicochemical properties of siRNA molecules bear some major challenges that need to be addressed. Unfortunately, siRNA is an extremely fragile molecule that is easily susceptible towards degradation by endogenous nucleases after systemic administration.

Moreover, as an oligonucleotide comprising a phosphate-ribose sugar backbone, siRNA molecules are hydrophilic and negatively charged, which is detrimental for passing the equally charged phospholipid bilayer of cell membranes *via* passive diffusion. Therefore, strategies to improve its stability and cellular delivery have been developed recently. Chemical modification of the RNA molecule, such as substituting the phosphate esters with phosphorothioate bonds can improve its resistance against exonucleases. Modifications of the 2'-OH ribose entity, including 2'-O-methylation or 2'-fluoro substitution, are common design options to favor superior thermodynamic persistence in siRNA duplexes. However, the most frequent approach to protect naked siRNA from degradation and to facilitate its cellular uptake is to incorporate RNA molecules into nanoparticles which serve as protective delivery vehicle upon administration.[95]

4.2 Endocytosis and intracellular fate of siRNA-loaded nanoparticles

For successfully initiating siRNA-mediated RNAi, it is obligatory to assure cellular internalization as its activity depends on its presence in the cytosol of an appropriated target-cell. Current siRNA-based therapeutics exploit two distinct strategies to fulfil the latter need.

siRNA-conjugates (*e.g.* Givosiran), which covalently couple molecules such as *N*-acetylgalactosamine (GalNAc) directly to the siRNA molecules, enable (I) strong plasma protein binding (> 90%), reducing renal clearance whilst prolonging the half-life of the drug and (II) selective targeting of an organ, mostly the liver.[96] GalNAc, for instance, introduces high affinity binding to the asialoglycoprotein receptor, which is overexpressed in hepatocytes, allowing for selective receptor-mediated endocytosis in the liver concomitantly reducing off-target effects. However, such approaches are primarily restricted to diseases which are based on a hepatic disorder.

Another approach to permit efficient as well as broadly applicable delivery of siRNA is its formulation within nanoparticles (NPs). The polymeric or lipid-based carriers (*e.g.* Patisiran) encapsulate or condense the cargo i.e., the siRNA, thereby shielding it from stressors upon administration. Simultaneously, the neutral or cationic surface charge of the carrier-cargo-assembly encourages cell-nanoparticle engagement and ultimately cellular internalization. In congruence with siRNA-conjugates, NPs may be functionalized to modify their pharmacokinetics and biodistribution, or to yield tissue-specific accumulation.[95-97]

Assuming systemic administration (*e.g.* intravenous injection), NPs need to maintain integrity within the vascular system, reach the organ of interest, leave the blood vessels and extravasate into the interstitium of the tissue to finally arrive at the cell of interest. Particles can then be internalized as a result adsorptive endocytosis by the cell membrane or by more concrete interaction with cell-surface receptors. Both scenarios fall in the category of pinocytosis, a general name for the energy-dependent uptake of a volume of extracellular fluid. Primarily through the invagination of the cell membrane,

colloidal dispersed material *e.g.* the polymeric nanoparticles, together with varying amounts of extracellular fluids are engulfed, which is recognized as endocytosis. On the contrary, for lipid nanoparticles (LNPs) membrane fusion, upon which LNPs associate with the phospholipid bilayer to form an intermediate state with the cell membrane, is postulated to be another mechanism of cellular entry.[98] During endocytosis, NPs are enclosed into intracellular vesicles *i.e.,* early endosomes that subsequently undergo diverse maturation, depending on their intracellular sorting. The endosomal payload may be subjected to endolysosomal degradation, translocated to other cytoplasmic compartments, or recycled towards the cell surface. However, for nanoparticles to successfully deliver their cargo, they must (I) assure the chemical integrity of the siRNA molecules during the endocytic processing but simultaneously (II) ensure endosomal escape and subsequent siRNA-release into the cytosol necessitating carrier-cargo disassembly.[99] Indeed, by choosing an appropriate nanocarrier design it is possible to modulate and improve intracellular siRNA delivery.

The pinocytic process can be further subdivided further into mechanisms entailing the uptake of large volumes of extracellular fluids *i.e.,* macropinocytosis and circular dorsal ruffles, and mechanisms that comprise the uptake of small volumes such as clathrin-mediated endocytosis, caveolae-mediated endocytosis as well as several clathrin- and caveolae-independent endocytic mechanisms.[100] As regards nanoparticles, micropinocytosis is described as general, non-specific route of internalization, whereas clathrin- and caveolae-meditated internalization particularly feature receptor-mediated endocytosis of ligand-functionalized nanocarriers.[101] However, it is most likely that uptake of one specific type of NP independent of functionalization, does not solely rely upon one single mechanism but includes the contribution of several pathways.

Nevertheless, clathrin-mediated endocytosis is considered the most widely used internalization pathway for cellular uptake of nanosized material as also described for transferrin and LDL receptor.[99] Upon ligand-receptor interaction, trimeric clathrin structures multimerize underneath the cell surface to form strongly curved invaginations termed clathrin-coated pits. Through the participation of a GTPase, the latter are pinched from the cell membrane to evolve to clathrin-coated vesicles intracellularly. After discarding the clathrin-coat, these early endosomes undergo acidification and fuse with other vesicular structures mostly deriving from the Golgi apparatus to mature into late endosomes. There within, the ligand-receptor complex starts to dissociate, and the endocytic payload is either recycled to the cell surface or is passed to lysosomes, which, due to low a pH and proteolytic enzyme activity, may degrade the internalized cargo.

The internalization route *via* caveolae may circumvent the harsh environment arising during the endo-lysosomal processing. Caveolae, flask-shaped invaginations in the plasma membrane, are enriched in caveolin proteins which associate with lipids such as cholesterol in the cell membrane to form so called “lipid rafts”. In congruence with clathrin-mediated endocytosis, GTP is required for the budding of the endocytic vesicle. The caveolae vesicle either fuses with early endosomes to succeed in a

similar fashion as described for clathrin-mediated vesicles or may develop into caveosomes which are devoid of proteolytic and acidic distress. The caveosomes are directed to the Golgi complex or are discharged through transcytosis.[99, 101] Considering the poor stability of the naked RNA molecule vis-à-vis lysosomal degradation, aiming for selective caveolae-meditated endocytosis may be advantageous for siRNA delivery.

4.3 Design of polymeric nanoparticles

The demand for systemic delivery of nucleic acids such as siRNA or mRNA has generated an enormous diversity of carriers/carrier materials, which enables to formulate the RNA molecules into nanoparticulate medicine. Among the materials to ensure complete encapsulation of the cargo as well as efficient cellular delivery, synthetic polymers or lipids are promising candidates, which are most frequently used. Their physico-chemical properties define encapsulation efficiency, *in* vivo stability, distribution and compatibility, cellular internalization as well as endosomal escape, which all together determine the *in vivo* efficacy of the drug.

In order to encapsulate RNA, most delivery materials comprise alkaline functional groups (*e.g.* secondary amines) that are facultatively protonated. Hence their pK_a and quantity is of importance. In its cationic state, they allow for efficient electrostatic self-assembly with the negatively charged RNA molecules to form nanosized, commonly spherical particles, namely polyplexes or micelleplexes. Most of the polymeric raw materials display a polycationic character (*e.g.* chitosan, polyethyleneimine (PEI)) even at physiological pH, giving rise to nanoparticles of overall positive surface charge. The extent of the cationic surface charge, which is estimated based on the zeta potential ζ, depends on the ratio of protonable amine units (N) within the polymer to phosphate groups (P) of the siRNA backbone, increasing with higher N/P-ratios. Excess amounts of the polymer enhance the siRNA-encapsulation efficiencies as well as cell-particle interactions but entail increased toxicity and renal clearance of the forming NPs on the other hand. A possible strategy to address the latter issue may include amphiphilic polymers that contain hydrophobic segments reducing the cationic charge density whilst still achieving effective siRNA delivery at lower toxicity.[102, 103] Contrarily, lipids such as used in Patisiran, are ionizable at acidic but neutral at physiological pH. Hence, the LNPs are formulated at low pH but, after re-buffering to a physiological pH, are adjusted to have a more or less neutral zeta potential, which persists *in vivo* and improves biocompatibility.[104]

The surface properties of the nanoparticles play a central role for their performance within the systemic circulation as well as for targeted delivery. As a consequence, surface functionalization (covalent and non-covalent) of particles and modifications of the raw polymer are set screws to adjust the surface properties according to the underlying desires. The highly positive zeta potential of polymeric NPs as well as van der Waals, hydrophobic, and several other attractive forces mediate protein adsorption on the particles' surface. This protein corona may include the adsorption of

opsonins, proteins that mark NPs for phagocytosis by immune cells of the reticuloendothelial system (RES). The activation of the RES enhances the elimination of nanoparticles from the circulation, thereby reducing the circulation half-life. Simultaneously, the adsorption of opsonins can induce many adverse effects (*e.g.* immunogenicity) or the loss of therapeutic efficacy. Therefore, it is advantageous to introduce functionalized polymers with stealth properties. These mostly hydrophilic entities such as polyethylene glycol (PEG), poloxamers or polysorbate provide NPs with a shell that partially shields them from plasma protein adsorption.[105] Additionally, the molecular size of the used stealth-polymers can be selected in a way to further fine-tune size, shape and surface charge of the resulting nanoparticles. For instance, adjusting the size can be necessary as particles with diameters < 10 nm are below the size cut-off of the glomerular filtration, leading to fast renal clearance, whereas particles with diameters > 200 nm are quickly removed from the blood stream as a result of enhanced RES activation with NPs, which accumulate in liver and spleen. Likewise, controlling the size is an effective mean to modulate cellular uptake of nanoparticles.[106] Moreover, functionalization of NPs permits to introduce a targeting moiety that can increase cellular internalization within a specific tissue or organ, other than liver and spleen, where nanomedicine naturally enriches. Furnishing NPs in sufficient quantity and density of such targeting ligands initiates ligand-receptor interactions between particles and cells, eventually causing receptor-mediated endocytosis. Ideally, introducing a targeting ligand can help to reduce the applied dose, reduce adverse effects and yield tissue-specific accumulation, hence, increase efficiency and safety profile of the drug delivery system. Functionalization for targeting purposes is frequently applied to NPs to be selectively internalized by cancer or immune cells and to treat inflammatory diseases. Commonly used ligands such as transferrin, folate, mannose-6-phosphate or hyaluronan are selected since their respective receptors are disease- or cell-type-specific and over-expressed biomarkers.[106, 107]

Lastly, an siRNA-containing delivery vehicle, after being successfully endocytosed, should guarantee the escape from the endo-lysosomal vesicular system to reach the cytosol of a targeted cell. Indeed, endosomal escape is probably still the major bottleneck for successful nucleic acid delivery. It is of utmost importance for the RNA cargo to leave the endosomes on time, as otherwise sorting towards the degrading factory *i.e.*, the lysosomal vesicles will reduce or even impede RNAi activity. To date, different theories exist to describe how polymeric NPs escape from the endosomes. According to the "proton sponge effect", polycationic structures such as PEI are able to buffer protons being actively pumped into the endosomal vesicles during their maturation. The influx of anions that are co-transported with the protons will results in a parallel influx of water increasing the osmotic pressure, ending in the rupture of the vesicles.[108] Other theories consider the formation of pores driven by the polymeric entities or vesicle rupture due to particle swelling to be the underlying cause of endosomal burst or membrane destabilization.[109] Novel designs of polymeric carries may include a chemical moiety that facilitates endosomal escape and siRNA release along the endo-lysosomal pathway. The principle of "pH responsive" elements that are cleaved from the polymeric chain upon acidification

within the endosomes is broadly applied. For instance, virus-inspired polymers for endosomal release (VIPER) are cationic copolymers that comprise a hydrophilic entity to engage with the siRNA as well as a pH-sensitive hydrophobic entity that includes the membrane-lytic peptide melittin. At an acidic pH melittin is exposed and interacts with the endosomal membrane to induce rupture and endosomal escape.[110] The acidic cleavage of polymer chains can also help the decomplexation of carrier and cargo, another prerequisite for effective siRNA delivery. Likewise, redox-sensitive linkers (*e.g.* disulfide bonds) within the polymer chain promote decompaction of the NPs and siRNA release. The latter strategy exploits high levels of glutathione present in the cytosol to induce carrier-cargo disassembly. Other such delivery strategies depend on spatially-restricted enzyme activity, such as is described for MMPs within cancerous tissues, to selectively release the payload from its vehicle within the tumor microenvironment.[109]

4.4 Targeting EMT with RNAi-delivering nanoparticles

Applying nanoparticles to deliver nucleic acid drugs for the treatment of cancer follows two circumstances that come along with the underlying pathophysiology. First, improper neovascularization triggered by pro-angiogenic factors (*e.g.* VEGF) released from stromal and cancerous cells entails a poorly fenestrated vascular endothelium surrounding tumors. The discontinuous and leaky endothelium facilitates extravasation of nanoparticles at the tumor side. Likewise, lymphangiogenesis in tumors is impaired, resulting in a defective lymphatic drainage system with a minimal uptake of interstitial fluid which especially affects slowly diffusing species such as nanoparticles. This phenomenon is recapitulated as “enhanced permeation and retention effect” (EPR) enabling passive tumor targeting by promoting accumulation of nanoparticles in the tumor microenvironment.[111] Second, the overexpression of distinct proteins, particularly cell surface proteins, which are uniquely upregulated in the cancerous tissue permits active targeting of tumors cells. As described in the previous section, functionalizing of polymeric vehicles with an appropriate ligand, features receptor-mediated endocytosis. The enhanced selectivity theoretically avoids off-target effects whilst improving cancer-specific NP internalization, complementary to the EPR effect.[111, 112]

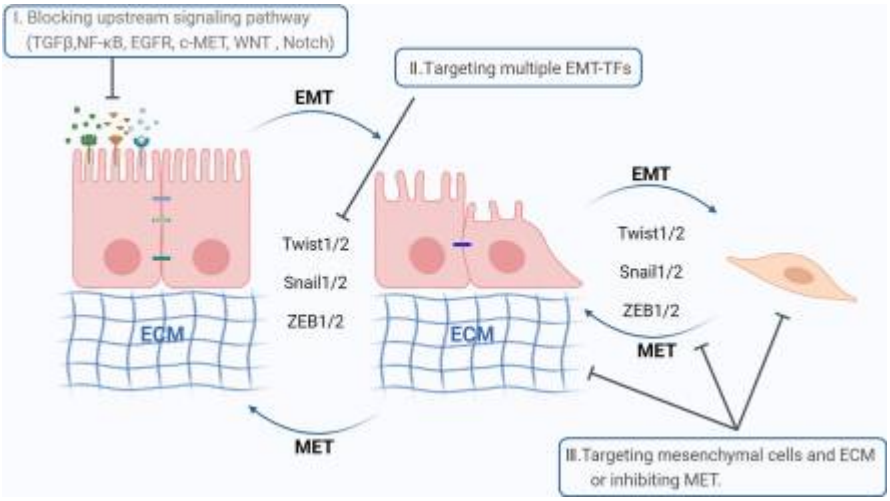

Figure 8. *Possible strategies to inhibit or revert EMT [47]*

As mentioned in Section 2.2, cells that undergo EMT/EMP-like changes acquire EMT-effector proteins that are indicative and specific for a mesenchymal phenotype. Consequently, from a nanoparticle-design perspective, the EMT program may provide surface receptors being possible candidates for active targeting strategies of anti-cancer agents. Notably, such targeted delivery is required since physiological EMT contributes to wound healing processes as well as stem cell homeostasis and differentiation of a variety of cell types. Hence, uncontrolled delivery of EMT-interfering drugs is expected to cause harmful adverse effects.[113] A possible strategy may exploit the cadherin-switching that occurs during EMT. Accordingly, Karnas *et al.*[114] designed a nanoparticulate system with surface-modified anti-N-cadherin antibody enabling the selective targeting of and uptake in EMT-undergone CTCs. Furthermore, integrins which promote mechanical attachment between cells and ECM as well as generate bidirectional cellular signaling, are known to participate during cancer cell invasion and directional migration. Upregulation of distinct integrin subunits as part of EMT reprograming[115] can be hi-jacked for selective nanoparticulate delivery. Arginylglycylaspartic acid (RGD) is a peptide motive that is part of many ECM molecules and promotes cell-ECM binding *via* integrins. Functionalization of nanocarriers with the RGD-motive is currently considered a promising design option to target integrin overexpressing cancer cells.[116] Lastly, the CD44 receptor is probably the most studied candidate for targeted delivery of breast cancer cells in the context of EMT. CD44, a transmembrane glycoprotein, binds to various ECM components, in particular hyaluronic acid (HA). Its surface expression is ubiquitous throughout the body, however crucially increased upon EMT induction, allowing for preferential targeting strategies.[117, 118] Its overexpression was correlated with TNBCs enabling a therapeutic approach for this otherwise hardly accessible subtype of breast cancer.[119] Besides covalent-linkage to the polymeric carrier, the polyanionic HA offers the possibility to be electrostatically bound to the surface of cationic polymers such as PEI or chitosan. However, only recently it was argued that alternative splicing of its pre-

mRNA, giving rise to variant CD44 isoforms, may be detrimental for CD44's usage as targeting receptor.[120]

Concerning the active pharmaceutical ingredient *i.e.*, siRNA or miRNA, of approaches that target EMT, sequences of the oligonucleotide antisense strand can be designed to be complementary to the mRNA of a master regulator of the EMT-EMP machinery. The so-induced RNAi may subsequently impair phenotypic plasticity or induce MET (**Figure 8**). However, the aforementioned adverse effects have to be considered when interfering with superordinate biomolecules such as EMT-TFs. Presumably, in this context, modulation of epigenetic regulatory molecules *e.g.* miRNAs or HDACs is safer to revert the mesenchymal phenotype. Indeed, preclinical studies demonstrated that delivery of synthetic miRNAs such as members of the miRNA-200 family can downregulate EMT-TF protein levels and inhibit stem-like properties and metastasis.[121] Similarly, HA-decorated PEI-based nanoparticles containing siRNA against multidrug resistance protein-1 (MRP-1) initiated responsiveness of TNBCs to doxorubicin leading to significant tumor reduction in an animal model.[122] Moreover, as was indicated in Section 3.3, inhibiting the autocrine feedback-loop of growth factors by downregulating their expression impedes EMT-induction or at least ceases the sustainability of the mesenchymal phenotype. However, such approaches not necessarily require RNAi to interfere with the signaling pathways, but may exploit antibodies or small molecules to impede ligand-receptor interactions. As such, currently available inhibitors of the receptor-tyrosine kinase EGFR or checkpoint-inhibitors blocking PD-L1 can be considered anti-EMT drugs.

Altogether, anti-EMT therapeutic strategies may not solely impede the dissemination, migration and invasion of cancer cells, including the prevention of metastatic lesions, but also extenuate stem-like properties and thereby restore cellular sensitivity towards and effectiveness of conventional chemotherapeutics.[113, 123]

5. References

[1] N. Gjorevski, C.M. Nelson, *Nature Reviews Molecular Cell Biology* **2011**, *12*(*9*): p. 581-593, DOI: 10.1038/nrm3168.

[2] B. Tiede, Y. Kang, *Cell Res.* **2011**, *21*(*2*): p. 245-257, DOI: 10.1038/cr.2011.11.

[3] N.Y. Fu, E. Nolan, G.J. Lindeman, J.E. Visvader, *Physiol. Rev.* **2020**, *100*(*2*): p. 489-523, DOI: 10.1152/physrev.00040.2018.

[4] J.E. Visvader, J. Stingl, *Genes Dev.* **2014**, *28*(*11*): p. 1143-58, DOI: 10.1101/gad.242511.114.

[5] K. Polyak, R. Kalluri, *Cold Spring Harb. Perspect. Biol.* **2010**, *2*(*11*): p. a003244, DOI: 10.1101/cshperspect.a003244.

[6] M.W. Conklin, P.J. Keely, *Cell Adhes. Migr.* **2012**, *6*(*3*): p. 249-260, DOI: 10.4161/cam.20567.

[7] G. Rauner, C. Kuperwasser, *Dev. Cell* **2021**, *56*(*13*): p. 1875-1883, DOI: https://doi.org/10.1016/j.devcel.2021.06.016.

[8] A. Avivar-Valderas, H.C. Wen, J.A. Aguirre-Ghiso, *Oncogene* **2014**, *33*(*48*): p. 5483-5490, DOI: 10.1038/onc.2013.554.

[9] F.R. James, S. Wootton, A. Jackson, M. Wiseman, E.R. Copson, R.I. Cutress, *Eur. J. Cancer* **2015**, *51*(*6*): p. 705-720, DOI: https://doi.org/10.1016/j.ejca.2015.01.057.

[10] N. Harbeck, F. Penault-Llorca, J. Cortes, M. Gnant, N. Houssami, P. Poortmans, K. Ruddy, J. Tsang, F. Cardoso, *Nature Reviews Disease Primers* **2019**, *5*(*1*): p. 66, DOI: 10.1038/s41572-019-0111-2.

[11] A. Srivastava, I. Jatoi, *Indian J. Surg.* **2021**, *83*(*2*): p. 273-274, DOI: 10.1007/s12262-021-02798-y.

[12] H. Sung, J. Ferlay, R.L. Siegel, **2021**, *71*(*3*): p. 209-249, DOI: 10.3322/caac.21660.

[13] P.H. Tan, I. Ellis, K. Allison, E. Brogi, S.B. Fox, S. Lakhani, A.J. Lazar, E.A. Morris, A. Sahin, R. Salgado, A. Sapino, H. Sasano, S. Schnitt, C. Sotiriou, P. van Diest, V.A. White, D. Lokuhetty, I.A. Cree, f.t.W.C.o.T.E. Board, *Histopathology* **2020**, *77*(*2*): p. 181-185, DOI: https://doi.org/10.1111/his.14091.

[14] B. Weigelt, J.S. Reis-Filho, *Nature Reviews Clinical Oncology* **2009**, *6*(*12*): p. 718-730, DOI: 10.1038/nrclinonc.2009.166.

[15] T. Sorlie, R. Tibshirani, J. Parker, T. Hastie, J.S. Marron, A. Nobel, S. Deng, H. Johnsen, R. Pesich, S. Geisler, J. Demeter, C.M. Perou, P.E. Lønning, P.O. Brown, A.L. Børresen-Dale, D. Botstein, *Proc. Natl. Acad. Sci. U. S. A.* **2003**, *100*(*14*): p. 8418-23, DOI: 10.1073/pnas.0932692100.

[16] C.M. Perou, T. Sørlie, M.B. Eisen, M. van de Rijn, S.S. Jeffrey, C.A. Rees, J.R. Pollack, D.T. Ross, H. Johnsen, L.A. Akslen, Ø. Fluge, A. Pergamenschikov, C. Williams, S.X. Zhu, P.E. Lønning, A.-L. Børresen-Dale, P.O. Brown, D. Botstein, *Nature* **2000**, *406*(*6797*): p. 747-752, DOI: 10.1038/35021093.

[17] C.F. Cowell, B. Weigelt, R.A. Sakr, C.K.Y. Ng, J. Hicks, T.A. King, J.S. Reis-Filho, *Mol. Oncol.* **2013**, *7*(*5*): p. 859-869, DOI: https://doi.org/10.1016/j.molonc.2013.07.005.

[18] M. van Seijen, E.H. Lips, A.M. Thompson, S. Nik-Zainal, A. Futreal, E.S. Hwang, E. Verschuur, J. Lane, J. Jonkers, D.W. Rea, J. Wesseling, P.t. on behalf of the, *Br. J. Cancer* **2019**, *121*(*4*): p. 285-292, DOI: 10.1038/s41416-019-0478-6.

[19] A. Vincent-Salomon, C. Lucchesi, N.g. Gruel, V. Raynal, G.l. Pierron, R.m. Goudefroye, F. Reyal, F.o. Radvanyi, R.m. Salmon, J.-P. Thiery, X. Sastre-Garau, B. Sigal-Zafrani, A. Fourquet, O. Delattre, f.t.b.c.s.g.o.t.I. Curie, *Clin. Cancer Res.* **2008**, *14*(*7*): p. 1956-1965, DOI: 10.1158/1078-0432.ccr-07-1465.

[20] J. Tchou, J. Conejo-Garcia, *Adv. Pharmacol.* **2012**, *65*: p. 45-61, DOI: 10.1016/b978-0-12-397927-8.00003-8.

[21] Y. Mao, E.T. Keller, D.H. Garfield, K. Shen, J. Wang, *Cancer metastasis reviews* **2013**, *32*(*1-2*): p. 303-315, DOI: 10.1007/s10555-012-9415-3.

[22] S.D. Soysal, A. Tzankov, S.E. Muenst, *Pathobiology* **2015**, *82*(*3-4*): p. 142-152, DOI: 10.1159/000430499.

[23] R.S. Stowers, A. Shcherbina, J. Israeli, J.J. Gruber, J. Chang, S. Nam, A. Rabiee, M.N. Teruel, M.P. Snyder, A. Kundaje, O. Chaudhuri, *Nature Biomedical Engineering* **2019**, *3*(*12*): p. 1009-1019, DOI: 10.1038/s41551-019-0420-5.

[24] K. Polyak, I. Haviv, I.G. Campbell, *Trends Genet.* **2009**, *25*(*1*): p. 30-38, DOI: https://doi.org/10.1016/j.tig.2008.10.012.

[25] T. Koorman, K.A. Jansen, A. Khalil, P.D. Haughton, D. Visser, M.A.K. Rätze, W.E. Haakma, G. Sakalauskaitè, P.J. van Diest, J. de Rooij, P.W.B. Derksen, *Oncogene* **2022**, *41*(*17*): p. 2458-2469, DOI: 10.1038/s41388-022-02258-1.

[26] S. Alowami, S. Troup, S. Al-Haddad, I. Kirkpatrick, P.H. Watson, *Breast Cancer Res.* **2003**, *5*(*5*): p. R129-35, DOI: 10.1186/bcr622.

[27] M.-K. Hayward, M.D. Allen, J.J. Gomm, I. Goulding, C.L. Thompson, M.M. Knight, J.F. Marshall, J.L. Jones, *npj Breast Cancer* **2022**, *8*(*1*): p. 109, DOI: 10.1038/s41523-022-00464-4.

[28] E.S. Knudsen, A. Ertel, E. Davicioni, J. Kline, G.F. Schwartz, A.K. Witkiewicz*, Breast Cancer Res. Treat.* **2012**, *133*(*3*): p. 1009-1024, DOI: 10.1007/s10549-011-1894-3.

[29] C. Gilles, D.F. Newgreen, H. Sato, E.W. Thompson, P. Savagner, Editor. **2005**, Springer US: Boston, MA. p. 297-315, DOI: 10.1007/0-387-28671-3_20.

[30] S. Bhatia, P. Wang, A. Toh, E.W. Thompson*, Front. Mol. Biosci.* **2020**, *7*, DOI: 10.3389/fmolb.2020.00071.

[31] J. Yang, P. Antin, G. Berx, C. Blanpain, T. Brabletz, M. Bronner, K. Campbell, A. Cano, J. Casanova, G. Christofori, S. Dedhar, R. Derynck, H.L. Ford, J. Fuxe, A. García de Herreros, G.J. Goodall, A.-K. Hadjantonakis, R.Y.J. Huang, C. Kalcheim, R. Kalluri, Y. Kang, Y. Khew-Goodall, H. Levine, J. Liu, G.D. Longmore, S.A. Mani, J. Massagué, R. Mayor, D. McClay, K.E. Mostov, D.F. Newgreen, M.A. Nieto, A. Puisieux, R. Runyan, P. Savagner, B. Stanger, M.P. Stemmler, Y. Takahashi, M. Takeichi, E. Theveneau, J.P. Thiery, E.W. Thompson, R.A. Weinberg, E.D. Williams, J. Xing, B.P. Zhou, G. Sheng, E.M.T.I.A. On behalf of the*, Nat. Rev. Mol. Cell Biol.* **2020**, *21*(*6*): p. 341-352, DOI: 10.1038/s41580-020-0237-9.

[32] M.A. Nieto, R.Y. Huang, R.A. Jackson, J.P. Thiery*, Cell* **2016**, *166*(*1*): p. 21-45, DOI: 10.1016/j.cell.2016.06.028.

[33] T. Brabletz, R. Kalluri, M.A. Nieto, R.A. Weinberg*, Nat. Rev. Cancer* **2018**, *18*(*2*): p. 128-134, DOI: 10.1038/nrc.2017.118.

[34] R. Kalluri, R.A. Weinberg*, J. Clin. Invest.* **2009**, *119*(*6*): p. 1420-8, DOI: 10.1172/jci39104.

[35] D. Haensel, X. Dai*,* **2018**, *247*(*3*): p. 473-480, DOI: 10.1002/dvdy.24561.

[36] H. Hashem*, Journal of Medical Histology* **2018**, *2*(*2*): p. 81-102, DOI: 10.21608/jmh.2019.7401.1046.

[37] V. Mittal*, Annual Review of Pathology: Mechanisms of Disease* **2018**, *13*(*1*): p. 395-412, DOI: 10.1146/annurev-pathol-020117-043854.

[38] W.L. Tam, R.A. Weinberg*, Nat. Med.* **2013**, *19*: p. 1438, DOI: 10.1038/nm.3336.

[39] S.N. Rubtsova, I.Y. Zhitnyak*,* **2021**, *22*(*4*), DOI: 10.3390/ijms22041821.

[40] J.J. Christiansen, A.K. Rajasekaran*, Cancer Res.* **2006**, *66*(*17*): p. 8319-26, DOI: 10.1158/0008-5472.can-06-0410.

[41] H. Son, A. Moon*, Toxicological research* **2010**, *26*(*4*): p. 245-252, DOI: 10.5487/TR.2010.26.4.245.

[42] V. Gensbittel, M. Kräter, S. Harlepp, I. Busnelli, J. Guck, J.G. Goetz*, Dev. Cell* **2021**, *56*(*2*): p. 164-179, DOI: 10.1016/j.devcel.2020.10.011.

[43] V. Graziani, I. Rodriguez-Hernandez, O. Maiques, V. Sanz-Moreno*, Trends Cell Biol.* **2022**, *32*(*3*): p. 228-242, DOI: 10.1016/j.tcb.2021.10.004.

[44] A. Dart*, Nature Reviews Cancer* **2017**, *17*(*4*): p. 205-205, DOI: 10.1038/nrc.2017.21.

[45] Y. Yang, H. Zheng, Y. Zhan, S. Fan*, American journal of translational research* **2019**, *11*(*9*): p. 5301-5312.

[46] M.K. Jolly, M. Boareto, B. Huang, D. Jia, M. Lu, E. Ben-Jacob, J.N. Onuchic, H. Levine*, Front. Oncol.* **2015**, *5*, DOI: 10.3389/fonc.2015.00155.

[47] Y. Huang, W. Hong, X. Wei*, J. Hematol. Oncol.* **2022**, *15*(*1*): p. 129, DOI: 10.1186/s13045-022-01347-8.

[48] J. Banyard, D.R. Bielenberg*, Connect. Tissue Res.* **2015**, *56*(*5*): p. 403-413, DOI: 10.3109/03008207.2015.1060970.

[49] M. Yilmaz, G. Christofori*, Cancer Metastasis Rev.* **2009**, *28*(*1*): p. 15-33, DOI: 10.1007/s10555-008-9169-0.

[50] B.-J. Choi, S.-A. Park, S.-Y. Lee, Y.N. Cha, Y.-J. Surh*, Sci. Rep.* **2017**, *7*(*1*): p. 15918, DOI: 10.1038/s41598-017-15139-5.

[51] M. Rauschner, L. Lange, T. Hüsing, S. Reime, A. Nolze, M. Maschek, O. Thews, A. Riemann*, J. Exp. Clin. Cancer Res.* **2021**, *40*(*1*): p. 10, DOI: 10.1186/s13046-020-01815-4.

[52] A. Riemann, M. Rauschner, M. Gießelmann, S. Reime, V. Haupt, O. Thews*, Neoplasia* **2019**, *21*(*5*): p. 450-458, DOI: https://doi.org/10.1016/j.neo.2019.03.004.

[53] H. Huang, S. Wright, J. Zhang, R.A. Brekken, *Biochim. Biophys. Acta* **2019**, *1866*(*11*): p. 118472, DOI: https://doi.org/10.1016/j.bbamcr.2019.04.002.
[54] N.A. Kuburich, P. den Hollander, J.T. Pietz, S.A. Mani, *Semin. Cancer Biol.* **2022**, *86*: p. 816-826, DOI: https://doi.org/10.1016/j.semcancer.2021.12.006.
[55] P. Alluri, L.A. Newman, *Surg. Oncol. Clin. N. Am.* **2014**, *23*(*3*): p. 567-577, DOI: 10.1016/j.soc.2014.03.003.
[56] D. Sarrió, S.M. Rodriguez-Pinilla, D. Hardisson, A. Cano, G. Moreno-Bueno, J. Palacios, *Cancer Res.* **2008**, *68*(*4*): p. 989-97, DOI: 10.1158/0008-5472.can-07-2017.
[57] M. Koleckova, J. Ehrmann, J. Bouchal, M. Janikova, A. Brisudova, J. Srovnal, K. Staffova, M. Svoboda, O. Slaby, L. Radova, K. Vomackova, B. Melichar, L. Veverkova, Z. Kolar, *Sci. Rep.* **2021**, *11*(*1*): p. 5145, DOI: 10.1038/s41598-021-84350-2.
[58] Q. Zeng, W. Li, D. Lu, Z. Wu, H. Duan, Y. Luo, J. Feng, D. Yang, L. Fu, X. Yan, *Proc. Natl. Acad. Sci. U. S. A.* **2012**, *109*(*4*): p. 1127-1132, DOI: 10.1073/pnas.1111053108.
[59] J. Felipe Lima, S. Nofech-Mozes, J. Bayani, J.M. Bartlett, *J Clin Med* **2016**, *5*(*7*), DOI: 10.3390/jcm5070065.
[60] Y. Wang, B.P. Zhou, *Chin. J. Cancer* **2011**, *30*(*9*): p. 603-11, DOI: 10.5732/cjc.011.10226.
[61] F. Lüönd, N. Sugiyama, R. Bill, L. Bornes, C. Hager, F. Tang, N. Santacroce, C. Beisel, R. Ivanek, T. Bürglin, S. Tiede, J. van Rheenen, G. Christofori, *Dev. Cell* **2021**, *56*(*23*): p. 3203-3221.e11, DOI: https://doi.org/10.1016/j.devcel.2021.11.006.
[62] M. Kapałczyńska, T. Kolenda, W. Przybyła, M. Zajączkowska, A. Teresiak, V. Filas, M. Ibbs, R. Bliźniak, Ł. Łuczewski, K. Lamperska, *Arch. Med. Sci.* **2018**, *14*(*4*): p. 910-919, DOI: 10.5114/aoms.2016.63743.
[63] F. Pampaloni, E.G. Reynaud, E.H. Stelzer, *Nat. Rev. Mol. Cell Biol.* **2007**, *8*(*10*): p. 839-45, DOI: 10.1038/nrm2236.
[64] C. Jensen, Y. Teng, *Front. Mol. Biosci.* **2020**, *7*, DOI: 10.3389/fmolb.2020.00033.
[65] Y. Imamura, T. Mukohara, Y. Shimono, Y. Funakoshi, N. Chayahara, M. Toyoda, N. Kiyota, S. Takao, S. Kono, T. Nakatsura, H. Minami, *Oncol. Rep.* **2015**, *33*(*4*): p. 1837-1843, DOI: 10.3892/or.2015.3767.
[66] E.P. Carter, R. Roozitalab, S.V. Gibson, R.P. Grose, *Trends in cancer* **2021**, *7*(*11*): p. 1033-1046, DOI: 10.1016/j.trecan.2021.06.009.
[67] S.A. Langhans, *Front. Pharmacol.* **2018**, *9*, DOI: 10.3389/fphar.2018.00006.
[68] C. Gaggioli, S. Hooper, C. Hidalgo-Carcedo, R. Grosse, J.F. Marshall, K. Harrington, E. Sahai, *Nat. Cell Biol.* **2007**, *9*(*12*): p. 1392-1400, DOI: 10.1038/ncb1658.
[69] J. Pape, M. Emberton, U. Cheema, *Frontiers in Bioengineering and Biotechnology* **2021**, *9*, DOI: 10.3389/fbioe.2021.660502.
[70] K. Unnikrishnan, L.V. Thomas, R.M. Ram Kumar, *Front. Oncol.* **2021**, *11*, DOI: 10.3389/fonc.2021.733652.
[71] G. Hassan, S.M. Afify, S. Kitano, A. Seno, H. Ishii, Y. Shang, M. Matsusaki, M. Seno, *Processes* **2021**, *9*(*1*): p. 45.
[72] A.R. Aref, R.Y.-J. Huang, W. Yu, K.-N. Chua, W. Sun, T.-Y. Tu, J. Bai, W.-J. Sim, I.K. Zervantonakis, J.P. Thiery, R.D. Kamm, *Integrative Biology* **2012**, *5*(*2*): p. 381-389, DOI: 10.1039/c2ib20209c.
[73] M. Plodinec, M. Loparic, C.A. Monnier, E.C. Obermann, R. Zanetti-Dallenbach, P. Oertle, J.T. Hyotyla, U. Aebi, M. Bentires-Alj, R.Y.H. Lim, C.-A. Schoenenberger, *Nature Nanotechnology* **2012**, *7*(*11*): p. 757-765, DOI: 10.1038/nnano.2012.167.
[74] A.T. Salminen, Z. Allahyari, S. Gholizadeh, M.C. McCloskey, R. Ajalik, R.N. Cottle, T.R. Gaborski, J.L. McGrath, *Frontiers in Medical Technology* **2020**, *2*, DOI: 10.3389/fmedt.2020.600616.
[75] C. Walter, J.T. Davis, J. Mathur, A. Pathak, *Integr. Biol. (Camb.)* **2018**, *10*(*6*): p. 342-355, DOI: 10.1039/c8ib00034d.
[76] S.G. Manore, D.L. Doheny, G.L. Wong, H.-W. Lo, *Front. Oncol.* **2022**, *12*, DOI: 10.3389/fonc.2022.866014.

[77] M. Sameni, D. Cavallo-Medved, O.E. Franco, A. Chalasani, K. Ji, N. Aggarwal, A. Anbalagan, X. Chen, R.R. Mattingly, S.W. Hayward, B.F. Sloane*, Breast Cancer Res.* **2017**, *19*(*1*): p. 56, DOI: 10.1186/s13058-017-0847-0.
[78] S. Saha, X. Duan, L. Wu, P.-K. Lo, H. Chen, Q. Wang*, Langmuir* **2012**, *28*(*4*): p. 2028-2034, DOI: 10.1021/la203846w.
[79] S. Agarwal, J.H. Wendorff, A. Greiner*, Polymer* **2008**, *49*(*26*): p. 5603-5621, DOI: https://doi.org/10.1016/j.polymer.2008.09.014.
[80] A. Greiner, J.H. Wendorff*, Angewandte Chemie International Edition* **2007**, *46*(*30*): p. 5670-5703, DOI: https://doi.org/10.1002/anie.200604646.
[81] P.D. Dalton, C. Vaquette, B.L. Farrugia, T.R. Dargaville, T.D. Brown, D.W. Hutmacher*, Biomaterials Science* **2013**, *1*(*2*): p. 171-185, DOI: 10.1039/C2BM00039C.
[82] J. Xue, T. Wu, Y. Dai, Y. Xia*, Chem. Rev.* **2019**, *119*(*8*): p. 5298-5415, DOI: 10.1021/acs.chemrev.8b00593.
[83] T.J. Sill, H.A. von Recum*, Biomaterials* **2008**, *29*(*13*): p. 1989-2006, DOI: https://doi.org/10.1016/j.biomaterials.2008.01.011.
[84] B. Sun, X.J. Jiang, S. Zhang, J.C. Zhang, Y.F. Li, Q.Z. You, Y.Z. Long*, Journal of materials chemistry. B* **2015**, *3*(*27*): p. 5389-5410, DOI: 10.1039/c5tb00472a.
[85] I.C. Um, D. Fang, B.S. Hsiao, A. Okamoto, B. Chu*, Biomacromolecules* **2004**, *5*(*4*): p. 1428-1436, DOI: 10.1021/bm034539b.
[86] A. Haider, S. Haider, I.-K. Kang*, Arabian Journal of Chemistry* **2018**, *11*(*8*): p. 1165-1188, DOI: https://doi.org/10.1016/j.arabjc.2015.11.015.
[87] B.A. Chinnappan, M. Krishnaswamy*,* **2022**, *14*(*18*), DOI: 10.3390/polym14183719.
[88] G.P. Huang, S. Shanmugasundaram, P. Masih, D. Pandya, S. Amara, G. Collins, T.L. Arinzeh*, Journal of Biomedical Materials Research Part A* **2015**, *103*(*2*): p. 762-771, DOI: https://doi.org/10.1002/jbm.a.35222.
[89] M.C. Amores de Sousa, C.A.V. Rodrigues, I.A.F. Ferreira, M.M. Diogo, R.J. Linhardt, J.M.S. Cabral, F.C. Ferreira*, Frontiers in Bioengineering and Biotechnology* **2020**, *8*, DOI: 10.3389/fbioe.2020.580135.
[90] S. Ferraris, S. Spriano, A.C. Scalia, A. Cochis, L. Rimondini, I. Cruz-Maya, V. Guarino, A. Varesano, C. Vineis*, Polymers (Basel)* **2020**, *12*(*12*): p. 2896.
[91] I.S. Padda, A.U. Mahtani, M. Parmar. **2022**, StatPearls Publishing

[92] R. Almeida, R.C. Allshire*, Trends Cell Biol.* **2005**, *15*(*5*): p. 251-258, DOI: 10.1016/j.tcb.2005.03.006.
[93] J.K.W. Lam, M.Y.T. Chow, Y. Zhang, S.W.S. Leung*, Molecular Therapy - Nucleic Acids* **2015**, *4*, DOI: 10.1038/mtna.2015.23.
[94] L. Aagaard, J.J. Rossi*, Adv Drug Deliv Rev* **2007**, *59*(*2-3*): p. 75-86, DOI: 10.1016/j.addr.2007.03.005.
[95] A. Paul, A. Muralidharan, A. Biswas, B.V. Kamath, A. Joseph, A.T. Alex*, OpenNano* **2022**, *7*: p. 100063, DOI: https://doi.org/10.1016/j.onano.2022.100063.
[96] M. Friedrich, A. Aigner*, Biodrugs* **2022**, *36*(*5*): p. 549-571, DOI: 10.1007/s40259-022-00549-3.
[97] J. Wang, Z. Lu, M.G. Wientjes, J.L. Au*, The AAPS journal* **2010**, *12*(*4*): p. 492-503, DOI: 10.1208/s12248-010-9210-4.
[98] J. Zhang, S. Shrivastava*,* **2019**, *11*(*11*): p. 10481-10491, DOI: 10.1021/acsami.8b21398.
[99] N.M. Zaki, N. Tirelli*, Expert Opinion on Drug Delivery* **2010**, *7*(*8*): p. 895-913, DOI: 10.1517/17425247.2010.501792.
[100] G.J. Doherty, H.T. McMahon*, Annu. Rev. Biochem.* **2009**, *78*: p. 857-902, DOI: 10.1146/annurev.biochem.78.081307.110540.
[101] D. Manzanares, V. Ceña*, Pharmaceutics* **2020**, *12*(*4*), DOI: 10.3390/pharmaceutics12040371.
[102] H. Wang, S. Zhang, J. Lv, Y. Cheng*, VIEW* **2021**, *2*(*3*): p. 20200026, DOI: https://doi.org/10.1002/VIW.20200026.

[103] N. Hartl, F. Adams, G. Costabile, L. Isert, M. Döblinger, X. Xiao, R. Liu, O.M. Merkel, *Nanomaterials* **2019**, *9*(*7*): p. 986.
[104] X. Hou, T. Zaks, R. Langer, Y. Dong, *Nature Reviews Materials* **2021**, *6*(*12*): p. 1078-1094, DOI: 10.1038/s41578-021-00358-0.
[105] T.U. Wani, S.N. Raza, N.A. Khan, *Polymer Bulletin* **2020**, *77*(*7*): p. 3865-3889, DOI: 10.1007/s00289-019-02924-7.
[106] N. Hoshyar, S. Gray, H. Han, G. Bao, *Nanomedicine (London, England)* **2016**, *11*(*6*): p. 673-92, DOI: 10.2217/nnm.16.5.
[107] S. Xu, B.Z. Olenyuk, C.T. Okamoto, S.F. Hamm-Alvarez, *Adv. Drug Del. Rev.* **2013**, *65*(*1*): p. 121-138, DOI: https://doi.org/10.1016/j.addr.2012.09.041.
[108] A. Parodi, C. Corbo, A. Cevenini, R. Molinaro, R. Palomba, L. Pandolfi, M. Agostini, F. Salvatore, E. Tasciotti, *Nanomedicine (London, England)* **2015**, *10*(*12*): p. 1923-40, DOI: 10.2217/nnm.15.39.
[109] B. Winkeljann, D.C. Keul, O.M. Merkel, *J. Control. Release* **2023**, *353*: p. 518-534, DOI: https://doi.org/10.1016/j.jconrel.2022.12.008.
[110] D. Baldassi, S. Ambike, M. Feuerherd, C.C. Cheng, D.J. Peeler, D.P. Feldmann, D.L. Porras-Gonzalez, X. Wei, L.A. Keller, N. Kneidinger, M.G. Stoleriu, A. Popp, G. Burgstaller, S.H. Pun, T. Michler, O.M. Merkel, *J. Control. Release* **2022**, *345*: p. 661-674, DOI: 10.1016/j.jconrel.2022.03.051.
[111] M.A. Subhan, S.S.K. Yalamarty, N. Filipczak, **2021**, *11*(*6*), DOI: 10.3390/jpm11060571.
[112] J. Yoo, C. Park, G. Yi, D. Lee, H. Koo, **2019**, *11*(*5*), DOI: 10.3390/cancers11050640.
[113] S. Brabletz, H. Schuhwerk, **2021**, *40*(*18*): p. e108647, DOI: 10.15252/embj.2021108647.
[114] K. Karnas, T. Strączek, C. Kapusta, M. Lekka, J. Dulińska-Litewka, **2021**, *16*: p. 6537-6552, DOI: 10.2147/ijn.s324354.
[115] Y. Masugi, K. Yamazaki, K. Emoto, K. Effendi, H. Tsujikawa, M. Kitago, O. Itano, Y. Kitagawa, M. Sakamoto, *Lab. Invest.* **2015**, *95*(*3*): p. 308-319, DOI: 10.1038/labinvest.2014.166.
[116] K. Ahmad, E.J. Lee, S. Shaikh, A. Kumar, K.M. Rao, S.-Y. Park, J.O. Jin, S.S. Han, I. Choi, *Semin. Cancer Biol.* **2021**, *69*: p. 325-336, DOI: https://doi.org/10.1016/j.semcancer.2019.08.030.
[117] A. Spadea, J.M. Rios de la Rosa, A. Tirella, M.B. Ashford, K.J. Williams, I.J. Stratford, N. Tirelli, M. Mehibel, *Mol. Pharm.* **2019**, *16*(*6*): p. 2481-2493, DOI: 10.1021/acs.molpharmaceut.9b00083.
[118] P. Kesharwani, R. Chadar, A. Sheikh, W.Y. Rizg, A.Y. Safhi, *Front. Pharmacol.* **2022**, *12*, DOI: 10.3389/fphar.2021.800481.
[119] G. Nabil, R. Alzhrani, **2021**, *13*(*4*), DOI: 10.3390/cancers13040898.
[120] J.M. Rios de la Rosa, A. Tirella, N. Tirelli, *Advanced Biosystems* **2018**, *2*(*6*): p. 1800049, DOI: https://doi.org/10.1002/adbi.201800049.
[121] M.A. Cortez, D. Valdecanas, X. Zhang, Y. Zhan, V. Bhardwaj, G.A. Calin, R. Komaki, D.K. Giri, C.C. Quini, T. Wolfe, H.J. Peltier, A.G. Bader, J.V. Heymach, R.E. Meyn, J.W. Welsh, *Mol. Ther.* **2014**, *22*(*8*): p. 1494-1503, DOI: 10.1038/mt.2014.79.
[122] Z.J. Deng, S.W. Morton, E. Ben-Akiva, E.C. Dreaden, K.E. Shopsowitz, P.T. Hammond, *ACS nano* **2013**, *7*(*11*): p. 9571-84, DOI: 10.1021/nn4047925.
[123] S. Jonckheere, J. Adams, D. De Groote, K. Campbell, G. Berx, S. Goossens, *Cells Tissues Organs* **2022**, *211*(*2*): p. 157-182, DOI: 10.1159/000512218.

Chapter II

An in-vitro approach to model EMT in breast cancer

This chapter is submitted for publication in *Int J Mol Sci* as:

Lorenz Isert, Aditi Mehta, Gabriele Loiudice, Altea Oliva, Andreas Roidl and Olivia Merkel; “An in-vitro approach to model EMT in breast cancer”

1. Abstract

During the progression from ductal carcinoma i*n situ* (DCIS) to invasive breast cancer (IBC), cells have to overcome the physically restraining basement membrane (BM) which compartmentalizes the epithelium from the stroma. Since the extracellular matrix (ECM) of the epithelial and stromal compartment is biochemically and physically distinct from one another, the progression demands a certain degree of cellular plasticity being essentially required for a primary tumor to become invasive. The Epithelial-to-Mesenchymal Transition depicts such a cell program equipping cancer cells with features allowing for dissemination from the epithelial entity and stromal invasion on the single-cell level. Here, we investigated the reciprocal interference between an altering tumor microenvironment and the EMT-phenotype *in vitro*. BM-typical collagen IV and stroma-typical collagen I coatings were applied as provisional 2-D matrices. Pro-inflammatory growth factors were introduced to improve tissue mimicry. Whereas the growth on coated surfaces did only slightly affect the EMT-phenotype, the combinatorial action of collagen with growth factor TGF-β1 induced prominent phenotypic changes. However, the EMT-induction was independent of the collagen type and cellular accessibility for EMT-like changes was strongly cell line dependent. Summarizing the entire body of data, we computed an EMT-phenotyping model that was used to decide on cellular EMT-status and estimate EMT-like changes. We confirmed that miR200c-mediated reversion of mesenchymal MDA-MB-231 cells is reflected by our EMT-phenotype model emphasizing its potential to predict the therapeutic efficacy of EMT-targeting drugs in the future.

2. Introduction

Epithelial-to-Mesenchymal Transition (EMT) is known as a crucial part of embryogenesis for nearly half a century, but its critical role in cancer metastasis was revealed only recently in the early 2000's.[1, 2] Since then, a continuous increase in the interest on understanding the role of EMT in cancer metastasis has been reflected in about 6000 publications in 2019.[3] While it is controversially discussed how to understand EMT and its relevance during and for metastasis [4], three key features are commonly attributed to EMT or EMT-like changes.

First, the loss of proteins characterizing an epithelial phenotype and the acquisition of mesenchymal proteins is considered the basis of EMT (EMT-hallmarks).[5] Driven by signals received from the tumor microenvironment (TME) [6], EMT-relevant transcription factors (e.g. SNAIL, SLUG, TWIST) downregulate epithelial and/or upregulate mesenchymal genes that cause the re-organization of the cell cytoskeleton.[1] The resultant phenotype is giving up its cobblestone-like epithelial morphology as the cell-cell junctions are abrogated and cells adopt a more spindle-like, elongated shape with a front-back polarity (Morphology). Third, as a consequence of epithelial depletions and mesenchymal

fortifications, cellular motility is highly increased (Motility). An additional feature is the enhanced secretion of extracellular matrix (ECM)-degrading enzymes, promoting motility and helping cells to better cope with migration and invasion that accompanies metastasis.[7]

Importantly, EMT has to be understood as a concept of cellular plasticity (Epithelial-to-Mesenchymal Plasticity (EMP)) and adaptability. It is a reversible and non-binary transition that is not necessarily completed but rather partially fulfilled (partial EMT).[3, 8] Intermediate hybrid states (E/M-states) possess both, epithelial and mesenchymal features and the degree of transition is governed by the contextuality of signaling within the tumor microenvironment, the developmental lineage of the distinct cancer types and (epi-) genetic alterations and regulations.[3, 9-11] This trans-differentiation between epithelial and mesenchymal phenotypes has been described for all kinds of carcinoma.[12] Aside from lung cancer, colorectal cancer, hepatocellular carcinoma and prostate cancer it is breast cancer that has been tremendously studied and proven clinically relevant in the context of EMT.[12-16] Based on gene expression profiling and clinical outcome, breast cancer can be classified into four intrinsic subtypes with specific molecular marker expression and increasing malignancies.[17] Luminal A and Luminal B subtypes express the estrogen receptor (ER) and the progesterone receptor (PR) (Luminal A > Luminal B) and both subtypes are fairly sensitive to endocrine therapies. HER2 subtype lacks the latter sensitivity (as being ER/PR negative) but displays an overexpression of human epidermal growth factor receptor 2 (HER2).[18, 19] Absence of ER and HER2 is descriptive for the basal-like subtype, which is considered a phenotype with high mutation load and poor prognosis.[20, 21] Triple negative breast cancer (TNBC), a subgroup, representing 70 - 80% of basal-like breast cancers, is characterized negative for ER, PR and HER2.[19, 22] It is the most aggressive form of breast cancer due to a synergism of poor treatment options and a high metastatic potential, which presumably relies on EMT-like changes enabling DCIS-to-IBC progression.[23-25]

The transmembrane protein E-cadherin can be considered as “the guardian” of an epithelial phenotype. The extracellular domains of E-cadherin of each cell entangle with the extracellular domains on neighboring cells, leading to the establishment of adherens junctions.[26] Once downregulated, it is not only the physical/mechanical rupture that dissolves the epithelial phenotype. Intracellularly bound β-catenin (within the cytoplasmic cell adhesion complex) can translocate into the nucleus once E-cadherin is internalized, and act as a transcription factor towards EMT.[27, 28]
It is well accepted, that a switch in cellular intermediate filament (IF) usage from cytokeratin to vimentin occurs during EMT.[3, 29] Vimentin is a network-forming type III intermediate filament and may be considered as the counterpart to E-cadherin, also because its expression is mainly restricted to mesenchymal cells.[30, 31] By maintaining cytoskeletal integrity and mechanical strength, vimentin cushions traction stress during single-cell migration.[32] Apart from this load-bearing function, vimentin promotes microtubule polarity which is a prerequisite for directed cell migration.[30, 33] Vimentin IF (VIF) maturation depends on microtubular transport. Whilst providing the infrastructure

for VIF network assembly, a long-lasting template of microtubule's architecture is simultaneously formed. Considering the fast turnover of microtubules (10 times faster than VIF), it appears, that vimentin's "memory" function eventually guides and enables persistent microtubules-mediated cell polarization and consequently directional migration.[34]

The EMT machinery can be induced by extracellular stimuli in multiple ways, mainly by soluble factors like TGF-β, EGF or HGF.[5, 35] However, it was shown that solid components of the ECM trigger EMT in lung cancer. Cells, cultured on a type I collagen gel activated autocrine TGF-β3 signaling, that in turn induced EMT, which is based on collagen I fiber recognition via integrins.[35] Likewise, Shawn P. Carey *et al.* created a 3-D collagen I matrix with defined mechanical properties, mimicking the stroma of the mammary gland. Incorporation of non-malignant breast epithelial cells into this scaffold upregulated mesenchymal genes, which was attributed to both, biochemical and mechanical stimuli of the matrix. Interestingly, insertion of the same cell line into a basement membrane - mimicking Matrigel (containing mainly collagen IV and laminin) could not provoke EMT-like changes. The authors concluded, that the distinct ECM composition of epithelial (Matrigel) and stromal tissue (collagen I) differentiated between EMT or not.[36] Furthermore, using a xenograft breast cancer mouse model, M. Vidal *et al.* reported that only cancer cells at the interface of the tumour and its stroma, i.e. cells that are directly exposed to the ECM of the stromal compartment express vimentin whereas cells in the core region of the tumor maintain cytokeratin expression.[37] Taken together, it appears that signals cancer cells receive from the distinct ECM comprised within the epithelial (DCIS) and stromal (IBC) compartment ultimately dictate the present phenotype and phenotypic changes. It remains elusive to what extent the combinatorial action of solid and soluble factors in each compartment participate during initial as well as sustained EMT induction.

In this study, we used two common collagen coatings (Globular type IV collagen and fibrillar type I collagen) as provisional matrices to depict the two opposing ECM components in the mammary gland (**Figure 1**). Globular type IV collagen is used as a part of the basement membrane (BM), the physiological substrate of the (myo-) epithelial layer. As described above, type I collagen (second coating) is the main extracellular compound within the stromal fraction. In a healthy tissue, it is well-separated from the epithelium via the BM (**Figure 1**), but leakage during tumor progression causes cell exposure to fibrillar type I collagen.

To stress and assess the concept of "contextuality of signaling" within the TME and its importance for EMT, breast cancer cells of distinct intrinsic subtypes were subjected to a combinatorial treatment with the different collagens and the prominent EMT-inducers, TGF-β1 or EGF. Single treatment with either soluble or solid ECM components served as reference. Initially, we defined the EMT-status of the four breast cancer cell lines based on morphological aspects, EMT-marker (*E-cadherin, CDH1 and Vimentin, VIM*) expression and migratory behavior. MCF7 (Luminal A) and HCC1954 (HER2) cells were found to hold strong epithelial characteristics, whereas the MDA-MB-231 cell line (TNBC) was

clearly attributed a mesenchymal phenotype. The second TNBC cell line MDA-MB-468 featured both, epithelial and mesenchymal characteristics (epithelial > mesenchymal), and therefore was considered an E/M-hybrid. We then monitored the three mentioned EMT features under exposure to a simplified model, taking MDA-MB-231 attributes as a positive control/reference. Cellular shape factor image analysis served as a powerful tool to predict EMT-like changes. Together with the input from protein and migration analysis, we were able to build up a computational EMT-model that hopefully helps to further understand the complexity of EMT. Besides using the model to predict EMT-phenotype and phenotypic changes that arise during cellular stimulations we exemplified its possible relevance in a miR200c inducible cell line for the facile evaluation of therapeutic efficacy of new drug candidates targeting EMT. Furthermore, our findings highlight that cellular responses are affected by combinatorial action of growth factors and ECM components requiring future 2D EMT-research to consider this context-dependency by applying similar experimental set-ups.

3. Material & Methods

3.1 Materials and cell culture

Formaldehyde solution (≥ 36%), 4′,6–diamidino–2-phenylindole dihydrochloride (DAPI), FluorSave reagent, DNase I (recombinant, RNase-free), cOmplete™, EDTA-free Protease Inhibitor Cocktail, Phosphatase Inhibitor Cocktail 2, RIPA buffer, Tris buffered saline powder, Ponceau S Stain, Tween 20, Amersham™ Protran® Western-Blotting-Membrane (nitrocellulose) and for cell culture Eagle's Minimum Essential Medium (EMEM), RPMI-1640 Medium, Dulbecco's modified eagle's medium (DMEM), fetal bovine serum (FBS), Penicillin-Streptomycin (Pen/Strep) solution, Dulbecco's Phosphate Buffered Saline (PBS), trypsin-EDTA solution 0.05 and 0.25%, 200 mM of L-glutamine solution and dimethyl sulfoxide (DMSO) were purchased from Sigma-Aldrich (Taufkirchen, Germany). GAPDH Monoclonal Antibody (ZG003), Pierce™ BCA Protein Assay Kit, Novex™ 10% Tris-Glycine Mini Gels (WedgeWell™ format, 15-well), Novex™ Value™ 4-20% Tris-Glycine Mini Gels (1.0 mm, 10-well), Page Ruler™ Plus Prestained Protein Ladder 10 to 250 kDa, Tris Glycin transfer buffer, SuperSignal™ West Pico PLUS Chemiluminescent Substrate, Rhodamine Phalloidin, High capacity cDNA synthesis kit, Power SYBR™ Green PCR Master Mix, PureLink™ RNA Mini Kit and for cell culture Leibovitz's L-15 Medium and MEM Non-Essential Amino Acids Solution (100X) were purchased from Thermo Fisher Scientific (Waltham, MA, USA). Hs_CDH1_Primer Assay (QT00080143), Hs_VIM_Primer Assay (QT00095795) and Hs_GAPDH_1_SG QuantiTect Primer Assay (QT00079247) were purchased from Qiagen (Hilden, Germany). Collagen I (sc-136154), Collagen IV (sc-29010), m-IgGκ BP-HRP (sc-516102), E-cadherin Antibody (G-10) and Vimentin Antibody (V9) were ordered from Santa Cruz Biotechnology (Dallas, Texas, USA). Rotiphorese 10x SDS Page, Rotilabo®-Blotting Papers and Methanol (blotting grade) were purchased

from Carl Roth (Karlsruhe, Germany). rh-TGF-β 1 (Transforming Growth Factor beta 1) and rh-EGF (Epidermal Growth Factor) were purchased from ImmunoTools (Friesoythe, Germany). HyClone trypan blue solution 0.4% in phosphate-buffered saline was obtained from FisherScientific (Hampton, NH, USA). Culture-Insert 2 Well in µ-Dish 35 mm was purchased from Ibidi (Gräfelfing, Germany). Laemmli loading buffer (4x) was purchased from VWR (Allison Park, PA, USA).

MCF7 (and MCF7 miR200c_KO) cells, a Luminal A breast cancer cell line, were cultured in EMEM supplemented with 10% FBS, 1x Pen/Strep, 1x MEM Non-Essential Amino Acids Solution and 2 mM glutamine. The HER2-positive breast cancer cell line HCC1954 was grown in RPMI-1640 Medium supplemented with 10% FBS and 1x Pen/Strep. MDA-MB-231 (and MDA-MB-231 i-miR200c) cells, a triple negative breast cancer (TNBC) cell line, were cultured in high glucose (4500 mg/L) DMEM. 10% FBS, 1x Pen/Strep and 2 mM glutamine were added to the medium. For miRNA induction medium is equipped with 5 µg/ml doxycycline hydrochloride as was described elsewhere.[38] The latter three cell lines were cultured in a humidified atmosphere with 5% CO_2 at 37°C. The second TNBC cell line MDA-MB-468 was grown in L-15 Medium supplemented with 20% FBS and 1x Pen/Strep. Those cells were held in a humidified incubator with 0% CO_2 at 37°C.

3.2 EMT marker – gene expression analysis

To compare EMT-marker RNA expression among the four cell lines, RT-qPCR was performed. Of each cell line 200.000 cells were seeded in a 6-well plate and cultured for 24 h. After the incubation, cells were harvested, and total RNA was isolated using the PureLink RNA mini kit according to the manufacturer's protocol with additional DNAse I digestion. Subsequently, 1000 ng of RNA was used to synthesize cDNA using the High capacity cDNA synthesis kit. In the following, E-cadherin- and vimentin-specific primers were used to amplify and quantify RNA using Power SYBR™ Green PCR Master Mix and the qTOWER real-time PCR thermal cycler (Analytik Jena, Jena, Germany). C_t values were normalized to GAPDH RNA expression, and delta C_t values were calculated for the comparison.

In order to quantify the miR200c expression levels, RNA was isolated using the peqGOLD Micro RNA kit (Peqlab Biotechnology GmbH, Erlangen, Germany), according to the manufacturer protocol. cDNA was synthesized with the qScript microRNA cDNA synthesis kit (Quantabio, Beverly, MA, USA). Since microRNAs are not polyadenylated, the polyA tailing reaction was performed by mixing 1 µg of RNA, 2 µL of Poly(A) Tailing Buffer, 1 µL Poly(A) polymerase, nuclease-free water up to 10 µL and incubated 60 minutes at 37°C followed by 5 minutes at 70°C. Subsequently, 9 µL of microRNA cDNA reaction mix was mixed with 1 µL reverse transcriptase and incubated 20 minutes at 42°C, plus 5 minutes at 85°C. RT-qPCR was performed in triplicates. The microRNA-191 was used as a housekeeper and each sample was analyzed in triplicates.

3.3 EMT-marker – protein level analysis

To define the EMT status, protein levels of CDH1 and VIM of the 4 cell lines were analyzed via Western blotting. Of each cell line 300.000 cells were seeded in a 6-well plate and cultured for 24h. Total protein extract was isolated after incubation. Briefly, cells were washed 3 times with PBS prior to cell lyses. To each well, 70 µl of proteinase- and phosphatase-inhibitor containing RIPA buffer was added, and cells were kept on ice for 30 minutes. Hereinafter, wells were thoroughly scraped, and the extracts were transferred into 1.5 ml Eppendorf tubes. After a 10 min centrifugation step at 4°C, total protein concentration was assessed according to the manufacturer's protocol (Pierce™ BCA Protein Assay Kit). Gels were loaded with 30 µg protein per sample and electrophoresis was run for 90 min at 120 mV. Subsequent to 1 h of protein transfer at 100 mV, blots were washed, blocked and incubated overnight using E-cadherin-, vimentin- and GAPDH-specific antibodies. HRP-bound secondary antibody was added for 1 h under exclusion of light before blots were developed.

As part of the EMT induction study, we first optimized the time points when to extract protein data. It should be noted that cell lines do not facultatively perform EMT and may exhibit different "transition dynamics" (fast vs. slow) upon GF treatment. Therefore we chose an optimized time point (72 h) and GF concentrations that allowed to detect EMT-like changes on the protein level in the cell lines used.

To do so, 300.000 cells were seeded to attach for 4 h. Samples included untreated cells, cells stimulated with growth factors and cells grown in collagen-coated wells (+/- growth factors). Afterwards control cells and cells growing only on collagen were washed with PBS, and pre-warmed medium was refilled. At this step, growth factors were included. Samples were either supplied with 10 ng/ml of TGF-β1 or 25 ng/ml EGF or both. Collagen I and IV coatings (2 µg collagen/cm^2) of the respective wells were prepared following the manufacturer's protocol in advance to the seeding. After 72 h incubation, samples were subjected to the aforementioned Western blotting protocol, and E-cadherin and vimentin protein levels were normalized to GAPDH-housekeeping protein level using the Image Lab™ software (Bio-Rad Laboratories, Hercules, CA, USA).

3.4 Confocal scanning microscopy – Morphological analysis

Confocal image analysis was used to assess and quantify morphological differences between cell lines and treatments. Experimental set-up was performed as described above. Briefly, sterile glass coverslips were distributed in a 24-well plate. Collagen coatings were conducted for the respective wells. Thereafter, 40.000 cells were seeded and attached for 4 h. After the growth factor treatment, cells were incubated for 72 h. Hereinafter, wells were washed 3 times with PBS before cells were fixed for 15 min with a 4% formaldehyde solution. To stain the actin cytoskeleton, cells were incubated with 8.25 µM rhodamine phalloidin solution for 40 min. Hereinafter, cells were washed another 3 times with PBS. Nuclei staining was achieved by 10 min incubation with a 0.5 µg/ml DAPI

solution. Finally, after an additional washing step, samples were mounted on glass slides using FluorSave and stored at 4°C until the next day. Fluorescence images were acquired using a laser scanning microscope (Leica SP8 inverted, Software: LAS X, Leica microsystems GmbH, Wetzlar, Germany) equipped with a HC PL APO CS2 40x/1.30 and 63x/1.40 oil immersion objective. Diode lasers (405 nm) and a semiconductor laser OPSL (552 nm) were chosen for excitation, emission was detected in blue (PMT1: 410–520 nm) and yellow (PMT2: 560nm – 760nm), respectively. Images were further processed with Fiji image analysis software.[39] Nuclear circularity was calculated as $C_N = \frac{4\pi A}{P^2}$, and the cellular aspect ratio as $A_R = \frac{d_{min}}{d_{max}}$. The axis ($d_{min}$ and d_{max}) were drawn manually.

3.5 Ibidi® migration assay

Migratory properties were analyzed as follows: To define the cellular EMT-status, 25.000 cells of each cell line were seeded in both wells of the Ibidi culture-insert. After 24h the inserts were carefully removed and the time until gap closure in between the two wells was monitored for up to 120 h using the Keyence BZ81000 Fluorescence microscope (Keyence, Osaka, Japan). Three to four pictures of different parts of the gaps were taken for each time point. The cell free area was analyzed based on a custom-made macro within the Fiji imaging software:

```
run("8-bit");
run("Bandpass Filter...", "filter_large=40 filter_small=3 suppress=None tolerance=5 autoscale saturate");
run("Sharpen");
run("Find Edges");
run("Find Edges");
setAutoThreshold("Default");
//run("Threshold...");
setThreshold(0, 100);
//setThreshold(0, 100);
setOption("BlackBackground", false);
run("Convert to Mask");
run("Find Edges");
run("Invert LUT");
run("Find Edges");'
run("Analyze Particles...", "size=10000-Infinity pixel show=Outlines display summarize");
```

Percentage gap closure was calculated according to the following equation:

$$\text{Gap closure [\%]} = (1 - \frac{\text{cell free area } t_h}{\text{cell free area } t_0}) \times 100$$

As part of the EMT induction study, cells were seeded at a density of 15.000 cells per well. Collagen coatings were prepared in advance. Similar to what has been described for the protein analysis, growth factors were supplemented after cell-attachment. Samples were incubated for 48 h before the culture-inserts were removed and migration was analyzed.

4. Results

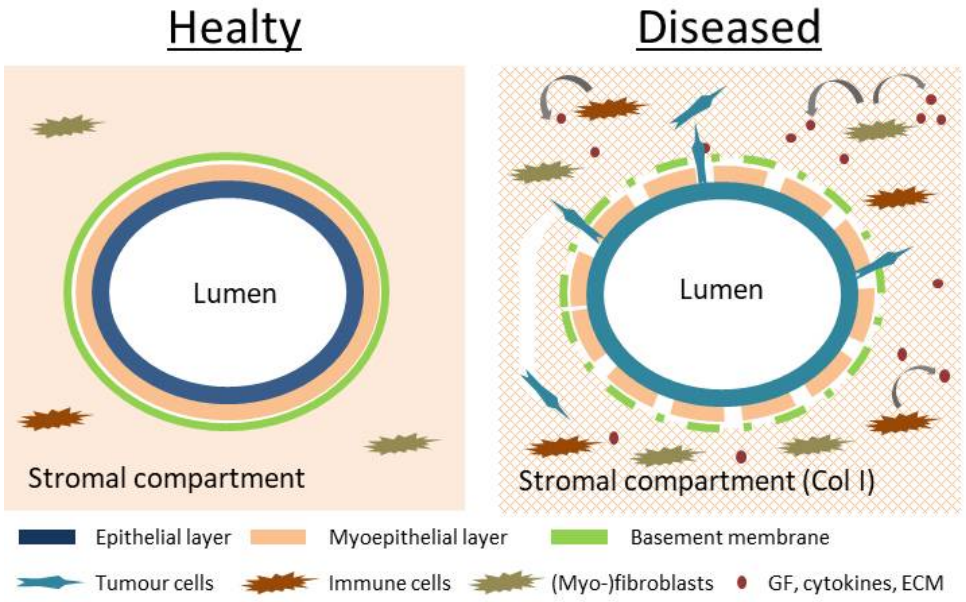

Separation of epithelial from stromal compartment via BM	Lack in basal lamina and/or lack of myoepithelial cells
(Myo-)fibroblasts, endothelial cells and presence of a few immune cells as part of normal immune surveillance	Elevated number of stromal/immune cells; Cancer associated cells like (Myo-)fibroblast, with altered gene expression and growth factor secretion; angio- and lymphangiogenesis
Tissue homoeostasis; Soft tissue; Normoxia	Desmoplastic ,stiffened tissue with increased deposition, crosslinking and remodeling of the ECM; Hypoxia

Figure 1. *Schematic cross-section of a mammary duct during cancer progression. The left panel shows a healthy tissue in the mammary gland. The mammary duct is formed by an epithelial layer surrounded by myoepithelial cells that are framed by the basement membrane. The stromal compartment is well separated from the epithelium which is also the case for DCIS. The right panel demonstrates tissue alteration as part of tumor progression as occur for IBCs. Defects in basement membrane and/or myoepithelial layer arise. Stromal and epithelial compartments are exposed to each other. The lower table lists the most prominent changes of the depicted tissue during tumor progression.*

4.1 EMT-status

4.1.1 EMT-markers

EMT is characterized by phenotypic changes in protein expression relying on extrinsic (GFs, hypoxia, ECM) and intrinsic (epigenetic) regulation.[40, 41] To define the EMT-status of our four breast cancer (BC) cell lines, assessing the expression of phenotypic protein markers (EMT-markers), is of fundamental importance. As described above, high levels of CDH1 are representative for an epithelial phenotype, whereas expression of VIM is a mesenchymal attribute. To this end, we performed Western blotting and qPCR analysis of the four breast cancer cell lines MCF7, HCC1954, MDA-MB-468 and MDA-MB-231 (**Figure 2 b,c**). Both, the Luminal A and the HER2-positive cell line strongly expressed E-Cadherin, whereas they lacked vimentin expression. Considerably lower level of E-Cadherin was detected for MDA-MB-468 (2-fold lower than for MCF7), but they co-expressed *VIM*. Furthermore, MDA-MB-231 was the only cell line to exhibit high levels of VIM showing absence of CDH1. We confirm that the intrinsic subtype nomenclature for breast cancer matches with EMT-marker expression and malignancy correlates with the less epithelial but rather mesenchymal phenotypic marker expression. To improve this still binary system, we decided to take additional aspects into account to define the EMT-status.

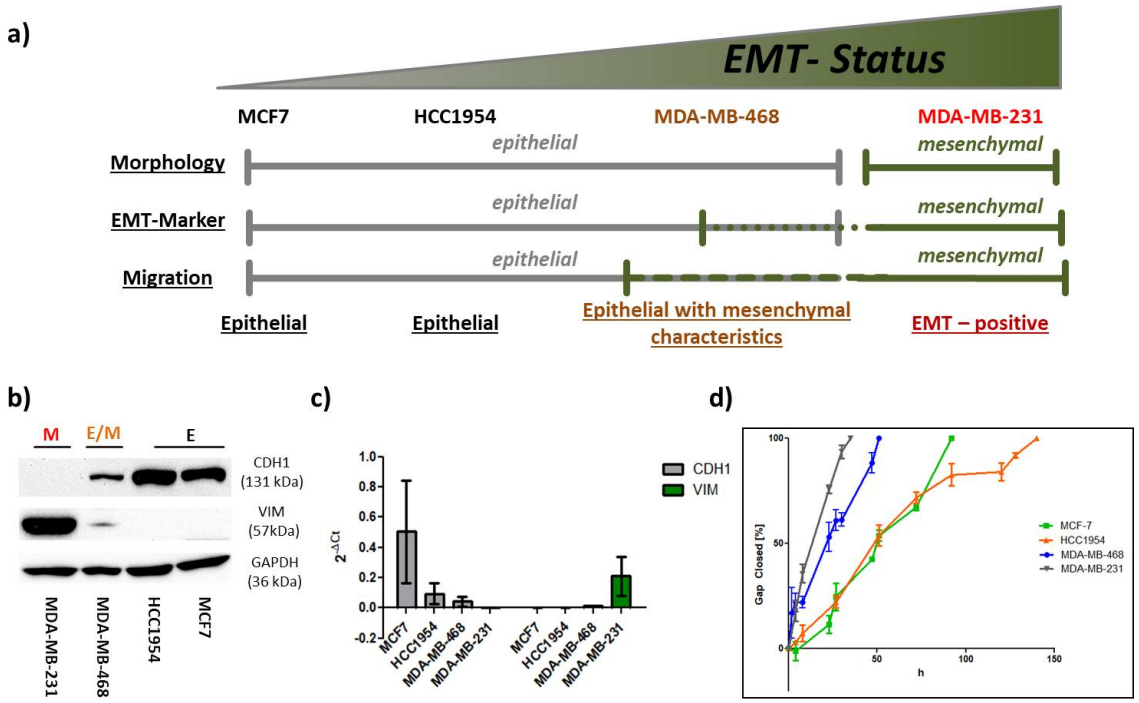

Figure 2. *Defining EMT-status of 4 breast cancer cell line.* ***a)*** *Summarising and defining the EMT-status according to the available data consisting of morphological, EMT-marker and motility assessment. MCF7 and HC1954 cell lines were shown to have epithelial (E) characteristics throughout the experiments. MDA-MB-468 cells were considered an E/M-hybrid cell line. MDA-MB-231 cell line consistently demonstrated mesenchymal (M) characteristics. They are considered an EMT-positive cell line.* ***b)*** *Protein levels of CDH1, VIM and GAPDH (housekeeping) of the 4 cell lines.* ***c)*** *mRNA expression of CDH1 and VIM gene are shown as* $2^{-\Delta Ct}$ *normalized to GAPDH mRNA expression.* ***d)*** *Ibidi® migration assay performed on 4 BC cell lines. Migration is analysed by comparing the percentage of gap closure [%] over time (h). Area/timepoint is calculated based on three marked spots within each gap (n = 2). Error bars represent SD.*

4.1.2 Migration

Cellular migration is strongly dependent on cell-cell and cell-ECM adhesion.[42] Considering transcriptional repression of CDH1 and other cell-cell adhesion molecules as part of EMT, it appears logical that the resultant phenotype exhibit increased motility. VIM and cytoskeletal-dependent cell polarization further enhance the migratory ability of cancer cells during the transition. Thus, to estimate the cellular EMT-status we also evaluated the migratory behavior of the different cell lines using a wound healing assay. Migration potential was quantified by means of percentage gap-closure over time starting from 0 % at t_0. **Figure 2d** shows that MCF7 and HCC1954 cells were able to close the gap at a similar rate. On the other hand, the other two cell lines MDA-MB-468 and MDA-MB-231 were 2 and 3 times faster, respectively. In a spheroid-based migration assay we confirmed that MDA-MB-231 cells, which fail to express CDH1 spread significantly faster (5-10 times) as the CDH1-positive cell line MCF7 (Supplementary data, **Figure S1**).

4.1.3 Morphology

Another feature of EMT is the re-structuring of the cytoskeleton based on spatiotemporal organization of actomyosin, microtubules, IF and other functional proteins.[27, 33, 43, 44] Thereby, the intrinsic mechanical properties of cells are altered, which lead to changes in cellular shape.[45, 46] Actin filament polymerization is a driving force for the switch from a basolateral to a front-back polarity during EMT.[47, 48] Fluorescently labeling the actin cytoskeleton allows for monitoring changes in cellular shape via confocal microscopy. To describe morphological changes in cancer cells the aspect ratio $A_{R,}$ the cellular minor axis divided by its major axis ($A_R = d_{min}/d_{max}$), has been used.[38, 49-51] In the context of EMT, a value close to 1 is attributed to an epithelial, cobblestone-like morphology, whereas values close to 0 describe a spindle-like appearance. We further evaluated nuclear pleomorphisms via nuclear circularity (C_N). Nuclear pleomorphisms are established to be clinically relevant in diseased tissues [52, 53], but unfortunately, standard 2-D *in vitro* cell culture results are not often able to link circularity to phenotypic changes. [52, 54] Since nuclear envelop proteins are directly physically entangled with cytoskeletal proteins and since nuclear dynamics are connected to cytoskeleton-mediated migration [55, 56], we expected changes in nuclear circularity during EMT progression.

Confocal imaging revealed pronounced clustering of cells for MCF7, HCC1954 and MDA-MB-468 cells, even though the latter cells appeared to bundle less tight (Figure 3). MDA-MB-231 did not cluster at all, but showed an elongated shape which is also confirmed by the image analysis. The aspect ratio of MDA-MB-231 (0.240 ± 0.157) was significantly lower in comparison to the other 3 cell lines, MCF7 (0.654 ± 0.136), HCC1954 (0.707 ± 0.128) and MDA-MB-468 (0.683 ± 0.170) which showed no significant differences amongst each other. A similar tendency was observed for the morphological assessment of the nucleus. Here, a circularity of 1 matches a perfect circle and decreasing values describe progression to ellipsoid shapes. Nuclei of MDA-MB-231 showed to have the most ellipsoid shapes (0.735 ± 0.101) that significantly differed from the other cell lines. Trending mean values of 0.808 ± 0.053 for HCC1954 and 0.877 ± 0.046 for MDA-MB-468 implied a stronger heterogeneity of nuclear circularity amongst the other 3 cell lines as compared to the A_R value.

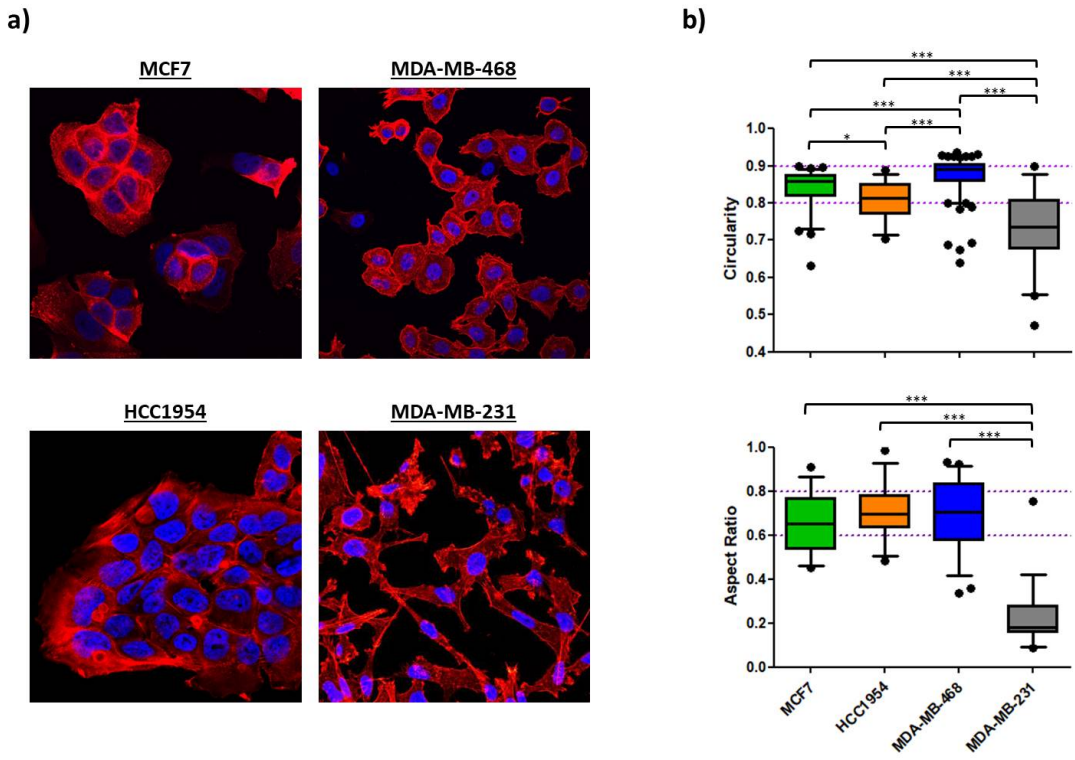

Figure 3. *Morphological analysis of the 4 BC cell lines.* ***a)*** *Confocal images of fixed cells recorded with a 63x objective. Nuclei are shown in blue (DAPI) and the actin cytoskeleton in red (TRITC). Cellular clustering and cuboidal shapes are typical epithelial features as shown for MCF7, HCC1954 and MDA-MB-468. F-Actin was predominantly organized in cortical bundles tightly associated with cell–cell adhesions. Mesenchymal MDA-MB-231 cells exhibited spindle-shaped morphologies and failed to form cellular islets.* ***b)*** *Image analysis via Fiji software is presented as Whiskers plot with 5-95 percentiles. Upper panel shows nuclear circularity C_N of the 4 cell lines (n_{nuclei} = 33 - 74). Nuclear circularities between 0.8 - 0.9 were assigned to epithelial cells (dotted lines). The lower panel shows cellular aspect ratio A_R of the 4 cell lines (n_{cells} = 25). A_R-values from 0.6 to 0.8 were attributed to epithelial cell shapes as indicated by the dotted lines. One-way ANOVA with Bonferroni multiple comparison test was performed in GraphPad Prism software (Graph Pad Software, La Jolla, CA, USA) to calculate P-values at 95% confidence interval.*

4.2 EMT induction

To understand which factors potentially play a role for EMT induction in the mammary gland, it is crucial to become acquainted with the tissue's architecture. As shown in **Figure 1** the epithelium of the mammary duct comprises a layer of milk-producing luminal cells, which is surrounded by myoepithelial cells. Apart from their contractile competence during lactation, myoepithelial cells produce the substrate of the epithelium, the basement membrane. This thin, but dense layer consists of collagen IV, laminin and proteoglycans and is bordering epithelial from stromal compartment [6]. The ducts are encircled by the microenvironment comprising ECM, predominantly collagen I, and stromal cells (e.g. fibroblasts, endothelial cells, leukocytes). In healthy tissues and DCIS, the luminal epithelial cells will not experience the environment of the stromal compartment. It is not before the breakage of

the BM of an invading tumor until epithelial cancer cells get in contact to collagen I and the multitude of factors (growth factors, cytokines, enzymes) secreted by cancer-associated cells during tumor progression [57-60]. It is strikingly evident that the resultant inflamed and desmoplastic stroma (**Figure 1**) bears a high potential to induce EMT.

4.2.1 EMT-markers

In the first place, to estimate the impact of the acellular stromal fraction of the mammary gland on our EMT-model, we confronted the three cell lines with collagen I (as major ECM component of the stroma) and the growth factors EGF and TGF-β1, respectively. In addition, we tried to further provoke EMT-like changes by combinatorial stimulation with all factors (**Figure 4**).

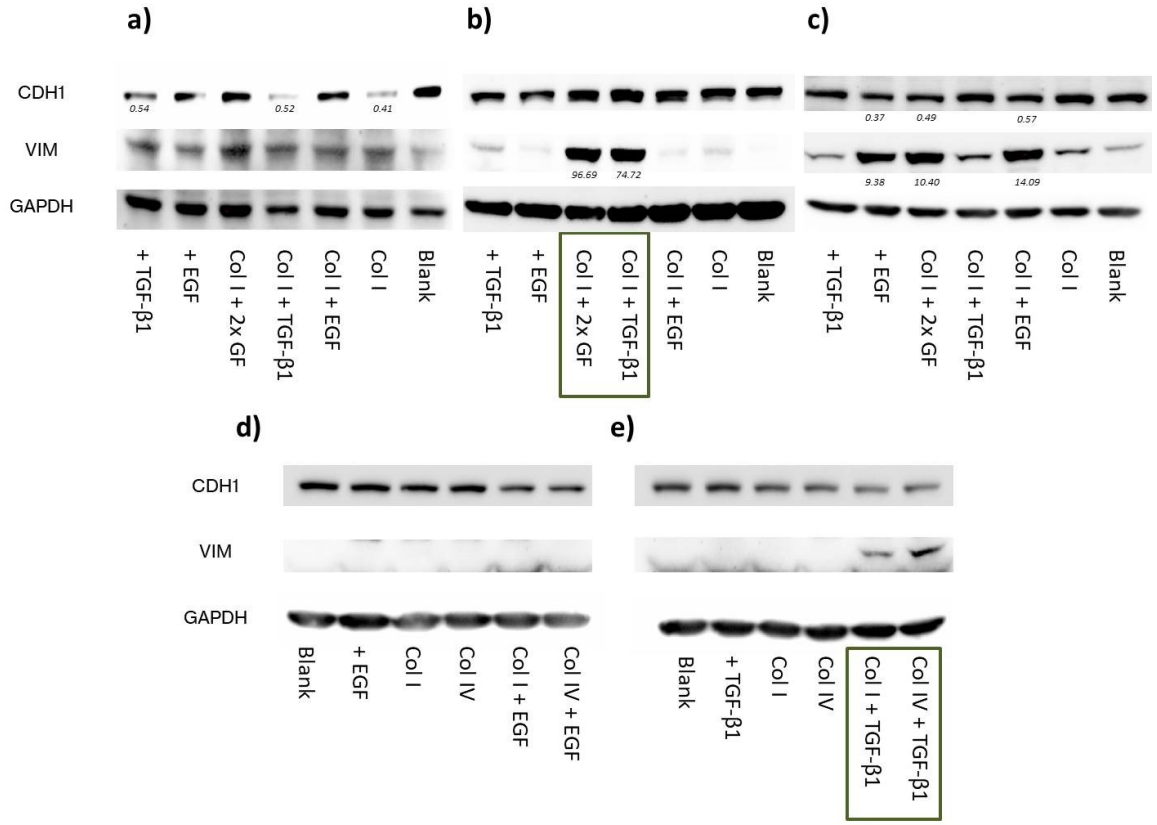

Figure 4. *Protein levels of CDH1, VIM and GAPDH (housekeeping) were assessed via Western blotting from 30 µg of the total protein extracts of MCF7, HCC1954 and MDA-MB-468 cell line as part of the EMT-induction study. Cells were subjected to multiple treatments as indicated. Numbers in the blots indicate fold-changes in protein levels normalized to untreated control cells (Blank) after 72 h incubation.* ***a)*** *EMT induction study in MCF7.* ***b)*** *EMT induction study in HCC1954* ***c)*** *EMT induction study in MDA-MB-468.* ***d)*** *EGF stimulation in HCC1954 dependent on collagen type.* ***e)*** *TGF-β1 stimulation in HCC1954 dependent on collagen type.*

MCF7 only showed minor changes in protein marker expression in comparison to untreated cells after 72h incubation (**Figure 4a**). Normalization with the housekeeping protein revealed that CDH1 protein levels of cells grown on collagen I were reduced to a similar extend as for TGF-β1 treatment (0.41 vs. 0.54). EGF appeared to have no impact on the EMT-markers. It rather abolished the effect of collagen I and TGF-β1 on CDH1 as part of a co-treatment. Combinatorial stimulation with collagen I and TGF-β1 did not further decrease E-cadherin expression (0.52). On the contrary, none of the treatments affected VIM levels.

Protein levels of the HCC1954 cell line demonstrated the importance of the concept of contextuality of signaling for EMT induction (**Figure 4b**). Single treatments and treatment of collagen I with EGF were inefficient to mediate phenotypic marker changes. Interestingly, the coaction of TGF-β1 with collagen I did imposingly enhance VIM protein expression (75-fold). This was also true when EGF was additionally added to the latter two. However, CDH1 protein levels were not stongly altered. Taken together, it appears that the growth on collagen I allowed for TGF-β1 to unfold its EMT-inducing capacities even if it only caused an incomplete pEMT.

In accordance to what has been reported elsewhere [61], EGF stimulation was able to drive EMT in MDA-MB-468 cells as demonstrated in **Figure 4c**. Both, CDH1 and VIM protein levels underwent EMT-typical changes. VIM was highly upregulated (9.4-fold) and CDH1 levels faded considerably (0.37). Combinatorial treatments with EGF did vaguely foster EMT induction in MDA-MB-468. Minor increase of VIM protein levels was observed under treatment with collagen I or TGF-β1 or with both.

As described above, invading tumors have to face the influence of collagen I once they have degraded the BM and enter the stromal compartment. Anyway, growing *in situ* carcinomas arising from luminal epithelial cells eventually interfere with collagen IV within the BM as they displace myoepithelial cells or the latter are depleted as a result of tumor progression.[57, 58] Consequently, examining the impact of collagen IV exerted on cancer cells which are under exposure to growth factors and comparing the outcome to growth on collagen I is of interest here.

Therefore, we included collagen IV in our EMT-marker study. Trilateral treatments (TGF-β1 + EGF + collagen) were excluded as they seemed to have no additive effect on EMT induction (data not shown). For MCF7 and MDA-MB-468 we confirmed phenotypic changes of EMT-protein levels of earlier findings (Supplementary data, **Figure S2**). In MCF7, after normalization, E-cadherin levels decreased for cell growth on collagen I under TGF-β1 stimulation to 60%. This decrease was even more pronouncedly on collagen IV (40%). On the contrary, VIM expression was unaffected by the tested treatments. Both collagens in combination with EGF did induce EMT-like changes in MDA-MB-468, but EGF was definitely the main cause to drive EMT (Supplementary data, **Figure S2**) as its single treatment exhibited the strongest effect on CDH1 and VIM levels.

Surprisingly, EMT induction experiments in HCC1954 cell line revealed that vimentin protein increment was independent of the collagen type when co-treated with TGF-β1 (**Figure 4e**). Thus, the data underline the necessity of collagen coatings for TGF-β1 to drive EMT. Again, it was mostly vimentin expression that changed whereas E-cadherin levels did hardly differ from untreated samples. EGF stimulation did not lead to phenotypic changes independently of the collagen type cells were seeded on (**Figure 4d**).

4.2.2 Morphology

The re-organization of the cytoskeleton as part of the EMT program converts cells into a phenotype with an increased motility and a spindle-like shape. As shown above, morphology of mesenchymal MDA-MB-231 cells significantly differed from the other three cell lines based on aspect ratio A_R and nuclear circularity C_N. EMT induction is expected to entail A_R and C_N approaching values comparable to those of MDA-MB-231 cells. The morphological analysis of confocal images is depicted in **Figure 5**.

Neither the A_R nor the C_N were significantly altered in the induction study for the MCF7 cell line (**Figure 5a**). The A_R of the sample co-treated with collagen IV and TGF-β1 (0.520 ± 0.195) showed the strongest deviation from the untreated cells (0.659 ± 0.122) whereas all C_N values remained comparable to control cells (0.801 ± 0.079).

Morphological assessment of confocal images of HCC1954 cells (**Figure 5b**) displayed significant decrease in nuclear circularity for TGF-β1 stimulated samples seeded on collagen I ($P < 0.05$) and collagen IV ($P < 0.001$). Remarkably, the A_R of the latter samples also strongly deviated from the untreated cells (0.801 ± 0.077) with 0.709 ± 0.062 and 0.689 ± 0.099, respectively, even if not statistically significantly. As can be seen in **Figure 5d**, cells treated solely with TGF-β1 did neither change shape nor cytoskeletal architecture in comparison to untreated cells. Once grown on either collagen I or collagen IV, actin bundles (stress fibers) were formed, and the cellular outgrowth and shape differed from the control.

Furthermore, analysis of MDA-MB-468 cells revealed that C_N was significantly reduced for all samples treated with EGF ($P < 0.001$) in comparison to the untreated cells (**Figure 5c**). Similarly to what has been observed in HCC1954, decrease in C_N was accompanied by a significant reduction of the aspect ratio, most prominently for EGF stimulation alone (Control: 0.695 ± 0.161 vs. EGF: 0.358 ± 0.129). Cell-cell contacts diminished, and cellular shape became elongated when exposed to EGF (**Figure 5e**). A_R and C_N values of the other treatments varied marginally from those of untreated cells. In another experiment (Supplementary data, **Figure S3**) we showed, that the degree of morphological change depended on the concentration of EGF. Applying concentrations from 10 ng/ml to up to 50 ng/ml during a 72h incubation period resulted in continuous reduction of A_R and C_N values implying a more pronounced EMT induction for higher concentrations of the growth factor. However, the highest

concentration of EGF (100 ng/ml) reverted the effects on A_R and C_N and cells exhibited rounded shapes similar to untreated cells. Consequently, there might be an optimal range of EGF concentration to induce EMT-like changes.

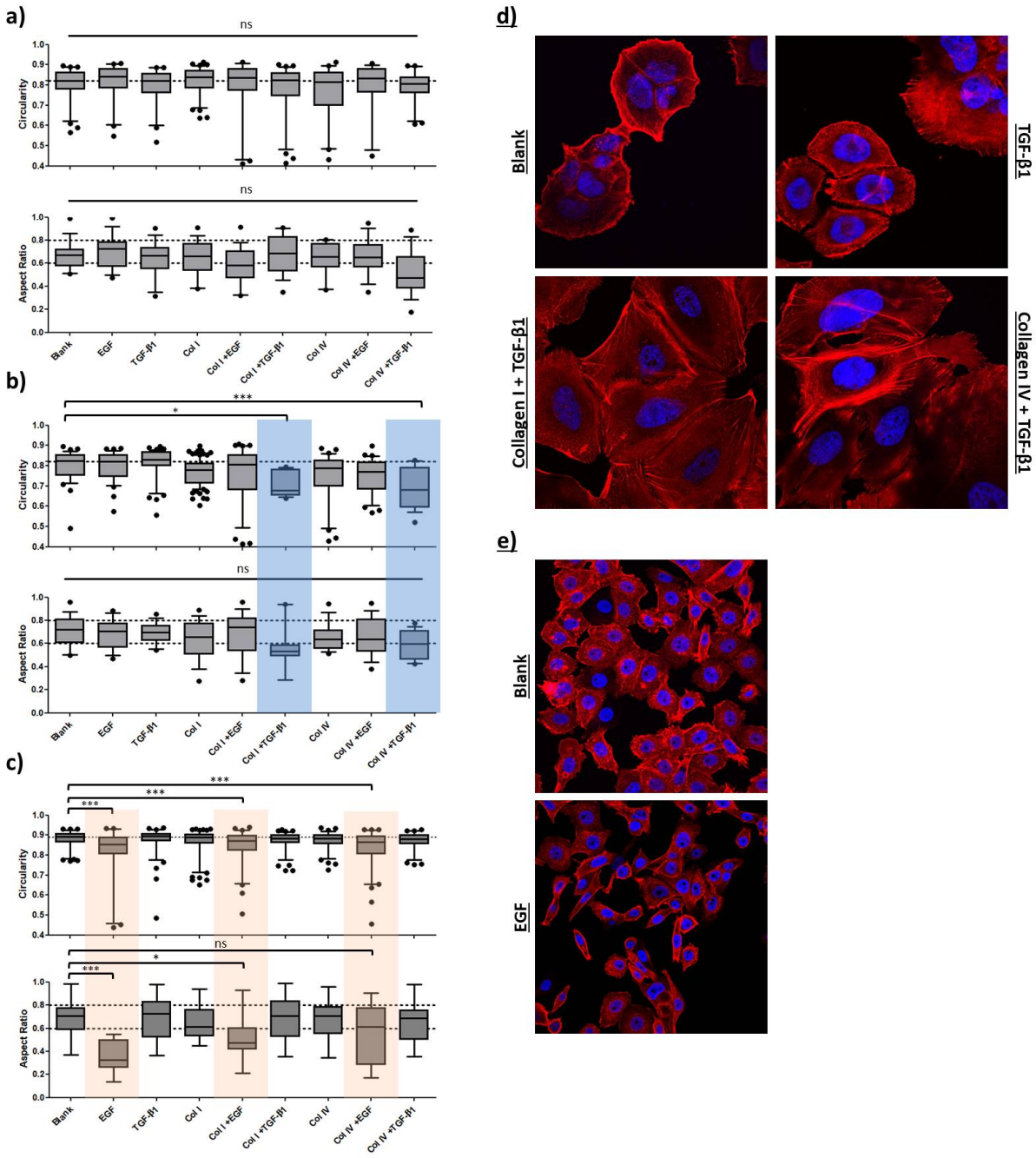

Figure 5. *Morphological analysis as part of the EMT-induction study. Confocal image analysis of fixed samples treated for 72 h. Cells were subjected to multiple treatments as indicated. Nuclear circularity C_N (upper panel) and cellular aspect ratio A_R (lower panel) were calculated using the Fiji software. Data is presented as Whiskers plot with 10-90 percentiles. One-way ANOVA with Dunnett's Multiple Comparison Test was performed in GraphPad Prism software to calculate P-values at 95% confidence interval.* ***a)*** *Shape factor analysis of MCF7*

cell treated with growth factors and/or grown on collagen demonstrated no significant changes in cellular morphologies. ***b)*** *Shape factor analysis of HCC1954 cell line showed significant alterations as part of a combinatorial treatment of TGF-β1 with collagen coatings (highlighted in blue).* ***c)*** *Shape factor analysis of MDA-MB-468 cells revealed significant decrease of C_N and A_R for EGF stimulation (highlighted in orange).* ***d)*** *Confocal images of fixed cells were recorded with a 63xobjective. Nuclei are shown in blue (DAPI) and the actin cytoskeleton in red (Phalloidin-TRITC). Cell growth of HCC1954 cells subjected to TGF-β1 treatment either grown on conventional glass coverslips or on collagen coated dishes. Combinatorial treatment resulted in restructuring of the cytoskeleton and stress fibre formation as part of the EMT program.* ***e)*** *Confocal images of fixed cells were recorded with a 40x (e) objective. MDA-MB-468 cell growth comparison between untreated cells (Blank) and EGF-treated cells. EGF stimulation resulted in loosened cell-cell junctions. Cells disseminated from epithelial clusters and exhibited more elongated shapes as compared to untreated cells.*

4.2.3 Migration

Based on our previous findings, we conducted migration assays with a focus on treatments that have shown considerable effects on EMT-marker expression and morphology during EMT induction.Apart from moderate changes in CDH1 levels after exposure to TGF-β1 or collagen I/IV, MCF7 cells mainly retained their phenotype. According to the migration analysis depicted in **Figure 6a**, these changes were insufficient to alter the migratory behavior of MCF7.

Additionally, we included combinatorial treatments for HCC1954 cells **(Figure 6b).** Interestingly, coaction of TGF-β1 and collagen I enhanced cellular motility. Time for completing gap closure was reduced to 56 h (vs. 96 h for untreated cells). No other treatment provoked similar changes. Even the combination of TGF-β1 with collagen IV had no impact on migration, in contrast to the morphological changes discussed above.

A striking effect on migration was observed for EGF treatment in MDA-MB-468 cells. Its presence accelerated cellular migration almost twofold. The time necessary to close the gap was reduced by 46% (28 h vs. 52 h). Of note, the migration under exposure to collagen IV was strongly decelerated. Cells required 72 h for a 100% gap closure. TGF-β1 and collagen I had no influence on the cellular motility in MDA-MB-468 **(Figure 6c)** which is in line with the lack of morphological effects discussed above.

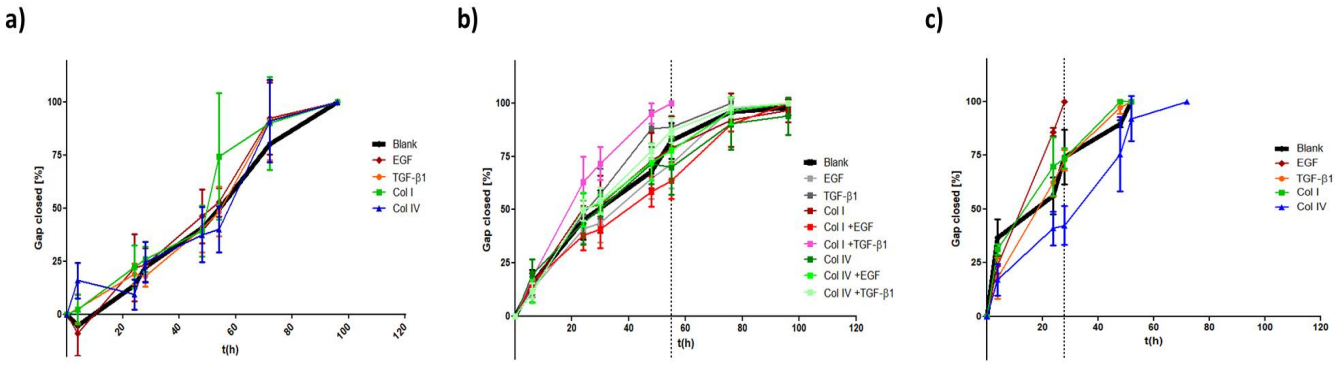

Figure 6. *Influence of EMT induction on migratory properties of BC cell lines. Ibidi® migration assay of MCF7 (**a**), HCC1954 (**b**) and MDA-MB-468 (**c**) are shown after 48 h incubation. Cells were subjected to multiple treatments as indicated. Migration is analyzed by comparing the percentage of gap closure [%] over time (h). Dotted lines depict time point of 100% gap closure of faster moving cells highlighting treatments that influence cellular migration.*

4.3 EMT-phenotyping model and its application

As indicated in **Figure 7**, we propose a phenotyping model to monitor EMT-status and EMT-like changes, which is essentially based on nuclear circularity (C_N) and cellular aspect ratio (A_R). We expanded it by queuing data from the aforementioned cellular EMT-protein marker settings and migratory behavior. Providing the M/E-ratio (normalized mesenchymal vimentin protein levels (M) divided by normalized E-cadherin protein levels (E)) for each treatment enabled us to correlate the magnitude of phenotypic transition on the protein level with the image-based shape analysis. Cellular motility, expressed as the apparent velocity v_a ([%] gap-closure per hour) further contributed to this model. Accordingly, rounded, slowly migrating epithelial-like cells are found in the upper right corner and highly motile mesenchymal-like cells in the lower left corner of the plot. Alongside the linear regression diagonal (A_R/C_N) of the control cells (dotted line), cellular phenotype is transiting from a low EMT- to a high EMT-status. A decrease in E-cadherin level is accompanied by a lowering of the A_R whereas the deformation of the nucleus (C_N values) showed a better correlation with vimentin upregulation.

In order to validate our model in the therapeutic context, we first quantified miR200c (microRNA200c) expression in the four cell lines. miR200c is known to fulfill a regulatory function regarding the epithelial-mesenchymal state of a cell as it directly inhibits the activity of pro-EMT transcription factors ZEB1 and ZEB2.[38] Therefore, miR200c expression is thought to correlate with E-cadherin expression and consequently with an epithelial phenotype. Indeed, miRNA expression analysis (**Figure 7b)** demonstrated high levels of miR200c to occur in epithelial MCF7 and HCC1954 cell lines. Moreover, miR200c expression was about halved in E/M-hybrid cell line MDA-MB-468 and absent in mesenchymal MDA-MB-231 cells. Hence, we clearly confirmed the correlation of miR200c expression levels and the underlying E/M phenotype.

Recently, it was show that the re-expression of miR-200c in vitro partially reverses the mesenchymal phenotype of MDA-MB-231 cancer cells, i.e. leading to a Mesenchymal-to-Epithelial transition (MET).[38] Using an miR200c inducible MDA-MB-231 cell line, we sought to exemplify a therapeutic intervention of targeting EMT *i.e.,* by inducing MET (**Figure 7c**). Strikingly, applying the miR200c inducible cell line for 48 h and 72 h to our model, we monitored morphological features to follow the linear regression diagonal ($y = 2.935x - 1.787$) calculated above. Setting the C_N-values in the equation predicted A_R-values of 0.245, 0.387 and 0.438 for 0 h, 48 h and 72 h time points, respectively, which were in relatively good agreement to the actual mean A_R-values (0.319, 0.421 and 0.546). Concomitantly, increased E/M-ratio and decreased apparent velocity were indicative for a transition towards a more epithelial phenotype, *i.e.* for the success of the modelled therapeutic intervention.

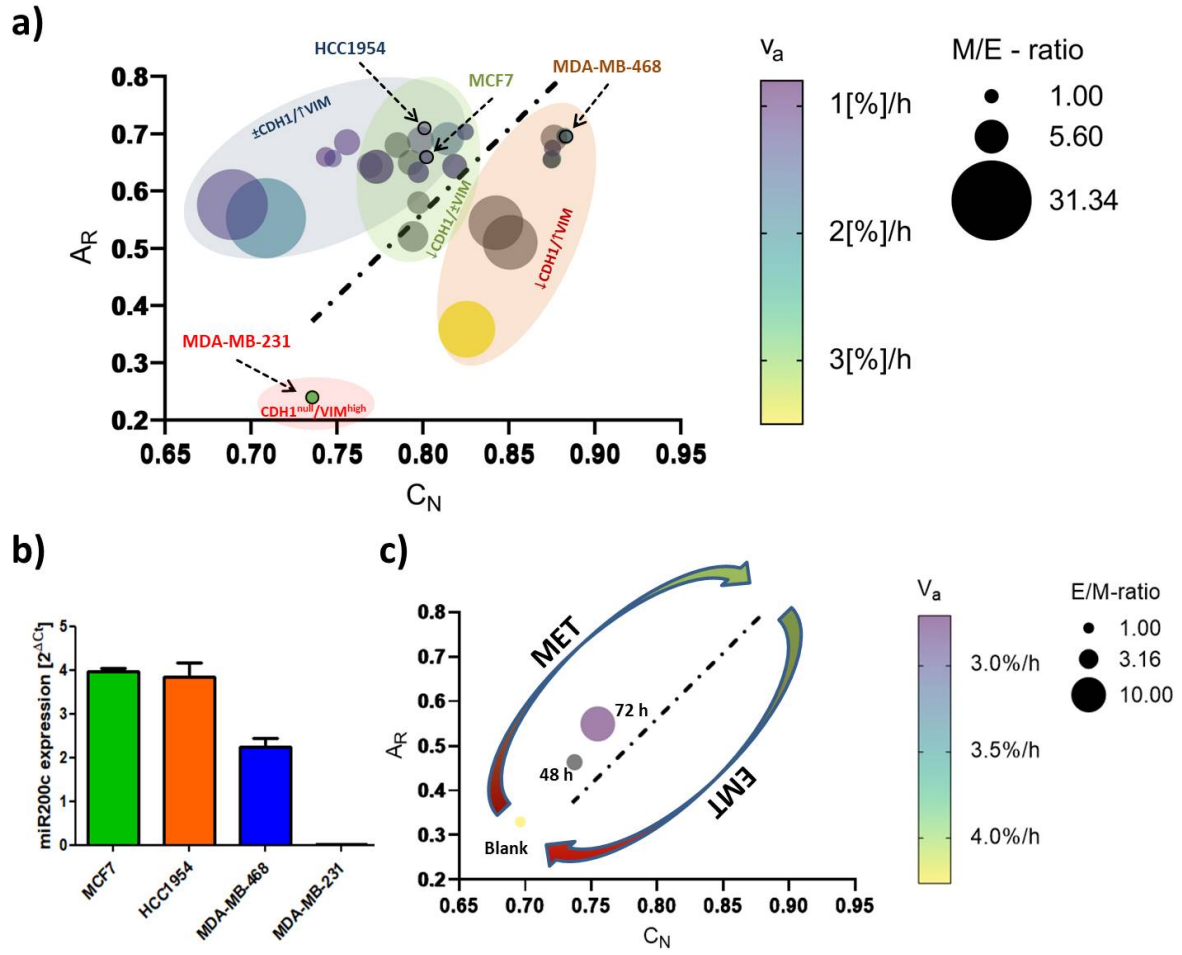

Figure 7. *EMT-phenotyping model for breast cancer. Summary of the data from the f cell lines merging EMT-marker protein levels, morphological and migration analysis (**a**). miR200c expression levels of the four cell lines (**b**). Applying miR-200c induction in MDA-MB-231 cells to test the EMT-model. Data was extracted after 48 h and 72h of DOX-dependent miR200c induction and compared to untreated (Blank) cells (**c**). Mean values of*

*nuclear circularity C_N, cellular aspect ratio A_R, apparent velocity v_a ([%] gap-closure per hour) and E/M- or M/E-ratio (= mesenchymal/epithelial-ratio on the protein level (VIM/CDH1)) were plotted in a multiple variable bubble plot. Results of the EMT induction study were included (**a**). M/E-ratio (E/M) of 1 indicates untreated control cells of each cell line and the respective controls are further indicated by an arrow. With increasing size of the bubbles, cells are approaching a protein set-up phenotypic for mesenchymal (**a**) or epithelial (**c**) cells. Colors of the bubbles indicate the migratory behavior with yellow representing the fastest moving cells. Grey bubbles were not attributed an apparent velocity. Ellipsoid, colored accentuations depict cell line-specific phenotypic changes with green representing MCF7 cells, purple HCC1954 cells, orange MDA-MB-468 cell line and red untreated sample of MDA-MB-231 cell line. The black dotted line shows the linear regression diagonal (A_R/C_N) of the control cells ($y = 2.935x – 1.787$; $R^2 = 0.62$)*

5. Discussion

Here, we established a simplified, EMT-relevant breast cancer model comprising 4 breast cancer cell lines. Biomimetic collagen coatings were shown to partially (cell line dependent) but not necessarily influence cellular EMT-phenotype upon growth factor stimulation. Surprisingly, other than reported elsewhere[36], the distinct collagen types did not differentially affect the phenotype and phenotypic transitions. Altogether, the triad of EMT-marker expression, morphology and migration was found to allow for a reasonable approximation of the present cellular EMT-status merging their input into a computational model phenotyping EMT in breast cancer, which we believe can serve as new platform to support EMT-related research.

Underlining the current understanding of EMT in cancer research [4, 5, 7, 8, 14, 27, 62, 63], (high) vimentin expression and absence of E-cadherin determined a fairly migratory phenotype with an elongated shape as was shown for the MDA-MB-231 cell line. Expression of the epithelial protein marker E-cadherin appeared to have a strong impact on morphological features as the three E-cadherin$^+$ cell lines studied here exhibited rounded shapes with A_R and C_N values close to a value of 1. Further, its expression was correlating with an immotile phenotype as long as vimentin was not co-expressed. Indeed, even low levels of vimentin protein could be correlated with increased cellular motility over vimentin$^-$ cells as was demonstrated for MDA-MB-468 cell line. In parallel to the classification of the intrinsic subtype nomenclature, epithelial characteristics vanished towards more malignant phenotypes whereas mesenchymal features concentrated in both TNBC cell lines (**Figure 2 and 3**).

In a recent study it was reported that Slug-mediated downregulation of E-cadherin, together with upregulation of vimentin impaired cellular morphology and increased cellular motility of the non-malignant breast epithelial cell line MCF10A.[64] Cellular circularity, which is interchangeable with the aspect ratio, was strongly decreased. Subsequent RNA interference with vimentin-targeting siRNA not only restored the circular cellular shape but also decelerated cellular motility. The authors

attributed vimentin a crucial role in influencing cellular morphology and motility, also because it may directly inhibit E-cadherin expression. In another study on breast cancer E-cadherin expression was proposed to be obligatory for a round polygon shape.[38] However, the findings of our EMT induction study suggest that an upregulation of vimentin and a concomitant downregulation of E-cadherin protein levels drive important morphological changes and strengthen migratory behavior, whereas merely downregulation of E-cadherin, concluded from the MCF7 cell line, was insufficient to significantly alter either of the latter two. As seen for MDA-MB-468, EGF stimulation significantly elongated cellular and nuclear morphology as part of a pronounced EMT-induction (↓ E-cadherin, ↑↑ vimentin). The A_R and C_N values of MDA-MB-231^{blank} (A_R = 0.240 ± 0.157; C_N = 0.735 ± 0.101) and MDA-MB-468^{+EGF} (A_R = 0.358 ± 0.129; C_N = 0.825 ± 0.102) essentially converged in a concentration-dependent manner (**Figure S2**) implying a shift from an E/M-hybrid with mostly epithelial characteristics towards a phenotype endowed with dominant mesenchymal functionalities (**Figure 5c and 7a**). Interestingly, upon EGF stimulation in MDA-MB-468, cellular migration was superior or at least the same to what has been observed for untreated MDA-MB-231. It took 24-28 h to close the gap in comparison to 30-35h for the already mesenchymal cell line. Moreover, we successfully transformed HCC1954 cells into a hybrid E/M phenotype entailing alterations of both shape factors and an acceleration of cellular motility. The wound healing migration assay revealed similar migratory properties under combinatorial treatment of TGF-β1 with collagen I, as was detected for MDA-MB-468^{blank} cells (56h vs. 50h). It appears that the strongly elevated vimentin protein level is the main driver for increased cellular motility, as E-cadherin level remained unaffected. Contradictory to these findings, combinatorial treatment of TGF-β1 with type IV collagen also shown to upregulate vimentin expression did not result in increased motility.

We can only speculate about the mechanistic causality explaining how a combinatorial treatment can provoke EMT-like changes while the single components fail to do so. In accordance to our data, Stephen T. Buckley *et al.* examined TGF-β1-induced EMT in human alveolar epithelial cells (AEC) and found that following TGF-β1 stimulation EMT induction was enhanced when cells were grown on a collagen I matrix as compared to growth on a glass surface.[43] They based their findings on changes in cellular shape factor and cellular stiffness to be superior to the simple growth factor treatment and emphasized the role of integrins (“ECM-receptors”) for EMT induction as was reported elsewhere.[65] In this work on EMT in fibrosis, the authors elegantly ruled out the possibility that growth of AECs on the ECM would lead to increased secretion of TGF-β1 which in turn drives EMT. Instead, they provided strong evidence that the αvβ6 integrin, a receptor that binds fibronectin, activates latent TGF-β1 signalling that causes cells to undergo EMT. Still, this cannot be the explanation in our case. Firstly, αvβ6 integrin is not known for binding any collagen type and secondly, their observation was independent of TGF-β1 supply. Nevertheless, literature offers two other explanations for how integrin-growth factor receptor (GFR) interplay may modulate cellular phenotypes.[66] GFR-ligand interactions can lead to cytosolic inside-out integrin receptor activation

or changes in expression pattern of integrin subunits.[67] Referring to our data, TGF-β1 signalling may have caused enhanced integrin activation/expression that would have resulted in intensified integrin signalling (through collagen-intergrin interaction), finally leading to EMT-like changes. On the other hand, integrins may co-opt in GFR signalling cascades. Signals emitting from integrin activation participate in downstream processes of GFR stimulation. Consequently, those kinds of interactions may not be the driving force for EMT, but rather scale up its dimension. Hence, we have to consider, that the 48h to 72h time scope of our EMT induction study was insufficiently long to detect TGF-β1-mediated EMT in HCC1954. However, our findings, together with the cited literature highlight the evident role of both contextuality of signalling and the tumor microenvironment for EMT induction *in vitro*. Such combinatorial actions might induce EMT in DCISs helping to overcome the physiological barrier, *i.e.* the basement membrane, whilst sustaining a (more) mesenchymal phenotype during stromal invasion.

Confocal imaging combined with image data analysis has been proven to be a powerful tool for addressing many kinds of biological questions. In the recent years, imaging has become increasingly relevant for studies on "phenomics", the quantification of the plurality of phenotypes that fully characterizes an organism.[68] Collective cellular properties such as cellular and subcellular morphologies are the result of genotypic expression pattern, whose quantification is readily susceptible via image data analysis.[69] In the context of EMT, a thoroughly planed study by Weikang Wang *et al*. stunningly demonstrated how live-cell imaging with subsequent deep image analysis disclosed heterogeneous transition dynamics upon TGF-β stimulation within one cell line.[70] They described a cell state in a 309-dimensional composite feature space of cell morphology and vimentin texture features and further revealed that spatiotemporal vimentin distribution allows for recording phenotypic alteration. The EMT-phenotyping model presented in our work is rather a snapshot approach as comparison of shape factors (C_N, A_R) was conducted at a specific time-point. As indicated in **Figure 9,** the morphological features coincided with EMT-marker expression and cellular motility. It is noteworthy that this computational model not only ranges EMT-phenotype and phenotypic changes, but presumably permits to differentiate between cell line specific transition-dynamics as indicated by the elliptic, colored areas in **Figure 7a.** To exemplify how this model can be used, we applied it to an miR200c inducible MDA-MB-231 cell line (**Figure 7c, Figure S4**).[51] miR200c expression, which is absent in untreated MDA-MB-231 cells, correlated with an epithelial phenotype (**Figure 7b**). The height of miR200c expression levels further discriminated between fully epithelial and partial epithelial characteristics. Induction of miR200c in the MDA-MB-231 cell line resulted in MET, resembling a potential therapeutic intervention targeting EMT. The success of miRNA induction after 48 h and 72 h resulting in increased nuclear circularity, and cellular aspect ratios closer to 1.0 can be appreciated as the shift from the left to the right alongside the regression diagonal. Simultaneously, the increasing E/M-ratio (= reciprocal M/E-ratio) and the decrease in ν_a are testifying to MET. Therefore, it may be sufficient to analyze one of the aforementioned shape factors in order to

predict the cellular E/M character as well as cellular motility. Thus, our model can estimate the impact of therapeutic approaches that target EMT-relevant factors on the EMT phenotype and may serve as an indicator to decide over new drug candidates during screening processes.

6. Conclusion

The Epithelial-to-Mesenchymal transition is an ambivalent issue in the field of cancer research particularly when it comes to its impact for breast cancer metastasis and the transition from DCIS to IBC. Studies, which show the independence of metastasis from EMT-phenotypic alterations, are scrutinizing the importance of EMT.[41, 71, 72] Nevertheless, the concept of pEMT has broadened up its interpretation and the increasing amount of literature assessing EMT from other perspectives (e.g. epigenetics, phenomics, biomechanics) is revitalizing the field of EMT. Even conventional cell culture set-up enable to study more complex interrelations such as the here presented contextual EMT induction which was partially dependent on the combinatorial action of collagen and soluble growth factors. Establishing a more biosimilar context and illuminating EMT from different angles provided us with data allowing for our own interpretation of phenotypic changes during EMT. We hope this model will contribute to a better understanding of EMT in breast cancer and that it potentially bears relevance for therapeutic applications.

7. References

[1] A. Cano, M.A. Pérez-Moreno, I. Rodrigo, A. Locascio, M.J. Blanco, M.G. del Barrio, F. Portillo, M.A. Nieto*, Nat. Cell Biol.* **2000**, *2*(*2*): p. 76-83, DOI: 10.1038/35000025.

[2] J.P. Thiery*, Nat. Rev. Cancer* **2002**, *2*(*6*): p. 442-54, DOI: 10.1038/nrc822.

[3] J. Yang, P. Antin, G. Berx, C. Blanpain, T. Brabletz, M. Bronner, K. Campbell, A. Cano, J. Casanova, G. Christofori, S. Dedhar, R. Derynck, H.L. Ford, J. Fuxe, A. García de Herreros, G.J. Goodall, A.-K. Hadjantonakis, R.Y.J. Huang, C. Kalcheim, R. Kalluri, Y. Kang, Y. Khew-Goodall, H. Levine, J. Liu, G.D. Longmore, S.A. Mani, J. Massagué, R. Mayor, D. McClay, K.E. Mostov, D.F. Newgreen, M.A. Nieto, A. Puisieux, R. Runyan, P. Savagner, B. Stanger, M.P. Stemmler, Y. Takahashi, M. Takeichi, E. Theveneau, J.P. Thiery, E.W. Thompson, R.A. Weinberg, E.D. Williams, J. Xing, B.P. Zhou, G. Sheng, E.M.T.I.A. On behalf of the*, Nat. Rev. Mol. Cell Biol.* **2020**, *21*(*6*): p. 341-352, DOI: 10.1038/s41580-020-0237-9.

[4] T. Brabletz, R. Kalluri, M.A. Nieto, R.A. Weinberg*, Nat. Rev. Cancer* **2018**, *18*(*2*): p. 128-134, DOI: 10.1038/nrc.2017.118.

[5] J. Banyard, D.R. Bielenberg*, Connect. Tissue Res.* **2015**, *56*(*5*): p. 403-413, DOI: 10.3109/03008207.2015.1060970.

[6] M.W. Conklin, P.J. Keely*, Cell Adhes. Migr.* **2012**, *6*(*3*): p. 249-260, DOI: 10.4161/cam.20567.

[7] H. Son, A. Moon*, Toxicological research* **2010**, *26*(*4*): p. 245-252, DOI: 10.5487/TR.2010.26.4.245.

[8] R. Kalluri, R.A. Weinberg*, J. Clin. Invest.* **2009**, *119*(*6*): p. 1420-8, DOI: 10.1172/jci39104.

[9] W.L. Tam, R.A. Weinberg, *Nat. Med.* **2013**, *19*: p. 1438, DOI: 10.1038/nm.3336.
[10] R.A. Weinberg, *The Biology of Cancer*, **2014**.
[11] T.Z. Tan, Q.H. Miow, Y. Miki, T. Noda, S. Mori, R.Y. Huang, J.P. Thiery, *EMBO Mol. Med.* **2014**, *6*(*10*): p. 1279-93, DOI: 10.15252/emmm.201404208.
[12] S.V. Vasaikar, A.P. Deshmukh, P. den Hollander, S. Addanki, N.A. Kuburich, S. Kudaravalli, R. Joseph, J.T. Chang, R. Soundararajan, S.A. Mani, *Br. J. Cancer* **2021**, *124*(*1*): p. 259-269, DOI: 10.1038/s41416-020-01178-9.
[13] J.H. Taube, J.I. Herschkowitz, K. Komurov, A.Y. Zhou, S. Gupta, J. Yang, K. Hartwell, T.T. Onder, P.B. Gupta, K.W. Evans, B.G. Hollier, P.T. Ram, E.S. Lander, J.M. Rosen, R.A. Weinberg, S.A. Mani, *Proc. Natl. Acad. Sci. U. S. A.* **2010**, *107*(*35*): p. 15449-54, DOI: 10.1073/pnas.1004900107.
[14] S.K. Bhowmik, E. Ramirez-Peña, J.M. Arnold, V. Putluri, N. Sphyris, G. Michailidis, N. Putluri, S. Ambs, A. Sreekumar, S.A. Mani, *Oncotarget* **2015**, *6*(*40*): p. 42651-60, DOI: 10.18632/oncotarget.4765.
[15] A. Prat, C.M. Perou, *Mol. Oncol.* **2011**, *5*(*1*): p. 5-23, DOI: 10.1016/j.molonc.2010.11.003.
[16] M. Scimeca, C. Antonacci, D. Colombo, R. Bonfiglio, O.C. Buonomo, E. Bonanno, *Tumour Biol.* **2016**, *37*(*4*): p. 5427-35, DOI: 10.1007/s13277-015-4361-7.
[17] T. Bao, N.E. Davidson, *Adv. Surg.* **2008**, *42*: p. 249-260, DOI: 10.1016/j.yasu.2008.03.002.
[18] G. Arpino, D. Generali, A. Sapino, L. Del Matro, A. Frassoldati, M. de Laurentis, P. Pronzato, G. Mustacchi, M. Cazzaniga, S. De Placido, P. Conte, M. Cappelletti, V. Zanoni, A. Antonelli, M. Martinotti, F. Puglisi, A. Berruti, A. Bottini, L. Dogliotti, *The Breast* **2013**, *22*(*2*): p. 109-120, DOI: https://doi.org/10.1016/j.breast.2013.01.016.
[19] L. Yin, J.-J. Duan, X.-W. Bian, S.-c. Yu, *Breast Cancer Res.* **2020**, *22*(*1*): p. 61, DOI: 10.1186/s13058-020-01296-5.
[20] T. Sorlie, R. Tibshirani, J. Parker, T. Hastie, J.S. Marron, A. Nobel, S. Deng, H. Johnsen, R. Pesich, S. Geisler, J. Demeter, C.M. Perou, P.E. Lønning, P.O. Brown, A.L. Børresen-Dale, D. Botstein, *Proc. Natl. Acad. Sci. U. S. A.* **2003**, *100*(*14*): p. 8418-23, DOI: 10.1073/pnas.0932692100.
[21] T.A. O'Meara, S.M. Tolaney, *Oncotarget* **2021**, *12*(*5*): p. 394-400, DOI: 10.18632/oncotarget.27877.
[22] P. Alluri, L.A. Newman, *Surg. Oncol. Clin. N. Am.* **2014**, *23*(*3*): p. 567-577, DOI: 10.1016/j.soc.2014.03.003.
[23] D. Sarrió, S.M. Rodriguez-Pinilla, D. Hardisson, A. Cano, G. Moreno-Bueno, J. Palacios, *Cancer Res.* **2008**, *68*(*4*): p. 989-97, DOI: 10.1158/0008-5472.can-07-2017.
[24] M. Koleckova, J. Ehrmann, J. Bouchal, M. Janikova, A. Brisudova, J. Srovnal, K. Staffova, M. Svoboda, O. Slaby, L. Radova, K. Vomackova, B. Melichar, L. Veverkova, Z. Kolar, *Sci. Rep.* **2021**, *11*(*1*): p. 5145, DOI: 10.1038/s41598-021-84350-2.
[25] Q. Zeng, W. Li, D. Lu, Z. Wu, H. Duan, Y. Luo, J. Feng, D. Yang, L. Fu, X. Yan, *Proc. Natl. Acad. Sci. U. S. A.* **2012**, *109*(*4*): p. 1127-1132, DOI: 10.1073/pnas.1111053108.
[26] J.J. Christiansen, A.K. Rajasekaran, *Cancer Res.* **2006**, *66*(*17*): p. 8319-26, DOI: 10.1158/0008-5472.can-06-0410.
[27] M. Yilmaz, G. Christofori, *Cancer Metastasis Rev.* **2009**, *28*(*1*): p. 15-33, DOI: 10.1007/s10555-008-9169-0.
[28] J.M. Lee, S. Dedhar, R. Kalluri, E.W. Thompson, *J. Cell Biol.* **2006**, *172*(*7*): p. 973-981, DOI: 10.1083/jcb.200601018.
[29] M.I. Kokkinos, R. Wafai, M.K. Wong, D.F. Newgreen, E.W. Thompson, M. Waltham, *Cells Tissues Organs* **2007**, *185*(*1-3*): p. 191-203, DOI: 10.1159/000101320.
[30] R.A. Battaglia, S. Delic, H. Herrmann, N.T. Snider, **2018**, *7*, DOI: 10.12688/f1000research.15967.1.
[31] H. Herrmann, H. Bär, L. Kreplak, S.V. Strelkov, U. Aebi, *Nat. Rev. Mol. Cell Biol.* **2007**, *8*(*7*): p. 562-573, DOI: 10.1038/nrm2197.

[32] N. Costigliola, L. Ding, C.J. Burckhardt, S.J. Han*, Proc. Natl. Acad. Sci. U. S. A.* **2017**, *114*(*20*): p. 5195-5200, DOI: 10.1073/pnas.1614610114.
[33] C.-Y. Liu, H.-H. Lin, M.-J. Tang, Y.-K. Wang*, Oncotarget* **2015**, *6*(*18*): p. 15966-15983.
[34] Z. Gan, L. Ding, Christoph J. Burckhardt, J. Lowery, A. Zaritsky, K. Sitterley, A. Mota, N. Costigliola, Colby G. Starker, Daniel F. Voytas, J. Tytell, Robert D. Goldman, G. Danuser*, Cell Syst.* **2016**, *3*(*3*): p. 252-263.e8, DOI: https://doi.org/10.1016/j.cels.2016.08.007.
[35] Y. Shintani, M. Maeda, N. Chaika, K.R. Johnson, M.J. Wheelock*, Am. J. Respir. Cell Mol. Biol.* **2008**, *38*(*1*): p. 95-104, DOI: 10.1165/rcmb.2007-0071OC.
[36] S.P. Carey, K.E. Martin, C.A. Reinhart-King*, Sci. Rep.* **2017**, *7*: p. 42088, DOI: 10.1038/srep42088.
[37] M. Vidal, L. Salavaggione, L. Ylagan, M. Wilkins, M. Watson, K. Weilbaecher, R. Cagan*, Am. J. Pathol.* **2010**, *176*(*6*): p. 3007-3014, DOI: 10.2353/ajpath.2010.090253.
[38] B. Ljepoja, C. Schreiber, F.A. Gegenfurtner, J. García-Roman, B. Köhler, S. Zahler, J.O. Rädler, E. Wagner, A. Roidl*, PLoS One* **2019**, *14*(*11*): p. e0224314, DOI: 10.1371/journal.pone.0224314.
[39] J. Schindelin, I. Arganda-Carreras, E. Frise, V. Kaynig, M. Longair, T. Pietzsch, S. Preibisch, C. Rueden, S. Saalfeld, B. Schmid, J.-Y. Tinevez, D.J. White, V. Hartenstein, K. Eliceiri, P. Tomancak, A. Cardona*, Nat. Methods* **2012**, *9*(*7*): p. 676-682, DOI: 10.1038/nmeth.2019.
[40] S. Bhatia, P. Wang, A. Toh, E.W. Thompson*, Front. Mol. Biosci.* **2020**, *7*, DOI: 10.3389/fmolb.2020.00071.
[41] M.K. Jolly, T. Celià-Terrassa*, J. Clin. Med.* **2019**, *8*(*10*): p. 1542.
[42] D. Schaeffer, J.A. Somarelli, G. Hanna, G.M. Palmer, M.A. Garcia-Blanco*, Mol. Cell. Biol.* **2014**, *34*(*18*): p. 3486-3499, DOI: 10.1128/MCB.00694-14.
[43] S.T. Buckley, C. Medina, A.M. Davies, C. Ehrhardt*, Nanomed. Nanotechnol. Biol. Med.* **2012**, *8*(*3*): p. 355-364, DOI: https://doi.org/10.1016/j.nano.2011.06.021.
[44] M.F. Coughlin, D.R. Bielenberg, G. Lenormand, M. Marinkovic, C.G. Waghorne, B.R. Zetter, J.J. Fredberg*, Clin. Exp. Metastasis* **2013**, *30*(*3*): p. 237-50, DOI: 10.1007/s10585-012-9531-z.
[45] E. Paluch, C.-P. Heisenberg*, Curr. Biol.* **2009**, *19*(*17*): p. R790-R799, DOI: https://doi.org/10.1016/j.cub.2009.07.029.
[46] T. Lecuit, P.-F. Lenne*, Nat. Rev. Mol. Cell Biol.* **2007**, *8*(*8*): p. 633-644, DOI: 10.1038/nrm2222.
[47] S.E. Leggett, A.M. Hruska, M. Guo, I.Y. Wong*, Cell Communication and Signaling* **2021**, *19*(*1*): p. 32, DOI: 10.1186/s12964-021-00713-2.
[48] J. Shankar, I.R. Nabi*, PLoS One* **2015**, *10*(*3*): p. e0119954-e0119954, DOI: 10.1371/journal.pone.0119954.
[49] Z.-X. Ren, H.-B. Yu, J.-S. Li, J.-L. Shen, W.-S. Du*, Biosci. Rep.* **2015**, *35*(*3*): p. e00202, DOI: 10.1042/BSR20150070.
[50] A. Sarkar, A. Barui, S. Sengupta, J. Chatterjee, S. Ghorai, A. Mukherjee. in *2015 37th Annual International Conference of the IEEE Engineering in Medicine and Biology Society (EMBC)*. **2015**. DOI: 10.1109/EMBC.2015.7319605.
[51] J. Kim, Y. Cao, C. Eddy, Y. Deng, H. Levine, W.-J. Rappel, B. Sun*, Proc. Natl. Acad. Sci. U. S. A.* **2021**, *118*(*10*): p. e2024780118, DOI: 10.1073/pnas.2024780118.
[52] M. Schöchlin, S.E. Weissinger, A.R. Brandes, M. Herrmann, P. Möller, J.K. Lennerz*, J. Pathol. Inform.* **2014**, *5*(*1*): p. 40, DOI: 10.4103/2153-3539.143335.
[53] G. Bussolati, F. Maletta, S. Asioli, L. Annaratone, A. Sapino, C. Marchiò, E.C. Schirmer and J.I. de las Heras, Editors. **2014**, Springer New York: New York, NY. p. 101-121, DOI: 10.1007/978-1-4899-8032-8_5.
[54] C. Rena, P. Hara, T.P. A*., Biochem. Cell Biol.* **2014**, *92*(*4*): p. 287-295, DOI: 10.1139/bcb-2013-0120 %M 25053513.
[55] P. Friedl, K. Wolf, J. Lammerding*, Curr. Opin. Cell Biol.* **2011**, *23*(*1*): p. 55-64, DOI: 10.1016/j.ceb.2010.10.015.
[56] T. Fischer, A. Hayn, C.T. Mierke*, Front. Cell Dev. Biol.* **2020**, *8*(*393*), DOI: 10.3389/fcell.2020.00393.

[57] J.B. Kim, R. Stein, M.J. O'Hare, *Tumour Biol.* **2005**, *26*(*4*): p. 173-85, DOI: 10.1159/000086950.
[58] K. Polyak, R. Kalluri, *Cold Spring Harb. Perspect. Biol.* **2010**, *2*(*11*): p. a003244, DOI: 10.1101/cshperspect.a003244.
[59] Y. Mao, E.T. Keller, D.H. Garfield, K. Shen, J. Wang, *Cancer metastasis reviews* **2013**, *32*(*1-2*): p. 303-315, DOI: 10.1007/s10555-012-9415-3.
[60] B.S. Wiseman, Z. Werb, *Science (New York, N.Y.)* **2002**, *296*(*5570*): p. 1046-1049, DOI: 10.1126/science.1067431.
[61] J.J. Campbell, A. Husmann, R.D. Hume, C.J. Watson, R.E. Cameron, *Biomaterials* **2017**, *114*: p. 34-43, DOI: 10.1016/j.biomaterials.2016.10.048.
[62] M.A. Nieto, R.Y. Huang, R.A. Jackson, J.P. Thiery, *Cell* **2016**, *166*(*1*): p. 21-45, DOI: 10.1016/j.cell.2016.06.028.
[63] B.D. Craene, G. Berx, *Nat. Rev. Cancer* **2013**, *13*: p. 97, DOI: 10.1038/nrc3447.
[64] K. Vuoriluoto, H. Haugen, S. Kiviluoto, J.P. Mpindi, J. Nevo, C. Gjerdrum, C. Tiron, J.B. Lorens, J. Ivaska, *Oncogene* **2011**, *30*(*12*): p. 1436-1448, DOI: 10.1038/onc.2010.509.
[65] K.K. Kim, M.C. Kugler, P.J. Wolters, L. Robillard, M.G. Galvez, A.N. Brumwell, D. Sheppard, H.A. Chapman, *Proc. Natl. Acad. Sci. U. S. A.* **2006**, *103*(*35*): p. 13180-13185, DOI: 10.1073/pnas.0605669103.
[66] J.S. Munger, D. Sheppard, *Cold Spring Harb. Perspect. Biol.* **2011**, *3*(*11*): p. a005017-a005017, DOI: 10.1101/cshperspect.a005017.
[67] G. Zambruno, P.C. Marchisio, A. Marconi, C. Vaschieri, A. Melchiori, A. Giannetti, M. De Luca, *J. Cell Biol.* **1995**, *129*(*3*): p. 853-65, DOI: 10.1083/jcb.129.3.853.
[68] D. Houle, D.R. Govindaraju, S. Omholt, *Nat. Rev. Genet.* **2010**, *11*(*12*): p. 855-866, DOI: 10.1038/nrg2897.
[69] K. Smith, F. Piccinini, T. Balassa, K. Koos, T. Danka, H. Azizpour, P. Horvath, *Cell Syst.* **2018**, *6*(*6*): p. 636-653, DOI: https://doi.org/10.1016/j.cels.2018.06.001.
[70] W. Wang, D. Douglas, J. Zhang, S. Kumari, M.S. Enuameh, Y. Dai, C.T. Wallace, S.C. Watkins, W. Shu, J. Xing, *Sci. Adv.* **2020**, *6*(*36*): p. eaba9319, DOI: 10.1126/sciadv.aba9319.
[71] H. Tian, R. Lian, Y. Li, C. Liu, S. Liang, W. Li, T. Tao, X. Wu, Y. Ye, X. Yang, J. Han, X. Chen, J. Li, Y. He, M. Li, J. Wu, J. Cai, *Nat. Commun.* **2020**, *11*(*1*): p. 5127, DOI: 10.1038/s41467-020-18929-0.
[72] M.K. Jolly, K.E. Ware, S. Gilja, J.A. Somarelli, H. Levine, *Mol. Oncol.* **2017**, *11*(*7*): p. 755-769, DOI: 10.1002/1878-0261.12083.

8. Supplementary data

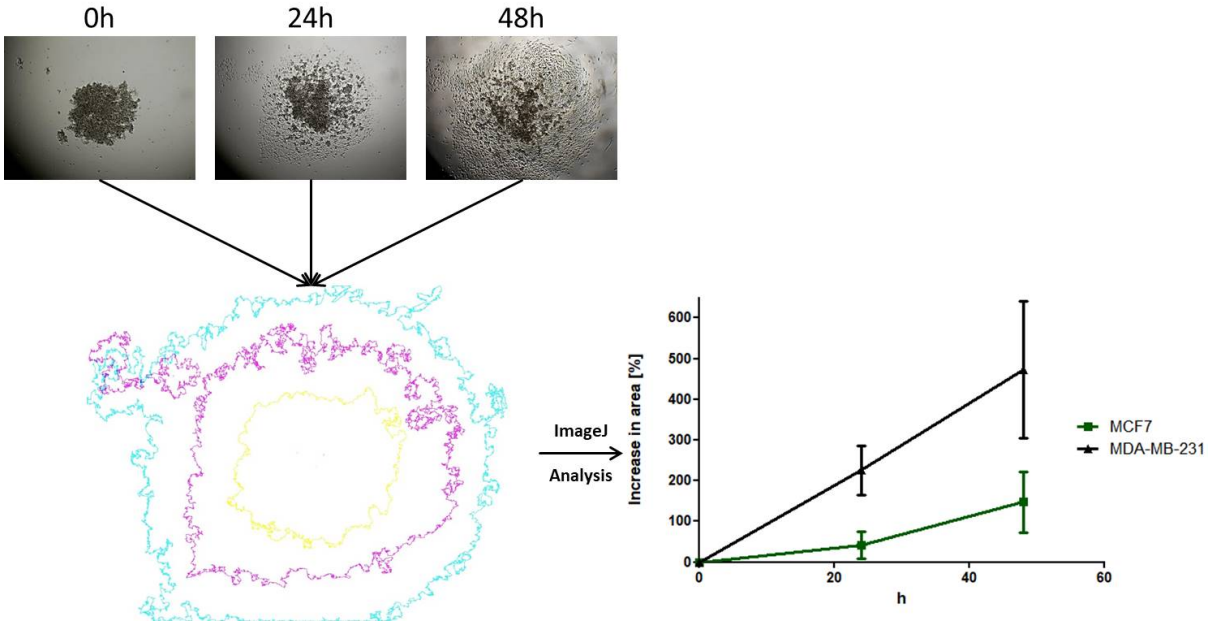

Figure S1. *Spheroid-based migration assay of MCF7 and MDA-MB-231 cell lines. Spheroids from a hanging-drop cell culture were transferred into a 96-well plate and its spreading was monitored after 24 h and 48 h by imaging and further analysed by Fiji image analysis software. Spreading was calculated as increase in cell area [%] in comparison to cell area at time point t = 0.*

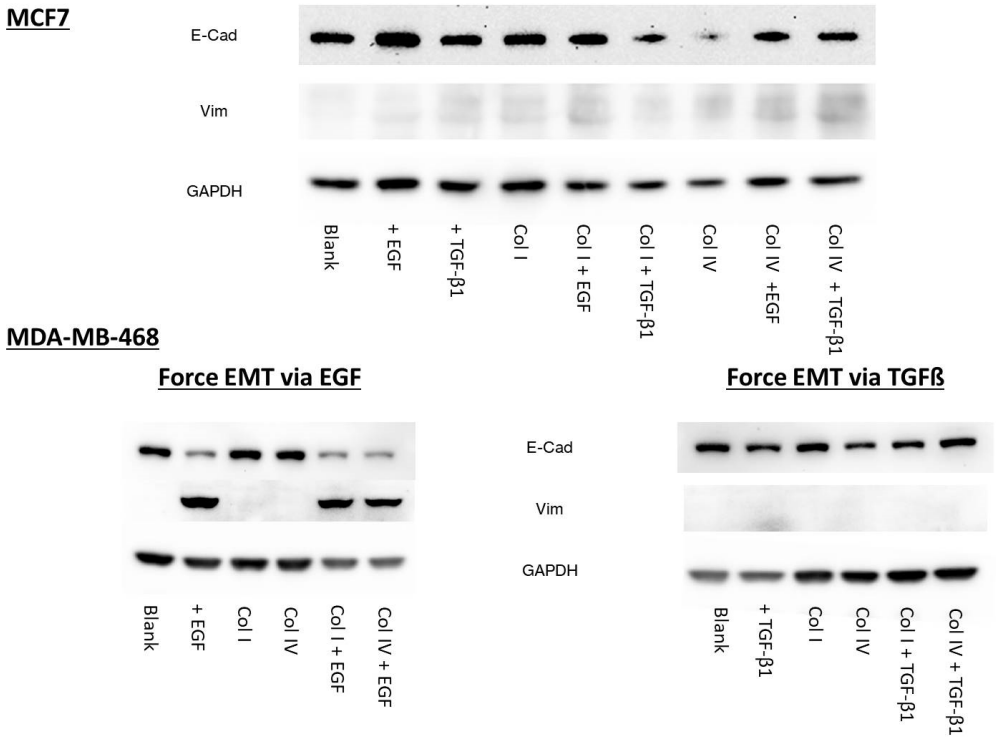

Figure S2. *Combinatorial treatment of growth factors and collagens. Protein levels of E-Cadherin, vimentin and GAPDH (housekeeping) were assessed via Western blotting from 30 µg of the total protein extracts of MCF7 and MDA-MB-468 cell line. Cells were subjected to multiple treatments as indicated. MCF7 cells dramatically decreased in E-cadherin protein levels upon growth on collagen IV and when grown on collagen I treated with TGF-β1. EGF stimulation induced EMT-like changes in MDA-MB-468.*

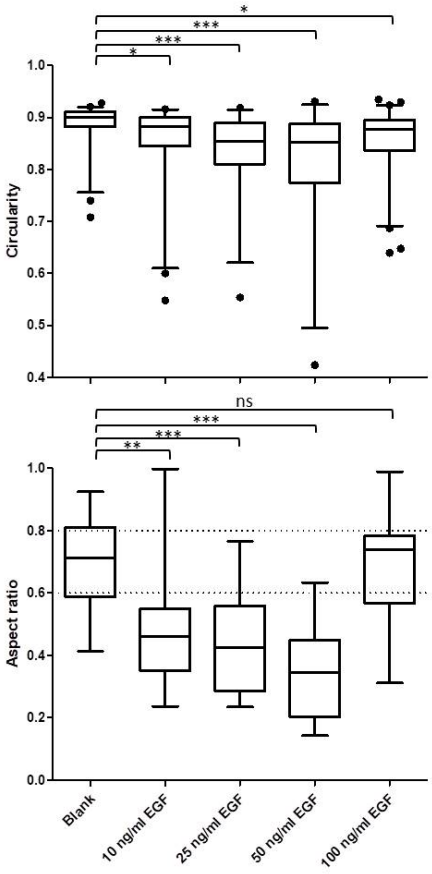

Figure S3. *EGF-concentration-dependant changes of morphological features in MDA-MB-468. Confocal image analysis of fixed samples treated for 72 h. Cells were treated with increasing concentration of EGF reaching from 0 ng/ml (Blank) to 100 ng/ml. Nuclear circularity C_N (upper panel) and cellular aspect ratio A_R (lower panel) were calculated using the Fiji software. Data is presented as Whiskers plot with 10-90 percentiles. One-way ANOVA with Dunnett's Multiple Comparison Test was performed in GraphPad Prism software to calculate p-values at 95% confidence interval. Morphological features gradually decreased in a concentration-dependent manner.*

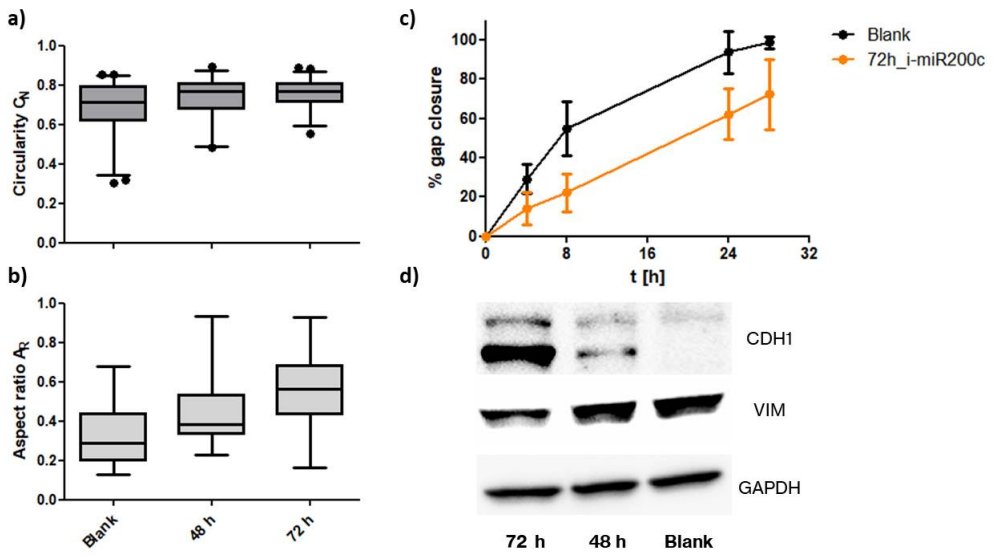

Supplementary Figure 4. *miR200c induction in a modified MDA-MB-231 cell line after 48/72 h. Morphological analysis from 63x confocal images of nuclei (**a**) (n > 80) and cytoskeleton (**b**) (n > 20). Ibidi® migration assay of untreated/blank cells (black line) and cells induced for 72 h (orange line) (**c**). Protein levels of E-Cadherin (CDH1) and Vimentin (VIM) depending on miRNA induction time (**d**).*

Chapter III

GASC1 and KDM6b: Epigenetic regulators as potential targets of EMT

1. Introduction

The activity of epigenetic factors decisively contributes to the EMT-phenotype during tumor progression and metastasis. Regulatory miRNA families such as miR-200 and miR-34 counteract the pro-EMT effects of transcription factors (ZEB1/2 and SNAIL, respectively) and thereby maintain the epithelial phenotype of cells.[1, 2] The functional relationship between histone-modifying enzymes that catalyze site-specific histone modifications and the EMT phenotype is instead more complex. The latter marks comprise acetyl- or methyl-groups being post-translationally removed or added to specific functional residues within the histone complex. For instance, histone methyltransferases that introduce a new methyl group are recognized at “writers” whereas demethylating enzymes are named “erasers”. The overall constitution of histone modifications defines the actual “histone code” which affects transcription of nearby genes.[3]

Lysine residues in histone tails can be mono, di, or trimethylated. GASC1 (gene amplified in squamous cell carcinoma-1), codes a histone demethylase for di- and trimethylated lysine 9 and 36 on histone H3 (H3K9me3/2 and H3K36me3/2). The H3K9me3/2 mark is generally associated with transcriptional repression and the formation of heterochromatin. Instead, H3K36me3/2 marks correlate with transcriptionally active genes and are thought to play an important role in suppressing incorrect transcription.[4] Recently, overexpression of the gene has been linked to an invasive cancer phenotype, which is partially due to its regulatory action on NOTCH-signaling, a transduction pathway contributing to EMT-like changes.[5, 6]

Likewise, KDM6b is a histone demethylase that presumably activates gene expression by removing repressive histone H3 lysine 27 trimethylation marks from chromatin. It was shown that TGF-β induced EMT upregulates KDM6b expression in mammary epithelial cells, which in turn actives transcription factor SNAIL by removing the repressive H3K27me3 mark from the SNAIL promoter to subsequently activate EMT.[7]

Consequently, both histone demethylases have been related to EMT or EMT-like changes in the past. Further elucidating such interrelations may enable to design new therapeutic strategies in order to oppose cancer progression. Here, it was shortly investigated, whether expression of the latter epigenetic factors plays a role in the cell line-based EMT *in vitro* model presented in Chapter II.

2. Materials & Methods

2.1 Material & cell culture

Hs_CDH1_Primer Assay (QT00080143), Hs_VIM_Primer Assay (QT00095795) and Hs_GAPDH_1_SG QuantiTect Primer Assay (QT00079247) were purchased from Qiagen (Hilden, Germany). Hs_GASC1 (Hs00379568_CE) and Hs_KDM6b (Hs00346696_CE) primers were ordered from Thermo Fisher Scientific (Waltham, MA, USA)

MCF7 cells were cultured in EMEM supplemented with 10% FBS, 1x Pen/Strep, 1x MEM Non-Essential Amino Acids Solution and 2 mM glutamine. The HER2-positive breast cancer cell line HCC1954 was grown in RPMI-1640 Medium supplemented with 10% FBS and 1x Pen/Strep. MDA-MB-231 and MDA-MB-231 i-miR200c cells were cultured in high glucose (4500 mg/L) DMEM. To the medium, 10% FBS, 1x Pen/Strep and 2 mM glutamine were added. For miRNA induction, the medium was supplemented with 5 µg/ml doxycycline hydrochloride (DOX) as described elsewhere.[2] The latter four cell lines were cultured in a humidified atmosphere with 5% CO_2 at 37°C. The MDA-MB-468 cell line was grown in L-15 Medium supplemented with 20% FBS and 1x Pen/Strep. Those cells were kept in a humidified incubator with 0% CO_2 at 37°C.

2.2 mRNA expression analysis

RT-qPCR-based expression analysis among the four cell lines was performed. Of each cell line, 200.000 cells were seeded in a 6-well plate and cultured for 24h. After the incubation, cells were harvested and total RNA was isolated using the PureLink RNA mini kit according to the manufacturer's protocol with additional DNAse I digestion. Subsequently, 1000 ng of RNA was used to synthesize cDNA using the High capacity cDNA synthesis kit (Applied Biosystems™, Waltham MA, USA). In the following GASC1-, KDM6, E-cadherin- and vimentin-specific primer were used to amplify and quantify RNA using Power SYBR™ Green PCR Master Mix and the qTOWER real-time PCR thermal cycler (Analytik Jena, Jena, Germany). Ct values were normalized to GAPDH RNA expression, and delta Ct- (ΔCt) and delta delta Ct- (ΔΔCt) values were calculated for the comparison. (n = 3)

EMT was induced in MDA-MB-468 cells by additionally supplementing L-15 Medium with 25 ng/ml or 50 ng/ml EGF for 72 h before extracting mRNA. Likewise, MET was induced in MDA-MB-231_i-miR200c by addition of 5 µg/ml DOX, and cells were cultured for one week in the DOX-containing medium before being subjected to RT-qPCR analysis.

3. Results

3.1 mRNA expression of demethylases in the four cell lines

RT-qPCR was performed to assess mRNA levels of KDM6b and GASC1 in the breast cancer cell lines. As described in Chapter II, among the four studied cancer cell lines, luminal A MCF7 as well as Luminal B/HER2^{positive} HCC1954 were attributed an epithelial phenotype, MDA-MB-468 as an E/M-hybrid and MDA-MB-231 cells as mesenchymal.

Accordingly, mRNA-expression of GASC1 was significantly different between the cell lines showing increased mRNA levels among the epithelial phenotypes (**Figure 1**). The highest expression was observed in HCC1954 cells, which was about 2-times elevated compared with GASC1 expression of MCF7 and MDA-MB-468 cells. Notably, the expression in mesenchymal MDA-MB-231 was marginal and significantly decreased in comparison to MCF7 and HCC1954 cell lines.

KDM6b expression, on the other hand, was significantly (6x) overexpressed in MCF7 compared to the other three cell lines (**Figure 1**).

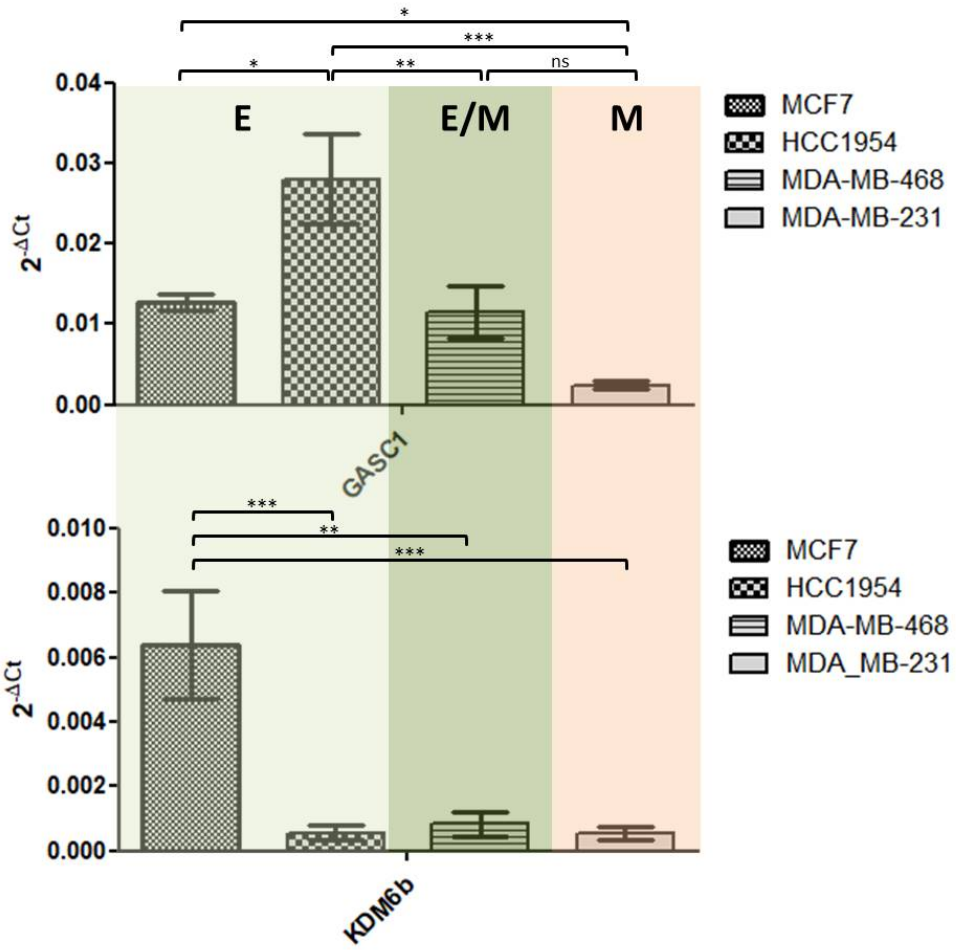

Figure 1. *mRNA expression of GASC1 (upper panel) and KDM6b (lower panel) in the four studied BC cell lines displayed as ΔCt-value (Error bars indicate SD). Statistical significance (n = 3) was calculated based on One-way ANOVA with Bonferroni multiple comparison test using GraphPad Prism software (Version 5.00*)

3.2 Changes of GASC1 and KDM6b upon EMT- and MET-induction

In Chapter II, it was demonstrated that MDA-MB-468 cells can be triggered to undergo EMT-like changes upon EGF stimulation. Therefore, the latter cell line was used as model cell line to investigate variations in mRNA expression of demethylases GASC1 and KDM6b upon EMT-induction. Likewise, the genetically engineered MDA-MB-231cell line (MDA-MB-231_i_miR200c[2]) was taken as model cell line to investigate changes that would occur during the reversal of a mesenchymal towards an epithelial phenotype upon miR200c induction (MET).

As shown in **Figure 1a**, both of the two applied EGF concentration resulted in EMT-like changes within the 72 h observation time frame indicated by significant downregulation of E-cadherin (CDH1) expression and upregulation of vimentin (VIM) expression. Demethylase expression levels of GASC1 as well as KDM6b were decreased by about 50% due to EGF stimulation, however, statistical significance was not reached. Interestingly, downregulation seemed to be more pronounced for lower EGF concentrations.

In contrast to EMT induction in MDA-MB-468 cells, miR200c-mediated MET entailed strong upregulation of CDH1 whilst downregulating VIM expression after 1 week of miR200c induction (**Figure 2b**). Furthermore, whereas KDM6b expression was only marginally decreased, GASC1 mRNA levels increased significantly to 200%.

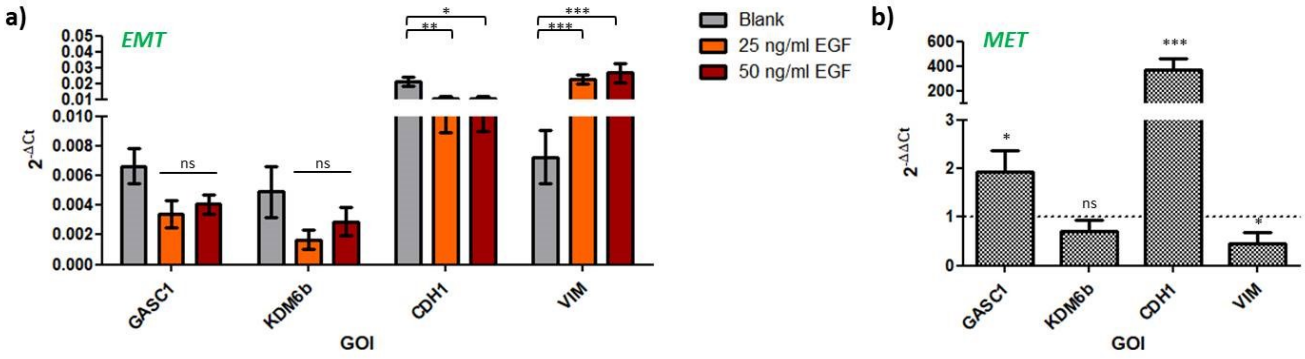

Figure 2. *mRNA expression analysis upon EMT and MET induction.* ***a)*** *MDA-MB-468 cells stimulated with EGF to undergo EMT.* ***b)*** *Genetically modified MDA-MB-231_i-miR200c induced to undergo MET.*

4. Discussion & Conclusion

Emerging evidence describes that deregulation of GASC1 and KDM6b demethylases entail decisive phenotypic consequences in various types of cancer. Therefore, interfering with those epigenetic factors holds promise for the design of novel anti-cancer therapies. For KDM6b, whether its expression is related to tumor suppressive or pro-oncogenic events is yet to be fully understood. Additionally, it is thought to follow a context-dependent regulation. Notably, signaling pathways of EMT-inducers such as growth factors EGF or TGF-β are thought to activate KDM6b transcription, promoting tumor progression and metastasis.[8] GASC1 over-amplification, on the other hand, is commonly linked to tumor progression in all kinds of carcinoma including breast cancer, prostate cancer and lung cancer. The potential oncogenic mechanism of GASC1 overexpression may be caused by delocalization of transcriptional regulators from target gene promoters, such a c-MYC oncogene, thereby activating oncogenes and increasing genomic instability due to loss of heterochromatin.[9]

Here, our cell line-based *in vitro* EMT-model was used to investigate whether a phenotype within the epithelial-mesenchymal spectrum could be linked to the expression levels of one of the demethylases. Furthermore, the course of GASC1 and KDM6b expression was monitored upon EMT and MET induction.

Indeed, mRNA expression analysis revealed enriched expression of GASC1 in epithelial and EMT-cell lines MCF7, HCC1954 and MDA-MB-468 but significantly lower expression in mesenchymal MDA-MB-231. In congruence with these findings, EGF-mediated EMT resulted in insignificant but visible downregulation of GASC1. These results support the theory that decreased GASC1 expression is phenotypic for mesenchymal-like cells. Simultaneously, MET induction in MDA-MB-231 cells i.e., the acquisition of a more epithelial-like phenotype lead to an enriched GASC1 expression further indicating a direct relation between EMT/MET-phenotype and GASC1. Despite the fact that most literature supports the notion that GASC1 overexpression contributes to tumor progression, a recent clinical study indicated elsewise. Berdel *et al.* [10] found that GASC1 is both a prognostic and a predictive factor for women with invasive breast cancer. Accordingly, patients with GASC1 positive tumors had a better breast cancer specific survival and improved response to anti-cancer therapies. In agreement with the here presented data, low GASC1 expression levels were associated with tumors of a more aggressive phenotype.

Regarding KDM6b, the underlying study revealed high expression in luminal MCF7 cell but comparably low expression among the other three cell lines. Therefore, on could argue that KDM6b downregulation is indicative for tumor progression. However, both EMT and MET induction lead to insignificantly but visibly decreased KDM6b mRNA levels, not allowing to draw a definite conclusion. As mentioned above, the contextual character, which may also affect different cell lines, could complicate a clear correlation between EMT-phenotypes to its expression. Correspondingly, a recent study on lung cancer attributed KDM6b a paradoxical role during EMT, since both its overexpression and inhibition led to the induction of EMT-like changes.[11] Hence, to exploit KDM6b as therapeutic target it is obligatory to further elucidate its regulatory, context-dependent functionalities.

To summarize, this study on four breast cancer cell lines demonstrated an interrelation between cellular EMT-status as well as EMT/MET-like changes with the expression levels of GASC1 and, even though less clear, with KDM6b. Notably, GASC1 expression, against the current understanding, seemed to be negatively related to tumor malignancy and EMT-phenotype. Additionally, it was found that KDM6b is not a straightforward target in breast cancer therapy.

5. References

[1] S. Brabletz, H. Schuhwerk, **2021**, *40*(*18*): p. e108647, DOI: 10.15252/embj.2021108647.

[2] B. Ljepoja, C. Schreiber, F.A. Gegenfurtner, J. García-Roman, B. Köhler, S. Zahler, J.O. Rädler, E. Wagner, A. Roidl, *PLoS One* **2019**, *14*(*11*): p. e0224314, DOI: 10.1371/journal.pone.0224314.

[3] J. Roche, R.M. Gemmill, H.A. Drabkin, *Cancers (Basel)* **2017**, *9*(*7*), DOI: 10.3390/cancers9070072.

[4] M.A. Ali, K. Mondal, Y. Jiao, S. Oren, Z. Xu, A. Sharma, L. Dong, *ACS Appl Mater Interfaces* **2016**, *8*(*32*): p. 20570-82, DOI: 10.1021/acsami.6b05648.

[5] Z. Wang, Y. Li, D. Kong, F.H. Sarkar, *Curr. Drug Targets* **2010**, *11*(*6*): p. 745-51, DOI: 10.2174/138945010791170860.

[6] G. Liu, A. Bollig-Fischer, B. Kreike, M.J. van de Vijver, J. Abrams, S.P. Ethier, Z.Q. Yang, *Oncogene* **2009**, *28*(*50*): p. 4491-4500, DOI: 10.1038/onc.2009.297.

[7] S. Ramadoss, X. Chen, C.Y. Wang, *J. Biol. Chem.* **2012**, *287*(*53*): p. 44508-17, DOI: 10.1074/jbc.M112.424903.

[8] C. Hua, J. Chen, S. Li, J. Zhou, J. Fu, W. Sun, W. Wang, *Front. Oncol.* **2021**, *11*, DOI: 10.3389/fonc.2021.779918.

[9] D.H. Lee, G.W. Kim, Y.H. Jeon, J. Yoo, S.W. Lee, S.H. Kwon, *The FASEB Journal* **2020**, *34*(*3*): p. 3461-3484, DOI: https://doi.org/10.1096/fj.201902584R.

[10] B. Berdel, K. Nieminen, Y. Soini, M. Tengström, M. Malinen, V.-M. Kosma, J.J. Palvimo, A. Mannermaa, *BMC Cancer* **2012**, *12*(*1*): p. 516, DOI: 10.1186/1471-2407-12-516.

[11] C. Lachat, D. Bruyère, A. Etcheverry, M. Aubry, J. Mosser, W. Warda, M. Herfs, E. Hendrick, C. Ferrand, C. Borg, R. Delage-Mourroux, J.-P. Feugeas, M. Guittaut, E. Hervouet, P. Peixoto, *Cancers (Basel)* **2020**, *12*(*12*): p. 3649.

Chapter IV

Cellular EMT-status governs contact guidance in an electrospun TACS-mimicking in-vitro model

Parts of this chapter are going to be submitted as scientific article:

Lorenz Isert, Mehak Passi, Benedikt Freystetter, Maximilian Grab, Andreas Roidl, Christoph Müller, Aditi Mehta, Harini G. Sundararaghavan, Stefan Zahler, Olivia M. Merkel; "Cellular EMT-status governs contact guidance in an electrospun TACS-mimicking in-vitro model"

1. Introduction

According to the International Agency for Research on Cancer, female breast cancer (BC) has become the largest cancer disease worldwide with a prevalence of 2.3 million new cases in 2020.[1] About 7% of patients suffer from a lethal outcome primarily due to metastasis. Therefore, optimizing breast cancer diagnostics and discovering new prognostic factors are still pressing needs to complement well-accepted clinico-pathological factors such as biomarker status (intrinsic subtypes), patient age, comorbidity, tumor size, tumor grade and number of involved axillary lymph nodes.[2] Macro- and microscopic histological features of the acellular fraction of the tumor microenvironment (TME) have recently gained attention in the field of breast cancer diagnostics. High breast tissue density as a consequence of increased collagen deposition is a crucial risk factor for developing breast cancer.[3, 4] Notably, tumor-associated collagen signatures (TACS) which are specifically structured nano- to micron-scaled fibrillar collagen (I) bundles resulting from collagen remodeling at the tumor-stromal interface are thought to facilitate tumor migration and invasion. They arise through the interplay of massive collagen deposition, proteolytic activity of secreted enzymes and contractile events from cells at the tumor boundary. Researchers proposed TACS to bear an undisclosed value as prognostic marker for BC as their identification was linked to pre-palpable tumors.[5] Studies analyzing the occurrence of TACS in patient-derived tissue samples revealed significant correlation of TACS with tumor grade and cancer prognosis.[6-8] According to this nomenclature TACS1-3 are representative for Ductal Carcinoma In-Situ (DCIS), whereas TACS4-8 identify the transition to Invasive Breast Cancer (IBC), where the basement membrane is transcended and cancer cells enter the stromal compartment. Importantly, TACS5 (directionally aligned collagen fibers) and TACS6 (chaotically/randomly aligned collagen fibers) at the invasive front of the tumor exhibited the strongest correlation with a poor prognosis [7] emphasizing the impact of particular topography and fiber orientation on metastasis in BC. Presumably, such collagen signatures are exploited as “migration highways”.[9] Cancer cells can travel on the latter to leave the epithelial entity of the primary tumor and disseminate either as collective (collective migration) or as single cells (mesenchymal or amoeboid migration) and invade through the stromal compartment to eventually reach the lymphatic or vascular system. However, the interaction between cancer cells and TACS remains to be fully elucidated.

Besides desmoplastic alteration, including the formation of TACS, within the stromal compartment explaining mechanical stiffening of the breast tissue [10] the micro-environmental cues and cell biology underlying cellular mechanics upon tumor progression are still mostly unknown. Being constantly in reciprocal exchange with the microenvironment enables and/or demands cancer cells to adjust cytoskeletal- and nuclear stiffness. This context-dependent biomechanical adaption of cancer cells during metastatic outgrowth was proposed to result from tissue peculiarities, mode of migration, actual step of metastasis and (epi-) genetic alterations.[11] To date, atomic force microscopy (AFM), micropipette aspiration, microfluidics or optical stretchers applied to 2-D and 3-D cell cultures

repeatedly demonstrated that cancer cells are significantly softer than their healthy or benign counterparts.[12-16] As regards breast cancer, Plodinec *et al.* [17] resolved the mechanical landscape of healthy breast tissues and defined stages of tumor progression. Accordingly, benign lesions increased in stiffness over healthy tissue which was attributed to ECM restructuring by fibroblast infiltration but samples kept the same, unimodal stiffness distribution. Invasive cancer however showed a unique, trimodal stiffness distribution profile (Peak 1: 0.6 kPa, Peak 2: 2.0 kPa, Peak 3: 5.8 kPa). The authors spatially divided this heterogeneity into cancer core region (Peak 1), cancer-infiltrated stroma (Peak 2), and collagen I-/laminin-rich stroma (Peak 3). They additionally detected in human cancer biopsies the soft phenotype to correlate with the expression of the biomarkers vimentin and desmin which are indicative for the Epithelial-to-Mesenchymal Transition (EMT). In view of this complex biomechanical landscape to approximate single cancer cell mechanics *in vitro,* it is therefore obligatory to provide a tissue-relevant context including the dimension and architecture of the microenvironment arising during cancer progression. The improved quality of data may help to use cell mechanics as biomarker for indicating cell states and to identify pathological phenotypes.

Bioengineering techniques such as tissue decellularization, (photo-)lithography, 3-D-bioprinting, electrospinning or hydrogel-based scaffolding aim to precisely mimic tissue's three dimensional architecture and (sub-)micron scale.[18] Creating an environment physically resembling *in vivo* conditions enables to study cues other than mere biochemical ones. This research field has recently revealed that micro- and nanoscale topographies, as are found in the TME, decisively influence cellular migration behavior and gene expression.[19-21] For example, cells migrating on structured surfaces prefer a migration angle in the direction parallel to the topography.[22] Such contact guidance cues of the extracellular matrix (ECM) strongly alter the morphological phenotype of (cancer) cells, and its coherency within the ECM governs the degree of morphological transition on the single-cell level [23]. *In vitro* studies showed that matrix alignment, as described for TACS, rather than matrix stiffness amend migration efficiency for BC cells by fostering directional persistence.[24, 25] Collagen I fiber alignment enhances breast cancer cell-ECM interaction thereby potentiating malignancy of the cellular phenotype.[26] Indeed, integrin-rich focal adhesions specifically align on topographical patterns allowing for anisotropic traction forces and cell polarization.[27] Interestingly, topography-based contact guidance depended strongly on cell-cell interactions. Epithelial clusters were shown to have a substantially lower response to topographic alignment than single cells.[27] These findings emphasize the EMT program during which cancer cells lose their epithelial properties (*e.g.* E-cadherin/cytokeratin expression, apico-basolateral polarity) and acquire mesenchymal characteristics (*e.g.* N-cadherin/vimentin expression, front-back polarity). EMT may play a pivotal role in topography-based contact guidance cells experience mirrored in the degree of interactions with topographical cues within the TME. Former *in vitro* and *in vivo* data has already linked EMT to increased breast cancer malignancy [28-30] but studies to link contact guidance cues of ECM microarchitecture to cellular phenotypes are not reported in the literature. EMT-like changes may

synergize with TACS as the latter provide the infrastructure for metastatic tumor outgrowth whereas EMT delivers the fuel necessary on a cellular level. Therefore, bioengineering applications with the goal to further understand the reciprocal relationship between tissue-relevant topographies such as TACS and EMT-like changes are of auspicious interest for future breast cancer diagnostic and to identify new potential targets for breast cancer therapies.

The ability of producing non-woven fiber mats bio-mimicking the physical dimension (10 nm to 30 µm) of native ECM has made electrospinning a versatile tool in the field of biomedicine and tissue engineering [31]. Electrospun scaffolds have been implemented as drug or gene delivery system [32, 33], as biosensor for cancer diagnostics [34, 35], as harbor for circulating tumor cells [36] or as 3D *in vitro* model.[37, 38] Thus, electrospinning has drawn conspicuous attention and its multifarious applicability is strongly appreciated.[39] In this study we describe the establishment of an electrospun 3D *in vitro* model of BC in the context of various cell culture-relevant applications. Electrospinning poly (ε-caprolactone) (PCL) fibers on cell culture coverslips enabled us to reproducibly create a topographical environment resembling TACS as is found in the diseased tissue of the mammary gland. By culturing breast cancer cell lines of distinct intrinsic subtypes and analyzing their behavior under exposure to the defined matrix-microarchitecture of the electrospun TACS-like *in vitro* model, we sought to address the following questions: (i) How do TACS-mediated contact guidance and EMT-phenotype interrelate, (ii) how does EMT/MET (Mesenchymal-to-Epithelial Transition) induction manipulate contact guidance, and finally (iii) how do phenotypic changes influence cell mechanics? By providing interdisciplinary insights we aimed to decipher the input fibrillar topographies exert on tumors within the mammary gland and their interrelation with cancer cell malignancy.

2. ***Material & Methods***

2.1 Materials and cell culture:

Polycaprolacton (M_N 80.000), 3-(Trimethoxysilyl)propyl methacrylate 98%, Formaldehyde solution (≥ 36%), Dichloromethane (DCM) anhydrous, *N,N*-Dimethylformamide (DMF) anhydrous, 4′,6–diamidino–2-phenylindole dihydrochloride (DAPI), FluorSave reagent, DNase I (recombinant, RNase-free), cOmplete™, EDTA-free Protease Inhibitor Cocktail, Phosphatase Inhibitor Cocktail 2, RIPA buffer, Tris buffered saline powder, Ponceau S Stain, Tween 20, Amersham™ Protran® Western-Blotting-Membrane (nitrocellulose) Eagle's Minimum Essential Medium (EMEM), RPMI-1640 Medium, Dulbecco's modified eagle's medium (DMEM), fetal bovine serum (FBS), Penicillin-Streptomycin (Pen/Strep) solution, Dulbecco's Phosphate Buffered Saline (PBS), trypsin-EDTA solution 0.05% and 0.25%, 200 mM of L-glutamine solution, doxycycline hydrochloride (DOX) and dimethyl sulfoxide (DMSO) were purchased from Sigma-Aldrich (Taufkirchen, Germany). GAPDH Monoclonal Antibody (ZG003), LIVE/DEAD™ Cell Vitality Assay Kit (C12 Resazurin/SYTOX™),

Green Pierce™ BCA Protein Assay Kit, Novex™ 10% Tris-Glycine Mini Gels (WedgeWell™ format, 15-well), Novex™ Value™ 4-20% Tris-Glycine Mini Gels (1.0 mm, 10-well), Page Ruler™ Plus Prestained Protein Ladder 10 to 250 kDa, Tris Glycin transfer buffer, SuperSignal™ West Pico PLUS Chemiluminescent Substrate, Hoechst 33342, Rhodamine Phalloidin, High capacity cDNA synthesis kit, Power SYBR™ Green PCR Master Mix, PureLink™ RNA Mini Kit and Leibovitz's L-15 Medium and MEM Non-Essential Amino Acids Solution (100X) were purchased from Thermo Fisher Scientific (Darmstadt, Germany). Collagen I (sc-136154), Collagen IV (sc-29010), m-IgGκ BP-HRP (sc-516102), COL1A2 antibody (H-9), Anti-Lamin A/C Antibody (636), Anti-Lamin B1 Antibody (B-10), E-cadherin Antibody (G-10) and Vimentin Antibody (V9) were ordered from Santa Cruz Biotechnology (Dallas, TX, USA). Hs_CDH1_Primer Assay (QT00080143), Hs_SNAI1_Primer Assay (QT00010010), Hs_VIM_Primer Assay (QT00095795), Hs_GAPDH_1_SG QuantiTect Primer Assay (QT00079247) and Hs_XBP1_1_SG QuantiTect Primer Assay (QT00068383) were purchased from Qiagen (Hilden, Germany). Rotiphorese 10x SDS Page, Rotilabo®-Blotting Papers and Methanol (blotting grade) were purchased from Carl Roth (Karlsruhe, Germany). rh-TGF-β 1 (Transforming Growth Factor beta 1) and rh-EGF (Epidermal Growth Factor) were acquired from ImmunoTools (Friesoythe, Germany). Laemmli loading buffer (4x) and round glass coverslips (Ø 13mm) were purchased from VWR (Ismaning, Germany). HyClone trypan blue solution 0.4% in phosphate-buffered saline was obtained from FisherScientific (Darmstadt, Germany). Injection Luer Lock needle, blunt end (Ø 0.7 x 30 mm) was purchased from Unimed S.A (Lausanne, Switzerland). Human CD44s Pan Specific Antibody was purchased from R&D Systems (Minneapolis, MN, USA). Braun Omnifix® Syringes (20 mL, Luer) were purchased from Neolab (Heidelberg, Germany).

MCF7 (and MCF7 miR200c_KO) cells, a Luminal A breast cancer cell line, were cultured in EMEM supplemented with 10% FBS, 1x Pen/Strep, 1x MEM Non-Essential Amino Acids Solution and 2 mM L-glutamine. The HER2-positive breast cancer cell line HCC1954 was grown in RPMI-1640 Medium supplemented with 10% FBS and 1x Pen/Strep. MDA-MB-231 (and MDA-MB-231 i-miR200c) cells, a triple negative breast cancer (TNBC) cell line, were cultured in high glucose (4500 mg/L) DMEM, and 10% FBS, 1x Pen/Strep and 2 mM glutamine were added to the medium. For miRNA induction in MDA-MB-231 i-miR200c cells, the medium was equipped with 5 µg/mL doxycycline hydrochloride which was replenished every 48h. The latter three cell lines were cultured in a humidified atmosphere with 5% CO_2 at 37 °C. The second TNBC cell line MDA-MB-468 was grown in L-15 Medium supplemented with 20% FBS and 1x Pen/Strep. These cells were grown in a humidified incubator with 0% CO_2 at 37 °C.

2.2 Electrospinning of TACS-like structures: set-up and processing of cell culture inserts

The used electrospinning system was self-constructed by the laboratory for tissue engineering and cardiovascular medical technology of the department of cardiac surgery at the Ludwig-Maximilian-University in Munich. Briefly, the test chamber included air conditioning for organic solvents to evaporate and contained molecular sieves to reduce humidity within the chamber. Either a static aluminum plate or a dynamic rotating cylinder was used as collectors to produce unaligned or aligned fibers, respectively. The cylinder (Ø 150 mm) itself was assembled out of 3D-printed constructs using the Keyence Agilista 3200W printer. The use of non-conductive AR – M2 (Keyence Corp, Osaka JP) acrylic polymer necessitated an additional wrapping step with aluminum foil to enable electrostatic attraction. A NEMA 17 motor (Nanotec Electronic GmbH, Feldkirchen, Germany) connected to a computer via an associated control card was used to drive the cylinder. The speed and direction of rotation were set using the "Plug & Drive Studio" (Nanotec) software. A high-voltage power supply from iseg GmbH (Radeberg, Germany) with a voltage range of 0 - 30kV (positive and negative) was used to generate the electric field. The voltage supply was coupled to the needle and the collector by means of a high-voltage cable. The flow rate of the polymeric solution was controlled by a laboratory syringe pump (Fusion 100, Chemyx Inc., Stafford, TX, USA).

PCL (20 g) was dissolved in 100 ml of DCM/DMF (40/60) 24 h prior to the electrospinning process. The solution was stirred over night at 400 rpm covered with aluminum foil to avoid evaporation of the organic solvents and degradation of PCL. To increase adhesion of fibers to glass coverslips, coverslips were incubated for 5 min in 4% (*v/v*) of 3-(Trimethoxysilyl)propyl methacrylate in absolute ethanol. The solution was removed and rinsed 3 times with pure ethanol. Coverslips were subsequently baked at 100 °C for 40 min. To produce cell culture inserts, optimized (methacrylated) coverslips were mounted either on the plate collector or rotating cylinder using double-sided adhesive tape as can be seen in **Figure S1a**. The rotation speed was set to 1800 rpm. A 20 mL syringe was loaded with the polymer (PCL) solution and connected to the syringe pump. The flow rate was set to 1.0 mL/h. The high-voltage supply (+ 7-10 kV) was connected to a needle (Ø 0.7 x 30 mm) placed 21 – 23 cm away from the collector. Opposite, constant charge was applied to the collector (- 1 kV). In case of the rotating cylinder, a sliding contact was used. To assure constant fiber deposition during the 10 min of the electrospinning process, Taylor cone formation was monitored at the tip of the nozzle. As shown in **Figure 1,** fiber-coated coverslips (FCCs) were consequently either subjected to SEM analysis or further processed to fulfill cell culture requirements. To remove excess amounts of organic solvents, FCCs were placed in a chemical hood for 48 h. Afterwards FCCs were sterilized using UV-light for 1 h and thereafter placed into a 24-well plate under sterile conditions where they were exposed to UV-light for another hour. Subsequently, for cell culture work, FCCs were coated with collagen (I/IV) as described elsewhere.[40] For AFM and live-cell imaging purposes, collagen-coated FCCs were fixed onto the surfaces of culture dishes. Therefore, 3 µL of silicon-based glue were placed in the center of

the bottom side of the FCCs and let dry under sterile conditions for 1 h prior to cell seeding. For the seeding process, 25.000 – 50.000 cells were suspended in 200 µL of the respective medium and then slowly pipetted on the scaffold starting at the center and spirally approaching the margin of the FCC with a blob emerging and covering the entire FCC. After 15 min of incubation, allowing cells to sediment onto the scaffold, each well was filled up with pre-warmed medium to 1 mL and subjected to various analyses.

2.3 Scanning electron microscopy (SEM)

The topography of TACS5- and TACS6-like scaffolds (FCCs) were examined by scanning electron microscopy (SEM) using a JSM-6510LVLGS, 25 kV (JEOL, Peabody, MA, USA). For imaging, scaffolds were sprinkled on a stub covered with double-sided carbon tape and sputter-coated with gold (Ernest Fullan) under vacuum for 60 s. Topographic features including fiber orientation, diameter and density were analyzed from the SEM images by processing with the Fiji imaging software (Version 2.30/1.53q).[41] Fiber orientation and distribution of orientation were analyzed from representative samples of each collector type using the OrientationJ plug-in (written by Daniel Sage). Fibers represented with the same color indicate same directionality. Fiber diameters and inter-fiber distances were manually calculated from 10.000x images taken from samples of 2 independent electrospinning runs per collector type.

2.4 GC analysis – Residual solvents

Residual DCM and DMF content was analyzed by static headspace-gas chromatography-mass spectrometry (HS-GC-MS). An Agilent Technologies 7890B gas chromatograph (Waldbronn, Germany), equipped with an Agilent J&W DB-624 UI ultra-inert capillary column (6% cyanopropyl phenyl and 94% polydimethylsiloxane) 30 m × 0.25 mm × 1.4 µm and an Agilent Technologies 7010B triple quadrupole detector with high efficiency source (HES) was used for analysis. Helium (99.999%) was used as mobile phase. DCM (HPLC grade), 1,2-dichloroethane (DCE, purity 97%), DMF (purity HPLC grade), DMF-d7 (purity 99.5%), and DMSO (purity HPLC grade) were purchased from Sigma-Aldrich (Schnelldorf, Germany). As samples, 15 mg fiber mesh (obtained from three independent electrospinning runs, respectively) were filled into a 20 mL headspace vial, 10 µL of DMF-d7 and DCE (each 10 µg/mL in DMSO) as internal standards were added, and the vial was closed tightly. After sealing, the sample was analyzed by HS-GC-MS (see Table 1). The MS was operated in single ion monitoring mode (SIM; EI 70 eV). The retention times and characteristic ions of DCM (5.6 min, m/z 84.1), DCE (internal standard; 8.2 min, m/z 62.1), DMF (9.8 min, m/z 73.2), and DMF-d7 (internal standard; 9.9 min, m/z 80.2) were used for identification and quantification.

Table 1: Conditions of static HS-GC-MS

Headspace sampler parameters		**GC-MS parameters**	
Agitator cycle	5 sec on, 2 sec off	Carrier flow rate	1.2 mL min^{-1}
Agitator speed	500 rpm	Split ratio	10 : 1
Agitator temperature	200 °C	Oven profile	40 °C for 6 min
			50 to 240 °C at 50 °C min^{-1}
			(hold time 2.5 min)
Sample incubation time	15 min	Transfer line temperature	250 °C
Syringe size	2.5 mL	Inlet temperature	200 °C
Syringe temperature	150 °C	Ion source temperature	230 °C
Injection volume	1.00 mL	Quadrupole temperature	150 °C

2.5 Cell viability

The cell viability of cells growing on TACS5- and TACS6-like (data not shown) structures was assessed by applying the LIVE/DEAD™ Cell Vitality Assay Kit (Invitrogen™) and subsequent fluorescence microscopy. For each sample, 35.000 MDA-MB-231 cells were seeded on collagen I – coated tissue plates, uncoated FCCs and coated FCCs. All samples were cultivated for 72 h and then stained according the manufacturer's protocol. Untreated cells on conventional culture dishes served as positive (live/red) control, whereas negative (dead/green) control cells were incubated for 30 min with ethanol 70% (*v/v*) prior to the analysis. Fluorescence images were recorded with the Keyence BZ81000 Fluorescence microscope (Keyence, Osaka, Japan). Images of transmitted light, green and red channel were taken simultaneously with a 20x objective and further analyzed with Fiji software. Percentages of living/dead cells was calculated in duplicates (with each sample > 100 cells), counting red/green fluorescence signals (cells) of the respective channels.

2.6 Confocal scanning microscopy – Morphological changes

Confocal laser scanning microscopy was used to assess morphological changes across different cell lines growing on glass coverslips, TACS5- and TACS6-like structures. As performed with the FCCs, coverslips were coated with collagen I and IV. Thereinafter, 35.000 – 50.000 cells of the respective cell lines were seeded in 24-well plates following the protocol described above. In case of growth

factor (GF) treatment, cells were allowed to attach within the first 4 h. Medium was then removed and replenished with GF-containing medium. Samples were either supplied with 10 ng/ml of TGF-β1 (MCF7 and HCC1954) or 25 ng/ml of EGF (MDA-MB-468). DMEM medium used for miR200c induction in modified MDA-MB-231 cells contained 5 µg/ml of doxycycline hydrochloride (DOX). After 72 h of incubation, wells were washed 3 times with PBS before cells were fixed for 15 min with a 4% formaldehyde solution. To stain the actin cytoskeleton, cells were incubated with 8.25 µM rhodamine-phalloidin solution for 40 min. Hereinafter, cells were washed another 3 times with PBS. Nuclei were stained with a 0.5 µg/ml DAPI solution for 10 min. Finally, after an additional washing step, samples were mounted on glass slides using FluorSave and stored at 4°C until the next day. Fluorescence images were acquired using a confocal laser scanning microscope (Leica SP8 inverted, Software: LAS X, Leica microsystems GmbH, Wetzlar, Germany) equipped with a HC PL APO CS2 63x/1.40 oil immersion objective. Diode lasers (405 nm) and a semiconductor laser OPSL (552 nm) were chosen for excitation. Emission was detected in blue (PMT1: 410–520 nm) and yellow (PMT2: 560nm – 760nm), respectively. Images were further processed with Fiji image analysis software. Nuclear circularity was calculated as $C_N = \frac{4\pi A}{P^2}$, (n > 30; A: area, P: perimeter), and the cellular aspect ratio as $A_R = \frac{d_{min}}{d_{max}}$, (n > 15). The axes ($d_{min}$ and d_{max}) were drawn manually. Results are given as Whiskers Plots with error bars indicating minimal and maximal values. One-way ANOVA with Bonferroni multiple comparison test was performed in GraphPad Prism software version 5.00 (Graph Pad Software, La Jolla, CA, USA) to calculate P-values at a 95% confidence interval.

2.7 Live cell imaging – Motility and contact guidance

Live cell imaging was performed using the Eclipse Ti inverted microscope (Nikon, Düsseldorf, Germany) with a 4/10 phase contrast objective and a charge-coupled device camera (DS-Qi1Mc; Nikon). After 48 to 72 h of incubation, nuclei of cancer cells were stained with Hoechst 33342 dye (Invitrogen™) according to the manufacturer's protocol. Briefly, cells were washed once with PBS and subsequently incubated for 20 min in the cell culture incubator in 300 µL of 0.5 µg/mL dye in PBS. Afterwards cells were washed another 2 times, and 1 ml of the respective medium was replenished. The 24-well plates were inserted into a 37°C heating and incubation system that was flushed with actively mixed 5% CO2 (0% in case of MDA-MB-468 cells) at a rate of 10 L/h, and the humidity was kept at 80% to prevent dehydration of cells. The cells were imaged in bright-field, and the nuclei were detected at 405 nm using the integrated fluorescence LED. Time-lapse videos were taken with a time interval of 5 min between images over 24 h.

2.8 Tracking of single-cell trajectories

For single-cell trajectories, the position of nuclei was analyzed using the TrackMate plugin within the Fiji software [42]. To extract nuclear circularity trajectory, the image series of the 405 nm channel was manually processed (*Enhance contrast (5.0%)* >> 2x *Smooth* >> *Convert to mask*) and further analyzed with "Mask detector" function of the TrackMate plugin (see Table 2).

2.9 EMT-marker expression – RT-qPCR

In 24-well plates, 40.000 cells of the respective cell line were seeded in triplicates. Importantly, to allow for the best possible comparison, all cells were seeded on collagen I coated coverslips or coated FCCs. GF and DOX supply was performed as described above. After 72 h incubation, cells were washed 3-times with PBS. Subsequently, 300 µL of ethanol-containing lysis buffer was added for 15 min. In order to maximize the amount of RNA for analysis, triplicates were pooled together prior to the RNA isolation step. Total RNA was isolated using the PureLink RNA mini kit according to the manufacturer's protocol with additional DNAse I digestion. Subsequently, 500 ng of RNA was used to synthesize cDNA using the High capacity cDNA synthesis kit. In the following, E-cadherin (CDH1)-, Snail (SNAI1)-, Vimentin (VIM)-, and XBP1-specific primers were used to amplify and quantify RNA using Power SYBR™ Green PCR Master Mix and the qTOWER real-time PCR thermal cycler (Analytik Jena, Jena, Germany). C_t values were normalized to GAPDH RNA expression, and delta C_t values were calculated for the comparison. One-way ANOVA with Bonferroni multiple comparison test was performed in GraphPad Prism software (Graph Pad Software, La Jolla, CA, USA) to calculate P-values at a 95% confidence interval (n = 4).

2.10 EMT-marker protein levels – Western blotting

In 24-well plates, 40.000 cells of the respective cell line were seeded in triplicates. Importantly, to have the best comparison possible, cells were seeded on collagen I coated coverslips or coated FCCs (here: TACS5). DOX was supplied as described above. After 72 h incubation, cells were washed 3 times with PBS prior to cell lyses. Subsequently, 60 µL of proteinase- and phosphatase-inhibitor containing RIPA buffer was added to one well (of a triplicate) and cells were kept on ice for 20 min. Thereinafter, wells were thoroughly scraped and the extract was transferred to the next well of a triplicate. This step was repeated again for the last well of a triplicate (including 20 min of incubation). This step was necessary to maximize the protein yield. Finally, pooled triplicates were transferred into 1.5 mL microcentrifuge tubes. After a 10 min centrifugation step at 4 °C, total protein concentration was assessed according to the manufacturer's protocol (Pierce™ BCA Protein Assay Kit). Gels were loaded with 30 µg protein per sample, and electrophoresis was run for 90 min at 120 mV. Subsequent to 1 h of protein transfer at 100 mV, blots were washed, blocked and incubated overnight using

CD44s-, CDH1-, VIM- and GAPDH-specific antibodies. HRP-bound secondary antibody was then added for 1 h under exclusion of light before blots were developed.

2.11 Atomic force microscopy (AFM)

JPK Nano Wizard 4 was used to carry out all the studies. All the stiffness measurements were performed in cell culture media using the AFM's contact mode. In contact mode, force spectroscopy mode was adapted. Tipless MLCT-D cantilevers (silicon nitride, resonance frequency 15 kHz, spring constant 0.03 N/m) glued to a glass bead (diameter determined by Fiji) were used to indent the cells. The spherical tip was used instead of sharp pyramid tips because they have a well-defined geometry and get a better assessment of the cellular elasticity by averaging over a large surface area [43-45]. These were calibrated with the contact-free method in liquid. The following parameters were used: set point 1 nN, z-length 10 µm and velocity 5 µm/s. The Petri dish was mounted onto the AFM stage and the cells were kept in cell culture media. A digital petri dish heater attached to the AFM stage was used to maintain the physiological temperature of 37°C during the indentation. For every sample, 3-5 cells were indented overall, and force curves were collected. For measuring nuclear stiffness, the area of the nucleus was selected, and the force curves were acquired taking certain points on the nucleus. One-way ANOVA with Bonferroni multiple comparison test was performed to calculate P-values at a 95% confidence interval (n = 3; *** $P < 0.0001$).

All images were acquired using the enhanced imaging QI mode of the AFM. Pyramidal tip MLCT-D silicon nitride cantilevers were used (spring constant 0.03 N/m and resonance frequency 15 kHz), and the following parameters were taken, set point: 1nN, z-length 2500 nm, pixel time 40 ms. The acquiring area of the grid was set according to the cell size, and the pixel ratio was 256 × 256. The data were analyzed using JPK data processing software. The stiffness/elastic modulus of the cells (Young's modulus) was calculated with the Hertzian contact model according to [46]:

$$E = \frac{3}{4} \cdot \frac{F \cdot (1 - \upsilon^2)}{\sqrt{\delta^3} \cdot \sqrt{R}}$$

The radius of the MLCT-D cantilever with the bead was calculated with Fiji ImageJ, and the sphere model was used to calculate the stiffness based on the force curves generated. In the software, the diameter, spring constant and sensitivity of the cantilever were indicated, and baseline and contact point were determined. For image analysis, height images were considered. The scale bar was set, and for MLCT-D pyramid tips the half-angle to the front was selected and set to 17.5 degrees. All images were then processed, and the height gradient determined the height of the cells compared to the substrate.

2.12 Statistical analysis

All statistical tests were performed with GraphPad Prism software Version 5.00. ($^{(*)}P < 0.05$; $^{(**)}P < 0.01$; $^{(***)}P < 0.001$)

3. *Results*

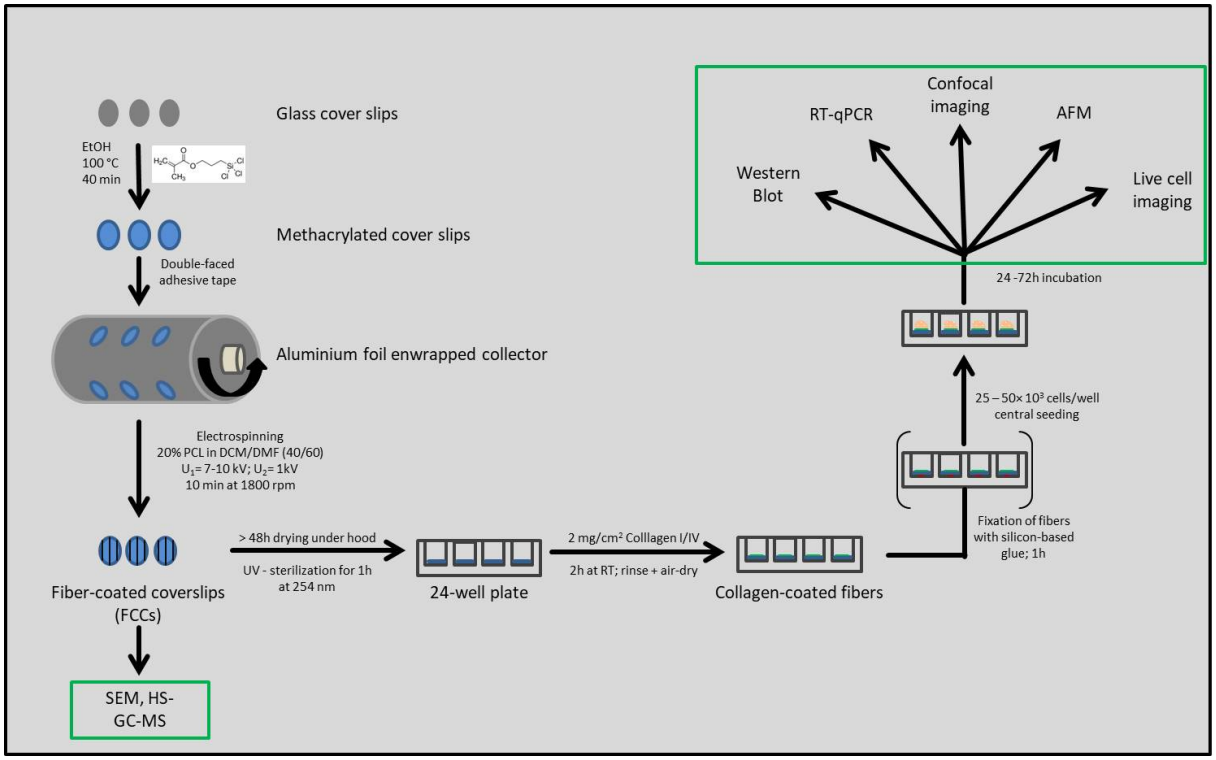

Figure 1. *Overview of preparation steps necessary to produce electrospun cell culture inserts (TACS-like scaffolds). Green windows highlight analytical methods used.*

3.1 Design, characterization and toxicological profile of a nanofiber breast cancer in-vitro model

3.1.1 Optimized electrospinning set-up enables to mimic TACS5 and TACS6 architecture

During the electrospinning process, the polymer jet emitting from the tip of the nozzle suffers from certain physico-chemical instabilities [47, 48] leading to a random fiber deposition on the opposing collector (*e.g.* plate collector). These whipping instabilities can be compensated by substituting the static collector with a rotating cylinder, which seizes the bending fibers and coils them around itself. The resulting fibers are ideally straightened and orientated in parallel to each other.

In order to obtain cell culture inserts, glass coverslips were mounted on the respective collectors which were fiber-coated (FCC) during the spinning process (Supplementary data, **Figure S1a**). The optimized electrospinning workflow is displayed in **Figure 1** including preparation steps necessary for subsequent *in* vitro assays. To test whether the choice of collector type can account for TACS5- and TACS6-like architectures (aligned vs. unaligned), respectively, scanning electron microscopy (SEM) was conducted after the spinning process. SEM imaging of FCCs revealed strong fiber alignment and straightening for samples spun with the rotating cylinder compared to random deposited fibers obtained from the plate collector (**Figure 2)**. Image analysis demonstrated highly efficient alignment (further indicated by equally colored fibers) of TACS5-like structures (**Figure 2a)**. The peak-like angle distribution was within a narrow range of 30°, and distribution intensity was close to 80.000 as compared to a chaotic fiber deposition with no preferred orientation angle (baseline: 7000; maximum: 15.000) for TACS6-like structures (**Figure 2b**). Analysis of SEM samples allowed for assessing fibers diameter and (maximal) inter-fiber distances (**Figure 2c/d)**. The mean fiber diameters of both set-ups resulted in similar values at a submicron scale. The mean diameter and inter-fiber distance of unaligned fibers were only slightly higher with 0.760 µm and 2.405 µm versus 0.664 µm and 2.022 µm for aligned fibers. It was thus confirmed that relative fiber orientation can be tuned without significantly affecting single fiber characteristics.

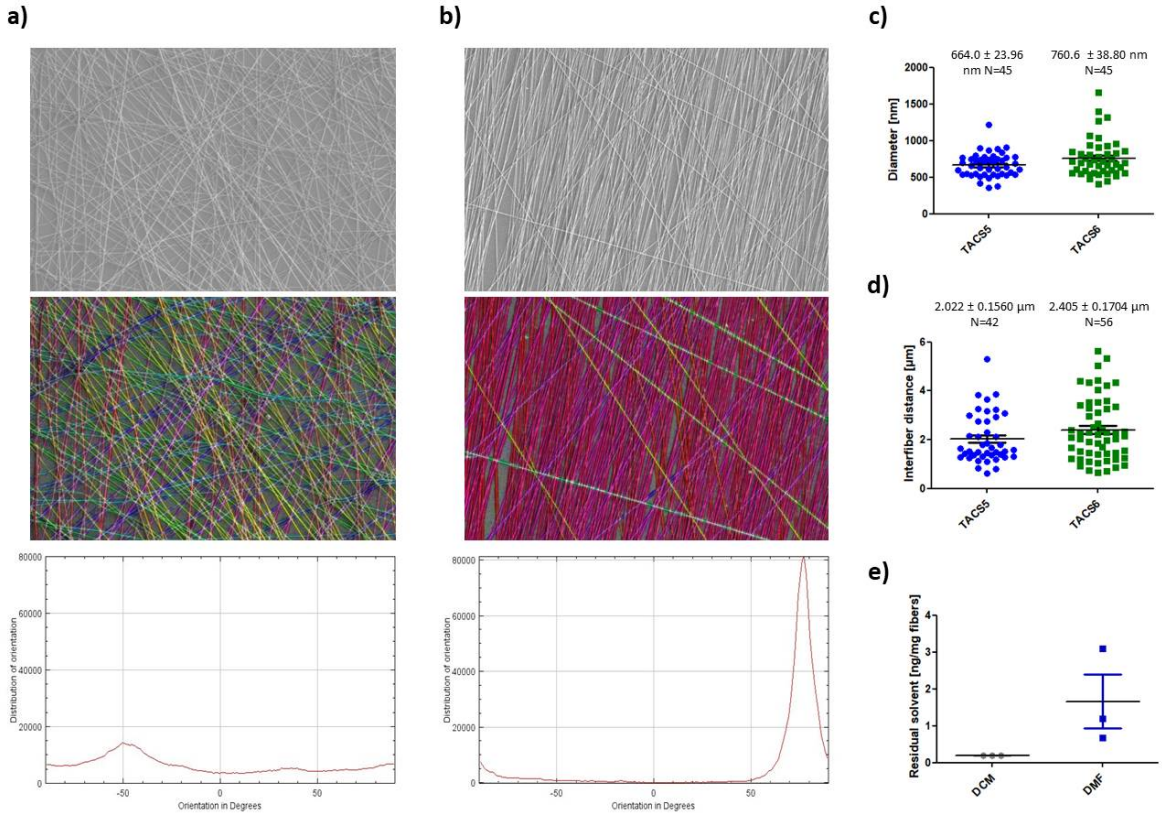

Figure 2. *SEM image analysis* ***(a, b)****: Upper panel shows representative SEM image of TACS6-* ***(a)*** *and TACS5-* ***(b)*** *like structures (10.000x magnification); mid panel highlights single fiber orientations with same colors representing same fiber orientation; lower panel depicts distribution intensity of fiber orientation (-90° to 90°). Fiber diameters* ***(c)*** *and interfiber distances* ***(d)*** *of TACS5- and TACS6-like structures analyzed with Fiji software. Errors indicate standard error of mean (SEM). Residual amount of organic solvents (DCM and DMF) in ng/mg fiber were analyzed with HS-GC-MS* ***(e)****.*

3.1.2 Standard collagen coating sufficiently deposits collagen on fibers improving biocompatibility and cellular spreading on TACS-mimics

Next, possible toxic effects of residual solvents or incompatibilities that would hinder cell growth on the fibrous matrix were evaluated. GC analysis of electrospun fibers revealed complete evaporation of DCM (below detection limit of 10 ng) and negligible residues of DMF (1.65 ng/mg) (**Figure 2e**).[49] However, PCL is an extremely hydrophobic polymer unsuitable for cellular attachment. Therefore, collagen coatings were applied to improve tissue-mimicry and to enhance cellular attachment on fibers. First, it was tested whether the standard collagen coating protocol (Santa Cruz Biotechnology, Inc.) deposits sufficient collagen on the fibrous scaffold. A fluorescently labeled, collagen-specific antibody was used to visualize collagen deposition *via* confocal microscopy. **Figure S1b** demonstrated that fibers (TLP) and green fluorescence (AF488-AB) co-localized for coated samples, implying effective collagen coating.

Further, biological compatibility of the *in vitro* model was investigated using a fluorescence-based cell viability assay. C_{12} -Resazurin can enter living cells, but requires metabolic activity to be processed to a fluorescent molecule (red live stain). On the other hand, healthy cells are impermeable for the fluorescent SYTOX Green dye (green dead stain) which only enters cells when their membrane integrity is lost leading to an intracellular fluorescence signal at 488 nm excitation. As shown in **Figure 3**, the positive control (untreated MDA-MB-231 cells) showed red fluorescence signals (99.5% of the cells) whereas the negative control (ethanol-treated MDA-MB-231) resulted in green fluorescence signals (100% of cells). Cell viability of cells growing on coated fibers remained mostly unaffected (4.6% dead cells), and collagen coating enabled widespread cellular infiltration within the scaffold. Without the coating, toxicity increased 3-fold to 15.1% of cells displaying a green fluorescence signal, and cells seemed to remain spatially clustered implying declined matrix infiltration (**Figure 3**). Taken together, not the residues of organic solvents but the hydrophobic nature of the PCL fiber surface posed a hurdle to cell viability. Regarding the better compatibility and improved bio-similarity of coated fibers, collagen I and IV coatings were applied throughout the subsequent *in vitro* evaluation.

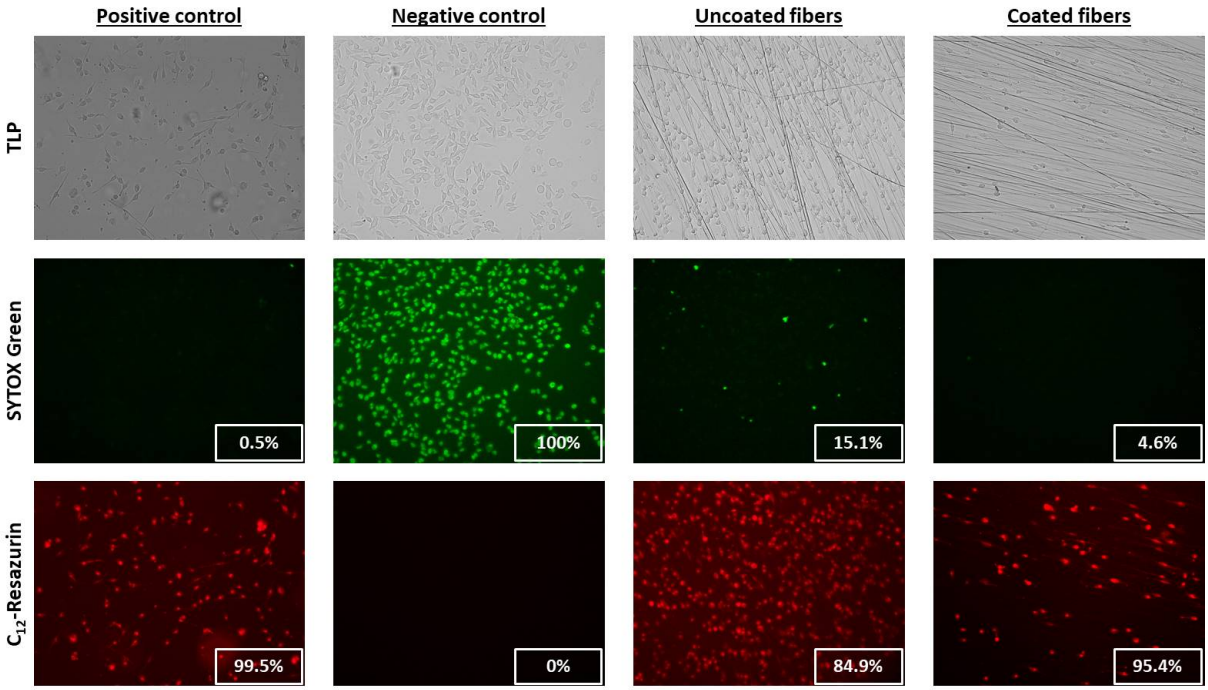

Figure 3. *Comparison of cell viability on conventional culture dishes (positive control) and TACS-mimicking scaffold with and without collagen coating. Ethanol treated cell represent negative control. Upper panel: Transmitted light photography (TLP); Mid panel: Fluorescence at 488 nm (dead stain); Lower panel: Fluorescence at 595 nm (live stain). White numbers indicate number of living/dead cells [%] of total amount of cells.*

3.2 *In vitro* evaluation of the bio-mimetic model

3.2.1 EMT-status governs cellular contact guidance through TACS5-mimicking topographies which induce EMT-like changes in breast cancer cells including the upregulation of XBP1

In a previous *in vitro* study on breast cancer, we established an EMT phenotyping system based on EMT-marker expression, morphological changes and cellular motility. Accordingly, MCF7 and HCC1954 cell lines were designated EMT-negative, MDA-MB-468 cells were considered as E/M-hybrid and MDA-MB-231 cells were identified EMT-positive. Further, significant alterations of cellular and nuclear morphologies, i.e. aspect ratio A_R and nuclear circularity C_N, predicted EMT-like changes on the protein level during growth factor-dependent EMT.[40]

Here, we monitored the three aforementioned features for breast cancer cells grown on the fibrous scaffolds. Morphological characteristics of the three studied cell lines were shown to remain unaffected when cells were growing on unaligned fibers (TACS6) as revealed by confocal imaging of fixed samples with subsequent image analysis (**Figure 4a-c)**. Likewise, TACS5-mimicking scaffold did not induce prominent changes in A_R and C_N values neither in MCF7 nor in HCC1954 cells (**Figure 4a/b)**. However, cell growth on aligned fibers resulted in significant ($P < 0.0001$) decrease of A_R and C_N for MDA-MB-468 cells, indicating strong cellular alignment on the scaffold. Cancer cells strongly dispersed within the scaffold in contrast to conventional 2D-cell culture and TACS6-like scaffolds where cells mostly bundled into sheet-like aggregates. On TACS5-like scaffolds, however, cells lost their cobblestone-like morphology ($A_R = 0.7540 \pm 0.1355$) and stretched towards a spindle-like shape ($A_R = 0.4063 \pm 0.1727$) (**Figure 4c**). Therefore, the MDA-MB-231 cell line was further included and confirmed that the degree of morphological transition of the nucleus caused by the aligned fiber arrangement is strongly dependent on EMT-status of the respective cell line (**Figure S2a**). Once more, only MDA-MB-468 and MDA-MB-231 exhibited significant alteration of C_N.

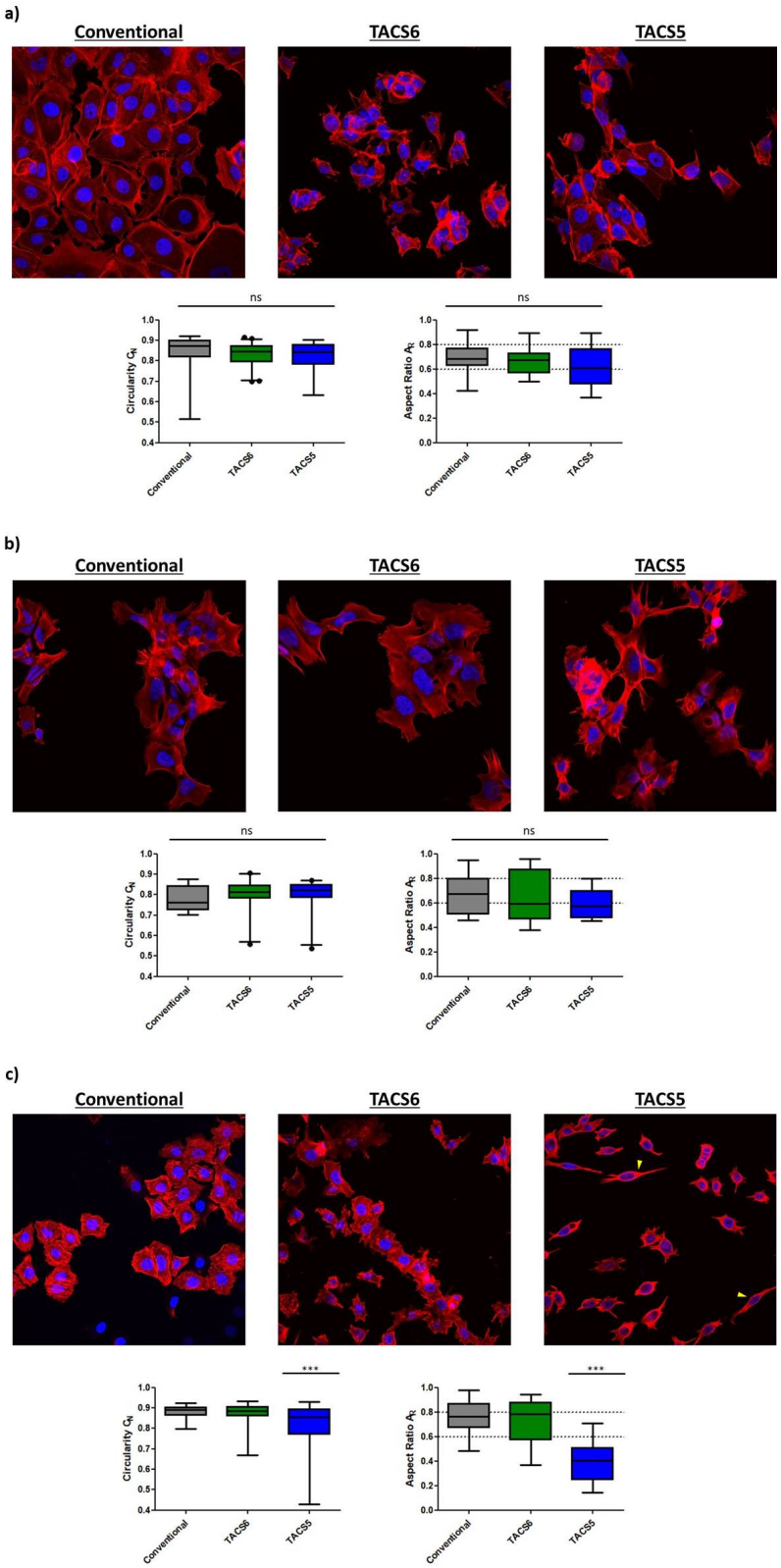

Figure 4. *Cell growth of MCF7 (**a**), HCC1954 (**b**) and MDA-MB-468 (**c**) cell line on conventional cell culture dishes and TACS-like scaffolds recorded with a confocal microscope (63x). The blue fluorescence (DAPI) represents the nucleus and the red fluorescence (Rhodamine-Phalloidin) depicts the actin cytoskeleton. Yellow arrows indicated mesenchymal-like morphologies. The graphs below demonstrate the morphological features nuclear circularity C_N (left) and aspect ratio A_R which were analyzed and calculated with the Fiji image software and plotted as Whiskers plot in GraphPad Prism 5 software.*

To address the question whether the observed morphological changes when grown on TACS5-like fibers were predictive for alteration in expression of EMT-related genes, qPCR analysis of cells grown on TACS5-like fibers was performed. Additionally, growth factor treatments known to cause EMT-like changes in the respective cell lines [40]were included. Thereby, the magnitude of transition between biochemical and topographical cues on the mRNA level was compared. Apart from E-cadherin (*CDH1*) and Vimentin (*VIM*) expression, mRNA levels of the transcription factors *SNAI1* and *XBP1* (X-box binding protein 1) genes were monitored. Snail was one of the first transcription factors to be correlated with EMT-like changes that include downregulation of CDH1 and upregulation of VIM.[50] XBP1 instead was only recently linked to EMT and metastasis and is thought to negatively influence cancer progression and outcome in all kinds of carcinomas.[51] **Figure 5a** summarizes relative mRNA expression (absolute values in **Figure S2b**) with green color indicating downregulation and orange color representing upregulation of gene expression. Hence, TACS5-like topographies decisively influenced gene expression depending on the respective cell line. It appeared, that accessibility to contact guidance cues increased with EMT-status (MCF7 < HCC1954 < MDA-MB-468). Overall, CDH1 expression was equally downregulated regardless of cell line and stimulatory cue. Besides moderate downregulation of CDH1, fiber topography induced significant upregulation of *XBP1* ($P < 0.001$) in MCF7. Similar to MCF7, *CDH1* expression decreased under the influence of TGF-β1 and fibers in HCC1954 cell line, respectively. Furthermore, TGF-β1 treatment significantly upregulated *VIM* (≈ 5.6 fold, $P < 0.001$) and *SNAI1* (≈ 3.5 fold, $P < 0.05$) gene expression. *VIM* expression was also affected by the fiber topographies but to a lower extent (≈ 1.7 fold(*)). *XBP1* mRNA levels remained unchanged for any condition tested. In contrast, *XBP1* (≈ 2.3 fold, $P < 0.01$), *SNAI1* (≈ 2.1 fold(*)) and *VIM* (≈ 1.9 fold(*)) expression were elevated in MDA-MB-468 cells grown on the fibrous matrix. Again, growth factor (EGF)-induced downregulation of *CDH1* was comparable to the fiber effect on MDA-MB-468 cells. Topography-induced downregulation of CDH1 protein levels was further confirmed by Western blotting analysis whereas VIM protein levels remained unaffected (**Figure 5c**). EGF stimulation also strongly increased mRNA levels of *VIM* (≈ 9.4 fold, $P < 0.001$) and *XBP1* (≈ 2.8 fold, $P < 0.01$) but surprisingly did not affect *SNAI1* expression.

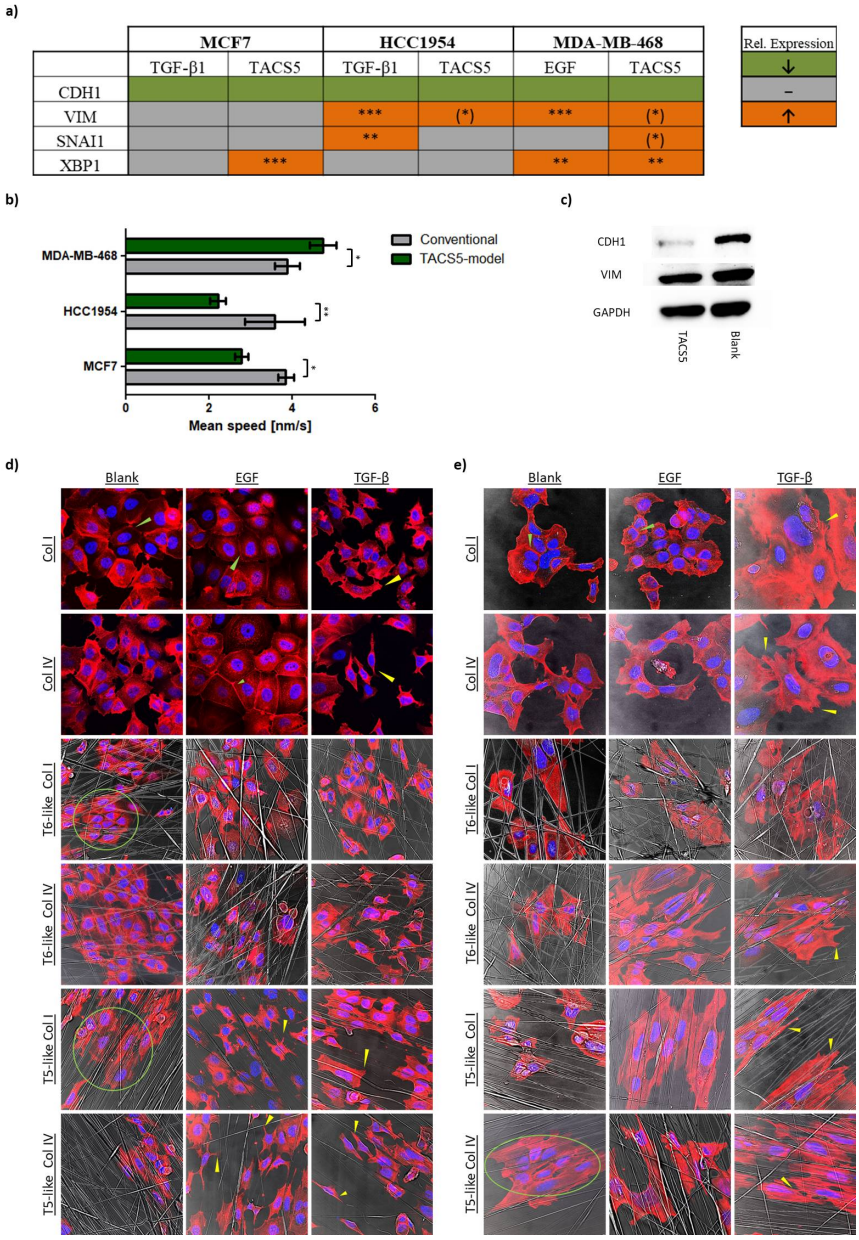

Figure 5. *Schematic representation of relative mRNA-expression of EMT-relevant marker (CDH1, VIM, SNAI1, XBP1) derived from MCF7, HCC1954 and MDA-MB-468 cells after 72 h incubation with growth factors or on TACS5-mimics. Colors define changes in relative mRNA expression as shown in the right box (green: down; grey: unchanged; orange: up). Stars indicate statistical significance. Stars in brackets (*) indicate statistical significance after exclusion of 1 out of 4 biological replicates (**a**). Mean migration speed of the latter three cell lines was recorded either on conventional coverslips or on TACS5-mimics. Means were calculated of three individual videos with n(cells) > 50. Errors indicate standard deviation (SD) (**b**). Western blot of MDA-MB-468 cell line stained with antibodies for CDH1 and VIM after 72h incubation on conventional coverslips or TACS5-mimics (**c**). Confocal images of MCF7 (**d**) and HCC1954 cells (**e**) under various conditions as indicated. Cells were stained for the nuclei (blue) and the cytoskeleton (red). To show the fibrous environment of the different TACS-mimics the TLP channel was included. Grey arrows/circles indicate strong cell-cell contacts and/or epithelial clustering of cancer cells. Yellow arrows emphasize mesenchymal-like morphologies/protrusions, cell-fiber interactions and/or strong cellular alignment with the scaffold.*

Another feature comprised in EMT-like changes is accelerated cellular motility. Using live cell imaging combined with fluorescently labelling of nuclei allowed to estimate cellular mean migration speed on both conventional coverslips and TACS5-mimicking scaffolds. As shown in **Figure 5b,** spontaneous random migration of cells was strongly influenced by TACS5-like topographies depending on the cell line. Mean speeds of MCF7 and HCC1954 cells were reduced by 28% and 38%, respectively. On the contrary, mean migration speed of MDA-MB-468 was significantly increased by 22% when cells were exposed to the fibrous matrix. Furthermore, differences in motility and contact guidance among all four cell lines growing on the TACS5 model were measured. Apart from mean migration speed track displacement, confinement ratio and mean directional change were also analyzed (for detailed information on these variables see **Table 2**). The latter three variables are representative of the directional persistence of contact guidance emanating from the *in vitro* model. The importance of directional persistence rises with an increase in both track displacement and confinement ratio and a decrease in mean directional change. MDA-MB-468 and MDA-MB-231 displaced significantly further (46% and 144%) than MCF7 (and HCC1954) during the 24 h observation period (**Figure S2c**). Surprisingly, as shown in **Figure S2e**, MDA-MB-468 cells were the fastest moving cells (4.76 nm/s) followed by MDA-MB-231 (3.32 nm/s), MCF7 (2.67 nm/s) and HCC1954 (2.12 nm/s). Finally, migration of MDA-MB-231 cells was the most efficient along the fibers as confinement ratio and mean directional change considerably differed from the other three cell lines (**Figure S2d/f**).

Track displacement	**Confinement Ratio**	**Mean directional change**
Measure of the distance [µm] between first (0 h) and last spot (24 h) of a track. It tells how far a cell has migrated away from its starting point but not the total distance it has been traveling.	= Linearity of forward progression $= \frac{track\ displacement\ [\mu m]}{total\ distance\ [\mu m]}$ The Confinement ratio indicates how efficient a cell displaced from its origin.	Measures the angle between two succeeding links which is then averaged over all links of a track. Low values indicate high consistency of directed migration/ migratory persistence and *vice versa*.

Table 2: *Description of variables calculated with the "Track analyzer" function of TrackMate plugin (Fiji software) [42] which were used to evaluate differences in contact guidance among cell lines and treatments.*

3.2.2 *TGF-β stimulation enhances contact guidance on TACS5-mimicking scaffolds and topographical cues potentiate EMT in HCC1954*

Cancer cells gain phenotypic plasticity during EMT-like changes which can improve cell-substrate interactions within the TME.[52] One major hurdle for cells to efficiently migrate through a porous matrix is the necessity to deform their nucleus. It is the greatest organelle of a cell which dictates cellular migration and invasion in cancer.[53, 54] Given that cellular migration of MCF7 and HCC1954 cells was impaired on TACS5-mimicking scaffolds and that cellular and nuclear morphology did not adapt to the fiber matrix (**Figure 4a/b**), we EMT was forced by addition of growth factors (EGF, TGF-β1) and two types of collagen surfaces (I/IV). Recording nuclear morphologies (circularity) allowed to monitor cellular plasticity and adaption upon stimulation. Confocal imaging of cancer cells indicated that growth factor treatment supported cancer cell spreading and alignment within the scaffolds (**Figure 5d/e**). Cell-cell contacts (green arrows) appeared to decrease and membrane protrusion (yellow arrows) prominently increased upon GF supply. GF stimulation fostered a mesenchymal-like morphology (yellow arrows) on TACS5-like mimics. These effects were remarkably true for HCC1954 cells treated with TGF-β1. Cells importantly aligned with fiber orientation on the TACS5-mimicking scaffolds resulting in significantly decreased C_N to for the respective HCC1954 samples (**Figure 6a**). C_N values for growth on TACS6-like structures were not altered significantly (**Figure 6b**) implying the need of unidirectional fiber orientation to fully seize topographical cues. Similar tendencies were found for MCF7 cell line (**Figure 5d**). Whereas untreated cells mainly clustered into sheet like aggregates (green circle) GF-supply enhanced cell-fiber interaction and promoted mesenchymal-like morphologies (yellow arrows). Here, especially TGF-β1 and EGF stimulation for growth on collagen IV coated TACS5-like fibers correlated with significant decrease of C_N and A_R (Data not shown).

To further evaluate the input combinatorial cues may exert on the cellular phenotype, mRNA expression of CDH1 and VIM in HCC1954 was analyzed. Effects of TGF-β1 stimulation and contact guidance cues of aligned fibers alone with their combined action were compared. As shown in **Figure 6c**, no differences in CDH1 expression among the three conditions were observed as the mean decrease of mRNA levels was between 18-20%. Interestingly, combinatorial treatment resulted in the highest increase of VIM mRNA expression being significantly distinct from TGF-β1 stimulation alone. A 15.2-fold increase in VIM levels compared to a 11.6-fold increase upon sole TGF-β1 treatment was recorded. Moreover the results confirmed that the topography of the TACS5-mimicking scaffolds depicts a sufficient cue to induce EMT-like changes in HCC1954 cells.

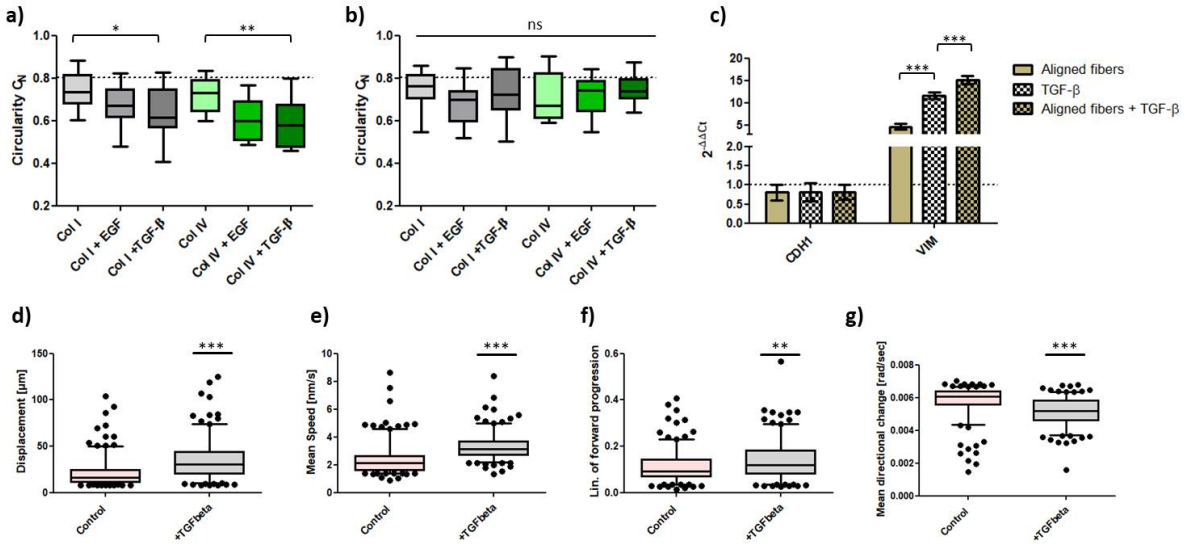

Figure 6. *Morphological alignment of nuclei of HCC1954 cells on TACS5- (**a**) and TACS6-like (**b**) scaffolds depending on growth factor stimulation (EGF, TGF-β1) and growth surfaces (collagen I/IV). C_N-values were plotted as Whiskers plot. The dotted line represents the mean C_N-value of control cells growing on conventional culture dishes (**a, b**). Relative mRNA expression of CDH1 and VIM in HCC1954 cells (**c**). $\Delta\Delta C_t$-values were calculated after 72 h of either growth on TACS5-mimics and/or treatment with 10 ng/mL TGF- β1 (n = 2). Errors show SD. Comparison of trajectory analysis of untreated (control) HCC1954 cells and cells treated with TGF-β1 using Fiji software (TrackMate) (**d-g**). Displacement, mean migration speed, confinement ration and mean directional change were plotted as whiskers plot (5-95 percentiles). Statistical significance was assessed with a t-test based on > 200 cells/condition.*

Next, track displacement, mean migration speed, confinement ratio and mean directional change were again analyzed to further test whether TGF-β1-induced EMT is beneficial for HCC1954 cells migrating on TACS5-scaffolds. **Figures 6d-g** display how TGF-β1 stimulation crucially affected motility of cancer cells migrating on the fibers. On average, cells migrated 70.5% further and 39.3% faster as control cells. According to confinement ratio (23% increase) and mean directional change (12% decrease) cells migrated more efficiently on the fibrous matrix than control cells, implying improved contact guidance.

3.2.3 Mesenchymal-to-Epithelial-Transition (MET)-like changes impair motility and contact guidance on TACS5-mimicking scaffolds

The data presented confirm that topographical cues influence breast cancer phenotype and *vice versa*. Indeed, it appeared that growth factor-induced EMT-like changes equip cancer cells with features to better exploit topographical input for cellular migration. To further confirm this observation and investigate whether MET-like changes have reverse effects on cell migration within fibrous networks, two genetically modified breast cancer cell lines were included. On the one hand, miR200c was stably knocked-out in MCF7 cells (EMT cell line), and on the other hand MDA-MB-231 cells were modified to inducibly express miR200c (MET cell line) under exposure to doxycycline (DOX).

First, it was investigated whether the two genetically engineered cell lines differed in EMT-marker expression from their respective wild type by using RT-qPCR. CDH1 and VIM mRNA levels from MCF7_WT cells were compared with the miR200c knock-out cell line (MCF7_KO), and mRNA expression of inducible MDA-MB-231 (MB231_i-miR200c) cells were compared with and without DOX stimulation. MiR200c knock-out in MCF7 resulted in a 50% loss of CDH1 expression and 3.2-fold increase of VIM mRNA levels. Conversely, DOX-induced miR200c expression lead to a 3.0-fold gain in CDH1 mRNA, and VIM expression was decreased by 40% (**Figure 7a**). Importantly, the presented data shows relative mRNA expression. Total CDH1 expression in MCF7_KO is still 500-fold higher than VIM expression and total VIM expression in MB231_i-miR200c is still 23-fold higher than CDH1 expression (Data not shown). CDH1 and VIM protein levels were affected in analogous manner for MB231_i-miR200c. Additionally, CD44s protein levels, known to be overexpressed in cancer stem cells and during EMT [29, 55] were partially depleted upon DOX stimulation further arguing for MET (**Figure 7b**).

Second, nuclear circularity and cell growth of MB231_i-miR200c cells in TACS5- and TACS6-mimicking scaffolds was monitored. Confocal images taken after 48 h incubation confirmed that unbiased cells strongly aligned with fiber orientation as already reported for MDA-MB-231 wild type cells (**Figure S2a**), whereas DOX-dependent miR200c induction critically impeded morphological polarization on the aligned fiber set-up (**Figure 7d**). Analysis of C_N confirmed impaired morphological adaption of MB231_i-miR200c under DOX exposure, as values were significantly elevated ($P < 0.05$). Instead, C_N-values of DOX-induced cancer cells (MET) growing on TACS5- and TACS6-topographies, respectively, equalized (**Figure 7c**).

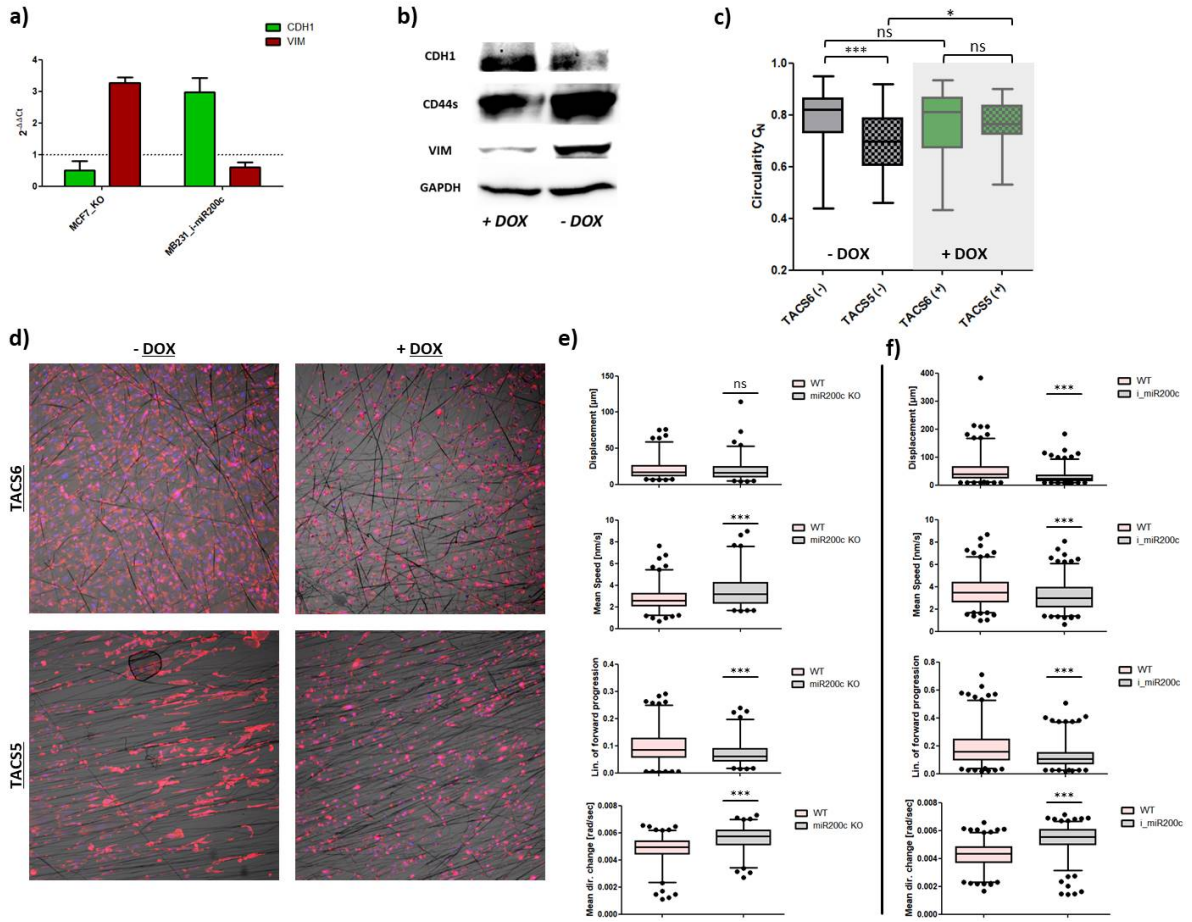

Figure 7. *Relative expression of CDH1 and VIM mRNA of MCF7_miR200c_KO and MDA-MB-231_i-miR200c (MB231_i-miR200c) cells in comparison to their wild type (**a**). Western blot of MB231_i-miR200c cells with and without doxycycline-dependent induction stained for EMT-relevant marker CDH1, VIM and CD44s (**b**). Whiskers plot showing alterations in C_N-values (from 40x images) in MB231_i-miR200c cells with and without doxycycline-dependent induction for growth on TACS5- and TACS6-like structures. One-way ANOVA with Bonferroni multiple comparison test was performed to calculate P-values at a 95% confidence interval (n(cells) > 50) (**c**). Respective confocal images of cells at 10x magnification. Cells were stained for nuclei (blue) and the cytoskeleton (red) (**d**). Comparison of trajectory analysis of WT cells with MCF7_KO (**e**) or MB231_i-miR200c (**f**), respectively, performed with Fiji software (TrackMate). Displacement, mean migration speed, confinement ration and mean directional change were plotted as whiskers plot (5-95 percentiles). Statistical significance was assessed with a t-test based on > 150 cells/condition.*

Third, to further illuminate how EMT-like (MCF7_KO) or MET-like (MB231_i-miR200c) alterations determine cellular motility on TACS5 mimics, live cell imaging-based trajectory analysis was conducted. miR200c KO hardly improved contact guidance even though cellular mean migration speed was significantly increased ($P < 0.0001$). Track displacement remained unchanged, but the confinement ratio decreased ($P < 0.001$) whereas mean directional change increased ($P < 0.001$) (**Figure 7e**). In contrast, miR200c induction not only reduced mean speed of MDA-MB-231 cells (WT: 3.625 ± 0.068 nm/s vs. i_miR200c: 3.151 ± 0.064 nm/s) but also significantly impaired contact

guidance based on track displacement, confinement ratio and mean directional change (**Figure 7f**). Taken together, MET-like changes appear to restrict cells in experiencing contact guidance by TACS-like structures.

3.2.4 EGF induces Mesenchymal-to-Amoeboid Transition (MAT) in MDA-MB-468 on TACS5-mimicking scaffolds

It was recently demonstrated that the triple negative breast cancer (TNBC) cell line MDA-MB-468 can be forced to undergo EMT-like changes triggered by EGF in conventional 2-D cell culture.[40, 56] Here, it was investigated whether EGF supply would also improve contact guidance and cellular motility in the TACS5-mimicking *in vitro* model as already shown for EMT induction in HCC1954. Live cell imaging with subsequent trajectory analysis confirmed elevated migration speed ($P < 0.0001$) in comparison to control cells (**Figure 8a**). Nevertheless, confinement-ratio decreased whereas mean directional change increased by 9.5% and 9.0%, respectively, indicating weakened direction persistence of migration (**Figure 8b/c)**. Moreover, track displacement remained unchanged during EGF treatment (**Figure 8d**).

To understand the dynamics of altered migration, trajectory analysis of nuclear circularity for the first 10 h of live cell imaging was applied (**Figure 8e**). As demonstrated above, a decrease in C_N is predictive for increased contact guidance and monitoring its kinetics may elucidate impaired adaption to the fibrous scaffold. Surprisingly, significant increases of mean C_N-values (dotted lines) were observed under EGF stimulation. **Figure 8e** also depicts a representative C_N track for each condition. Nuclear circularity of the control cells shifted towards lower values below 0.7 whereas EGF-treated samples mostly retained C_N values around 0.9. Snap-shots of control cells clearly highlighted that cells aligned with fiber orientation by elongated morphologies and profound cellular ingrowth, which is also indicated by the above mentioned decrease in C_N (**Figure 8f**). Contrariwise, EGF-treated cells exhibited rounded, spherical morphologies similar to the amoeboid phenotype, and cells seemed to "roll" over the matrix instead of using membrane protrusions (characteristic of mesenchymal migration) to creep along the fibers (**Supplementary Video 1 and 2**). Consequently, growing on TACS5-like structures fostered a mesenchymal phenotype (EMT) which converted towards an amoeboid phenotype upon EGF treatment (MAT).

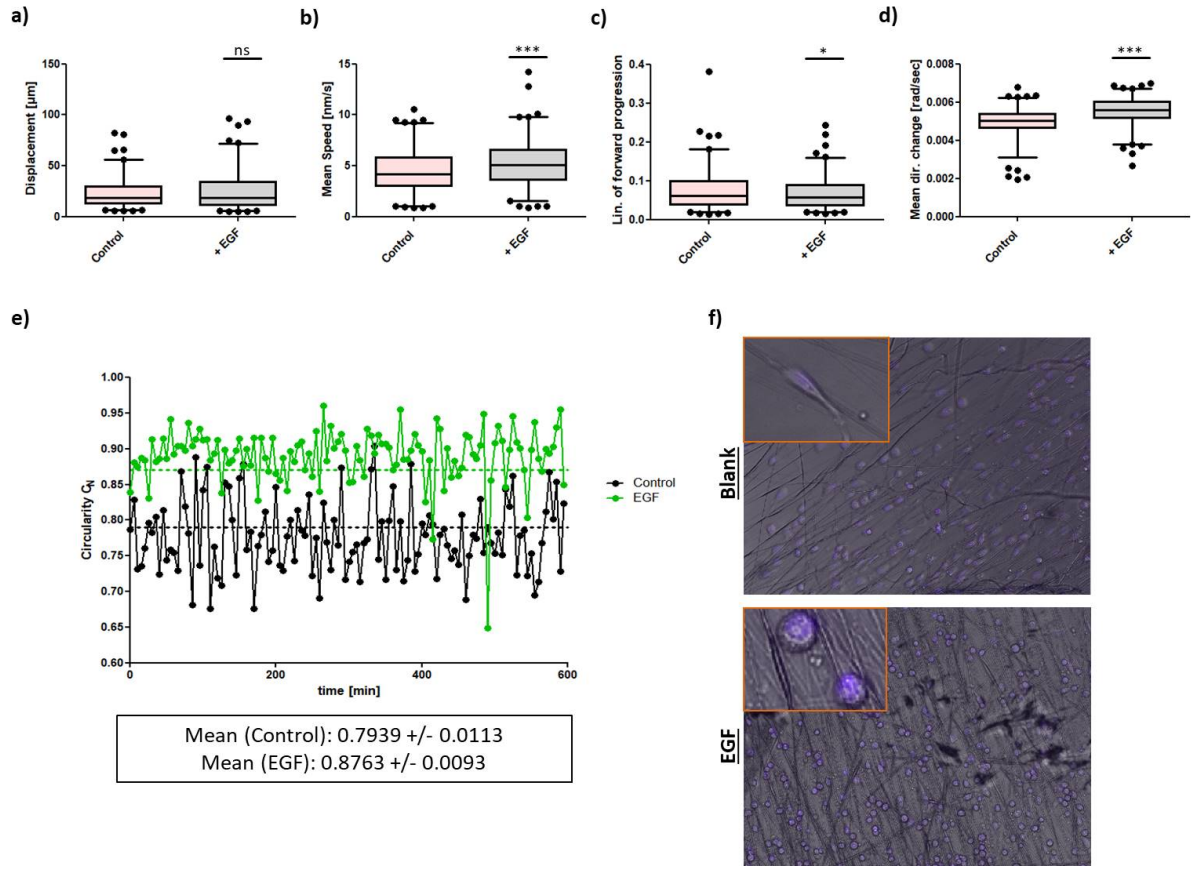

Figure 8. *Comparison of trajectory analysis of untreated (control) MDA-MB-468 cells and cells treated with EGF using Fiji software (TrackMate). Displacement, mean migration speed, confinement ration and mean directional change were plotted as whiskers plot (5-95 percentiles). Statistical significance was assessed with a t-test based on > 200 cells/condition (**a-d**). Comparison of trajectory analysis of nuclear circularity (C_N) of untreated (control) MDA-MB-468 cells and cells treated with EGF using Fiji software. Errors depict SEM of 30 trajectories, respectively. Dotted lines in graph represent mean C_N. Lines show a representative trajectory of C_N for control (black) and EGF-treated (green) cells (**e**). Snapshots of live cell images highlighting differences in cellular and nuclear morphologies between control cells and EGF-treated cells. Overlay of TLP and 405 nm channel with purple colors showing nuclei of MDA-MB-468 cells. Orange windows depict zoom-in (**f**).*

3.3 Biomechanical evaluation of breast cancer cell lines: Comparison of conventional 2D cell culture with TACS5-mimicking *in vitro* model

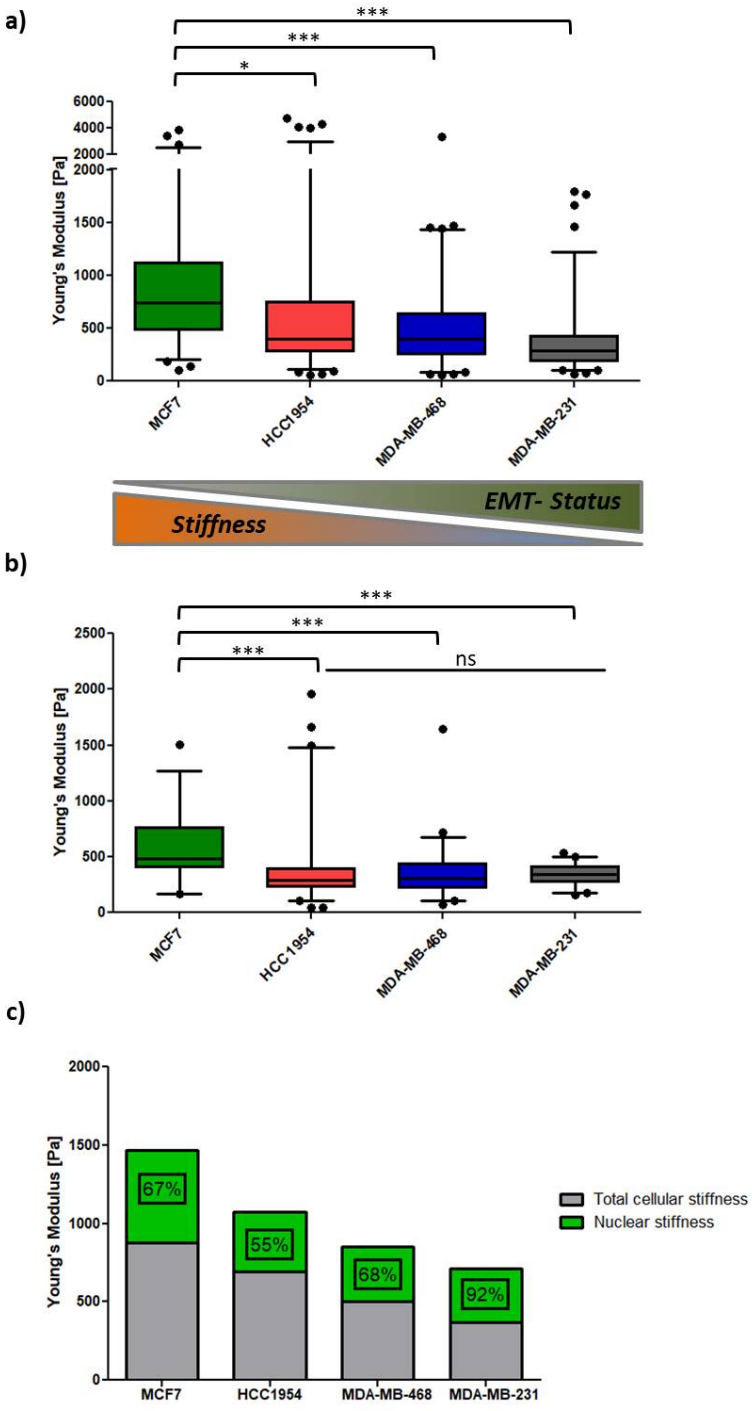

Figure 9. *Total cellular stiffness of the 4 breast cancer cell lines shown as Whiskers plot (5-95 percentiles) (**a**). Nuclear stiffness of the 4 breast cancer cell lines shown as Whiskers plot (5-95 percentile) (**b**). Nuclear stiffness stacked over total cellular stiffness of the 4 breast cancer cell lines. Numbers indicate percentage of nuclear stiffness over total cellular stiffness (**c**).*

3.3.1 EMT-status inversely correlates with total cellular stiffness

It is well accepted, that high-grade tumor cells are softer than their benign or low-graded counterparts. Accordingly, it is beneficial for invasive cancer cells to possess a certain degree of mechanical deformability whilst migrating and invading through the porous matrix of the stromal compartment. Here, total cellular stiffness and nuclear stiffness of single cells were estimated by applying atomic force microscopy (AFM) either framing the whole cell, or focusing on the nucleus. Elastic Young's modulus [Pa] was quantified, which is considered to depict a good approximation of cellular stiffness.[57, 58] Cell mechanics of the four cell lines were significantly distinct from each other. As demonstrated in **Figure 9a**, total cellular stiffness linearly decreased wit EMT-status from 769.5 ± 54.52 Pa (MCF7) to 372.1 ± 20.82 Pa (MDA-MB-231). This very tendency was not observed for measurements of nuclear stiffness. Besides MCF7 cells reflecting the highest Young's modulus (590.0 ± 280.0 Pa), nuclear stiffness of the other three cell lines were not differing significantly from each other (**Figure 9b**). However, as shown in **Figure 9c**, nuclear stiffness of the most invasive MDA-MB-231 cells strongly contributed to the overall stiffness (92%) whereas the latter contribution was less important for the other three cell lines (55-68%). This underlines, that the nucleus of this mesenchymal cell line poses the main physical restriction for invasion. Lamins (A/C, B), nuclear envelope proteins, are thought to determine the physical properties of the nucleus. In disagreement to current literature [59, 60], high protein levels of Lamin B1 instead of Lamin A/C correlated with increased nuclear stiffness in the studied breast cancer cell lines (**Supplementary data Figure S3**).

3.3.2 Early EMT-like events entail cellular/cytoskeletal stiffening during biochemically and topographically induced EMT

One could conclude from the latter findings that EMT-induction would result in decreased total cellular stiffness and nuclear stiffness. To challenge this hypothesis MDA-MB-468 cells were first stimulated with EGF for 24 h or 48 h and subsequently assessed regarding cell mechanics (**Figure 10a-c**). As shown in **Figure 10a,** epithelial cancer cells adopted a spindle-like morphology already after 24 h incubation. Contradictory to our expectations, total cellular stiffness significantly increased upon EGF-treatment within the observed timeframe. Mean values of Young's moduli increased by39.6% and 28.9%, respectively (**Figure 10b**). In parallel to the elevated total cellular stiffness, nuclear stiffness increased by 17.6% within the first 24 h. However, after 48 h mean values of Young's modulus lay 21.4% below the values of control cells implying softening of the nucleus (**Figure 10c**).

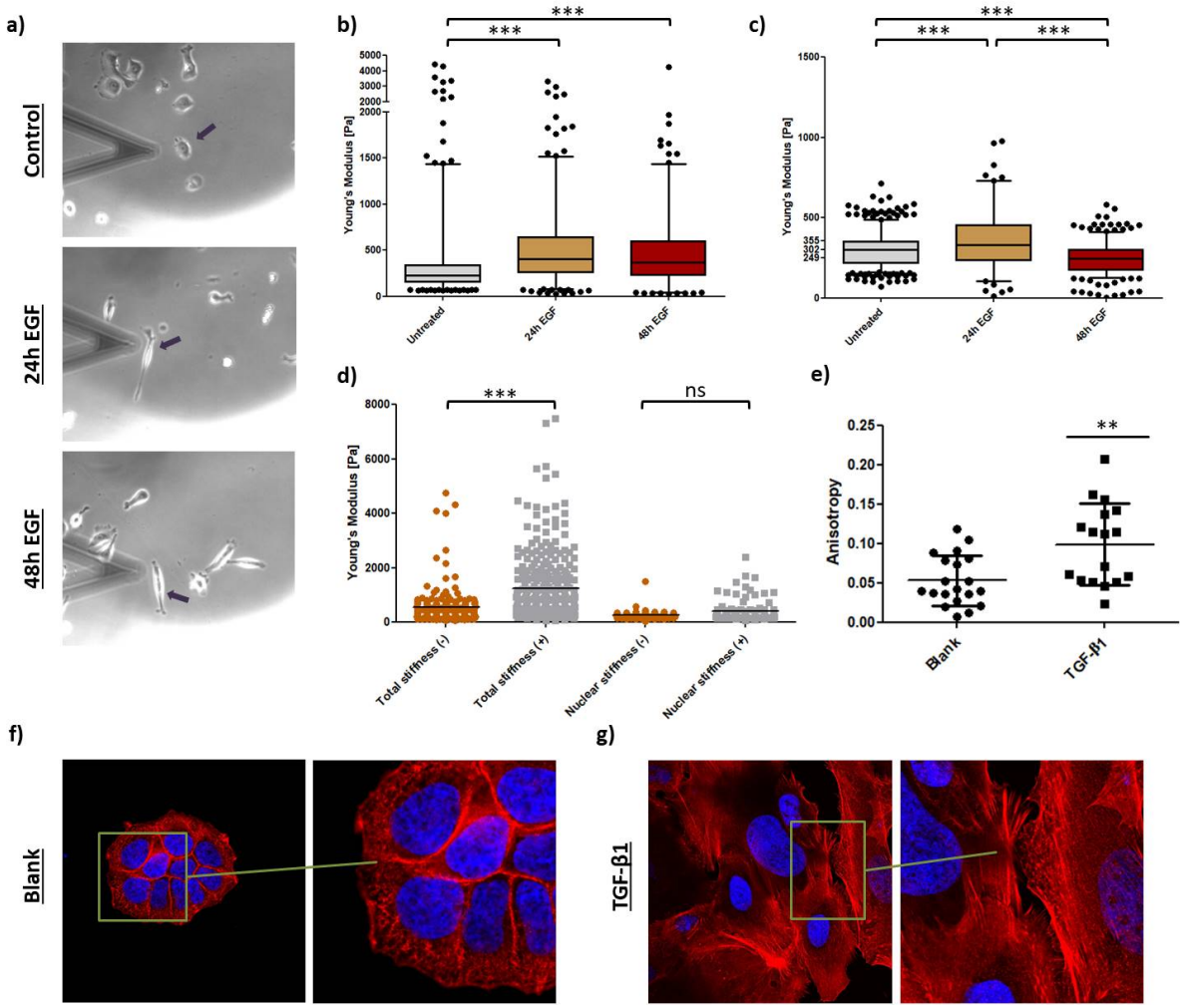

Figure 10. *TLP images of MDA-MB-468 cells measured in AFM contact mode. Black arrows indicate analyzed cell (**a**). Total cellular stiffness of MDA-MB-468 cells treated with EGF for 24 and 48 h (**b**). Nuclear stiffness of MDA-MB-468 cells treated with EGF for 24 and 48 h (**c**). Total cellular stiffness of HCC1954 cells treated with TGF-β1 for 48 h (**c**). Nuclear stiffness of MDA-MB-468 cells treated with TGF-β1 for 48 h (**d**). Anisotropy of actin fibers of control HCC1954 cells compared with TGF-β1 stimulated cells (t-test; $P < 0.005$) (**e**). Confocal images of untreated (**f**) and TGF-β1-treated (**g**) HCC1954 cells showing nuclei (blue) and actin cytoskeleton (red) at 63x magnification. Right panel (zoom-in) highlights actin cytoskeleton architecture to either show a cross-linked network (**f**) or parallel stress fibers (**g**).*

Second, to validate these findings similar experiments were conducted with the HCC1954 cell line. Additionally, confocal scanning microscopy was performed to monitor changes of the actin cytoskeleton. The aim of this experiment was to identify the cell compartment being responsible for alterations of cell mechanics. Interestingly, total cellular stiffness elevated significantly upon TGF-β1 stimulation (**Figure 10d**). The mean of the Young's modulus increased by 117.9% (from 564.4 Pa to 1230.0 Pa) being even superior to EGF-induced elevation in MDA-MB-468. However, no significant alteration of nuclear stiffness was measured for cells being treated with TGF-β1. Furthermore, image analysis illustrated cytoskeletal rearrangements explaining the dramatic cell stiffening. Whereas the

actin network seemed to be crosslinked and randomly orientated in control cells (**Figure 10f**), TGF-β1-induced EMT elongated HCC1954 cells and entailed restructuring of actin bundles with the formation of stress fibers (**Figure 10g**). Actin fibers significantly parallelized in comparison to the network-like actin fibers of control cells (**Figure 10e**).

Subsequently, it was assessed whether cell growth on TACS5-topographies would lead to similar biomechanical changes as were observed for growth factor-induced EMT trying to correlate changes in EMT-marker expression with cell mechanics. Cellular stiffness between cells growing either on collagen I-coated coverslip or coated fibers was compared. The Young's modulus remained unaffected in MCF7 cells (**Figure 11a**) and only slightly increased in MDA-MB-231 cells (**Figure 11d**) under exposure to the TACS5-mimicking scaffold. Interestingly, a significant ($P < 0.0001$) increase in cellular stiffness occurred in HCC1954 (**Figure 11b**) and MDA-MB-468 (**Figure 11c**) cells growing on the fibrous matrix. The Young's moduli increased by 72.9% and 95.2%, respectively, comparable to GF-mediated EMT induction.

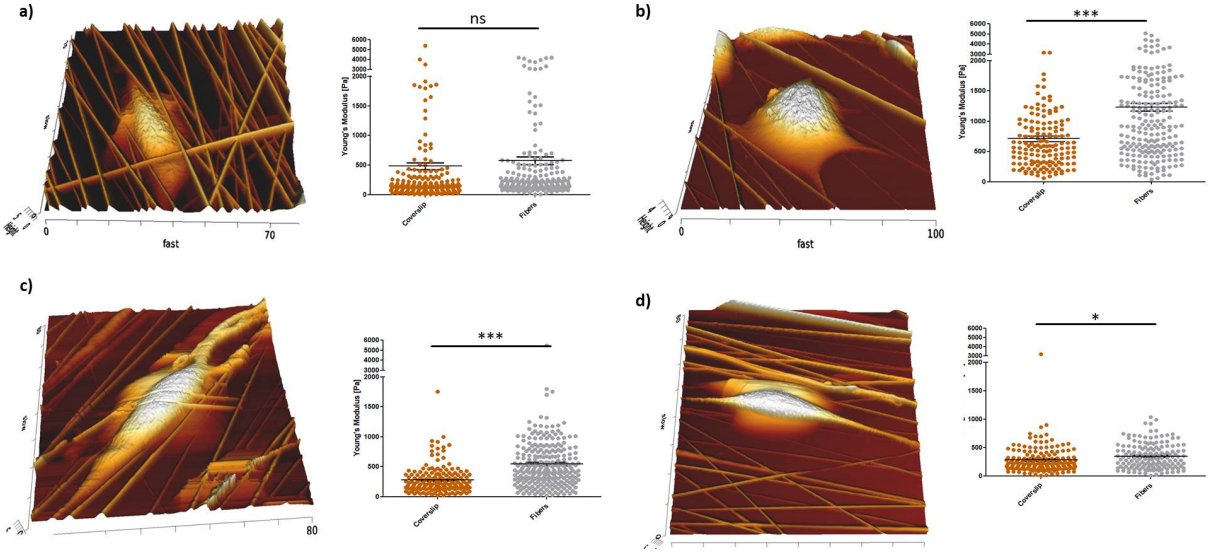

Figure 11, *AFM analysis of MCF7 (**a**), HCC1954 (**b**), MDA-MB-468 (**c**) and MDA-MB-231 (**d**) cell lines growing on TACS5-like scaffolds. Left panel shows surface topography. Right panel depicts total cellular stiffness of the respective cell lines growing either on conventional culture dishes or TACS5-mimics.*

4. Discussion

The goal of the underlying *in vitro* study was to reproducibly create a 3D electrospun matrix that accounts for topography and dimension of tumor-associated collagen signatures as they are found in the diseased tissue of the mammary gland. Upon the spinning process the choice of two distinct collector types, namely rotating mandrel and plate collector, allowed for mimicking TACS5 or TACS6 structures, respectively. SEM images revealed that optimized PCL fibers deposited on coverslips have either a parallel (mandrel) or a random (plate) relative orientation. Fiber diameters were in a range of 400 - 1700 nm with comparable mean inter-fiber distances (2.0 µm vs. 2.4 µm). Naturally occurring collagen structures were shown to have widths ranging from a few hundred nanometers to one micron [61] and interfiber distances (analyzed from breast cancer patient-derived tissues) between 2 µm and 3 µm.[62] Thus, the optimized electrospinning set-up allowed imitating the *in vivo* architecture of collagen fibers not only by producing scaffolds mimicking TACS5 and TACS6-specific orientation but also through their submicron scale and fiber density.

Despite their biocompatibility and ideal mechanical properties PCL fibers are known for their unfavorable characteristics for cell attachment.[63-65] Their hydrophobic nature and low surface energy pose a major obstacle to cell-substrate adhesion, which is essential for the biological performance of the scaffold. Initial cellular attachment and spreading on the matrix dominate the functional activity as both determine further proliferation, migration, differentiation and gene expression of cells.[66] With tissue-specific collagen I coatings subsequent to the spinning process, cell spreading, biocompatibility and bio-mimicry were simultaneously improved. Confocal laser scanning microscopy displayed homogenous deposition of collagen on the fibrous matrix (**Figure S1**). Combined with negligible cytotoxic events on the collagen-coated fibers, the *in vitro* model was established.

Several earlier studies demonstrated that breast cancer cells seeded on fibrous 3D scaffolds acquired a more malignant phenotype entailing EMT-like changes as compared to conventional 2D cell culture.[67-71] Such cellular responses to topographical cues are referred to as contact guidance. Responses comprise cellular polarization, alignment, altered cell motility and gene expression. Accordingly, the magnitude of transition appeared to be determined by physical characteristics of the fiber matrix and biological aspects of the implemented cells. This included the scale (nanometric vs. micrometric) and the orientation of the topography (unidirectional vs. multidirectional), the size and type of cells and the interrelation between cell-characteristic size and substrate dimension.[67-73] Furthermore, it was recently indicated that the epithelial/mesenchymal-state of a cell influences the degree of contact guidance cells experience from a given topography.[27] Indeed, by assessing cellular morphology, migratory properties and EMT-marker expression it can be concluded that low (high) EMT-status related to weak (strong) contact guidance on the TACS-mimicking *in vitro* model.

CDH1$^+$/VIM$^-$ MCF7 and HCC1954 (epithelial) cells retained their morphological features (C_N, A_R) on TACS5 and TACS6-mimicking scaffolds, respectively, whereas CDH1$^+$/VIM$^+$ MDA-MB-468 cells (E/M-hybrid) and CDH1$^-$/VIM$^+$ MDA-MB-231 (mesenchymal) cells strongly aligned and elongated after 72 h cell growth on TACS5-like, but not on TACS6-like topographies (Figure 4, Figure S2). The observed strong alterations of cytoskeletal and nuclear morphology on TACS5-like topographies coincided with EMT-phenotypic gene expression pattern in MDA-MB-468 cells (↓CDH1, ↑VIM, ↑SNAI, ↑XBP1, **Figure 5a**) underlining the predictive importance of (sub-)cellular morphologies. Contrarily, MCF7 cells which were shown to hardly adapt their morphology mostly retained their epithelial expression pattern. Even more strikingly, trajectory analysis of MCF7, HCC1954 (despite upregulation of VIM) and MDA-MB-468 cells grown on TACS5-scaffolds revealed two opposing effects on cellular motility depending on EMT-status. Migration of fully epithelial cells was impeded whereas mean migration speed increased for more mesenchymal MDA-MB-468 cells (**Figure 5b**). These findings are in line with an earlier study showing cells to preferentially align and migrate in the direction of continuous unidirectional (TACS5-like) substrates but to randomly orientate and migrate on multidirectional pattern (TACS6-like).[73] On the other hand, besides the fiber directionality, the EMT-status depicted a major element to decide over cellular responses as only cell lines with mesenchymal characteristics essentially polarized and increased their motility on the fibrous matrix. Since purely epithelial cancer cells exhibit strong cell-cell but fewer cell-matrix interactions, their less frequent focal adhesions [74-76] might explain low EMT-status to impede topographically induced transitions. As shown in **Figures 4** and **5,** an epithelial phenotype dispersed within the TACS5-micking matrix would therefore seek to establish cell-cell contacts, whereas more mesenchymal phenotypes would more likely interact with the matrix. Presumably, focal adhesion-mediated recognition of topographical patterns induced cell polarization and actomyosin contractility which in turn, also by affecting chromatin arrangement, modulated transcriptional programming of EMT-related genes.[77-79]

Apart from high EMT-status correlating with increased contact guidance, biochemically induced EMT resulted in stronger overall EMT-like changes than topographical triggers within the 72 h period of incubation (**Figure 5a**, **Figure S2b**). Growth factor stimulation caused similar downregulation of CDH1 mRNA levels in all three cell lines but a 3.5- to 4.7-fold higher upregulation of VIM (HCC1954 and MDA-MB-468). This observation corroborates findings of Saha *et al.* [68] showing the same EMT-relevant genes to be affected by contact guidance with stronger growth factor-mediated changes. Moreover, to the best of our knowledge, this study is the first report to link XBP1 to contact guidance. In two of three cell lines, a significant upregulation after 72 h of cell growth on the fibers was observed (**Figure S2b**). XBP1 is known to upregulate SNAI1 expression, thereby inducing EMT-like changes [51, 80] which is in accordance to our findings as both, XBP1 and SNAI1 were upregulated in the MDA-MB-468 cell line. Simultaneously, significant upregulation of XBP1 mRNA via EGF-mediated EMT in MDA-MB-468 cells was found, previously shown to cause chemo-

resistance in colorectal cancer [81], thus supporting XBP1's importance for EMT. However, future studies have to clarify and confirm to what extent XPB1 participates in contact guidance. Possibly, TACS5-like topographies spatially confined cells, inducing ER stress and unfolded protein response (UPR), which are the underlying mechanism of XBP1 activation providing survival advantage in cancer cells.[82]

Possibly, cell-characteristic sizes of MCF7 and HCC1954 cells (or nuclei) failed to match with the dimensions of the topography, suggesting steric hindrance, which would explain the extenuated contact guidance in those cell lines (**Figure 4a-b**, **5b**) However, by inducing EMT-like changes via GF stimulation in cells growing on the matrix, EMT-status was attributed to be the main driver of contact guidance. At the same time MET-like changes impaired contact guidance which underscores its delicate reciprocal relation with cellular EMT-phenotype (**Figure 6** and **7**)

For instance, TGF-β1-mediated downregulation of CDH1 and upregulation of VIM enabled HCC1954 cells to significantly align on the TACS5-like scaffold with an increased motility and directional persistence as compared to control cells **Figure 6a,d-f**). Similarly, Ravikrishnan *et al.* [69] showed that HGF-dependent EMT-induction was required for epithelial cells to disintegrate, interact with and migrate along nanofibers, which was not observed without preceding treatment. As proposed elsewhere, E-Cadherin-based cell-cell junctions (adherens junctions) may have restrained contact guidance of the aligned matrix as they counteract the anisotropic cell-substrate interaction.[27] Thus, EMT-induction in HCC1954 by downregulating CDH1 loosened up adherens junctions, facilitating cell-fiber interactions. Additionally, the lack of the intermediate filament vimentin in fully epithelial cells has to be considered for contact guidance. It was shown that vimentin specifically aligns with grooved patterns in adult meningeal cells [83] as well as crucially effected focal adhesion maturation .[75, 76] Since vimentin templates microtubule-mediated directional migration [84], it appears plausible that its presence and/or upregulation entails enhanced contact guidance. This is in accordance with miR200c-dependent MET induction in MDA-MB-231 cells, shown to downregulate vimentin protein levels, resulting in significantly reduced contact guidance on TACS5-like topographies (**Figure 7**). Cellular alignment and directed migration was restricted upon MET induction. However, miR200c KO in MCF7 for EMT-induction only marginally elevated contact guidance, possibly because CDH1 mRNA expression was still dominating VIM expression.

As mentioned above, shifting HCC1954 cells into an E/M-hybrid phenotype resulted in increased cellular alignment and enhanced motility on TACS5 structure i.e. fostered contact guidance (**Figure 6**). Most importantly, VIM mRNA expression elevated concomitantly which was even superior to GF-mediated EMT alone (**Figure 6c**, 15.2-fold vs. 11.6-fold higher). Consequently, acquisition of mesenchymal features through TGF-R signaling may have potentiated cell-matrix interactions and subsequently synergized with contact guidance exerted on cells. However, EMT induction in HCC1954 did possibly not depend on the fiber topography but on the 3D environment itself structure

and spatial arrangement of surface receptors was shown to differ from 2D in 3D environments, potentially leading to altered outside-in signaling upon receptor stimulation [85, 86].

Contributions from the nucleus, the actin cytoskeleton, microtubules, intermediate filaments and cell membrane define the mechanical properties of a single cell as a whole and are additionally altered by interactions with adjacent cells and the pericellular ECM.[13] Since EMT-like changes comprise fundamental reorganization of the entire cytoskeleton, major deviations of cell mechanics among cells of different EMT-status and upon transition were expected.

First, assessing cellular and nuclear stiffness using AFM indentation revealed Young's moduli of total cellular stiffness to decrease with increasing EMT-status of the cell lines (MCF7 > HCC1954 > MDA-MB-468 > MDA-MB-231). This data (**Figure 9a**) is in accordance with the current understanding of literature since the EMT-status, according to the definition used in this study, aligns with cancer cell malignancy which is itself thought to inversely correlate to cellular stiffness.[12-16, 87] However, probing nuclear stiffness revealed some inconsistencies compared to the literature. With the nucleus being the largest organelle of a cell, its stiffness is considered to decisively influence migration and invasion.[54] Cancer cells have to accomplish remarkable deformations of the nucleus, and the entire cell, as they navigate through the tiny pores and confinements of the stromal compartment, necessitating the nucleus to bear a certain degree of mechanical plasticity upon invasion. It was in line with recent findings that nuclei of poorly invasive MCF7 cells were less compliant than nuclei of highly invasive MDA-MB-468 and MDA-MB-231 cells.[53] However, nuclei are thought to be considerably stiffer than the surrounding cytoskeleton [54] which was not the case in this study.

Second, the change of mechanical properties of cells upon EMT induction was investigated. The above findings would imply softening of cancer cells during the transition towards a mesenchymal, more invasive phenotype. However, several studies conducted on this topic revealed controversial findings. Whereas some groups detected cell stiffening upon GF-mediated EMT [88, 89], others reported cells to soften during the process.[90-92] This study supports the "stiffening theory" as total cellular stiffness significantly increased within a 24 h to 48 h timeframe in two separate cell lines induced with two distinct GFs (**Figure 10 a-d**). This stiffening phenomenon was attributed in part to changes in the actin cytoskeleton at the cell cortex. Phalloidin staining of HCC1954 cells demonstrated strongly aligned actin bundles under TGF-β1 stimulation (**Figure 10e,g**). It was repeatedly disclosed that presence of such stress fibers made of F-actin correlate with elevated cellular stiffness, and that fiber disassembly entails cell softening [93-96]. Moreover, Tavares *et al.* [96] revealed that pre-metastatic changes of breast cancer cells led to an initial cytoskeleton-based cell stiffening before converting into a malignant but softer phenotype. Indeed, regarding nuclear stiffness in MDA-MB-468 cells, the onset of EMT mediated stiffening, which may rely on cytoskeleton re-arrangements, but finally caused softening of the nucleus. This may explain the contradictory findings across different research groups as it emphasizes the role of incubation/transition time for

biomechanical evaluation of the EMT process. Another factor that might affect cell mechanics during EMT is the intermediate filament vimentin whose biomechanical role is only vaguely understood. It has been proposed that vimentin's viscoelastic properties maintain mechanical integrity of cells during the process of invasion, and its expression was correlated to cell stiffening in lung and breast cancer cells.[88, 97, 98] However, the sole expression of vimentin does not or even reversely correlate with cell stiffness as demonstrated by the mechanical evaluation of the four breast cancer cell lines studied here (**Figure 9a**). MDA-MB-231 cells expressing the highest levels of vimentin exhibited the lowest Young's modulus. To clarify whether the observed upregulation of vimentin as part of EMT in HCC1954 and MDA-MB-468 cells is causing increased cell stiffness, further studies on the spatio-temporal relationship of vimentin network assembly and cellular stiffness need to be conducted. Presumably, as proposed elsewhere, geometry and organization of the vimentin network, which changes upon EMT, as well as interactions with other cells dictate vimentin's contribution to overall cell mechanics, which seems to be ultimately context-dependent.[97, 99]

Third, to approximate the impact the topographical landscape (i.e. TACS) arising during tumor progression within the mammary gland exerts on breast cancer cell mechanics, total cellular stiffness after 48 h of cell growth on the TACS5 scaffold or on collagen I coated coverslips was evaluated. The data obtained is in very well confirms prior findings on each cell line. MCF7 cells being hardly influenced by contact guidance showed no deviation of the Young's modulus from 2D cell culture (**Figure 11a**). Similarly, MDA-MB-231 cells, which exhibit already polarized morphologies in conventional cell culture [40], only slightly stiffened on the TACS5-like matrix. We hypothesize that contact guidance of the aligned matrix increased the proportion of the polarized cell populations in MDA-MB-231 cells leading to overall higher stiffness values as compared to conventional growth. Most strikingly, HCC1954 and MDA-MB-468 cells, which have been shown to undergo prominent EMT-like changes on the TACS5-like scaffold, concomitantly increased their cellular stiffness (**Figure 11b,c**). This is in particular interesting as biochemically induced EMT resulted in comparable cell stiffening in those cell lines. As a consequence, we propose transient stiffening of breast cancer cells as a new marker for EMT-like changes. In future experiments, longer time intervals of the biomechanical evaluation need to be assessed to further study the kinetics of cellular mechanics of the EMT process to answer remaining questions. Gladinin *et al.* [88] proposed that cells at the margin of an invasive tumor performing EMT benefit from transient stiffening as it helps them to adapt to mechanics of foreign ECM and to redirect cellular migration within the early phase of metastasis. Interrupting this mechanical adaption may consequently be a promising strategy to prevent cells from disseminating from the primary tumor.

As described above, some contradictions between this study and the current literature were found concerning biomechanical studies on cancer cells. One explanation for theses discrepancies could be the use of different biophysical techniques, culture dishes or probing parameters to assess cell

mechanics throughout different studies.[58] Furthermore, examining single cell mechanics, as shown here, or mechanics of epithelial layers as performed by others [91, 98] potentially results in distinct outcomes as cell-cell entanglements reorganize the cytoskeleton, affecting biophysical properties of cells. Additionally, since cytoskeletal components cover the nucleus it can be challenging to solely probe the mechanical input of the nucleus alone. However, as nuclear stiffness was measured to be consistently lower than total cellular stiffness, even after pronounced alterations of the cytoskeleton, we expect AFM indentation parameters to be the main cause of the observed deviations whereas the cytoskeleton's contribution to nuclear stiffness was negligible in this study.

In this study we mainly focused on TACS5-like topographies as their potential to induce morphological changes resembling EMT-like changes was found superior in our initial experiments which prompted us to deepen the analysis towards this direction. However, we still want to shortly discuss our findings beyond TACS5 or EMT.

From a morphological point of view, TACS6-like structures seem to promote cellular phenotypes characteristic to epithelial cells. For instance, HCC1954 cells retained rounded cell shapes and nuclear morphologies (high C_N-values) even after TGF-β1 induced EMT when growing on the TACS6-mimicking scaffold (**Figure 6b**). Likewise, mesenchymal MDA-MB-231 cells that are known to exhibit elongated morphologies (low C_N- and A_R-values) on conventional cell culture dishes [40, 100] and to strongly align on TACS5-mimicking topographies acquired epithelial-like cell shapes and nuclei on the TACS6-like matrix (**Figure 7c**). Additionally, miRNA200c-dependant MET induction of genetically modified MDA-MB-231 cells growing on the aligned fiber set-up led to nuclear shapes that resembled the ones on TACS6-like topographies (w/o miR200c induction) implicating related influence on cellular phenotype. Interestingly, this goes in line with findings of Wang *et al.*. They recently demonstrated that nanostructured architectures (produced via electrodepostion) within a range of 100 to 500 nm to induce GSK-3 mediated MET-like changes in MDA-MB-231 breast cancer cells including cellular rounding and the upregulation of epithelial gene expression.[101] This not necessarily means that metastatic outgrowth is impeded by TACS6-like structures as they promote MET but rather that cells on these collagen signatures possibly prefer other modes of migration like collective migration recently proposed to be the main driver of metastasis.[102]

Furthermore, we coincidentally monitored a process termed Mesenchymal-to-Amoeboid Transition (MAT) upon EGF stimulation in the MDA-MB-468 cell line. "Amoeboidness" is currently believed to be an additional phenotype within the universe of EMT introducing further cellular plasticity and survival advantage in many types of cancers.[103] The amoeboid phenotype is characterized by a rounded, spherical morphology and is driven by low substrate adhesion and high levels of RHO–ROCK-driven Myosin II activity.[103, 104] In the past decades it has been overlooked as 2D cell culture does not easily support this phenotype and only with 3D cell cultures arising MAT and its importance for metastasis could be recognized. Indeed, it is believed that the amoeboid state represents

the end of the EMAT (Epithelial-to-Mesenchymal-to-Amoeboid Transition) spectra with amoeboidness to develop upon matrix confinement [105], strong downregulation of E-cadherin [103, 106] and to entail cancer stem cell (CSC)-like properties [107] as well as increased velocity of migration [108], all of which was true in the case of our study. The fibrous TACS5-like matrix posed a physical confinement for cancer cells. After stimulation with EGF E-cadherin depleted in MDA-MB-468 cells whilst migration speed increased significantly. We further observed EGF-mediated CD44v-to-CD44s receptor isotype switching (data not shown) which is an indicator for gaining CSC features.[55] MDA-MB-468 cell line displayed spindle-like morphologies under EGF exposure in 2D cell culture (**Figure 10a**) but converted into a spherical amoeboid phenotype on our 3D TACS5-mimicking model (**Figure 8f**) leading to topography and/or 3-dimensionality to be key determinants for MAT induction in this case. So far, universal markers characterizing the amoeboid phenotype are missing.[103] Our approach of using cell trajectory analysis combined with monitoring (nuclear) circularity over time is promising to detect the Mesenchymal-to-Amoeboid Transition and has the potential to be implemented as tool in future research on (E)MAT.

Taken together, this study provides strong evidence that TACS5-like structures not only support but also promote EMT-like changes in breast cancer cells. Contact guidance highly depends on EMT-status not necessarily requiring a complete transition into a fully mesenchymal phenotype. Epithelial depletions and/or mesenchymal acquisitions resulting in E/M-hybrids suffice to improve contact guidance of single cells. At the same time, it appears that increased contact guidance potentiates malignancy of breast cancer cells leading to a positive feedback-loop that eventually leads to reinforced EMT and metastatic outgrowth. Studies that aim to decipher the mechanistic cause and underlying biology of this feedback-loop are therefore required as its *in vivo* relevance seems to be indisputable in the case of breast cancer.[6-8, 109, 110]

5. ***Conclusion***

The intense micro-environmental alterations epithelial cancer cells experience alongside the process of tumor progression in the tissue of the mammary gland bear a huge potential to trigger phenotypic changes and to promote malignancy. Apart from biochemical cues and their well-known molecular mechanism which influence the phenotype of a cell, today's cancer research further considers biophysical aspects such as mechanotransduction and the input ECM microarchitectures exert on cellular behavior i.e. contact guidance. Indeed, dozens of *in vitro* studies have tried to resolve the impact an increasingly stiffened matrix has on cancer migration and invasion, gene expression and malignancy.[111-116] Only a few of them included considerations on topographical cues even though they were found to be patho-physiologically relevant in the case of breast cancer.[6-8, 109, 110] Electrospun 3D *in vitro* models comprise the ability to design scaffolds that respect such micro-

architectural features (*e.g.* TACS) including the sub-micron scale and the tissue density. Our study underscores recent findings that cell behavior on electrospun matrices importantly differs (*e.g.* EGF induced EMT vs. MAT in MDA-MB-468) from 2D cell culture [117-119] rendering such biomimetic approaches indispensable for preclinical research. Combining 3D *in vitro* models with advanced analytical techniques holds promise to study cellular phenotypes in a more sophisticated, *in vivo*-like environment. Here, AFM analysis of cells growing on the TACS5-like *in vitro* model revealed for the first time to the best of our knowledge, that cellular response to contact guidance of nanofibers not only biochemically but also biophysically resemble the process of EMT.

Both, EMT-phenotypic changes that occur on the cellular level and re-structuring of the acellular fraction of the stromal compartment coincide during breast cancer. Their co-action presumably results in a positive feedback-loop that is sustaining tumor progression, ultimately leading to metastatic outgrowth. A plausible strategy to inhibit this feedback-loop is to prevent cells from transitioning into a (partial) mesenchymal phenotype. Directly targeting EMT has already been proposed to inhibit metastasis and drug resistance of cancer cells.[120, 121] However, attempts in this direction face a vast diversity of signaling pathways causing the transition. Simultaneously, impeding the desmoplastic alterations of the TME depicts an alternative to circumvent the malignant interplay. A promising intervention concerns the lysyl oxidase LOX which contributes to tumor progression by cross-linking collagen fibers.[122] Another approach includes the targeting of cancer-associated fibroblasts (CAF) which actively participate in the remodeling of the ECM.[123] Since EMT and TACS are likely to synergize in the tissue of the mammary gland, it is eventually necessary to combine targeting of EMT and tissue remodeling for future attempts to successfully treat invasive breast cancer.

6. References

[1] H. Sung, J. Ferlay, R.L. Siegel, **2021**, *71*(*3*): p. 209-249, DOI: 10.3322/caac.21660.

[2] G. Arpino, D. Generali, A. Sapino, L. Del Matro, A. Frassoldati, M. de Laurentis, P. Pronzato, G. Mustacchi, M. Cazzaniga, S. De Placido, P. Conte, M. Cappelletti, V. Zanoni, A. Antonelli, M. Martinotti, F. Puglisi, A. Berruti, A. Bottini, L. Dogliotti, *The Breast* **2013**, *22*(*2*): p. 109-120, DOI: https://doi.org/10.1016/j.breast.2013.01.016.

[3] N.F. Boyd, G.S. Dite, J. Stone, A. Gunasekara, D.R. English, M.R. McCredie, G.G. Giles, D. Tritchler, A. Chiarelli, M.J. Yaffe, J.L. Hopper, *N. Engl. J. Med.* **2002**, *347*(*12*): p. 886-94, DOI: 10.1056/NEJMoa013390.

[4] S. Alowami, S. Troup, S. Al-Haddad, I. Kirkpatrick, P.H. Watson, *Breast Cancer Res.* **2003**, *5*(*5*): p. R129-35, DOI: 10.1186/bcr622.

[5] P.P. Provenzano, K.W. Eliceiri, J.M. Campbell, D.R. Inman, J.G. White, P.J. Keely, *BMC Med.* **2006**, *4*(*1*): p. 38, DOI: 10.1186/1741-7015-4-38.

[6] G. Xi, J. He, D. Kang, S. Xu, W. Guo, F. Fu, Y. Liu, L. Zheng, L. Qiu, L. Li, C. Wang, J. Chen, *Biomedical Optics Express* **2021**, *12*(*10*): p. 6558-6570, DOI: 10.1364/BOE.433281.

[7] G. Xi, W. Guo, D. Kang, J. Ma, F. Fu, L. Qiu, L. Zheng, J. He, N. Fang, J. Chen, J. Li, S. Zhuo, X. Liao, H. Tu, L. Li, Q. Zhang, C. Wang, S.A. Boppart, J. Chen, *Theranostics* **2021**, *11*(*7*): p. 3229-3243, DOI: 10.7150/thno.55921.

[8] M.W. Conklin, J.C. Eickhoff, K.M. Riching, C.A. Pehlke, K.W. Eliceiri, P.P. Provenzano, A. Friedl, P.J. Keely, *Am. J. Pathol.* **2011**, *178*(*3*): p. 1221-32, DOI: 10.1016/j.ajpath.2010.11.076.

[9] C.-Y. Su, A. Burchett, M. Dunworth, J.S. Choi, A.J. Ewald, E.H. Ahn, D.-H. Kim, *Biomaterials* **2021**, *275*: p. 120922, DOI: https://doi.org/10.1016/j.biomaterials.2021.120922.

[10] P. Schedin, P.J. Keely, *Cold Spring Harb. Perspect. Biol.* **2011**, *3*(*1*), DOI: 10.1101/cshperspect.a003228.

[11] V. Gensbittel, M. Kräter, S. Harlepp, I. Busnelli, J. Guck, J.G. Goetz, *Dev. Cell* **2021**, *56*(*2*): p. 164-179, DOI: 10.1016/j.devcel.2020.10.011.

[12] G. Runel, N. Lopez-Ramirez, J. Chlasta, I. Masse, *Cells* **2021**, *10*(*4*): p. 887.

[13] J.R. Staunton, B.L. Doss, S. Lindsay, R. Ros, *Sci. Rep.* **2016**, *6*(*1*): p. 19686, DOI: 10.1038/srep19686.

[14] M.F. Coughlin, D.R. Bielenberg, G. Lenormand, M. Marinkovic, C.G. Waghorne, B.R. Zetter, J.J. Fredberg, *Clin. Exp. Metastasis* **2013**, *30*(*3*): p. 237-50, DOI: 10.1007/s10585-012-9531-z.

[15] V. Swaminathan, K. Mythreye, E.T. O'Brien, A. Berchuck, G.C. Blobe, R. Superfine, *Cancer Res.* **2011**, *71*(*15*): p. 5075-80, DOI: 10.1158/0008-5472.can-11-0247.

[16] S.E. Cross, Y.-S. Jin, J. Tondre, R. Wong, J. Rao, J.K. Gimzewski, *Nanotechnology* **2008**, *19*(*38*): p. 384003, DOI: 10.1088/0957-4484/19/38/384003.

[17] M. Plodinec, M. Loparic, C.A. Monnier, E.C. Obermann, R. Zanetti-Dallenbach, P. Oertle, J.T. Hyotyla, U. Aebi, M. Bentires-Alj, R.Y.H. Lim, C.-A. Schoenenberger, *Nature Nanotechnology* **2012**, *7*(*11*): p. 757-765, DOI: 10.1038/nnano.2012.167.

[18] K. Unnikrishnan, L.V. Thomas, R.M. Ram Kumar, *Front. Oncol.* **2021**, *11*, DOI: 10.3389/fonc.2021.733652.

[19] J.-P. Kaiser, A. Reinmann, A. Bruinink, *Biomaterials* **2006**, *27*(*30*): p. 5230-5241, DOI: https://doi.org/10.1016/j.biomaterials.2006.06.002.

[20] A. Curtis, C. Wilkinson, *Biomaterials* **1997**, *18*(*24*): p. 1573-1583, DOI: https://doi.org/10.1016/S0142-9612(97)00144-0.

[21] R.J. Petrie, A.D. Doyle, K.M. Yamada, *Nature Reviews Molecular Cell Biology* **2009**, *10*(*8*): p. 538-549, DOI: 10.1038/nrm2729.

[22] S. Lenhert, M.-B. Meier, U. Meyer, L. Chi, H.P. Wiesmann, *Biomaterials* **2005**, *26*(*5*): p. 563-570, DOI: https://doi.org/10.1016/j.biomaterials.2004.02.068.

[23] J. Kim, Y. Cao, C. Eddy, Y. Deng, H. Levine, W.-J. Rappel, B. Sun, *Proc. Natl. Acad. Sci. U. S. A.* **2021**, *118*(*10*): p. e2024780118, DOI: 10.1073/pnas.2024780118.

[24] Kristin M. Riching, B.L. Cox, Max R. Salick, C. Pehlke, Andrew S. Riching, S.M. Ponik, Benjamin R. Bass, Wendy C. Crone, Y. Jiang, A.M. Weaver, Kevin W. Eliceiri, Patricia J. Keely, *Biophys. J.* **2014**, *107*(*11*): p. 2546-2558, DOI: https://doi.org/10.1016/j.bpj.2014.10.035.

[25] A. Ray, Z.M. Slama, R.K. Morford, S.A. Madden, P.P. Provenzano, *Biophys. J.* **2017**, *112*(*5*): p. 1023-1036, DOI: https://doi.org/10.1016/j.bpj.2017.01.007.

[26] W. Han, S. Chen, W. Yuan, Q. Fan, J. Tian, X. Wang, L. Chen, X. Zhang, W. Wei, R. Liu, J. Qu, Y. Jiao, R.H. Austin, L. Liu, *Proceedings of the National Academy of Sciences* **2016**, *113*(*40*): p. 11208-11213, DOI: doi:10.1073/pnas.1610347113.

[27] A. Ray, O. Lee, Z. Win, R.M. Edwards, P.W. Alford, D.-H. Kim, P.P. Provenzano, *Nat. Commun.* **2017**, *8*(*1*): p. 14923, DOI: 10.1038/ncomms14923.

[28] J.H. Taube, J.I. Herschkowitz, K. Komurov, A.Y. Zhou, S. Gupta, J. Yang, K. Hartwell, T.T. Onder, P.B. Gupta, K.W. Evans, B.G. Hollier, P.T. Ram, E.S. Lander, J.M. Rosen, R.A. Weinberg, S.A. Mani, *Proc. Natl. Acad. Sci. U. S. A.* **2010**, *107*(*35*): p. 15449-54, DOI: 10.1073/pnas.1004900107.

[29] M. Scimeca, C. Antonacci, D. Colombo, R. Bonfiglio, O.C. Buonomo, E. Bonanno, *Tumour Biol.* **2016**, *37*(*4*): p. 5427-35, DOI: 10.1007/s13277-015-4361-7.

[30] M.I. Kokkinos, R. Wafai, M.K. Wong, D.F. Newgreen, E.W. Thompson, M. Waltham, *Cells Tissues Organs* **2007**, *185*(*1-3*): p. 191-203, DOI: 10.1159/000101320.
[31] S. Agarwal, J.H. Wendorff, A. Greiner, *Polymer* **2008**, *49*(*26*): p. 5603-5621, DOI: https://doi.org/10.1016/j.polymer.2008.09.014.
[32] R. Toshkova, N. Manolova, E. Gardeva, M. Ignatova, L. Yossifova, I. Rashkov, M. Alexandrov, *Int. J. Pharm.* **2010**, *400*(*1-2*): p. 221-33, DOI: 10.1016/j.ijpharm.2010.08.039.
[33] P.O. Rujitanaroj, Y.C. Wang, J. Wang, S.Y. Chew, *Biomaterials* **2011**, *32*(*25*): p. 5915-23, DOI: 10.1016/j.biomaterials.2011.04.065.
[34] S.W. Han, W.G. Koh, *Anal. Chem.* **2016**, *88*(*12*): p. 6247-53, DOI: 10.1021/acs.analchem.5b04867.
[35] M.A. Ali, K. Mondal, Y. Jiao, S. Oren, Z. Xu, A. Sharma, L. Dong, *ACS Appl Mater Interfaces* **2016**, *8*(*32*): p. 20570-82, DOI: 10.1021/acsami.6b05648.
[36] Y. Zhao, Z. Fan, M. Shen, X. Shi, *Advanced Materials Interfaces* **2015**, *2*(*15*): p. 1500256, DOI: https://doi.org/10.1002/admi.201500256.
[37] F. Serio, A.F. da Cruz, A. Chandra, C. Nobile, G.R. Rossi, E. D'Amone, G. Gigli, L.L. del Mercato, C.C. de Oliveira, *Int. J. Biol. Macromol.* **2021**, *188*: p. 764-773, DOI: https://doi.org/10.1016/j.ijbiomac.2021.08.069.
[38] Y.J. Kim, H.I. Bae, O.K. Kwon, M.S. Choi, *Int. J. Biol. Macromol.* **2009**, *45*(*1*): p. 65-71, DOI: 10.1016/j.ijbiomac.2009.04.003.
[39] S. Chen, S.K. Boda, S.K. Batra, X. Li, J. Xie, *Advanced Healthcare Materials* **2018**, *7*(*6*): p. 1701024, DOI: https://doi.org/10.1002/adhm.201701024.
[40] L.M. Isert, A.; Loiudice, G.; Oliva, A.; Roidl, A.; Merkel, O., *Preprints 2023* **2023**, *2023030147*, DOI: https://doi.org/10.20944/preprints202303.0147.v1.
[41] J. Schindelin, I. Arganda-Carreras, E. Frise, V. Kaynig, M. Longair, T. Pietzsch, S. Preibisch, C. Rueden, S. Saalfeld, B. Schmid, J.-Y. Tinevez, D.J. White, V. Hartenstein, K. Eliceiri, P. Tomancak, A. Cardona, *Nat. Methods* **2012**, *9*(*7*): p. 676-682, DOI: 10.1038/nmeth.2019.
[42] J.-Y. Tinevez, N. Perry, J. Schindelin, G.M. Hoopes, G.D. Reynolds, E. Laplantine, S.Y. Bednarek, S.L. Shorte, K.W. Eliceiri, *Methods* **2017**, *115*: p. 80-90, DOI: https://doi.org/10.1016/j.ymeth.2016.09.016.
[43] B.A. Smith, B. Tolloczko, J.G. Martin, P. Grütter, *Biophysical journal* **2005**, *88*(*4*): p. 2994-3007.
[44] R. Mahaffy, S. Park, E. Gerde, J. Käs, C.-K. Shih, *Biophysical journal* **2004**, *86*(*3*): p. 1777-1793.
[45] Q. Li, G.Y. Lee, C.N. Ong, C.T. Lim, *Biochemical and biophysical research communications* **2008**, *374*(*4*): p. 609-613.
[46] H.-J. Butt, B. Cappella, M. Kappl, *Surface science reports* **2005**, *59*(*1-6*): p. 1-152.
[47] J. Xue, T. Wu, Y. Dai, Y. Xia, *Chem. Rev.* **2019**, *119*(*8*): p. 5298-5415, DOI: 10.1021/acs.chemrev.8b00593.
[48] A. Greiner, J.H. Wendorff, *Angewandte Chemie International Edition* **2007**, *46*(*30*): p. 5670-5703, DOI: https://doi.org/10.1002/anie.200604646.
[49] J. Zhang, D. Zhou, L. Zhang, Q. Lin, W. Ren, J. Zhang, L. Nadeem, G. Xu, *Dose Response* **2017**, *15*(*4*): p. 1559325817744450, DOI: 10.1177/1559325817744450.
[50] Y. Wang, J. Shi, K. Chai, X. Ying, B.P. Zhou, *Curr. Cancer Drug Targets* **2013**, *13*(*9*): p. 963-972, DOI: 10.2174/15680096113136660102.
[51] S. Chen, J. Chen, X. Hua, Y. Sun, R. Cui, J. Sha, X. Zhu, *Biomed. Pharmacother.* **2020**, *127*: p. 110069, DOI: 10.1016/j.biopha.2020.110069.
[52] S.N. Rubtsova, I.Y. Zhitnyak, **2021**, *22*(*4*), DOI: 10.3390/ijms22041821.
[53] T. Fischer, A. Hayn, C.T. Mierke, *Front. Cell Dev. Biol.* **2020**, *8*(*393*), DOI: 10.3389/fcell.2020.00393.
[54] P. Friedl, K. Wolf, J. Lammerding, *Curr. Opin. Cell Biol.* **2011**, *23*(*1*): p. 55-64, DOI: 10.1016/j.ceb.2010.10.015.

[55] E. Olsson, G. Honeth, P.-O. Bendahl, L.H. Saal, S. Gruvberger-Saal, M. Ringnér, J. Vallon-Christersson, G. Jönsson, K. Holm, K. Lövgren, M. Fernö, D. Grabau, Å. Borg, C. Hegardt*, BMC Cancer* **2011**, *11*(*1*): p. 418, DOI: 10.1186/1471-2407-11-418.

[56] J. Cursons, K.-J. Leuchowius, M. Waltham, E. Tomaskovic-Crook, M. Foroutan, C.P. Bracken, A. Redfern, E.J. Crampin, I. Street, M.J. Davis, E.W. Thompson*, Cell Communication and Signaling* **2015**, *13*(*1*): p. 26, DOI: 10.1186/s12964-015-0106-x.

[57] Q. Luo, D. Kuang, B. Zhang, G. Song*, Biochimica et Biophysica Acta (BBA) - General Subjects* **2016**, *1860*(*9*): p. 1953-1960, DOI: https://doi.org/10.1016/j.bbagen.2016.06.010.

[58] L. Sirghi, *Atomic Force Microscopy indentation of living cells*, *Vol. 1*. **2010**.

[59] P. Friedl, K. Wolf, J. Lammerding*, Curr. Opin. Cell Biol.* **2011**, *23*(*1*): p. 55-64, DOI: 10.1016/j.ceb.2010.10.015.

[60] J.S. Lee, C.M. Hale, P. Panorchan, S.B. Khatau, J.P. George, Y. Tseng, C.L. Stewart, D. Hodzic, D. Wirtz*, Biophys. J.* **2007**, *93*(*7*): p. 2542-52, DOI: 10.1529/biophysj.106.102426.

[61] C. Bodelon, M. Mullooly, R.M. Pfeiffer, S. Fan, M. Abubakar, P. Lenz, P.M. Vacek, D.L. Weaver, S.D. Herschorn, J.M. Johnson, B.L. Sprague, S. Hewitt, J. Shepherd, S. Malkov, P.J. Keely, K.W. Eliceiri, M.E. Sherman, M.W. Conklin, G.L. Gierach*, Breast Cancer Res.* **2021**, *23*(*1*): p. 105, DOI: 10.1186/s13058-021-01482-z.

[62] S.M. Kakkad, M. Solaiyappan, P. Argani, S. Sukumar, L.K. Jacobs, D. Leibfritz, Z.M. Bhujwalla, K. Glunde*, J Biomed Opt* **2012**, *17*(*11*): p. 116017-116017, DOI: 10.1117/1.JBO.17.11.116017.

[63] N. Ninan, B. Joseph, R.M. Visalakshan, R. Bright, C. Denoual, P. Zilm, Y.B. Dalvi, P.V. Priya, A. Mathew, Y. Grohens, N. Kalarikkal, K. Vasilev, S. Thomas*, Materials Advances* **2021**, *2*(*20*): p. 6620-6630, DOI: 10.1039/D1MA00444A.

[64] H. Ehtesabi, F. Massah*, Materials Today Sustainability* **2021**, *13*: p. 100075, DOI: https://doi.org/10.1016/j.mtsust.2021.100075.

[65] Y. Zhu, C. Gao, J. Shen*, Biomaterials* **2002**, *23*(*24*): p. 4889-4895, DOI: https://doi.org/10.1016/S0142-9612(02)00247-8.

[66] S. Miroshnichenko, V. Timofeeva, E. Permyakova, S. Ershov, P. Kiryukhantsev-Korneev, E. Dvořaková, D.V. Shtansky, L. Zajíčková, A. Solovieva, A. Manakhov*, Nanomaterials* **2019**, *9*(*4*): p. 637.

[67] Y.K. Girard, C. Wang, S. Ravi, M.C. Howell, J. Mallela, M. Alibrahim, R. Green, G. Hellermann, S.S. Mohapatra, S. Mohapatra*, PLoS One* **2013**, *8*(*10*): p. e75345, DOI: 10.1371/journal.pone.0075345.

[68] S. Saha, X. Duan, L. Wu, P.-K. Lo, H. Chen, Q. Wang*, Langmuir* **2012**, *28*(*4*): p. 2028-2034, DOI: 10.1021/la203846w.

[69] A. Ravikrishnan, T. Ozdemir, M. Bah, K.A. Baskerville, S.I. Shah, A.K. Rajasekaran, X. Jia*, ACS Applied Materials & Interfaces* **2016**, *8*(*28*): p. 17915-17926, DOI: 10.1021/acsami.6b05646.

[70] A. Jana, I. Nookaew, J. Singh, B. Behkam, A.T. Franco, A.S. Nain*, FASEB J.* **2019**, *33*(*10*): p. 10618-10632, DOI: 10.1096/fj.201900131R.

[71] J. Park, D.-H. Kim, S.R. Shah, H.-N. Kim, Kshitiz, P. Kim, A. Quiñones-Hinojosa, A. Levchenko*, Nat. Commun.* **2019**, *10*(*1*): p. 2797, DOI: 10.1038/s41467-019-10729-5.

[72] C. Leclech, C. Villard*, Frontiers in Bioengineering and Biotechnology* **2020**, *8*, DOI: 10.3389/fbioe.2020.551505.

[73] J. Mai, C. Sun, S. Li, X. Zhang*, Biomed. Microdevices* **2007**, *9*(*4*): p. 523-531, DOI: 10.1007/s10544-007-9060-8.

[74] G.F. Le Bras, K.J. Taubenslag, C.D. Andl*, Cell adhesion & migration* **2012**, *6*(*4*): p. 365-73, DOI: 10.4161/cam.21326.

[75] M.G. Mendez, S.-I. Kojima, R.D. Goldman*, The FASEB Journal* **2010**, *24*(*6*): p. 1838-1851, DOI: https://doi.org/10.1096/fj.09-151639.

[76] C.-Y. Liu, H.-H. Lin, M.-J. Tang, Y.-K. Wang*, Oncotarget* **2015**, *6*(*18*): p. 15966-15983.

[77] S.E. Leggett, A.M. Hruska, M. Guo, I.Y. Wong*, Cell Communication and Signaling* **2021**, *19*(*1*): p. 32, DOI: 10.1186/s12964-021-00713-2.

[78] K. Wagh, M. Ishikawa, D.A. Garcia, D.A. Stavreva, A. Upadhyaya, G.L. Hager, *Trends Cell Biol.* **2021**, *31*(*6*): p. 457-472, DOI: https://doi.org/10.1016/j.tcb.2021.02.008.

[79] W. Liu, A. Padhi, X. Zhang, J. Narendran, M.A. Anastasio, A.S. Nain, J. Irudayaraj, *ACS nano* **2022**, *16*(*7*): p. 10754-10767, DOI: 10.1021/acsnano.2c02660.

[80] H. Li, X. Chen, Y. Gao, J. Wu, F. Zeng, F. Song, *Cell. Signal.* **2015**, *27*(*1*): p. 82-89, DOI: https://doi.org/10.1016/j.cellsig.2014.09.018.

[81] M. Huo, Y. Zhao, X. Liu, Y. Gao, D. Zhang, M. Chang, M. Liu, N. Xu, H. Zhu, *J. Cancer* **2020**, *11*(*15*): p. 4464-4473, DOI: 10.7150/jca.44234.

[82] W. Shi, Z. Chen, L. Li, H. Liu, R. Zhang, Q. Cheng, D. Xu, L. Wu, *J. Cancer* **2019**, *10*(*9*): p. 2035-2046, DOI: 10.7150/jca.29421.

[83] M.E. Manwaring, J.F. Walsh, P.A. Tresco, *Biomaterials* **2004**, *25*(*17*): p. 3631-3638, DOI: https://doi.org/10.1016/j.biomaterials.2003.10.043.

[84] Z. Gan, L. Ding, Christoph J. Burckhardt, J. Lowery, A. Zaritsky, K. Sitterley, A. Mota, N. Costigliola, Colby G. Starker, Daniel F. Voytas, J. Tytell, Robert D. Goldman, G. Danuser, *Cell Syst.* **2016**, *3*(*3*): p. 252-263.e8, DOI: https://doi.org/10.1016/j.cels.2016.08.007.

[85] M. Pickl, C.H. Ries, *Oncogene* **2009**, *28*(*3*): p. 461-468, DOI: 10.1038/onc.2008.394.

[86] C. Jensen, Y. Teng, *Front. Mol. Biosci.* **2020**, *7*, DOI: 10.3389/fmolb.2020.00033.

[87] C. Alibert, B. Goud, J.-B. Manneville, *Biol. Cell* **2017**, *109*(*5*): p. 167-189, DOI: https://doi.org/10.1111/boc.201600078.

[88] E. Gladilin, S. Ohse, M. Boerries, H. Busch, C. Xu, M. Schneider, M. Meister, R. Eils, *Sci. Rep.* **2019**, *9*(*1*): p. 7667, DOI: 10.1038/s41598-019-43409-x.

[89] T.H. Wu, Y.W. Chiou, W.T. Chiu, M.J. Tang, C.H. Chen, M.L. Yeh, *Biomed. Microdevices* **2014**, *16*(*3*): p. 465-78, DOI: 10.1007/s10544-014-9849-1.

[90] T. Watanabe, A. Takahashi, K. Suzuki, M. Kurusu-Kanno, K. Yamaguchi, H. Fujiki, M. Suganuma, *Int. J. Cancer* **2014**, *134*(*10*): p. 2373-2382, DOI: https://doi.org/10.1002/ijc.28582.

[91] L.D. Osborne, G.Z. Li, T. How, E.T. O'Brien, G.C. Blobe, R. Superfine, K. Mythreye, *Mol. Biol. Cell* **2014**, *25*(*22*): p. 3528-3540, DOI: 10.1091/mbc.e14-05-1015.

[92] Y.-Q. Chen, H.-Y. Lan, Y.-C. Wu, W.-H. Yang, A. Chiou, M.-H. Yang, *J. Cell. Mol. Med.* **2018**, *22*(*8*): p. 3837-3846, DOI: https://doi.org/10.1111/jcmm.13656.

[93] J. Guck, S. Schinkinger, B. Lincoln, F. Wottawah, S. Ebert, M. Romeyke, D. Lenz, H.M. Erickson, R. Ananthakrishnan, D. Mitchell, J. Käs, S. Ulvick, C. Bilby, *Biophys. J.* **2005**, *88*(*5*): p. 3689-3698, DOI: https://doi.org/10.1529/biophysj.104.045476.

[94] K. Bhadriraju, L.K. Hansen, *Exp. Cell Res.* **2002**, *278*(*1*): p. 92-100, DOI: https://doi.org/10.1006/excr.2002.5557.

[95] B. Doornaert, V. Leblond, E. Planus, S. Galiacy, V.M. Laurent, G. Gras, D. Isabey, C. Lafuma, *Exp. Cell Res.* **2003**, *287*(*2*): p. 199-208, DOI: https://doi.org/10.1016/S0014-4827(03)00114-9.

[96] S. Tavares, A.F. Vieira, A.V. Taubenberger, M. Araújo, N.P. Martins, C. Brás-Pereira, A. Polónia, M. Herbig, C. Barreto, O. Otto, J. Cardoso, J.B. Pereira-Leal, J. Guck, J. Paredes, F. Janody, *Nat. Commun.* **2017**, *8*(*1*): p. 15237, DOI: 10.1038/ncomms15237.

[97] Y. Messica, A. Laser-Azogui, T. Volberg, Y. Elisha, K. Lysakovskaia, R. Eils, E. Gladilin, B. Geiger, R. Beck, *Nano Lett.* **2017**, *17*(*11*): p. 6941-6948, DOI: 10.1021/acs.nanolett.7b03358.

[98] N. Costigliola, L. Ding, C.J. Burckhardt, S.J. Han, *Proc. Natl. Acad. Sci. U. S. A.* **2017**, *114*(*20*): p. 5195-5200, DOI: 10.1073/pnas.1614610114.

[99] L.S. Rathje, N. Nordgren, T. Pettersson, D. Rönnlund, J. Widengren, P. Aspenström, A.K. Gad, *Proc. Natl. Acad. Sci. U. S. A.* **2014**, *111*(*4*): p. 1515-20, DOI: 10.1073/pnas.1300238111.

[100] B. Ljepoja, C. Schreiber, F.A. Gegenfurtner, J. García-Roman, B. Köhler, S. Zahler, J.O. Rädler, E. Wagner, A. Roidl, *PLoS One* **2019**, *14*(*11*): p. e0224314, DOI: 10.1371/journal.pone.0224314.

[101] Z. Wang, F. Xia, M. Labib, **2020**, *14*(*5*): p. 5324-5336, DOI: 10.1021/acsnano.9b07350.

[102] Y. Yang, H. Zheng, Y. Zhan, S. Fan, *American journal of translational research* **2019**, *11*(*9*): p. 5301-5312.
[103] V. Graziani, I. Rodriguez-Hernandez, O. Maiques, V. Sanz-Moreno, *Trends Cell Biol.* **2022**, *32*(*3*): p. 228-242, DOI: 10.1016/j.tcb.2021.10.004.
[104] A. Guzman, R.C. Avard, **2020**, *133*(*8*), DOI: 10.1242/jcs.236778.
[105] Y.-J. Liu, M. Le Berre, F. Lautenschlaeger, P. Maiuri, A. Callan-Jones, M. Heuzé, T. Takaki, R. Voituriez, M. Piel, *Cell* **2015**, *160*(*4*): p. 659-672, DOI: https://doi.org/10.1016/j.cell.2015.01.007.
[106] S. Lehmann, V. Te Boekhorst, J. Odenthal, R. Bianchi, S. van Helvert, K. Ikenberg, O. Ilina, S. Stoma, J. Xandry, L. Jiang, R. Grenman, M. Rudin, P. Friedl, *Curr. Biol.* **2017**, *27*(*3*): p. 392-400, DOI: 10.1016/j.cub.2016.11.057.
[107] A. Emad, T. Ray, T.W. Jensen, M. Parat, R. Natrajan, S. Sinha, P.S. Ray, *Breast Cancer Res.* **2020**, *22*(*1*): p. 74, DOI: 10.1186/s13058-020-01304-8.
[108] K. Talkenberger, E.A. Cavalcanti-Adam, A. Voss-Böhme, A. Deutsch, *Sci. Rep.* **2017**, *7*(*1*): p. 9237, DOI: 10.1038/s41598-017-09300-3.
[109] E.A. Brett, M.A. Sauter, H.-G. Machens, D. Duscher, *Cancer & Metabolism* **2020**, *8*(*1*): p. 14, DOI: 10.1186/s40170-020-00221-w.
[110] G. Xi, L. Qiu, S. Xu, W. Guo, F. Fu, D. Kang, L. Zheng, J. He, Q. Zhang, L. Li, C. Wang, J. Chen, *BMC Med.* **2021**, *19*(*1*): p. 273, DOI: 10.1186/s12916-021-02146-7.
[111] E.L. Baker, J. Lu, D. Yu, R.T. Bonnecaze, M.H. Zaman, *Biophys. J.* **2010**, *99*(*7*): p. 2048-2057, DOI: https://doi.org/10.1016/j.bpj.2010.07.051.
[112] K.R. Levental, H. Yu, L. Kass, J.N. Lakins, M. Egeblad, J.T. Erler, S.F.T. Fong, K. Csiszar, A. Giaccia, W. Weninger, M. Yamauchi, D.L. Gasser, V.M. Weaver, *Cell* **2009**, *139*(*5*): p. 891-906, DOI: 10.1016/j.cell.2009.10.027.
[113] R.S. Stowers, A. Shcherbina, J. Israeli, J.J. Gruber, J. Chang, S. Nam, A. Rabiee, M.N. Teruel, M.P. Snyder, A. Kundaje, O. Chaudhuri, *Nature Biomedical Engineering* **2019**, *3*(*12*): p. 1009-1019, DOI: 10.1038/s41551-019-0420-5.
[114] A.A. Narkhede, J.H. Crenshaw, R.M. Manning, S.S. Rao, *Journal of Biomedical Materials Research Part A* **2018**, *106*(*7*): p. 1832-1841, DOI: https://doi.org/10.1002/jbm.a.36379.
[115] M. Kalli, T. Stylianopoulos, *Front. Oncol.* **2018**, *8*, DOI: 10.3389/fonc.2018.00055.
[116] S.C. Wei, L. Fattet, J.H. Tsai, Y. Guo, V.H. Pai, H.E. Majeski, A.C. Chen, R.L. Sah, S.S. Taylor, A.J. Engler, J. Yang, *Nat. Cell Biol.* **2015**, *17*(*5*): p. 678-88, DOI: 10.1038/ncb3157.
[117] S. Cai, H. Xu, Q. Jiang, Y. Yang, *Langmuir* **2013**, *29*(*7*): p. 2311-8, DOI: 10.1021/la304414j.
[118] A.A. Bulysheva, G.L. Bowlin, S.P. Petrova, W.A. Yeudall, *Biomedical Materials* **2013**, *8*(*5*): p. 055009, DOI: 10.1088/1748-6041/8/5/055009.
[119] M. Rabionet, M. Yeste, T. Puig, J. Ciurana, *Polymers (Basel)* **2017**, *9*(*8*): p. 328, DOI: 10.3390/polym9080328.
[120] S. Jonckheere, J. Adams, D. De Groote, K. Campbell, G. Berx, S. Goossens, *Cells Tissues Organs* **2022**, *211*(*2*): p. 157-182, DOI: 10.1159/000512218.
[121] B. Du, J.S. Shim, *Molecules (Basel, Switzerland)* **2016**, *21*(*7*), DOI: 10.3390/molecules21070965.
[122] S.D. Soysal, A. Tzankov, S.E. Muenst, *Pathobiology* **2015**, *82*(*3-4*): p. 142-152, DOI: 10.1159/000430499.
[123] J. Tchou, J. Conejo-Garcia, *Adv. Pharmacol.* **2012**, *65*: p. 45-61, DOI: 10.1016/b978-0-12-397927-8.00003-8.

7. Supplementary data

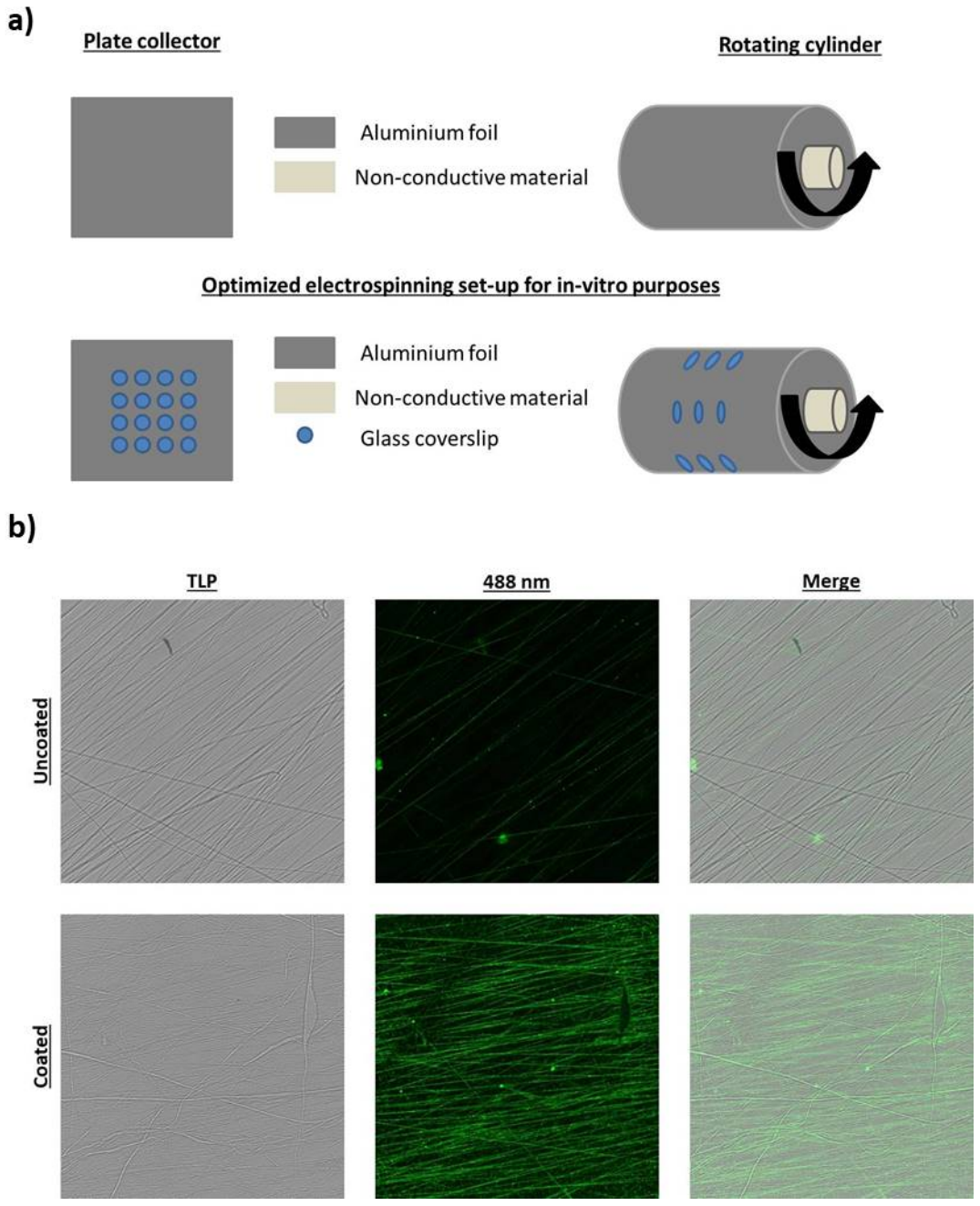

Supplementary Figure S1. *Schematic illustration of electrospinning set-ups: Plate collector and rotating cylinder were chosen to produced unaligned and aligned fibers, respectively (**a**). Confocal images of non- and collagen I-coated fiber scaffolds. Collagen was detected at 488 nm after incubation with primary and secondary antibody pair (**b**).*

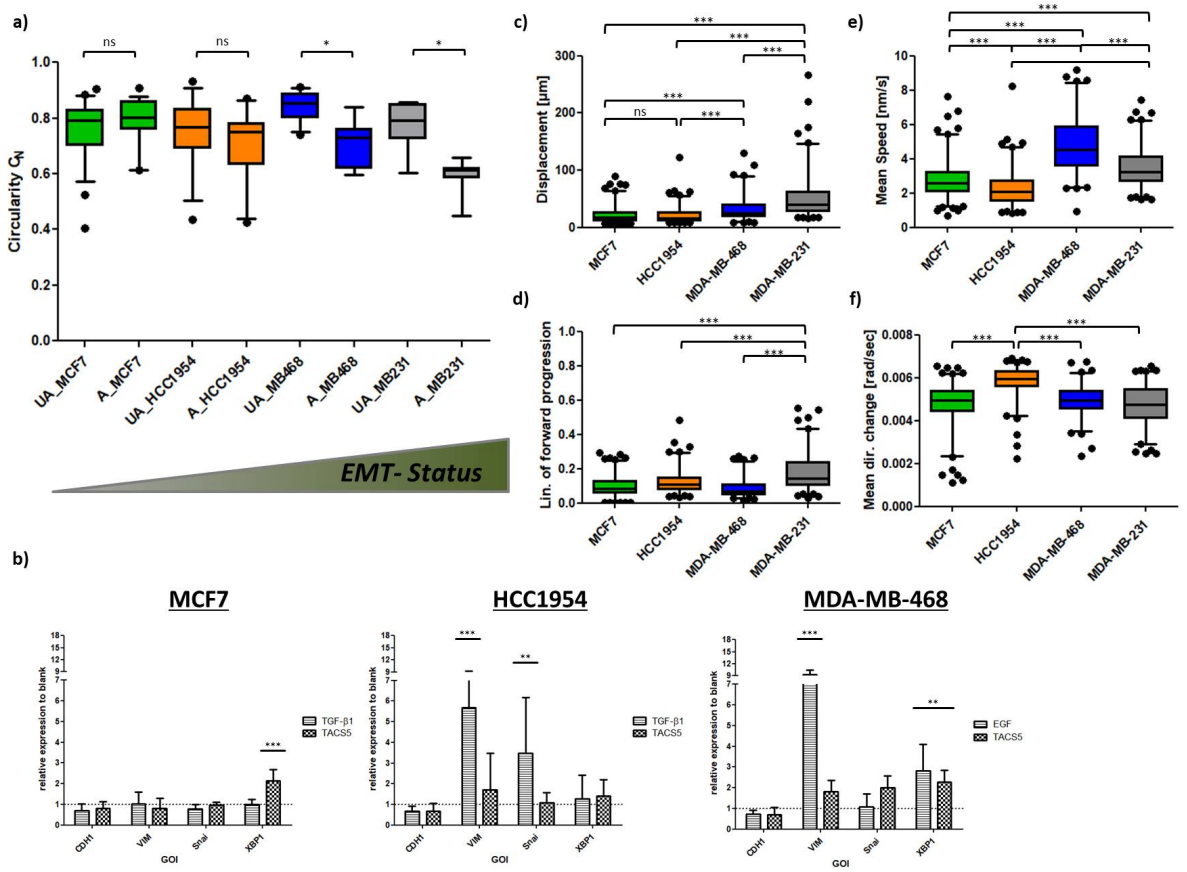

Supplementary Figure S2. *Differences in nuclear circularity (C_N) between TACS6- (UA = unaligned) and TACS5-like (A =aligned) scaffold among the 4 breast cancer cell lines (**a**). mRNA levels of EMT-markers after GF-stimulation or growth on TACS5 scaffolds (**b**). Trajectory analysis of cellular migration on TACS5 in vitro model (**c-f**). Variables are shown as Whiskers plot (5-95 percentiles)*

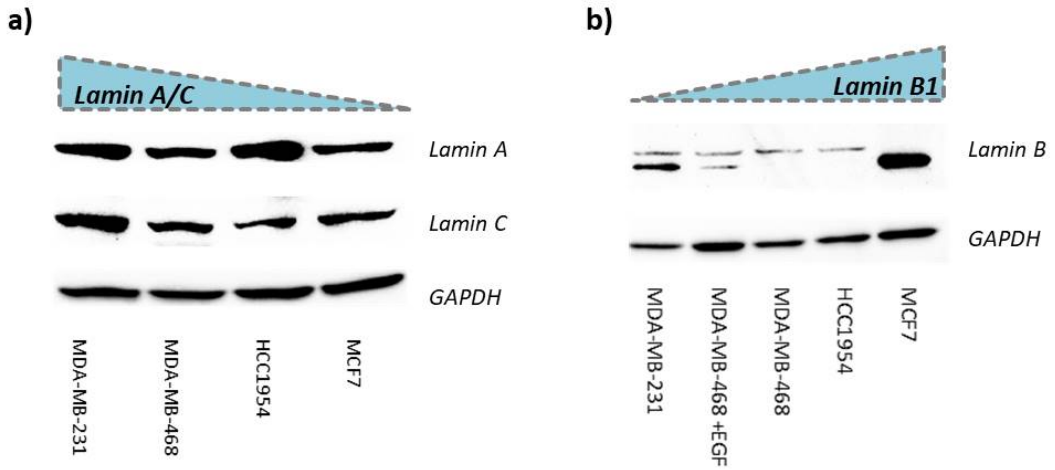

Supplementary Figure S3. *Lamin A/C and Lamin B protein levels of various breast cancer cell lines*

Chapter V

Upholding hyaluronic acid's multi-functionality for nucleic acid drug delivery to target EMT in breast cancer

Parts of this chapter are going to be submitted as scientific article:

Lorenz Isert, Irene Gialdini, Thi My Hanh Ngo, Gabriele Loiudice, Don C. Lamb and Olivia M. Merkel; "Upholding hyaluronic acid's multi-functionality for nucleic acid drug delivery to target EMT in breast cancer"

1. Introduction

Targeted drug delivery employing nanoparticulate formulations such as liposomes (e.g. Doxil®), lipid-based nanoparticles (LNPs), polymer-drug conjugates, polymeric nanoparticles (micelles, polyplexes), or inorganic nanoparticles exploits two major circumstances for successful cancer treatment. [1] First, passive targeting on the basis of the enhanced permeability and retention (EPR) effect, arising from the leaky endothelium and poor lymphatic clearance within the tumor tissue, enables nanomedicine to accumulate at the tumor site.[2] Second, ligand-mediated targeting via ligand immobilization on the particle surface provides nano-formulations with cell-receptor selectivity. Due to cancer type-dependent overexpression of surface proteins, unique nanoparticle-cancer cell interaction profiles can be specifically established by choosing the specific targeting moiety for the respective cancer disease.[2, 3] However, the mode of ligand presentation (density, coupling chemistry vs. non-covalent modification), ligand-receptor affinity and the absolute receptor quantity and recycling rates are crucial factors for efficient receptor-mediated endocytosis necessitating careful nanocarrier design.[3-7] Importantly, the physico-chemical properties of a drug delivery system, such as hydrophobicity, size and surface charge, are defined by the characteristics of the carrier and its cargo. Additionally, they are significantly changed by surface modifications introduced for receptor targeting strategies. In its totality, this "synthetic identity" determines the "biological identity" of nanoparticles which can be understood as their ultimate physico-chemical features acquired *in vivo* as a result of interaction/opsonization with biomolecules. In other words, the particle's fate and the therapeutic efficacy strongly rely on the quantity and type of biomolecules bound to the nanocarrier surface as they pilot systemic clearance, on/off-tissue accumulation and receptor-ligand interaction. All these factors strongly depend on the chosen carrier design.[8]

The naturally occurring polysaccharide and glycosaminoglycan hyaluronic acid (HA) offers a multitude of features that are desirable and required for the clinical use of nanomedicines, such as its biocompatibility, biodegradability and biosafety profile. In addition, the endogenously expressed hyaladherins, *i.e.* hyaluronan-binding proteins (CD44, RHAMM, HARE, LYVE-1), allow HA-containing drug delivery systems to be internalized via receptor-mediated endocytosis [9, 10]. Whereas HARE and LYVE-1 receptors are considered to be detrimental for the clinical implementation of HA-functionalized drugs as they promote hepatic and lymphatic clearance, respectively [9, 11], the CD44 receptor is a promising candidate due to cancer-specific overexpression in many types of tissues [12-14]. The low molecular weight standard isoform of CD44 (~85 kD, CD44s) is ubiquitously expressed but often correlates in expression with cancer conferring stem-like properties.[15] However, there are 9 higher molecular weight variant isoforms (CD44v), which contain a variable number of exon insertions (v1–v10) coding for peptides located in the juxta membrane ectodomain.[16] Notably, the expression of the variant CD44v isoforms is mainly restricted to cancer cells [17, 18] which was recently exploited for the design of novel anti-cancer therapies.[16,

18, 19] However, recent data on the uptake kinetics of fluorescently labeled HA indicated that endocytosis of cancer cell lines expressing the CD44v isoforms is inferior to CD44s-mediated endocytosis.[20] As was postulated by de la Rosa et al., the increased size of isoform variants may lead to steric hindrance during the engagement of particles with the cell surface.[11] Thus, even though functionality of HA-based targeted drug delivery was well studied in the past, the significance of CD44v isoforms for nanoparticulate therapeutics has been mostly neglected so far. It is also plausible that the increased size of the isoform variants facilitates receptor-mediated endocytosis as the HA-binding domain is exposed at a greater distance from the cell surface.[11] Since literature reports support both hypotheses, it is important to elucidate potentially distinct nanoparticle uptake mechanism and kinetics between CD44s and CD44v isoforms.

The Epithelial-to-Mesenchymal Transition (EMT) is a reversible, dynamic differentiation process that cancer cells exploit to disseminate from the primary tumor site and to invade into and through the stromal compartment. EMT commonly results in systemically circulating tumor cells and metastasis in a distant organ or tissue.[21, 22] A hallmark of the transition comprises the downregulation of E-cadherin (CDH1) [23], the responsible surface protein establishing adherens junctions that define the strengths of cell-cell contacts [24, 25]. In breast cancer, disease malignancy correlates with EMT which in turn correlates with overexpression of CD44 [26-29]. More precisely, it was found that low-grade (luminal) epithelial breast cancer cell lines showed low expression levels of both CD44s and CD44v isoform. In less differentiated cancer phenotypes, certain CD44v isoforms were predominantly overexpressed whereas cells displayed only marginal expression levels of CD44s standard isoform. In contrast, strongly malignant mesenchymal, basal-like phenotypes only expressed high levels of CD44s receptor underlining its importance for the course of EMT.[28, 30] Since the phenomenon of EMT is thought to be spatially restricted to the tumor-stromal boundary [31, 32] , EMT-specific cell surface markers such as CD44s/v hold great promise for targeted drug delivery, in particular for nanomedicines which are prone to interact with surface receptors at the tumor margin but do not passively penetrate the tumor.[33, 34] Thus, the heterogeneity of CD44 isotypes that occurs at different EMT-stages may ultimately govern the therapeutic efficiency of HA-presenting nanocarriers. Combining the CD44-targeting approach with the silencing of biomolecules responsible for EMT could be a powerful strategy to prevent cancer progression or even metastasis whilst avoiding off-target cytotoxicity. Finally, targeting cancer cells via the CD44 receptor offers a possible therapeutic strategy to tackle the otherwise "undruggable" nature of triple-negative breast cancer which is frequently linked to an EMT-positive phenotype.[35]

In this study, gold standard branched, high-molecular weight poly(ethylenimine) (PEI) was used as polymer material to evaluate HA-mediated features for drug delivery in the context of breast cancer and EMT. The polycation PEI efficiently condenses negative siRNA molecules to form polyplexes (Px) that bear a cationic zeta potential. Most carboxyl-groups within the HA polymer are deprotonated

at physiological pH [36] allowing for electrostatic adsorption on positively charged Px (HAPx). Here, three distinct strategies for how to non-covalently immobilize HA on/in polyplexes are presented, and their overall impact on the resulting physico-chemical properties and cellular *in vitro* performance are discussed.

2. ***Material & Methods***

1. Materials and cell culture:

Branched Poly(ethyleneimine) (PEI) M_n = 10 kDa (408727), HEPES (4-(2-hydroxyethyl)–1-piperazineethanesulfonic acid), heparin sodium salt, formaldehyde solution (≥ 36%), , 4′,6–diamidino–2-phenylindole dihydrochloride (DAPI), FluorSave reagent, DNase I (recombinant, RNase-free), cOmplete™, EDTA-free Protease Inhibitor Cocktail, Phosphatase Inhibitor Cocktail 2, RIPA buffer, Tris buffered saline powder, Ponceau S Stain, Tween 20, Amersham™ Protran® Western-Blotting-Membrane (nitrocellulose) and for cell culture Eagle's Minimum Essential Medium (EMEM), RPMI-1640 Medium, Dulbecco's modified eagle's medium (DMEM), fetal bovine serum (FBS), Penicillin-Streptomycin (Pen/Strep) solution, Dulbecco's Phosphate Buffered Saline (PBS), trypsin-EDTA solution 0.05% and 0.25%, 200 mM of L-glutamine solution, and dimethyl sulfoxide (DMSO) were obtained from Sigma-Aldrich (Taufkirchen, Germany). GAPDH Monoclonal Antibody (ZG003), Green Pierce™ BCA Protein Assay Kit, , Lipofectamine2000, Novex™ 10% Tris-Glycine Mini Gels (WedgeWell™ format, 15-well), Novex™ Value™ 4-20% Tris-Glycine Mini Gels (1.0 mm, 10-well), Page Ruler™ Plus Prestained Protein Ladder 10 to 250 kDa, Tris Glycin transfer buffer, SuperSignal™ West Pico PLUS Chemiluminescent Substrate, Rhodamine Phalloidin, High capacity cDNA synthesis kit, Power SYBR™ Green PCR Master Mix, PureLink™ RNA Mini Kit and for cell culture Leibovitz's L-15 Medium and MEM Non-Essential Amino Acids Solution (100X) were purchased from Thermo Fisher Scientific (Darmstadt, Germany). Hs_GAPDH_1_SG QuantiTect Primer Assay (QT00079247) and Hs_XBP1_1_SG QuantiTect Primer Assay (QT00068383) were obtained from Qiagen (Hilden, Germany). Rotiphorese 10x SDS Page, Rotilabo®-Blotting Papers and Methanol (blotting grade) were purchased from Carl Roth (Karlsruhe, Germany). rh-TGF-β 1 (Transforming Growth Factor beta 1) and rh-EGF (Epidermal Growth Factor) were bought from ImmunoTools (Friesoythe, Germany). Laemmli loading buffer (4x) and round glass coverslips (Ø 13mm) were purchased from VWR (Allison Park, PA, USA). Alexa Fluor® 488 anti-human CD44 antibody (103015) and Alexa Fluor® 488 isotype control antibody (400625) were purchased from Biolegend (San Diego, CA, USA). Human CD44s Pan Specific Antibody and Hyaluronan (HA) (Medium MW; 119 kDa; GLR004; LOT: 1580675) were bought from R&D Systems (Minneapolis, MN, USA). Amine-modified eGFP siRNA (5′-pACCCUGAAGUUCAUCUGCACCACcg, 3′-ACUGGGACUUCAAGUAGACGGGUGGC), and scrambled siRNA (5′-

pCGUUAAUCGCGUAUAAUACGCGUat, 3′-CAGCAAUUAGCGCAUAUUAUGCGCAUAp) were purchased from Integrated DNA Technologies (Leuven, Belgium). Anti-XBP1 antibody (ab37152) was purchased from Abcam (Cambridge, UK). HyClone trypan blue solution 0.4% in phosphate-buffered saline was obtained from FisherScientific (Hampton, NH, USA). E-cadherin Antibody (G-10) and mouse IgG kappa binding protein (m-IgGκ BP) conjugated to Horseradish Peroxidase (HRP) (sc-516102) were ordered from Santa Cruz Biotechnology (Dallas, Texas, USA). XBP1 siRNA (5'-CACCCUGAAUUCAUUGUCU[dT][dT], 3-AGACAAUGAAUUCAGGGUG[dT][dT]) was obtained from Qiagen (Hilden, Germany) based on a publication by Chen et al..[37]

MCF7 luminal A breast cancer cells were cultured in EMEM supplemented with 10% FBS, 1x Pen/Strep, 1x MEM Non-Essential Amino Acids Solution and 2 mM glutamine. The HER2-positive breast cancer cell line HCC1954 was grown in RPMI-1640 Medium supplemented with 10% FBS and 1x Pen/Strep. MDA-MB-231 triple negative breast cancer (TNBC) cells were cultured in high glucose (4500 mg/L) DMEM. 10% FBS, 1x Pen/Strep and 2 mM glutamine were added to the medium. The latter three cell lines were cultured in a humidified atmosphere with 5% CO_2 at 37°C. The second TNBC cell line MDA-MB-468 was grown in L-15 Medium supplemented with 20% FBS, 2 mM glutamine and 1x Pen/Strep in a humidified incubator with 0% CO_2 at 37°C.

2. Preparation and characterization of polyplexes

2.2.1 Hyaluronic acid-coating of polyplexes

Three different approaches were evaluated to nanoprecipitate/complexate anionic hyaluronic acid (HA) on the surface of positively charged PEI polyplexes. The indicated HA:PEI ratios (1:10, 1:5, 1:2.5, 1:1, 2.5:1, 5:1, and 10:1) depict weight ratios. The implemented amounts of PEI and siRNA were based on optimized standard PEI polyplexes at an N/P-ratio (Nitrogen-to-phosphate ratio) of 5 with 100 pmol of siRNA and were kept the same throughout the different procedures. siRNA and HA stock solutions were dissolved in RNAase-free water whereas PEI was dissolved in sterile-filtered 10 mM HEPES at pH 7.4. Subsequent dilutions were made in sterile-filtered 10 mM HEPES at pH 7.4:

(1) "2-step coating": In the first step, PEI-siRNA core polyplex-intermediates were produced. Therefore, the PEI solution was mixed with 100 pmol of siRNA (volumes 1:1) by gently pipetting up and down to form PEI polyplexes (Px) during a 20 min incubation step. In order to obtain HA-coated Px (HAPx) the Px containing solution was transferred into another Eppendorf tube containing HA solutions (V(HA) = 15% of Px volume) of varying concentrations, and mixtures were incubated for another 40 mins.
(2) "Inverse 2-step coating": In the first step, PEI-HA core polyplexes were produced. Therefore, the PEI solution was mixed with varying amounts of HA (volumes 1:1) by gently pipetting up and down. After 20 min of incubation, Px of different HA:PEI-ratios were transferred into Eppendorf tubes containing 100 pmol of siRNA (V(siRNA) = 15% of Px volume) which were incubated for another 40 min allowing for maximum complexation.

(3) "1-step-coating": The PEI solution and the anionic components (HA and siRNA) were mixed in one single step. Therefore, 100 pmol of siRNA was combined with varying amounts of HA (1:10 to 10:1) in the same tube. Subsequently, the HA/siRNA-blend was mixed with the PEI solution (1:1) to form HAPx during 60 min of incubation.

The final volume of colloidal (HA)Px solution was kept constant for all three procedures.

2.2.2 Dynamic Light Scattering (DLS) and Laser Doppler Anemometry (LDA)

The Zetasizer Nano ZS (Malvern Instruments, Malvern, UK) was used to measure hydrodynamic size (*z*-average), polydispersity index (PDI) and ζ-potential of the aforementioned polyplexes. In order to assess particle sizes and PDIs, 100 µL of freshly prepared (HA)Px were added to a disposable cuvette and measured by DLS at 173° backscatter running with three automatic scan cycles. For the measurement of ζ-potential, the 100 µL of polyplexes were recovered and carefully re-dispersed in 600 µL of 10 mM HEPES pH 7.4. The 7x dilution was filled into a Zeta Cell (Zeta Sizer series, Malvern, UK) and measured by LDA. Results are shown as mean ± SD (n=3).

For the long-term storage study, polyplexes were prepared in 10 mM HEPES pH 7.4 as described above using the 3 coating methods, aliquoted and stored at room temperature (RT) under exclusion of light. DLS measurements were performed at 0h, 24h, 48h, 72h, 96h, 168h (1 week), 336h (2 weeks), 672h (4 weeks) and 1008h (6 weeks), respectively.

2.2.3 SYBR Gold assay – Encapsulation of siRNA

To completely encapsulate siRNA within polyplexes, generally an excess of PEI (here: N/P-ratio of 5) is used. However, co-encapsulation of HA and siRNA within one particle may electrostatically and sterically impair siRNA encapsulation. To clarify whether siRNA is released from the nanoparticles during the coating process the SYBR Gold Assay was used. HAPx of different HA:PEI ratios (w/w) were prepared in HEPES 10 mM (pH 7.4). Subsequently, 100 µL of each polyplex solution was distributed in a white FluoroNunc 96-well plate (FisherScientific, Hampton, NH, USA). A 4X SYBR Gold solution (30 µL) was added to each well, and the plate was incubated for 10 min in the dark. A fluorescence plate reader (Tecan SPARK, Tecan, Männedorf, Switzerland) was utilized to determine the fluorescence intensity of the different ratios (λ_{Ex} = 492 nm; λ_{Em} = 555 nm). Free siRNA served as 100% reference value. Measurements were carried out in triplicates, and the results were shown as mean value ± SD (n=2).

2.2.4 Heparin/SYBR Gold competition assay –Polyplex stability over polyanions

Polyanionic species such as proteins, glycosaminoglycans in serum compete with siRNA for the cationic amine groups of PEI *in vivo*, potentially releasing the siRNA from the particles. Therefore, the heparin competition assay was conducted to assess the stability of the HAPx system in presence of the competing polyanion heparin under physiologic conditions (10 mM HEPES at pH 7.4). Freshly

prepared aliquots of 100 µL (HA)Px nanoparticles were distributed in a white FluoroNunc 96-well plate. In the following, 10 µL of previously prepared heparin concentrations (0, 0.125, 0.25, 0.5, 1, 2 units/well) were added to each well. After 30 min of incubation, 30 µL of a 4X SYBR gold dilution was added to each well for the detection of free siRNA. The plate was then incubated for 10 min under exclusion from light. Fluorescence measurements and free siRNA calculation were performed as described for the SYBR Gold assay above. The measurement was executed in triplicate, and results are shown as mean value ± SD (n=3).

2.2.5 *Fluorescence quenching-based assay (FQbA) – Polyplex stability in presence of serum proteins*

The polyplex assembly results in a compaction of siRNA and cationic polymer molecules. In case of fluorescently labeled siRNA, the fluorescent entities tend to converge in a way, which causes self-quenching of the dye upon excitation, leading to decreased overall fluorescence intensity [38]. This phenomenon was exploited to monitor polyplex compaction and de-compaction. Thereby, one can approximate colloidal stability of particles with de-quenching indicating particle disassembly. Here, amine-modified siRNA was labeled with succinimidyl ester (NHS) modified Alexa Fluor 647 (AF647) (Life Technologies, Carlsbad, California, USA) following the manufacturer's protocol. (HA)Px particles were prepared with 100 pmol of AF647-labeled siRNA as described above. Of each particle suspension, 10 µL was pipetted in a white FluoroNunc 96-well plate and filled up to a total volume of 100 µL. Colloidal stability was assessed at three different conditions: dispersed in 10 mM HEPES pH 7.4 (standard buffer), 10% FBS (*in vitro*-like) and 90% FBS (*in vivo*-like). Fluorescence intensity was determined at the interval of 15 min for 4 h with a fluorescence plate reader (λ_{Ex} = 630 nm; λ_{Em} = 680 nm). As 100% reference value, 10 pmol of free A647 siRNA diluted in 100 µL of the respective medium was used, and time-dependent fluorescence intensities were always related to the respective value of free AF647 siRNA. The relative fluorescence to free siRNA is calculated as:

$$rel.Fluorescence = \frac{Fluorescence\ of\ particles\ at\ t(x)}{Fluorescence\ of\ free\ siRNA\ at\ t(x)} \leq 1.0$$

Measurements were performed in triplicate, and the results are shown as mean value ± SD.

2.2.6 *Fluorescence Correlation Spectroscopy (FCS) – Polyplex stability over serum proteins*

If not otherwise stated, Px and 2-step-coated HAPx (HA to PEI ratio of 2.5 to 1) were prepared as described above with a 25/27mer non-coding siRNA, 15% of which was labeled with ATTO643 according to the above-mentioned protocol. For the FCS measurements, the nanoparticle preparations were then diluted 1:10 in HEPES, 10% or 90% FBS. As controls, 5 nM ATTO643 and 25 nM siRNA-ATTO643 solutions were prepared in HEPES, 10% or 90% FBS. For the comparison of the effect of different HA:PEI ratios (Figure S3), both the uncoated and coated polyplexes were prepared with the same 25/27mer non-coding siRNA, 30% of which was labeled with Alexa Fluor 647 (AF647). As

control, a 30 nM solution of siRNA-AF647 was measured in HEPES. For the measurements, the particles were diluted 1:10 in HEPES. Of each sample, 20-30 µL was added to an 8-well LabTek I slide (VWR) previously passivated with 1% Tween20 to prevent adsorption of the labeled material to the glass surface.

The FCS measurements were performed on a home-built confocal microscope as described elsewhere [39]. A pulsed diode laser of 635 nm wavelength (LDH-P-C-635M, PicoQuant), at a laser power of 2 µW before the objective, was used for all the FCS measurements. The measurements were performed using a 60X water immersion objective (Plan Apo 60x WI/NA 1.27, Nikon). The fluorescence emission was separated from the excitation pathway with a quad-line 405/488/561/635 beamsplitter (Semrock), spectrally filtered with a 635 nm longpass (AHF) emission filter and then detected with an avalanche photodiode detector (Count® Single Photon Counting Module, Laser Components). The alignment of the system was routinely checked by measuring an aqueous solution of ATTO655 with FCS.

The FCS data were acquired with Fabsurf, a home-written C# program, by recording the photons with the avalanche photodiode (APD) on a time-correlated single-photon-counting card (TCSPC, SPC-150 Becker and Hickl) for a period of 5-15 min. The correlation analyses were performed with PIE Analysis in MATLAB (PAM) [40]. The autocorrelation functions (ACFs) were fit with a diffusion model with up to three-components depending on the sample, assuming a 3D Gaussian focus shape:

$$G(\tau) = \frac{\gamma}{(N_1+N_2+N_3)^2}\left\{\left[N_1\left(1+\frac{4D_1\tau}{\omega_r^2}\right)^{-1}\left(1+\frac{4D_1\tau}{\omega_z^2}\right)^{-\frac{1}{2}}\right] + \left[N_2\left(1+\frac{4D_2\tau}{\omega_r^2}\right)^{-1}\left(1+\frac{4D_2\tau}{\omega_z^2}\right)^{-\frac{1}{2}}\right] + \left[N_3\left(1+\frac{4D_3\tau}{\omega_r^2}\right)^{-1}\left(1+\frac{4D_3\tau}{\omega_z^2}\right)^{-\frac{1}{2}}\right]\right\}.$$

Here, τ represents the time delay of the correlation, D_i the diffusion coefficient of the species i and ω_r and ω_z indicate the lateral and axial focus sizes, respectively. The shape factor γ is $2^{-3/2}$ for a 3D Gaussian focus. N_i represents the average number of fluorescent molecules in the observation volume. It should be noted that in this model, all the components are assumed to have equal brightness. However, if an accurate quantification of N_i is desired, the relative brightness of each species should be included in the analyses.[41]

The fitting of the ACF of the siRNA-AF647 constitutes the only exception to the use of the abovementioned fitting model. Indeed, this sample was fit with a one-component diffusion model with a triplet fraction:

$$G(\tau) = \frac{\gamma}{\mathrm{N}}\left(\left(1+\frac{4D\tau}{\omega_r^2}\right)^{-1}\left(1+\frac{4D\tau}{\omega_z^2}\right)^{-\frac{1}{2}}\right)\left(1+\frac{T}{1-T}e^{\tau/\tau_T}\right)$$

where T is the triplet fraction and τ_T is the triplet time constant.

The size of the nanoparticle was retrieved from the fitted diffusion coefficient D according to the Stokes-Einstein equation:

$$D = \frac{kT}{6\pi\eta R}$$

where k is Boltzmann's constant, η is the solvent viscosity at temperature T, and R is the molecular radius.

3. In-vitro evaluation of HA-coated polyplexes in four breast cancer cell lines

2.3.1 Immunostaining/Flow cytometry – Cell surface expression of CD44 receptor (CD44-R) in breast cancer

For each experiment, 50.000 cells of MCF7, HCC1954, MDA-MB-468 and MDA-MB-231 cell lines were seeded in triplicates in a 24-well plate. After 48 h, cells were washed 3x with sterile PBS and harvested. Subsequently, cells were centrifuged at 400 g for 5 min and the supernatant was discarded. In the next step, 100.000 cells of each cell line were re-dispersed in 50 µL of PBS containing 2 µg/ml of AF488-labeled CD44-R-specific or isotype control antibody, respectively. Blank samples were treated with neither antibody. After 30 min of incubation at 4°C, 1 ml of PBS was added, cells were vortexed, centrifuged and the supernatant was removed. Following an additional washing step, cells were re-suspended in 400 µL of PBS with 2 mM EDTA, and samples were analyzed using an Attune® NxT flow cytometer (Thermo Fisher Scientific) with 488 nm excitation and 530/30 emission filter. All cells were gated according to morphology based on forward/sideward scattering, and 10.000 gated events were evaluated per sample. Results are shown as mean ± SD (n=2)

To test for CD44-R expression upon EMT induction, 50.000 cells of MCF7, HCC1954 and MDA-MB-468 cell line were incubated for 48 h in 10 ng/ml TGF-β1 and 50 ng/ml EGF containing medium, respectively. Afterwards receptor expression was carried out as described above. Results are shown as mean ± SD (n=2)

2.3.2 Flow cytometry - Cellular uptake of HAPx depending on cell line and coating procedure

For each cell line, 50.000 cells were seeded in duplicates in a 24-well plate. After 24 h, cells were washed with PBS and transfected with 100 µL of freshly prepared polyplexes (Px and HAPx (1:10 to 10:1)) containing 100 pmol AF488-siRNA in 400 µL of the respective medium. After 0.25, 1, or 4 h incubation, medium in the wells was filled up to 1 ml. After another 0.75, 3, or 20 h of incubation, cells were washed 3x times with PBS and harvested. Centrifuged cell pellets were re-suspended in 500 µL of PBS with 2 mM EDTA, and particle uptake was analyzed using an Attune® NxT flow cytometer with 488 nm excitation and 530/30 emission filter. Forward/sideward scatter and laser

intensity were kept the same for all the cell lines and time points to enable intercellular comparison of nanoparticle endocytosis. Results are shown as mean ± SD (n=2)

To assess, whether HAPx are specifically taken up via CD44-R-HA interaction, a HA-competition uptake experiment was performed. Therefore, 50.000 MDA-MB-468 cells were transfected with PEI polyplexes (Px) and HAPx 2.5:1 and their uptake was compared among three different experimental conditions:

(1) Regular procedure as explained above (24 h).
(2) Pre-incubation with free HA for 2 h before transfection: L-15 medium was supplemented with 0.5 mg/ml HA. Upon transfection, medium was removed and cells were transfected in fresh HA-free medium as described above.
(3) HA competition: 2 h before transfection, L-15 medium was supplemented with 0.5 mg/ml HA. Upon transfection, medium was removed and cells were transfected in HA-containing medium (0.5 mg/ml) as described above.

2.3.3 Confocal Scanning microscopy – Intracellular fate of polyplexes

Confocal image analysis was used to assess and quantify co-localization of polyplexes with lysosomes after cellular internalization. Briefly, sterile glass coverslips were distributed in a 24-well plate. Thereafter, 50.000 cells were seeded to attach for 24 h. Polyplexes were prepared with AF647-labeled siRNA as described above, and cells were transfected for 24 h. During the last hour of transfection, media was supplemented with LysoTracker™ Green DND-26 (Invitrogen) lysosomal stain according to the manufactures protocol. Hereinafter, wells were washed 3 times with PBS before cells were fixed for 15 min with a 4% formaldehyde solution. Cells were washed another 3 times with PBS. Nuclear staining was achieved by 10 min incubation with a 0.5 µg/ml DAPI solution. Finally, after an additional washing step, samples were mounted on glass slides using FluorSave and stored at 4°C until the next day. Fluorescence images were acquired using a laser scanning microscope (Leica SP8 inverted, Software: LAS X, Leica microsystems GmbH, Wetzlar, Germany) equipped with a HC PL APO CS2 40x/1.30 and 63x/1.40 oil immersion objective. Diode lasers (405 nm and 638 nm) and a semiconductor laser OPSL (488 nm) were chosen for excitation, emission of blue (PMT1: 410 nm – 488 nm), green (HyD3: 495 nm – 625 nm) and red (PMT2: 643 nm – 785 nm) dyes, was detected respectively. Images were further processed with the JACoP plug-in of Fiji image analysis software [42]. For the co-localization analysis of each HAPx species, at least 4 cells of 3 samples were manually outlined to reduce background noise. Thresholds of the green and red channel were manually adjusted and kept constant within the respective cell line. One-way ANOVA with Dunnett's Multiple Comparison Test was performed in GraphPad Prism software to calculate p-values at 95% confidence interval.

2.3.4 *RT-qPCR – XBP1 knockdown in MDA-MB-231 cells*

For the gene silencing experiment, 24 h prior to transfection 200.000 MDA-MB-231 cells were seeded in a 6-well-plate and incubated until the next day. Cells were transfected with 100 µL of Px or HAPx polyplexes produced by "2-step coating" and containing 100 pmol of XBP1 or scrambled siRNA. Positive controls consisted of Lipofectamine2000 lipoplexes while negative controls consisted of blank/untreated cells. After 24 h, cells were harvested and processed to isolate total RNA using the PureLink RNA mini kit according to the manufacturer's protocol (Life Technologies, Carlsbad, California, USA). cDNA was synthetized from total RNA using the high-capacity cDNA synthesis kit (Applied Biosystems, Waltham, Massachusetts, USA). Afterwards, the obtained cDNA was diluted 1:10 and a qPCR was performed using the SYBR™ Green PCR Master Mix (Thermo Fisher Scientific) with primers for human GAPDH (Qiagen, Hilden Germany) for normalization. Cycle thresholds were acquired by auto setting within the qPCRsoft software (Analytic Jena AG, Jena, Germany). Values are given as mean ± SD.

2.3.5 *Western Blotting*

Protein levels of CDH1, XBP1, CD44s and CD44v in the four cell lines were analysed via Western blotting. Of each cell line, 300.000 cells were seeded in triplicates in a 6-well plate and cultured for 24 h. Total protein extract was isolated after incubation. Briefly, cells were washed 3 times with PBS prior to cell lyses. To each well, 70 µL of proteinase- and phosphatase-inhibitor containing RIPA buffer was added, and cells were kept on ice for 30 min. Hereinafter, wells were thoroughly scraped, and the extracts were transferred into 1.5 ml Eppendorf tubes. After a 10 min centrifugation step at 4°C, total protein concentration was assessed according to the manufacturer's protocol (Pierce™ BCA Protein Assay Kit). For protein extraction of the transcription factor XBP1, the "Nuclear Extraction Kit" was utilized according to the manufacturer's protocol (Abcam, Cambridge, UK). Gels were loaded with 30 µg protein per sample, and electrophoresis was run for 90 min at 120 mV. After 1 h of protein transfer at 100 mV, blots were washed, blocked and incubated overnight using CDH1-, XBP1-, CD44- and GAPDH-specific antibodies. The HRP-bound secondary antibody was added for 1h under exclusion of light before blots were developed using TF's Pico PLUS chemiluminescence substrate for ECL.

3. Results & Discussion

The most rational way to non-covalently immobilize anionic molecules as targeting moiety on the surface of PEI polyplexes is to first produce core PEI-siRNA nanoparticles bearing a positive zeta potential subsequently allowing for electrostatically driven adsorption of negatively charged HA ("2-step-coating"; **Figure 1a**) similar to previously described layer-by-layer approaches.[43] A less conventional approach includes the initial formation of PEI-HA intermediates which will then interact with siRNA in a subsequent step ("Inverse 2-step-coating"; **Figure 1b**). Whereas the polyplexes obtained with this approach may suffer from poorer ligand exposure on the polyplex surface, they can possibly modulate the release properties of siRNA from the polyplexes, which is still a major concern in current nucleic acid drug delivery.[44, 45] The incorporation of HA into the core could attenuate PEI-siRNA (electrostatic) interactions, potentially facilitating siRNA release. Alternatively, the coating process can be simplified by blending the anionic components (HA and siRNA) and combining them directly with cationic PEI in one single step ("1-step-coating"; **Figure 1c**). However, this uncontrolled assembly may also fail to adequately expose the targeting ligand on the polyplex surface resulting in impaired CD44-HA interaction and polyplex internalization.

In the first part of this manuscript the physico-chemical differences between polyplexes obtained by various coating procedures and with different HA:PEI-ratios were addressed with a focus on their impact on particle stability in presence of *in vivo*-relevant competing biomolecules. *In vitro* uptake and CD44-isotype selectivity with respect to particle characteristics were subject of the second part.

3.1 Physico-chemical characterization and stability of HA-coated polyplexes

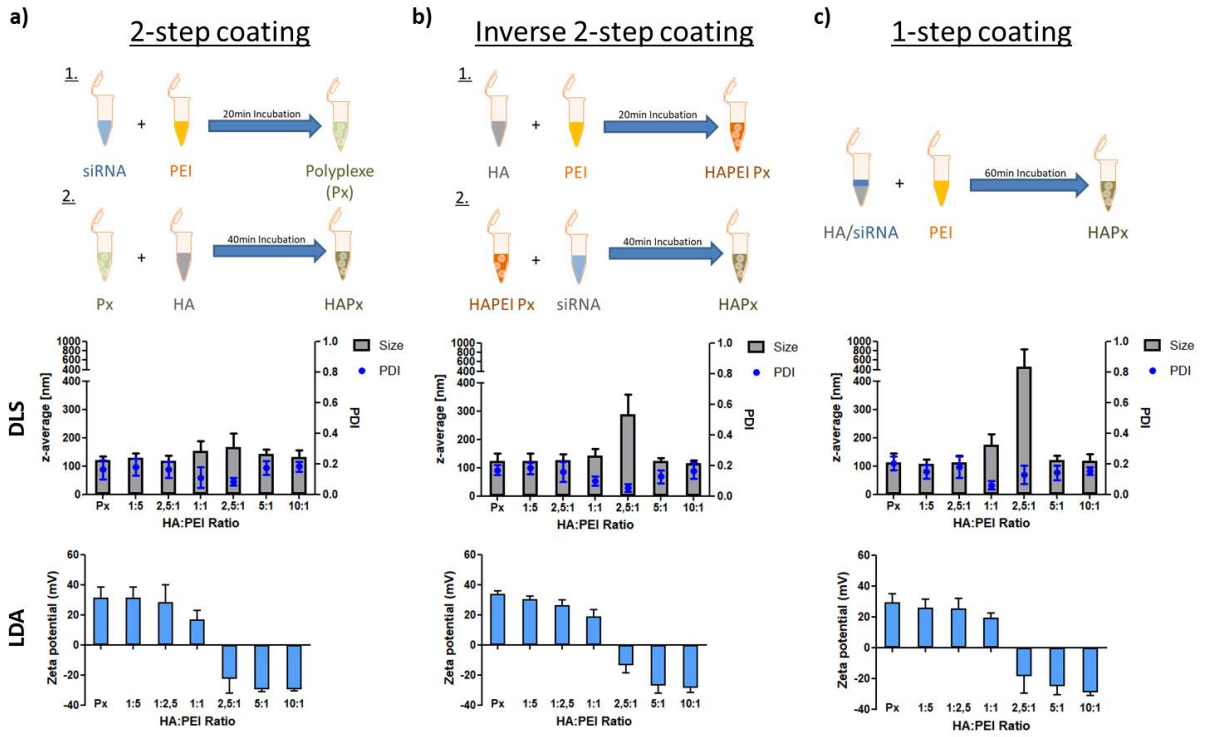

Figure 1. *Physico-chemical characterization of polyplexes produced via* ***(a)*** *2-step coating* ***(b)*** *inverse 2-step coating* ***(c)*** *1-step coating depending on HA:PEI ratio (n = 3). The upper panel shows a scheme that summarizes the particle preparation protocols. The central panel depicts particles' hydrodynamic diameter (shown as z-average, left y-axis) and polydispersity index (PDI, right y-axis). The lower panel displays zeta potentials of the respective particles.*

3.1.1 HA-coated polyplexes of near neutral surface charge show desirable monodisperse size distribution but impaired long-term colloidal stability

To assess differences among the three mentioned coating procedures and to evaluate successful immobilization of varying amounts of HA on/in the polyplexes while keeping PEI and siRNA amounts constant at a N/P 5, the particles were examined by DLS and LDA analysis. In summary, all three approaches successfully produced polyplexes of comparably favorable sizes and PDIs. The successive drop in zeta potential (ζ) with increasing amount of HA implies effective coating of polyplexes (**Figure 1**). Physico-chemical characteristics did mainly depend on the chosen HA:PEI-ratio (w/w) and not necessarily on the coating procedure resulting in three major groups of nanoparticles.

In the first group, Px and HAPx with 1:5 or 1:2.5 coating ratios exhibited mean sizes around 110-130 nm, mean PDIs from 0.13 to 0.18 and a strong positive surface charge of 26-36 mV ($HAPx^{+\zeta}$). The second group HAPx with 1:1 and 2.5:1 ratios depicted particles transitioning from a positive to negative zeta potential (+19 mV to -18 mv) with increased sizes of 160-300 nm and even above 400 nm (2.5:1) for the 1-step-coating ($HAPx^{\pm\zeta}$). Here, the coating approach had a decisive impact on particle sizes, especially for HAPx 2.5:1 with close-to-neutral zeta potential, where the least size increase was observed for HAPx obtained by standard 2-step coating. Similar to these findings, Tirella *et al.* as well as Yamada *et al.* produced bigger-sized HA:polycation complexes at stoichiometry ratios close to the effective complexation between positive and negative charges.[46, 47] In group 2, net-charges may have balanced to form polyplexes of almost neutral zeta potential. The missing electrostatic repulsion consequently leads to polyplex aggregation. Besides their bigger sizes, group 2 HAPx exhibited a desirable, monodisperse particle distribution with PDIs ranging from 0.04 to 0.11. In the third group, strongly negatively charged (-26 to -30 mV) HAPx with 5:1 and 10:1 ratios formed smaller particles of 120 to 140 nm in size ($HAPx^{-\zeta}$) but exhibited a broader particle size distribution (PDI: 0.10 to 0.18). Given the similar sizes and zeta potentials of the latter two ratios, it appears that at an HA:PEI weight-ratio of 5:1 maximum HA-binding capacity of polyplexes has occurred. Further addition of HA therefore rather increases the excess amount of HA in the solution which has to be considered particularly in *in vitro* uptake experiments due to possible competition for CD44 receptor binding.

Regarding the dynamic nature of electrostatically driven polyplex assembly and the excess amounts of PEI and/or HA present in a polyplex suspension, it is of interest whether intra- and inter-particulate rearrangements/interactions or "particle-particle bridging" affect colloidal stability of the nano-formation in the long term. **Supplementary Figure S1** displays the course of polyplex sizes during 6 weeks of storage at room temperature (23°C). Px, $HAPx^{+\zeta}$ and $HAPx^{-\zeta}$ showed sustained stability with minor deviations of the hydrodynamic diameter and even improved PDIs, mostly below 0.1 (data not shown). However, the magnitude of size change depended on the coating procedure with a minimal mean change in size for the 2-step coating (11%) and a maximal mean change for the 1-step coating (29%). This very tendency was also observed to a greater extent for $HAPx^{\pm\zeta}$ particles. This group of HAPx was the least stable, especially HAPx 1:1 which aggregated within the first 2 to 4 weeks (d_h + 272 - 618%). As mentioned above, the weaker electrostatic repulsion at near-neutral zeta potential is expected to cause particle aggregation over time. Irrespective of the latter, it is thought that immobilization of hydrophilic molecules on particle surfaces attracts significant amounts of water molecules leading to a "hydration shell" [48, 49]. HA-coating is therefore expected to introduce additive repulsive forces that are contributing to the long term stabilizing of a nano-formulation. The formation of such a HA-corona was already shown to significantly improve colloidal stability of

chitosan particles, even for lyophilization purposes [50, 51]. However, the monitored timeframe in our study was presumably too short to detect differences in stability between coated and uncoated polyplexes.

3.1.2 HA-coating improves polyplex stability in presence of polyanionic species at neutral pH

Upon systemic administration polyplexes face a variety of stressors including shear stress and opsonization by biomolecules such as proteins, lipids and polysaccharides that determine their stability and clearance from the circulation, and thus ultimately their therapeutic efficacy.[52, 53] Anionic species within the serum may not only bind to the surface of cationic nanoparticles, altering physico-chemical properties, but also competitively replace/displace anionic siRNA molecules from their binding sites within the nanoparticles, compromising the therapeutic efficacy.

Consequently, it was verified whether during the different HA-coating procedures complete siRNA encapsulation was achieved. To this end, SYBR-gold assays were performed, where only freely accessible RNA causes intercalation-based fluorescence increase. As shown in **Figure 2a,** siRNA was efficiently encapsulated at all HA:PEI ratios regardless of the coating procedure. Marginal release (< 2%) of siRNA was observed starting from HAPx 2.5:1 on but remained stable even at higher ratios (20:1). Overall, it was concluded that the siRNA displacement by HA is insignificant within our range of HA:PEI ratios.

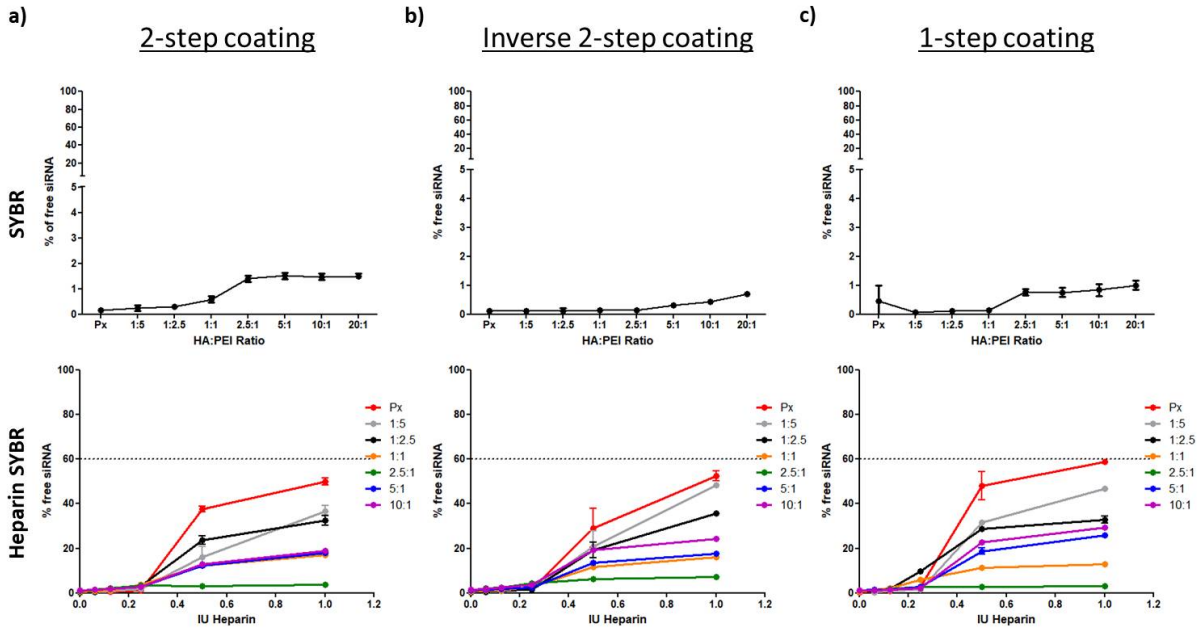

Figure 2. *HA:PEI-ratio (w/w) dependent siRNA encapsulation efficiency (upper panel) and siRNA release profile at pH 7.4 (lower panel) of particles produced via* ***(a)*** *2-step coating,* ***(b)*** *inverse 2-step coating, or* ***(c)*** *1-step coating assessed by SYBR gold intercalation with siRNA (n = 2). The lower panel demonstrates relative*

SYBR gold fluorescence intensity with respect to heparin competition (international units [IU]). Black dotted line represents maximal siRNA release of uncoated Px particles at the highest heparin concentration (1 IU).

Subsequently, it was tested whether HA-coating can improve polyplex stability in presence of polyanionic species found in the systemic circulation. According to the DLVO theory, a negative zeta potential of PEI nanoparticles should avoid interaction with anionic species caused by increased repulsion [48]. Therefore, polyplexes were incubated with increasing concentrations of the polysaccharide heparin as a model polyanion dissolved in 10 mM HEPES pH 7.4 ranging from 0 IU to 1 IU/sample. Subsequently, SYBR-gold dye was added to detect released siRNA. **Figure 2b** demonstrates comparable release profiles for the 3 coating procedures with Px to extensively release siRNA at 0.5 IU heparin, reaching a maximum of 50 - 60% at 1.0 IU heparin. Interestingly, coating of Px particles with HA significantly affected siRNA release at high heparin concentrations, where RNA release was successively reduced below 10% with increasing amount of HA until charge-neutral HAPx were obtained. Surprisingly, even low HA:PEI-ratio (1:5 and 1:2.5) exhibiting similar physico-chemical characteristics as Px showed improved stability against heparin (35 - 50% release). Contradictory to our expectations, the siRNA release at 1 IU heparin of strongly negatively charged $HAPx^{-\zeta}$-species increased up to 30% indicating polyplex instabilities at higher excess HA. (**Figure S2**). Based on our results, it can be hypothesized that bigger-sized, near-neutral polyplexes (HAPx 1:1 and 2.5:1) are able to incorporate higher amounts of siRNA molecules per particle, decreasing their total accessibility for heparin.

To summarize, HA-coating is a suitable measure to enhance polyplex stability in presence of polyanions, possibly improving *in vivo* endurance. The “stealth effect” was influenced by both zeta potential/HA-loading and particle size. However, as observed for group 3 HAPx, incorporation of a high HA-amount may have weakened siRNA binding, which in turn facilitates siRNA release. It is noteworthy that all coating procedures, theoretically exposing siRNA molecules differently on the particle surface (e.g. 2-step vs. Inverse 2-step) resulted in comparable release profiles.

3.1.3 *Near-neutral HAPx species incur a smaller protein corona and show improved stability in high protein content environments*

The adsorption of proteins on the surface of nanoparticles that occurs during systemic circulation is referred to as protein corona formation [54]. Its dimension and composition is highly dependent on physico-chemical properties of the nanoparticles [55, 56]. Thus, alterations of the latter characteristics via HA-coating of polyplexes are prone to affect protein-particle interaction and thereby overall stability.

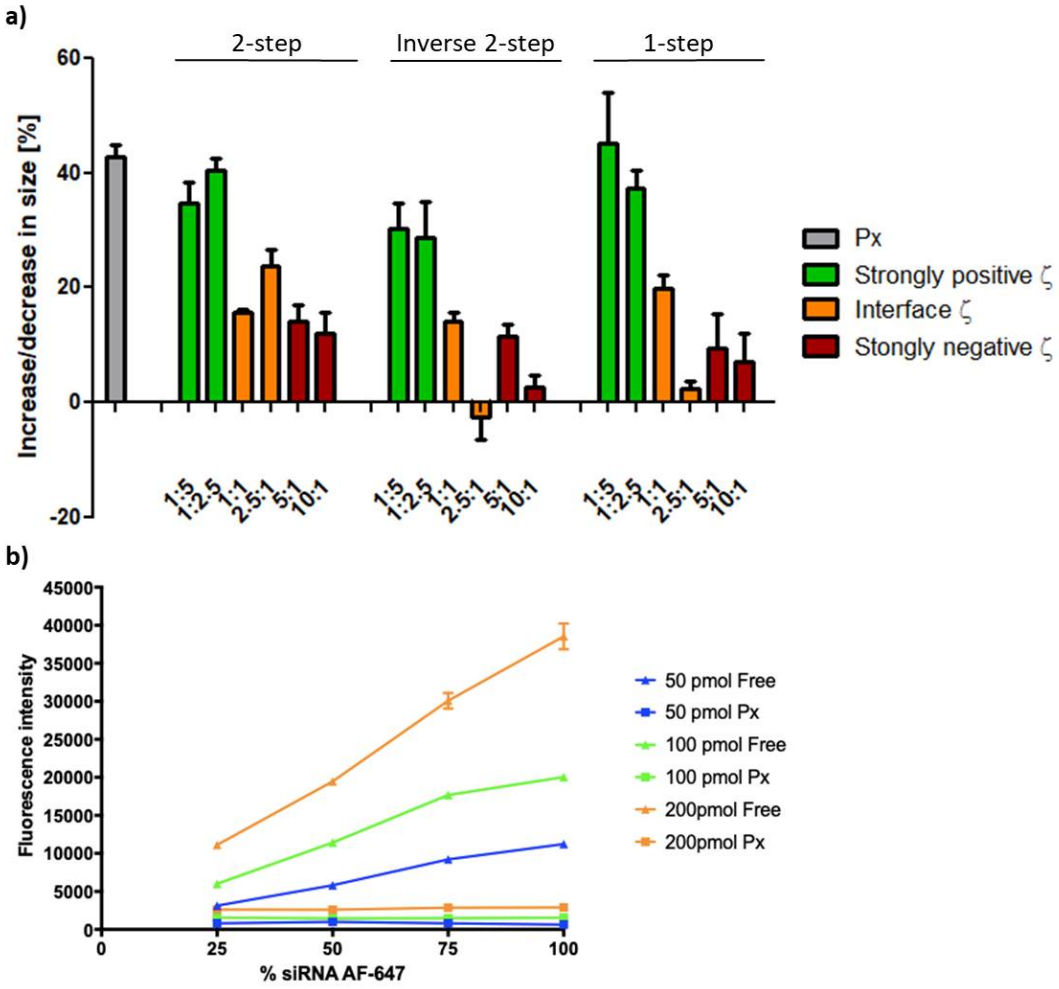

Figure 3. *(**a**) Change of hydrodynamic diameter [± %] of nanoparticles after incubation in 2% FBS compared to sizes in 10 mM HEPES (pH 7.4) depending on HA:PEI-ratio and coating procedure. Colors of bars indicate distinct (HA)Px-groups: Px (grey), HAPx$^{+\zeta}$ (green), HAPx$^{\pm\zeta}$ (orange), HAPx$^{-\zeta}$ (red). (**b**) Self-quenching of AF647 dye based on the labeled/unlabeled siRNA-ratio (%) during polyplex assembly: Px (squares) with 50 (blue), 100 (green) and 200 pmol (orange) siRNA at ratios of 25/75, 50/50, 75/25 and 100/0 were compared to respective amounts of free siRNA (triangles)*

To estimate the influence HA-coating exerted on protein corona formation, Px and HAPx were incubated in buffer containing 2% FBS. DLS results of the particles after incubation were compared to particles incubated in FBS-free buffer. Exposure to 2% FBS led to a charge inversion for all formerly positively or neutrally charged particles. The resulting negative zeta potentials ranging from -15 to -30 mV imply intense absorption of proteins on the surface of the nanoparticles. Regarding the size increment of the polyplexes, the three physico-chemically defined particle groups mentioned above can be clearly discriminated, but not the coating procedures (**Figure 3a**). The sizes of strongly positively charged polyplexes (including Px) considerably increased by 29 - 45%. The maximal size increment was reduced to 25% for charge-neutral nanoparticles HAPx$^{\pm\zeta}$. This effect was even more

reduced for polyplexes bearing a strong negative zeta potential ($HAPx^{-\zeta}$). Those particles only deviated by 2 - 14% from their original size. To conclude, HA-coating equipped polyplexes with electrostatic shielding- and stealth-properties that partially prevented particle-FBS interaction.

However, an environment of 2% FBS neither reflects *in vitro* nor *in vivo* conditions. To investigate polyplex stability under such conditions a fluorescence-based assay that relies on de-quenching (FQbA) to approximate polyplex stability was applied. As can be seen in **Figure 3b,** fluorescence intensity of non-complexed siRNA was linearly increasing with increasing proportions of labeled siRNA (triangles). The hight of fluorescence intensity depended on the amount of pmol used (colored lines). Contrary, the intensity of fluorescently-labeled siRNA was remarkably quenched upon complexation with PEI (squares)Surprisingly, maximal quenching occurred even at low proportion of labeled siRNA (25% of total siRNA content) within the nanoparticles independent of total pmol siRNA (colored lines) applied. Consequently, polyplex rearrangement, disassembly or siRNA release should increase spacing of fluorescent molecules causing its intensity to be partially restored. This de-quenching phenomenon was exploited to indirectly evaluate polyplex stability over time incubated in 10 mM HEPES (buffer), 10% FBS (*in vitro* conditions) and 90% FBS (*in vivo* conditions).

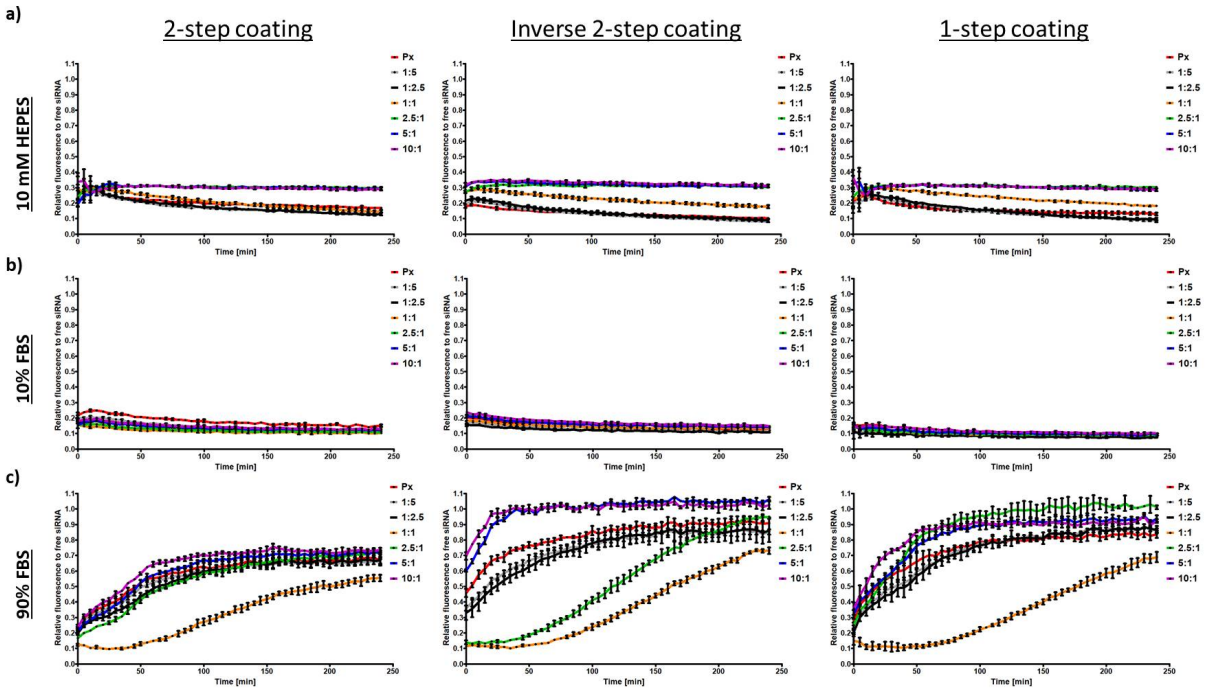

Figure 4. *HA:PEI-ratio dependent stability of HAPx in 10 mM HEPES pH 7.4* ***(a)*** *10% FBS* ***(b)*** *and 90% FBS* ***(c)*** *prepared by 2-step coating, inverse 2-step coating and 1-step coating method. (Data points indicate mean ± SD, n = 3). Release/decompaction of AF647-labeled siRNA is indicated by increase in fluorescence intensity (de-quenching).*

As can be seen from **Figure 4a** fluorescence intensity (FI) was reduced to 20 - 35% of maximum intensity (free siRNA) in regular buffer and remained low over the 240 min of observation, indicating sustained stability of polyplexes. The distinct coating methods did not considerably affect the course of quenching. However, it was possible to separate HAPx groups based on their overall surface charge. Notably, FI of positively charged $HAPx^{+\zeta/\pm\zeta}$ decreased over time to 10% of maximal intensity whereas it remained constant at 30% for negatively charged $HAPx^{-\zeta/\pm\zeta}$. Presumably, condensation of siRNA molecules within $HAPx^{+\zeta/\pm\zeta}$ was intensified during incubation resulting in enhanced quenching of the dye. At the same time, the higher fraction of HA within $HAPx^{-\zeta/\pm\zeta}$ could have impeded this phenomenon due to intra-particulate electrostatic repulsion or steric hindrance. Fluctuations in the fluorescence intensity observed in the first 10 min might be explained by the reorganization of polyplexes after being pipetted into the well plate.

Further, the data suggests all nano-formulations to be stable in 10% FBS-containing buffer (**Figure 4b**). Quenching levels started and persisted at 10-20% of maximum FI. The drop of the FI-baseline in comparison to the FBS-free buffer can be explained by reinforced polyplex condensation. It is well documented [57, 58] that elevated external osmotic pressure in 10% FBS-containing buffers leads to particle shrinkage which in turn explains enhanced fluorescence quenching of labeled siRNA molecules.

Upon incubation in 90% FBS, however, polyplexes initiated disassembly as indicated by pronounced de-quenching within the first 120 min (**Figure 4c**). This time, $HAPx^{+\zeta}$ and $HAPx^{\pm\zeta}$ polyplexes outperformed uncoated Px and $HAPx^{-\zeta}$. Strikingly, the latter polyplexes (HAPx 5/10:1) de-quenched considerably faster and to a higher extent than standard Px which was especially true for the "Inverse 2-step coating" (100% after 30 min vs. <90% after 240 min). PEI-HA core polyplexes with a high HA content may have facilitated release of surface-bound siRNA molecules due to a weakened PEI-siRNA attraction, accounting for the fast release. Indeed, a similar effect was observed by Greco *et al.* for co-incorporation of anionic species into mPEG-b-P(APNBMA) polyplexes. They demonstrated facilitated release of siRNA once PAA, bearing a high anionic charge density, was co-encapsulated which they related to altered nucleic acid binding properties [45].

Remarkably, HAPx 2.5:1 (green line) and in particular HAPx 1:1 (orange line) displayed an overall superior stability. In case of HAPx 2.5:1, the de-quenching levels of standard Px were only reached after about 100 min (2-step) to 190 min (Inverse 2-step). HAPx 1:1 showed a completely different and unpredicted FI profile. Particles remained intact over the first 100 min and then slowly disassembled, still remaining quenched by 35-45 % at the end of the observation time period. Earlier studies highlighted bigger particle sizes (smaller surface area over volume) and near–neutral surface charges of nanocarriers to reduce protein-particle interaction, resulting in improved colloidal stability [59-61].

In summary, considering the maximum de-quenching levels after 240 min, particles produced via 2-step coating were more stable in *in vivo*-like conditions than the others. The latter findings encouraged us to further investigate their stability in high protein content environments using FCS.

3.1.4 FCS as powerful tool to discriminate 2-step coated HAPx groups and to assess stability in high protein content environments

Fluorescence Correlation Spectroscopy (FCS) relies on the non-stochastic nature of fluorescence-emmitted photons detected in the observation volume of a confocal microscope. Time-dependent fluctuations of the fluorescence signals are analyzed with an autocorrelation analysis which delivers information about sample concentration, brightness and mobility (translational diffusion) [41]. Similar to the work by Nuhn *et al.* [62] using the autocorrelation function (ACF) allowed us to discriminate between intact polyplexes and free siRNA molecules, thanks to their great difference in size and thus diffusion coefficient. This enabled us to assess polyplex stability in different buffer environments and to compare distinct (HA)Px groups.

As shown in **Figure S3** un-complexed fluorescently-labeled siRNA showed an early ($\tau = 10^{-5}$ s) and fast decaying ACF (red line) in HEPES buffer. Once complexed with PEI (Px, blue line) the ACF shifted towards the right ($\tau = 10^{-3}$ s), implying slower diffusive behavior of the formed polyplexes. Notably, $HAPx^{+\zeta/-\zeta/\pm\zeta}$ polyplexes behaved differently from uncoated Px as demonstrated by their distinct ACF profiles. By fitting the obtained diffusion coefficient D into the Stoke-Einstein equation, we were able to calculate the hydrodynamic diameter which was in good conformity to the DLS data presented above.

According to the de-quenching assay, polyplexes remained intact in HEPES and 10% FBS buffer but disrupted upon incubation in 90% FBS. HAPx 2.5:1 was found to be a promising candidate since it showed superior stability in high protein content environment as well as against heparin compared with uncoated Px. Consequently, FCS analysis was used to compare Px and HAPx 2.5:1 with a focus on *in vivo*-like conditions.

Figure 5a displays well-separated ACF profiles of free siRNA, Px and HAPx in HEPES buffer measured right after particle preparation and after 120 min of incubation. In accordance with the above findings, neither of the formulations showed alteration in their diffusion profile, implying sustained stability. The bigger size of HAPx, and thereby slower diffusion, is reflected in the shift of the respective ACF curves to a slower time scale. Likewise, investigations on stability in 10% FBS-containing buffer confirmed persistent polyplex integrity for both formulations (**Figure 5b**). However, in 90% FBS we expected fast disassembly kinetics what prompted us to measure at 0, 30, 60 and 90 min time points. Strikingly, as is shown in **Figure 5c** ACF of uncoated Px instantly approached ACF

of free siRNA at t_o, indicating fast and nearly complete polyplex disassembly upon administration as described before [63]. At later incubation times, ACF of Px and siRNA superposed, emphasizing complete particle rupture and siRNA release. In contrast, the ACF profile of HAPx at t_o mostly resembled the one in HEPES/10% FBS (**Figure 5d**). Still, the decay curve flattened towards earlier time points being indicative for the appearance of a second, fast-diffusing component i.e. free/un-complexed siRNA. At t_{30}, this flattening phenomenon got increasingly pronounced as the ACFs of HAPx and free siRNA further converged. Hence, the portion of intact particles decreased over time concomitantly releasing siRNA from the complex. The data further suggests that after 60 and 90 min, the majority of polyplexes dissembled. However, a small percentage of HAPx seemed to persist. As demonstrated in **Figure S4a-f**, this tendency was reproducible among other biological replicates underlining the advantageous stability profile of HAPx particles.

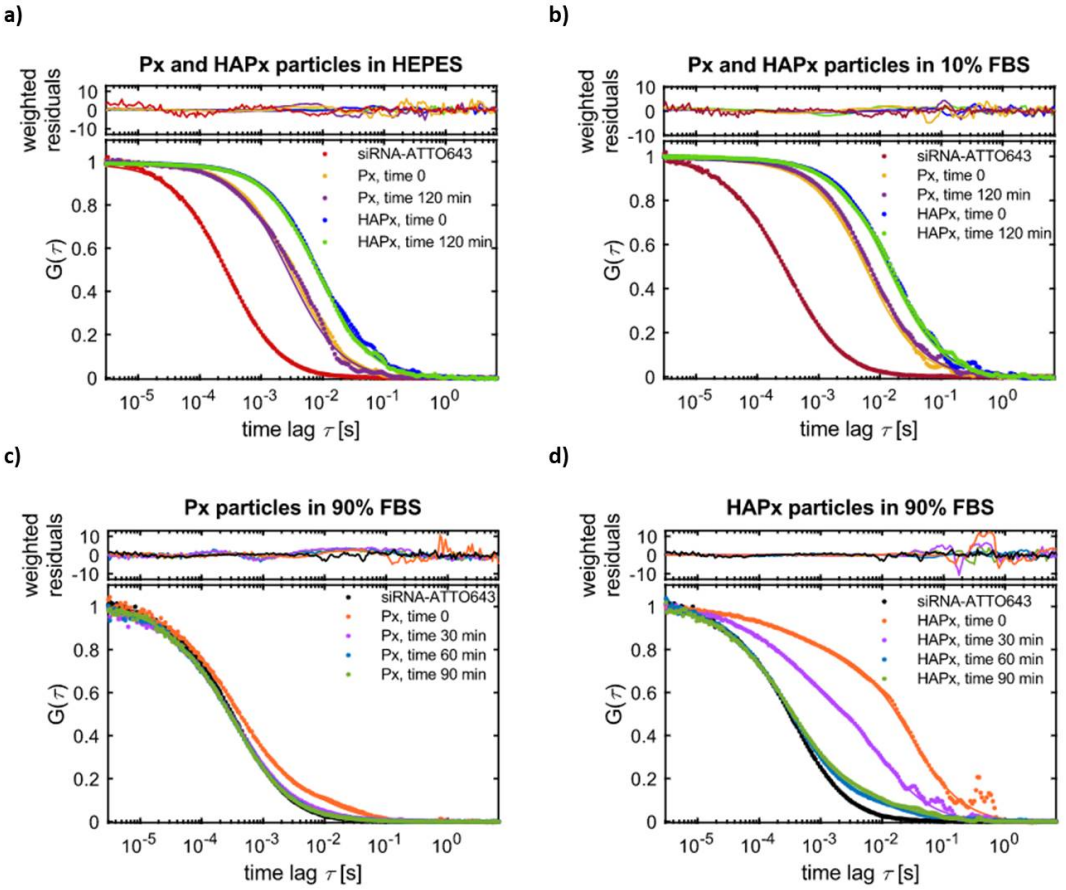

Figure 5. *FCS analysis of naked Px particles and coated HAPx particles. The particles were prepared with 15% ATTO643-labeled non-coding siRNA and 85% unlabeled 25/27mer siRNA directed versus eGFP. HAPx particles were formulated at an HA:PEI ratio of 2.5:1.* ***(a)*** *Representative autocorrelation functions (ACFs) of naked Px particles and coated HAPx particles in 10 mM HEPES buffer immediately after dilution and 2 h later.* ***(b)*** *Representative ACFs of naked Px particles and coated HAPx particles in 10% FBS immediately after dilution and 2 h later.* ***(c)*** *Representative ACFs of uncoated Px particles at different time points of incubation in 90% FBS. Note that the ACFs relative to the time points from 30 to 90 min largely overlap with the siRNA-ATTO643 curve.* ***(d)*** *Representative ACFs of coated HAPx particles at different time points of incubation in 90% FBS.*

In accordance with FQbA, FCS measurements confirmed superior stability of HA-coated polyplexes ($HAPx^{\pm\zeta}$) over uncoated Px. However, considering the single molecule selectivity and higher sensitivity of FCS, it appeared that disassembly kinetics at *in vivo*-like conditions were underestimated by the de-quenching assay. Px disrupted immediately after administration to high protein content buffer whereas HAPx remained stable for at least 30-60 min which can be at least partially attributed to differences in their surface properties.

As the majority of proteins adsorbed on nanomaterials possess an isoelectric point < 7.4, positively charged nanocarriers are particularly vulnerable to adsorption events *in vivo* [8]. Indeed, it was reported that polyplexes made from branched, high molecular weight PEI induced aggregation of blood cells, conformational changes of proteins and impaired blood coagulation [64]. These toxic effects were mainly attributed to the physico-chemical properties, in particular to the highly positive surface charge and the resulting interaction potential of the drug delivery system. Likewise, strongly positively charged nanoparticles are prone to rapid systemic clearance since they preferentially interact with negatively charged proteoglycans present at the glomerular basal membrane or are internalized by macrophages of the reticuloendothelial system (RES) after opsonization [8, 64, 65]. Instead, the present study demonstrates how HA-coating of cationic polyplexes allows fine-tuning of physico-chemical characteristics decreasing biomacromolecule-particle interaction and thereby potentially enhancing biological performance of the drug delivery system *in vivo*. A near-neutral zeta potential increased stability against competing polyanions. As was postulated by Zheng *et al*. this will inevitably result in decreased interaction with macrophages and consequently prolong the half-life of the nanocarriers during systemic circulation [66]. Likewise, the modified surface chemistry of HA-coated particles decisively influences protein corona formation and affects colloidal stability in high protein environments. With our results, we confirm previous theories on stealth- and electrostatic shielding properties of HA-bearing nanosystems employing DLS and fluorescence-based approaches [33, 50, 67-69]. Our results further corroborate a report about the modification of the synthetic identity of chitosan nanoparticles via HA-coating resulting in a strikingly altered biological identity for reduced immunogenicity of the formed protein corona [70]. HA-coating can thus be considered a selective tool to improve the immunogenicity profile of upcoming nanomaterials.

3.2 *In vitro* evaluation of HAPx in a cell line based EMT-model

3.2.1 Proof of concept: CD44 surface expression relates to EMT-status and EMT-induction

Despite their apparent utility in improving polyplex stability, HA-coatings furnish nanoparticles with a targeting moiety for selective endocytosis via the HA-binding proteins CD44 or RHAMM. Even though the CD44s receptor is ubiquitously expressed throughout the body, its overexpression in cancer tissue makes it a valuable candidate for HA-based targeted drug delivery [33, 67, 71]. Likewise, RHAMM, another transiently expressed cell surface receptor binding HA, was shown to be frequently

overexpressed in cancer tissue [72] and supposedly participates in CD44-independent HA internalization [73]. Following the aim to specifically target EMT undergoing/undergone cells via CD44-mediated uptake, the importance of surface CD44 expression in a recently established breast cancer cell line EMT-model [23] was first evaluated. Accordingly, EMT-status increased in the chosen cell lines in the order of MCF7 < HCC1954 < MDA-MB-468 < MDA-MB-231. As depicted in **Figure 6a**, CD44 expression increased with higher EMT-status. Consequently, the four cell lines were classified into $CD44^{low}$ (MCF7), $CD44^{medium\text{-}low}$ (HCC1954), $CD44^{medium\text{-}high}$ (MDA-MB-468) and $CD44^{high}$ (MDA-MB-231) expressing cells. Simultaneously, a possible contribution of RHAMM–mediated internalization to overall HA-mediated uptake was excluded as none of the cell line showed relevant surface expression of RHAMM protein (**Figure S5a**).

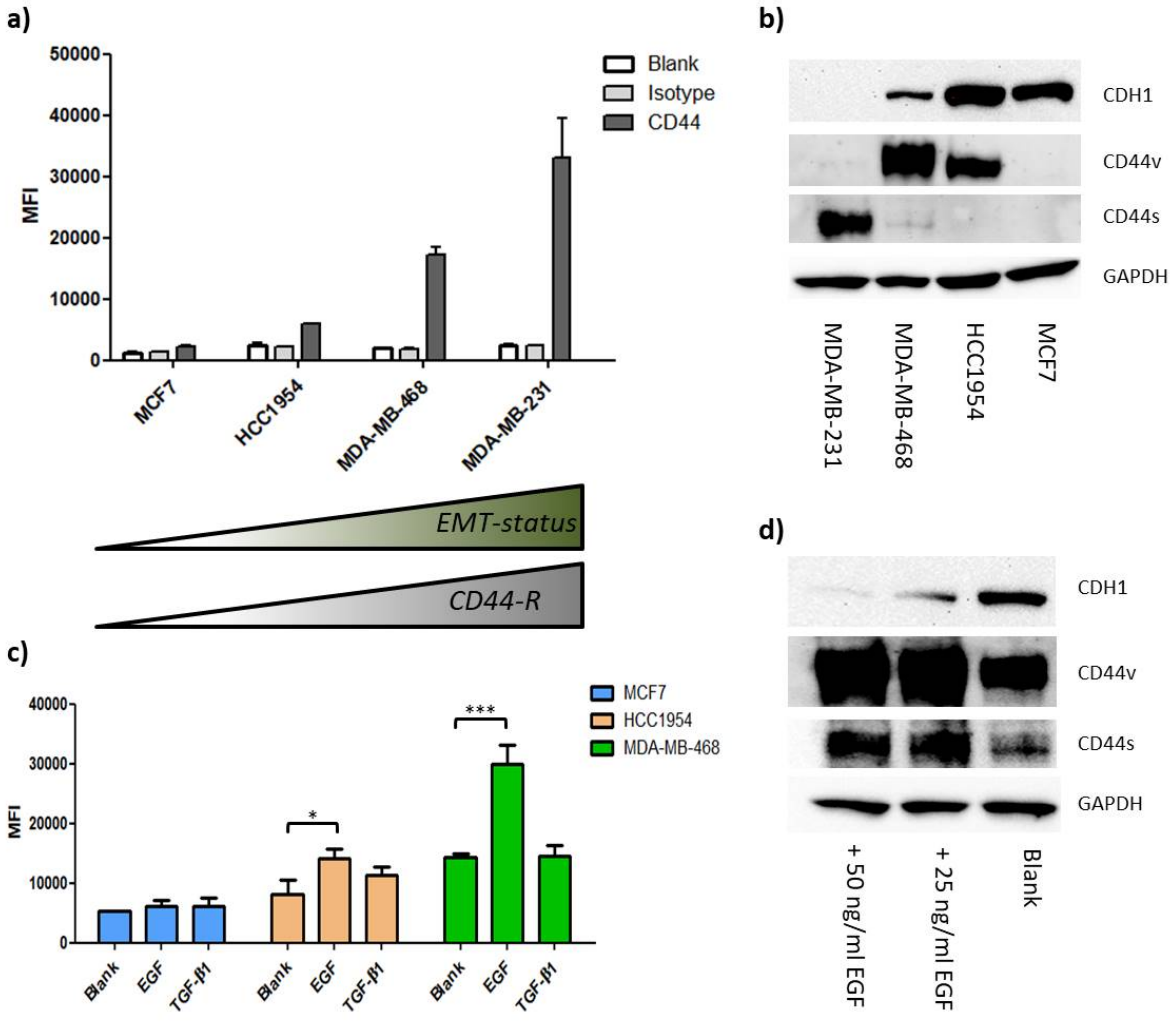

Figure 6. ***(a)*** *Surface CD44 expression in four breast cancer cell lines measured via flow cytometry. Bars show mean fluorescence intensity (MFI). Error bars indicate SD* ***(b)*** *Comparison of protein levels of epithelial marker CDH1, CD44s/v isotypes and GAPDH.* ***(c)*** *Surface pan-CD44 expression in various breast cancer cell lines after growth factor-mediated EMT induction measured via flow cytometry.* ***(d)*** *Protein levels of CDH1, CD44s/v isotypes and GAPDH depending on EGF concentration in MDA-MB-468 cells.*

Additionally, expression of CD44 isoforms in the four cell lines was assessed with Western blotting. Staining for CD44-R with a pan-CD44 antibody allows detection of all CD44 species, as it binds to a conserved region of the protein across splicing variants. As demonstrated in **Figure 6b**, cell lines strongly differed in total CD44-R isotype protein patterns. Epithelial-like MCF7 cells (high levels of CDH1) did not show significant bands for low molecular weight CD44s nor for high molecular weight CD44v. High levels of CD44s were instead observed in mesenchymal-like (absence of CDH1) MDA-MB-231, while CD44v isoforms were not detected. On the contrary, epithelial-like HCC1954 and E/M-hybrid MDA-MB-468 cells exhibited important levels of CD44v (MB-468 > HCC1954) but no/marginal signals for CD44s.. Western blotting only depicts total protein contents and does not differentiate between intracellular and surface CD44 protein. Together with the data obtained by flow cytometry, however, it was concluded that CD44s surface expression seems restricted to EMT-positive MDA-MB-231 cells ($CD44s^{high}$), whereas CD44v-isotypes were dominant in HCC1954 ($CD44v^{low}$) and MDA-MB-468 ($CD44v^{high}$) cell lines. Finally, MCF7 cells lacked expression of both CD44s and CD44v isoforms ($CD44^{null}$). Notably, these findings were congruent with recent studies that highlight CD44-isoform expression heterogeneities among differently graded breast cancer [20, 28].

To further relate CD44 expression to EMT-like changes, the three epithelial cell lines were exposed to EMT-inducers TGF-β1 and EGF (**Figure 6c**). EGF treatment entailed significant upregulation of CD44 in HCC1954 ($P < 0.05$) and MDA-MB-468 ($P < 0.001$) shifting cells into $CD44^{medium\text{-}high}$ and $CD44^{high}$ expressing cells, respectively. On the contrary, TGF-β1 did not provoke similar changes. In a recent publication [23] we demonstrated that TGF-β1 only induces considerable EMT-like changes in HCC1954 in co-action with collagen I/IV. Subsequently, to test which CD44-isoform was affected by the upregulation, Western blotting analysis was performed. As shown in **Figure 6d** EGF-mediated EMT induction in MDA-MB-468 cells, reflected by the decline in CDH1 protein levels, induced the co-expression of CD44s aside from CD44v isoform. Indeed, it is known that overexpression of CD44s receptor is a hallmark of cancer stem cells [12] and that during the course of EMT, cells gain stem-like properties including the so-called “CD44 isotype switching” [28, 74]. Therefore, the effects of cancer progression on CD44-isotypes may influence uptake efficiency and kinetics of drug delivery systems containing HA in cancer cells.

Based on the above findings, we sought to address the following topics regarding HA-mediated drug delivery: 1. Influence of coating procedures and the underlying physico-chemical characteristics of HAPx nanocarriers on particle uptake as a function of CD44 isotype/EMT-status. 2. Uptake kinetics of the respective CD44 isoforms. 3. Improvement of transfection efficiency via HA-coating of polyplexes.

3.2.2 *Highly selective uptake and increased endocytosis of HAPx$^{\pm\zeta}$ in CD44-overexpressing EMT-positive BC cell lines*

In order to verify HA-mediated endocytosis of the different HAPx species and to reveal the influence of the coating procedure, flow cytometry after 24 h of incubation with nanoparticles was conducted (**Figure 7**). To visualize the impact physico-chemical characteristics of HAPx species exert on cellular uptake, hydrodynamic diameter d_h (green line) and zeta potential ζ (orange line) were superimposed with the relative uptake to Px (dotted lines) in the various cell lines. According to CD44 cell surface expression levels, the highest uptake was expected to occur in MDA-MB-231 cells with HAPx in comparison to Px. However, polyplex internalization was found to be more complex with its magnitude to depend on CD44 isotype, HAPx species and coating procedure.

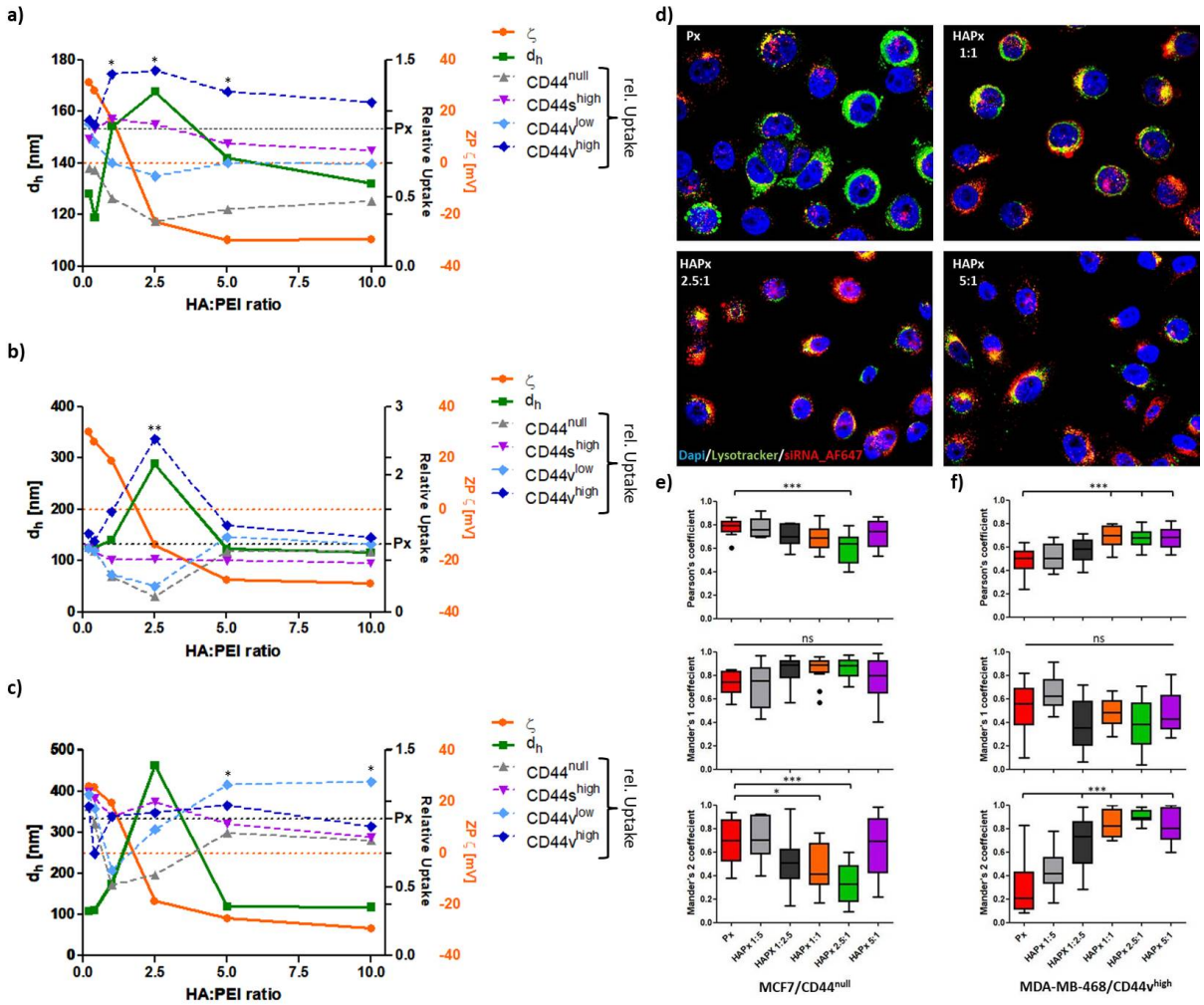

Figure 7. *CD44 (isotype, expression level) and HA:PEI-ratio dependent cellular uptake of HAPx particles produced via* ***(a)*** *2-step coating* ***(b)*** *inverse 2-step coating and* ***(c)*** *1-step coating measured by flow cytometry. Mean relative uptake normalized to Px (black, right y-axis) is shown as dotted line with grey (CD44^{null} MCF7), purple (CD44s^{high} MB-231), light blue (CD44v^{low} HCC1954) and dark blue (CD44v^{high} MB-468) color indicating cell line/CD44-isotype expression level. Solid lines represent mean physico-chemical properties of respective HAPx species with hydrodynamic size (green) and zeta potential (orange) shown on the left and right y-axis,*

respectively. Black dotted line ($y_{right,\ black}$) indicates uptake levels of uncoated Px particles (y = 1). Orange dotted line ($y_{right,\ orange}$) depicts zeta potential at 0 mV. ***(d)*** *Confocal images of MDA-MB-468 cells transfected with different 2-step coated HAPx polyplexes containing AF647-labeled siRNA (red) for 24 h. Cells were stained for nuclei (DAPI, blue) and endo/lysosomal compartments (Lysotracker®, green). Yellow color indicates intracellular co-localization of particles with lysosomes.* ***(e-f)*** *JACoP co-localization analysis (n(cells) ≥ 12) of AF647-labeled siRNA (red) and Lysotracker (green) in MCF7* ***(e)*** *and MDA-MB-468* ***(f)*** *cell lines transfected HAPx for 24 h. Pearson's correlation coefficient (upper panel) and Manders' correlation coefficients 1 (central panel, "red-in-green") and 2 (lower panel, "green-in-red") are shown as whiskers plot.*

Overall, the course of uptake from particles produced via "2-step coating" mostly resembled the one of inversely-coated particles. Instead, 1-step-coated polyplexes followed a different internalization tendency implying distinct HA-surface presentation among the coating procedures.

Notably, uptake of HAPx in $CD44^{null}$ (grey dotted line) and $CD44v^{low}$ (light blue dotted line) cell lines decreased considerably with increasing HA:PEI-ratio as compared to uncoated Px ($CD44^{null}$ < $CD44v^{low}$) following a similar trend throughout the coating procedures with a minimum uptake for $HAPx^{\pm\zeta}$ polyplexes. The latter formulations were internalized up to 77% less (MCF7, **Figure 7b**) whereas $HAPx^{-\zeta}$ polyplexes internalization approached uptake levels of Px. These findings can be explained referring to the physico-chemical characteristics of the different polyplex groups. Smaller, highly positively charged $(HA)Px^{+\zeta}$ exhibited the strongest interaction potential with the negatively charged surface of the cell membrane. $HAPx^{-\zeta}$ displayed similar (small) sizes but had decreased cellular interaction due to their negative zeta potential. Both, the bigger sizes and decreased/negative surface charges of $HAPx^{\pm\zeta}$ were detrimental for endocytosis of nanoparticles accounting for the lowest uptake. In total, the course of uptake was indirectly proportional to the hydrodynamic diameter of polyplexes. It further appeared that CD44 expression still contributed to the 20% increase in overall mean uptake of HAPx in $CD44v^{low}$ over $CD44^{null}$ cells, which was particularly relevant for high HA-content polyplexes $HAPx^{-\zeta}$ produced via 1-step coating (**Figure 7c**)

Strikingly, the course of internalization showed a different picture for $CD44v^{high}$ (dark blue dotted line) and $CD44s^{high}$ (purple dotted line) cell lines, confirming a clear relationship between HA:PEI-ratio and maximum uptake for $HAPx^{\pm\zeta}$ species (140 - 252% of Px, **Figure 7a and b**). Here, relative nanoparticle internalization was directly proportional to the hydrodynamic diameter of polyplexes, whereas the contribution of the zeta potential was insignificant. In another experiment using a higher molecular weight HA we confirmed the role of the HA:PEI-ratio (**Figure S5b)**. However, uptake tendency was not consistent among the three coating procedures since uptake of 1-step coated HAPx in MDA-MB-468/231 remained mostly unchanged independent of the HA:PEI ratio (**Figure 7c**). We believe that the distinct ways of how HA is presented at the surfaces of the particles explain the discrepancies among the coating methods. Surprisingly, the gain in particle uptake in $CD44s^{high}$ MDA-

MB-231 cells was marginal, but it was significant in CD44v^{high} MDA-MB-468 cells (**Figure 7a and b**) despite lower total surface receptor expression.

Although, according to the physico-chemical evaluation of HAPx, coating procedures had moderate influence on particle properties and stability, *in vitro* uptake pointed elsewise. Apparently, HA-molecules were differentially exposed on the particle surface among the particles obtained with the three coating methods. It was proposed that polyplex morphology and intra-particulate arrangements of HA-coated nanoparticles decisively impact HA-presentation and thereby tune the affinity towards its receptor CD44 [50, 58]. Since our data implies superior HA-surface presentation of "2-step"-coated polyplexes with subsequent HA-CD44 interaction to be more likely to occur, the following uptake experiments were restricted to this coating procedure.

Uptake via receptor-mediated endocytosis will eventually guide nanoparticles towards endo/lysosomal compartments. To elicit their intracellular fate and to compare and quantify the opposing course of internalization between CD44^{null} and CD44v^{high} cell lines (**Figure 7a**) confocal imaging was combined with "JACoP" (ImageJ) co-localization analysis. The Pearson's correlation coefficient (PCC) was used to assess the linear relationship between the signal intensities of two fluorophores, where a value of 1 corresponds to complete positive correlation and a value of 0 indicates no correlation [75-77]. However, the significance of the PCC for co-localization events is disputable as values are highly sensitive to differences in signal intensities of the respective channels and to background noises, hence to thresholding. Instead, the Manders' correlation coefficients (M_1 and M_2) depict a less biased measure to analyze the extent of spatial co-occurrence of two fluorophores with values of 1 reflecting 100% co-localization [78, 79]. Here, the M1 coefficient relates to the proportion of polyplexes that are trapped in lysosomes whereas the M2 coefficient indicates the proportion of endosomes containing polyplexes. Notably, Pearson's and Manders' coefficient synergize as the latter quantifies signal co-occurrence and the former quantifies the correlation within the co-occurring signal.

Confocal images showed elevated accumulation of 2-step coated HAPx 1:1, 2.5:1 and 5:1 within lysosomes of CD44v^{high} MDA-MB-468 cells indicated by pronounced co-localization (orange) of labeled siRNA (red) with the LysoTracker^{TM} (green) stain after 24 h of incubation (**Figure 7d**). HA-coated polyplexes showed juxtanuclear positioning, indicative for successful receptor-mediated endocytosis which was less frequently observed for Px particles.

According to the JACoP image analysis shown in **Figure 7e**, strong association of uncoated Px was observed with lysosomes of CD44^{null} MCF7 cells as indicated by a median PCC of 0.80. The PCC decreased for HA-coated species, which was significant in the case of HAPx 2.5:1 ($P < 0.001$). Simultaneously, the fraction of endo/lysosomes bearing HAPx$^{\pm\zeta}$ species (M_2) was significantly reduced to less than 50 %. Still, most internalized particles accumulated within lysosomes independent of HA:PEI-ratio ($0.75 < M_1 < 0.90$). Instead, endocytosis of uncoated Px in CD44v^{high} MDA-MB-468

cells revealed the lowest correlation with lysosomes (**Figure 7f**). Notably, the PCC of HAPx 1:1, 2.5:1 and 5:1 was significantly elevated ($P < 0.001$) which is in good agreement with data obtained from flow cytometry (**Figure 7a**). Likewise, the proportion of lysosomes comprising HAPx 1:2.5 and the latter three polyplex types was significantly increased compared to uncoated Px. 70-90% of lysosomes co-localized with these HAPx opposed to only 28.5% (mean M_2-value) for Px. However, the fraction of polyplexes reaching lysosomes was insignificantly distinct among the nano-formulations but on average less than observed in $CD44^{null}$ MCF7 cells.

To summarize, HA-functionalization of polyplexes entailed overall increased association (PCC) of particles with lysosomes in CD44v-expressing cells but decreased association in CD44 deficient MCF7 cells. Presumably, the contribution of HA/CD44-mediated endocytosis enabled HAPx species to accumulate in a higher fraction of lysosomes compared with overall lower uptake in the $CD44^{null}$ cell line, possibly due to the unfavorable physico-chemical characteristics of HA-coated polyplexes as well as lacking CD44 expression (M_2). The data further suggest that all polyplexes were preferentially taken up via active endocytosis mechanisms referring to the high fraction of particles co-occurring in lysosomes (M_1), regardless of coating. The substantially lower fraction of M_1 in MDA-MB-468 than in MCF7 cells may be indicative for enhanced endosomal escape but may also relate to differences of the endocytic machinery.

The former uptake results ($CD44^{null}$<$CD44v^{low}$<$CD44s^{high}$<$CD44v^{high}$, **Figure 7a, d-f**) were suggestive of HA/CD44-interplay to determine the effectiveness of HAPx particle internalization. To further confirm HA/CD44-mediated endocytosis to be responsible for increased nanoparticle internalization, uptake of Px and HAPx 2.5:1 in MDA-MB-468 cells in presence of excess amounts of HA was compared. Theoretically, free HA binds to and saturates the CD44-R, impeding receptor mediated endocytosis of HAPx. As shown in **Figure S5c**, mere pre-incubation with HA did not affect internalization, whereas HA competition did. The MFI value of HAPx decreased to the same level as observed for uncoated Px denoting CD44-HA interaction to be the main cause of elevated particle uptake of HAPx polyplexes.

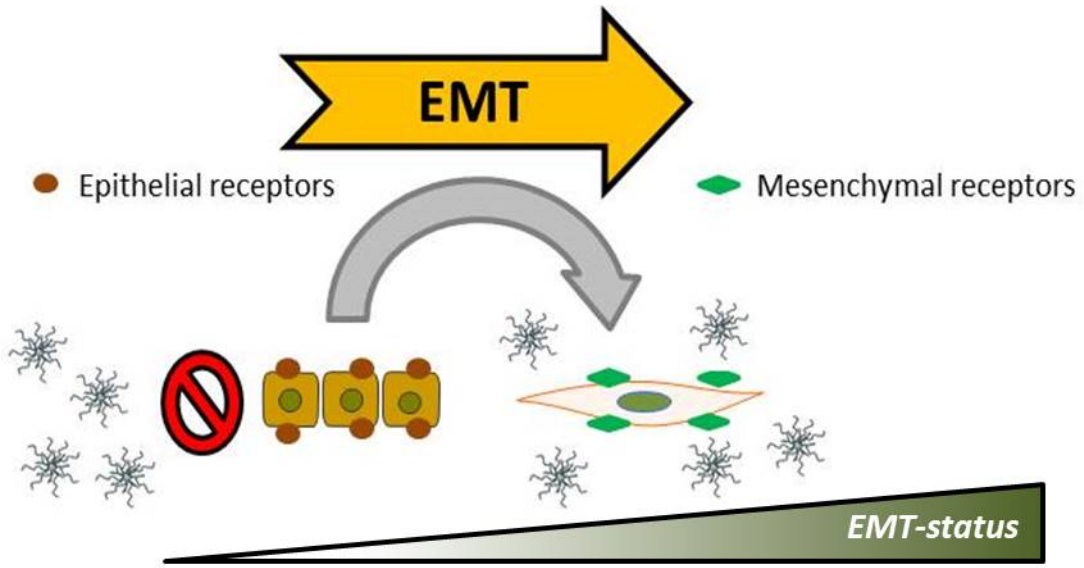

	CD44^{null}	CD44v^{low}	CD44v^{high}	CD44s^{high}
Relative Uptake Px	1.0	1.03	1.24	0.83
Rel. Uptake HAPx 2.5:1	1.0	2.11	5.56	2.64
ΔMFI Px:HAPx [%]	- 68.0	- 34.5	+ 42.4	+2.9

Figure 8. *Uptake-selectivity of HA-coated polyplexes over uncoated Px for mesenchymal phenotype in breast cancer cells.*

3.2.3 CD44-R isoforms follow different uptake kinetics

A potential positive linear relationship between EMT-status and CD44-expression is however, further complicated by the existence of distinct isoforms as well as by the phenomenon of isotype switching, altering the CD44v/s-expression ratio as was demonstrated by growth factor-mediated EMT induction in MDA-MB-468 (**Figure 6c/d**). Thus, particle uptake after 48 h of EGF-dependent EMT induction was examined. Notably, overall particle uptake nearly doubled for the highest (50 ng/ml) EGF concentration while the superior uptake of HA-coated polyplexes disappeared (**Figure S5d).** More malignant phenotypes seem to be capable of internalizing a higher fraction of particles regardless of coating. Indeed, it was recently revealed that mesenchymal cells or cells induced to undergo EMT exhibited hastened endo/lysosome maturation and accelerated endocytoses/endocytic recycling processes than epithelial phenotypes [80]. Moreover, the different CD44-isotypes expressed at the cell surface before and after EMT-induction could have influenced endocytosis of HAPx polyplexes. Consequently, approaches targeting EMT or malignant breast cancer via CD44-HA interaction need to consider the CD44-isotype switching possibly leading to different uptake kinetics of the distinct isoforms.

To further distinguish between CD44v- and CD44s-mediated uptake, earlier time points (1 h and 4 h) after transfection with Px and HAPx (1:2.5, 1:1 and 2.5:1) in CD44v^{high}/CD44s^{low} MDA-MB-468 and CD44v^{low}/CD44s^{high} MDA-MB-231 cells were investigated. CD44v^{low}/CD44s^{low} MCF7 cell line (CD44^{null}) was included as negative control, as a cell line in which HA-CD44 related internalization does not importantly contribute to overall particle uptake. Our data revealed increased uptake (167%) of HAPx 1:1 in CD44s^{high} cells already 1 h after transfection. On the contrary, uptake of the same HAPx species was dramatically reduced in CD44^{null} (5% of Px) and CD44v^{high} (23% of Px) cell lines (**Figure 9a**). However, internalization of HAPx 1:1 stagnated in CD44s^{high} cells(137% of Px after 4 h) but considerably increased to over 345% in CD44v^{high} cells after 4 h (**Figure 9b**). At the same time, transfection with both HAPx$^{\pm\zeta}$ species remained below 20% of Px in CD44^{null} cells, underlining the interrelation of high CD44 (s/v) expression and HAPx uptake. HAPx 1:2.5, physico-chemically resembling Px particles, showed a minor but overall comparable uptake profile as uncoated Px in CD44^{null} cells. However, it appeared that even little amounts of HA improved uptake after 4 h in CD44s/v expressing cell lines.

In summary, the uptake study performed at different time points implies two major findings.

Ultimately, the first finding implicated by this uptake study is that the conceptual idea of specifically targeting EMT i.e., a more mesenchymal phenotype via HA-CD44-R interaction could be realizable by means of HA-coatings of polyplexes. Referring to **Figure 8**, HAPx$^{\pm\zeta}$ polyplexes displayed a highly selective uptake for EMT-positive cell lines MDA-MB-468 and MDA-MB-231. Selectivity was confirmed by decreased uptake (compared to uncoated Px) in epithelial MCF7 (- 68.0%) and HCC1954 cells (- 34.5%) but concomitant increase in mesenchymal cells (2.6- to 5.6-fold). Likewise, HA-coated octa-arginine gene vectors efficiently induced transgene expression in CD44^{high} HCT116 cancer cells which was instead significantly compromised in CD44^{low} NIH3T3 cells [47]. Since MCF7 cells exhibit features of differentiated mammary epithelium [81], our data suggest that HA-coated nanoformulations could preferrably interact with CD44^{high} malignant cancer cells, sparing healthy epithelium in comparison. It is thought that ligand distribution on the nanoparticle surfaces governs the efficacy of receptor-mediated endocytosis with uniform ligand distribution leading to optimal uptake [82]. Indeed, the precise formulation development of HA-coated nanoparticles was found to be key for the desired targeting concept. HA:PEI-ratio, coating strategy and the resulting physico-chemical differences heavily impacted its success.

Second, our data indicate that CD44s-R uptake kinetics are faster in the early phase but probably suffer from receptor saturation at later time points compared with CD44v-R (**Figure 7/9**). CD44s^{high} MDA-MB-231 cells after 1h incorporated HAPx 1:1 particles twice as fast as in case of CD44v^{high} MDA-MB-468 and about 6-times faster than in CD44^{null} MCF7 cells. However, after 24 h, this beneficial effect was no longer observed with values similar to Px uptake. These findings are in great conformity with a study by Spadea *et al.* who investigated uptake of fluorescently-labeled HA in the

same cell lines [20]. They assigned MDA-MB-231 cells as efficient "HA uptaker" with a high score for HA binding after 1 h and a moderate score for internalization after 24 h. In contrast, CD44v expressing MDA-MB-468 cells were attributed a low HA binding capacity (1h) and poor levels of internalization (24h). This goes in line with our data confirming minimal uptake after 1 h (**Figure 9a**). However, this observation is in contrast to the observed superior HAPx uptake in this cell line after 4 h and 24 h. More precisely, MFI values of HAPx 1:1 in CD44v^{high} cells increased 10-fold in between the 1 h and 4 h time point and remained elevated (1.42-fold normalized to Px) after 24 h. Instead, cells transfected with uncoated Px only exhibited a 3-fold increase in the same timeframe (1-4 h). Thus, from our data we conclude slower but increased net uptake via the CD44v-R isoform(s) as compared to CD44s-R. However, possible cell line peculiarities regarding endocytic processing [83] and the fact that HA-decorated particles were used rather than free HA leaves room for additional interpretation. Notably, the glycosylation state of CD44, which is cell line dependent, inversely correlates with HA-binding capacity [11]. Furthermore, as stated elsewhere [58, 82, 84], the degree of receptor clustering which depends on particle dimension, ligand exposure and differences in receptor densities (**Figure 6a**) affects the total number of uptake events further complicating the scenario. In line with the mentioned literature, bigger-sized HAPx$^{\pm\zeta}$ species showed the highest uptake explained by their physical size allowing for extended cross-linking of CD44 receptors once engaging with the cellular membrane. Likewise, a strong positive zeta potential seemed to generally relate to higher particle internalization as compared to negatively charged HAPx polyplexes. Moreover, uptake strategies via the CD44s-R supposedly suffer from receptor saturation which was found to be a result of the slow CD44-R turnover and re-presentation at the cell surface after HA binding [57, 58, 85]. Interestingly, studies indicated CD44v isoform turnaround time to be faster [11], attenuating the receptor saturation effect as was observed in CD44v^{high} MDA-MB-468 cells (**Figure 7a, Figure 9a/b)**.

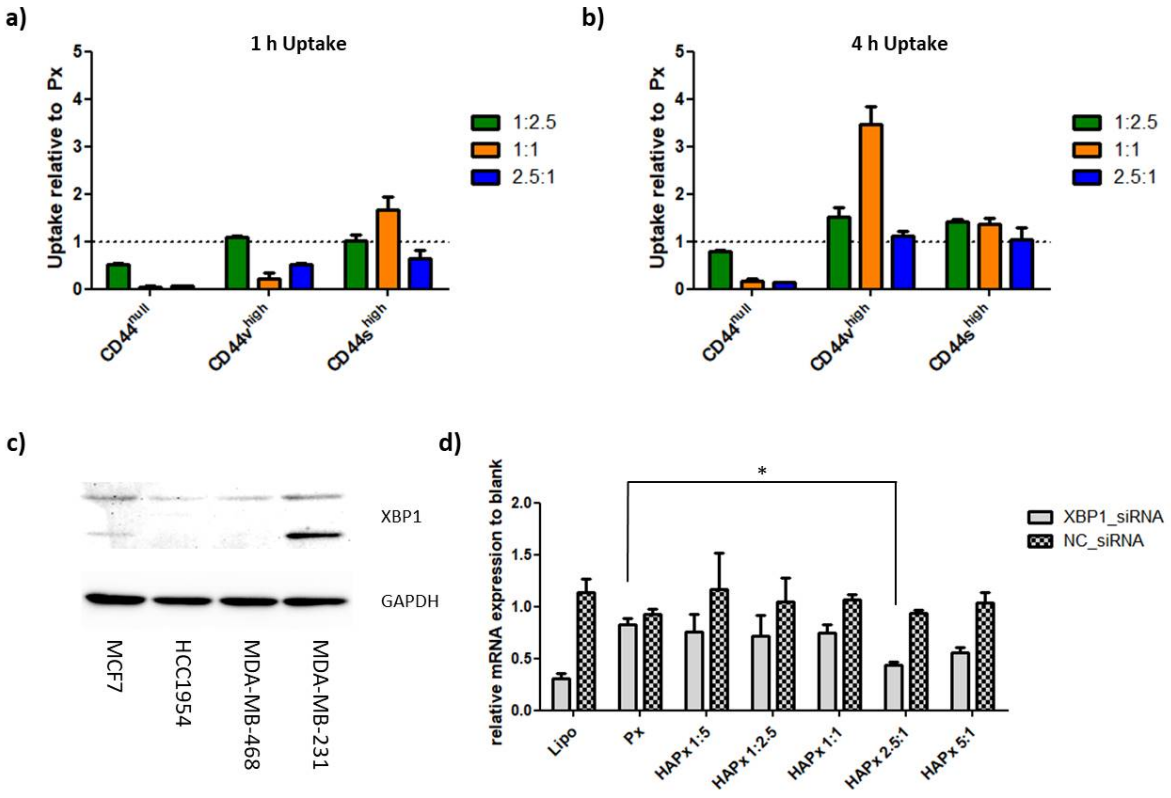

Figure 9. *Cellular uptake of HAPx 1:2.5, 1:1 and 2.5:1 in CD44^{null}, CD44v^{high} and CD44s^{high} cell lines measured via flow cytometry after 1 h* ***(a)*** *and 4 h* ***(b)*** *of incubation. Uptake is shown as relative MFI to uptake of Px particles (black dotted line).* ***(c)*** *Protein levels of XBP1 in the 4 breast cancer cell lines assessed from a nuclear protein extract.* ***(d)*** *XBP1 mRNA knockdown in MDA-MB-231 cells analyzed via RT-qPCR. Results are shown as ΔΔCt-values with error bars indicating the standard deviation SD (n=2)*

3.2.4 *HAPx showed improved but HA:PEI-ratio dependent silencing of XBP1 transcription factor in MDA-MB-231 cells*

Finally, gene silencing efficiency (48 h) of HAPx species (2-step coating) compared to uncoated Px was examined. A possible molecular target regarding EMT is the transcription factor XBP1 (X-box binding protein 1). Recently, besides our group showing EMT induction to entail upregulation of XBP1 in breast cancer (see Chapter IV) its relevance for EMT was proposed in several other publications [37, 86-88]. Indeed, high XBP1 protein levels were found in mesenchymal MDA-MB-231 cells compared to the other three cell lines (**Figure 9c**).

Transfection of MDA-MB-231 cells (CD44s^{high}) with XBP1_siRNA containing lipoplexes (Lipofectamine^{TM} 2000) resulted in considerable downregulation of XBP1 mRNA (70%) confirming

the effectiveness of RNAi (**Figure 9d**). Notably, transfection with PEI-polyplexes (Px) was insufficient to decisively decrease mRNA expression. Introduction of HA via 2-step coating slightly improved knockdown efficiency for HAPx 1:5, 1:2.5, 1:1 and 5:1, but the only polyplex formulation mediating significant gene silencing ($P < 0.05$, 55%) was HAPx 2.5:1.

Consequently, consistent with data of the uptake study, knockdown efficiency was improved via HA-coating but the formulation has to be optimized particularly with regards to HA:PEI-ratio. We believe, however, that the enhanced knockdown was not only due to increased particle uptake within the first 24h, but also due to alteration in nucleic acid binding and/or siRNA-release properties of HA-containing polyplexes. In further studies, release kinetics of HAPx polyplexes need to be investigated, and knockdown studies comparing the three different coating procedures must be included to further elicit impact of coating procedures on therapeutic efficacy of HA-coated polyplexes (**Figure 1-3**). Moreover, a comparison of knockdown efficiency as a function of CD44 isotype expression would definitely contribute to overall understanding of HA-mediated drug delivery.

4 Conclusion

Nanoparticulate drug delivery systems comprising HA surface modifications provide carriers with targeting- and stealth-features which are required to achieve tumor-specific accumulation, reduce off-target effects and to increase half-life and stability upon systemic administration. They are also clinically promising candidates in the context of the treatment of cancers undergoing EMT. Notably, more complex, HA-functionalized polymeric nanocarriers were shown to fit into the "3S-Transition" concept hypothesized for efficient drug delivery in cancer [33, 68]. Accordingly, HA-functionalization fulfills stability, surface and size transitions requirements as it helps the carrier to protect the drug cargo during circulation for selective interaction with and release in tumor cells via CD44-mediated endocytosis. Moreover, these carriers may also be accessible for enzymatic size reduction of particles at the tumor site considered to be beneficial for their in-depth penetration and therapeutic efficacy.

Indeed, this study demonstrates the versatile character of HA-coated polyplexes with regard to *in vitro* stability and biological performance. Whereas physico-chemical characteristics of differently coated polyplex formulations were shown to be mostly comparable, the coating procedure was identified as a crucial factor during cellular uptake experiments. Ultimately, the ease of the coating methodology and the resultant benefits for particle stability, cell uptake and cancer cell-specificity are upholding the value of HA-coated nanocarriers for drug delivery. HA-coatings provide a therapeutic option for the treatment of otherwise undruggable aggressive types of breast cancer such as those that undergo EMT. The ambiguous nature of CD44 isoforms in receptor-mediated endocytosis, however, may require CD44-expression profiling of patient tumor samples to predict the success of HA-based drug delivery in anticancer therapy and needs to be considered in *in vitro* experiments as well.

5. References

[1] Y. Min, J.M. Caster, M.J. Eblan, A.Z. Wang, *Chem. Rev.* **2015**, *115*(*19*): p. 11147-11190, DOI: 10.1021/acs.chemrev.5b00116.

[2] V. Sanna, M. Sechi, *ACS Med. Chem. Lett.* **2020**, *11*(*6*): p. 1069-1073, DOI: 10.1021/acsmedchemlett.0c00075.

[3] M. Srinivasarao, C.V. Galliford, P.S. Low, *Nature Reviews Drug Discovery* **2015**, *14*(*3*): p. 203-219, DOI: 10.1038/nrd4519.

[4] C.M. Paulos, J.A. Reddy, C.P. Leamon, M.J. Turk, P.S. Low, *Mol. Pharmacol.* **2004**, *66*(*6*): p. 1406-14, DOI: 10.1124/mol.104.003723.

[5] G. Onzi, S.S. Guterres, A.R. Pohlmann, L.A. Frank. **2021**, Springer International Publishing: Cham. p. 1-13, DOI: 10.1007/978-3-030-51519-5_109-1.

[6] K. Ulbrich, K. Holá, V. Šubr, A. Bakandritsos, J. Tuček, R. Zbořil, *Chem. Rev.* **2016**, *116*(*9*): p. 5338-5431, DOI: 10.1021/acs.chemrev.5b00589.

[7] A.C. Marques, P.J. Costa, S. Velho, M.H. Amaral, *J. Control. Release* **2020**, *320*: p. 180-200, DOI: https://doi.org/10.1016/j.jconrel.2020.01.035.

[8] C.D. Walkey, W.C.W. Chan, *Chem. Soc. Rev.* **2012**, *41*(*7*): p. 2780-2799, DOI: 10.1039/C1CS15233E.

[9] V.M. Platt, F.C. Szoka, Jr., *Mol. Pharm.* **2008**, *5*(*4*): p. 474-486, DOI: 10.1021/mp800024g.

[10] J.M. Rios de la Rosa, P. Pingrajai, M. Pelliccia, A. Spadea, E. Lallana, A. Gennari, I.J. Stratford, W. Rocchia, A. Tirella, N. Tirelli, *Advanced Healthcare Materials* **2019**, *8*(*24*): p. 1901182, DOI: https://doi.org/10.1002/adhm.201901182.

[11] J.M. Rios de la Rosa, A. Tirella, N. Tirelli, *Advanced Biosystems* **2018**, *2*(*6*): p. 1800049, DOI: https://doi.org/10.1002/adbi.201800049.

[12] J.M. Wickens, H.O. Alsaab, P. Kesharwani, K. Bhise, M. Amin, R.K. Tekade, U. Gupta, A.K. Iyer, *Drug Discov. Today* **2017**, *22*(*4*): p. 665-680, DOI: 10.1016/j.drudis.2016.12.009.

[13] W.-Y. Huang, J.-N. Lin, J.-T. Hsieh, S.-C. Chou, C.-H. Lai, E.-J. Yun, U.G. Lo, R.-C. Pong, J.-H. Lin, Y.-H. Lin, *ACS Applied Materials & Interfaces* **2016**, *8*(*45*): p. 30722-30734, DOI: 10.1021/acsami.6b10029.

[14] S. Misra, P. Heldin, V.C. Hascall, N.K. Karamanos, S.S. Skandalis, R.R. Markwald, S. Ghatak, *FEBS J.* **2011**, *278*(*9*): p. 1429-43, DOI: 10.1111/j.1742-4658.2011.08071.x.

[15] H. Xu, M. Niu, X. Yuan, K. Wu, A. Liu, *Experimental Hematology & Oncology* **2020**, *9*(*1*): p. 36, DOI: 10.1186/s40164-020-00192-0.

[16] C. Chen, S. Zhao, A. Karnad, J.W. Freeman, *J. Hematol. Oncol.* **2018**, *11*(*1*): p. 64, DOI: 10.1186/s13045-018-0605-5.

[17] L.T. Senbanjo, M.A. Chellaiah, *Front. Cell Dev. Biol.* **2017**, *5*, DOI: 10.3389/fcell.2017.00018.

[18] M. Hassn Mesrati, S.E. Syafruddin, M.A. Mohtar, A. Syahir, *Biomolecules* **2021**, *11*(*12*): p. 1850.

[19] S. Porcellini, C. Asperti, S. Corna, E. Cicoria, V. Valtolina, A. Stornaiuolo, B. Valentinis, C. Bordignon, C. Traversari, *Front. Immunol.* **2020**, *11*, DOI: 10.3389/fimmu.2020.00099.

[20] A. Spadea, J.M. Rios de la Rosa, A. Tirella, M.B. Ashford, K.J. Williams, I.J. Stratford, N. Tirelli, M. Mehibel, *Mol. Pharm.* **2019**, *16*(*6*): p. 2481-2493, DOI: 10.1021/acs.molpharmaceut.9b00083.

[21] H. Son, A. Moon, *Toxicological research* **2010**, *26*(*4*): p. 245-252, DOI: 10.5487/TR.2010.26.4.245.

[22] J. Banyard, D.R. Bielenberg, *Connect. Tissue Res.* **2015**, *56*(*5*): p. 403-413, DOI: 10.3109/03008207.2015.1060970.

[23] L.M. Isert, A.; Loiudice, G.; Oliva, A.; Roidl, A.; Merkel, O., *Preprints 2023* **2023**, *2023030147*, DOI: https://doi.org/10.20944/preprints202303.0147.v1.

[24] M.A. Nieto, R.Y. Huang, R.A. Jackson, J.P. Thiery, *Cell* **2016**, *166*(*1*): p. 21-45, DOI: 10.1016/j.cell.2016.06.028.
[25] M. Yilmaz, G. Christofori, *Cancer Metastasis Rev.* **2009**, *28*(*1*): p. 15-33, DOI: 10.1007/s10555-008-9169-0.
[26] M. Scimeca, C. Antonacci, D. Colombo, R. Bonfiglio, O.C. Buonomo, E. Bonanno, *Tumour Biol.* **2016**, *37*(*4*): p. 5427-35, DOI: 10.1007/s13277-015-4361-7.
[27] S.V. Vasaikar, A.P. Deshmukh, P. den Hollander, S. Addanki, N.A. Kuburich, S. Kudaravalli, R. Joseph, J.T. Chang, R. Soundararajan, S.A. Mani, *Br. J. Cancer* **2021**, *124*(*1*): p. 259-269, DOI: 10.1038/s41416-020-01178-9.
[28] R.L. Brown, L.M. Reinke, M.S. Damerow, D. Perez, L.A. Chodosh, J. Yang, C. Cheng, *J. Clin. Invest.* **2011**, *121*(*3*): p. 1064-74, DOI: 10.1172/jci44540.
[29] H. Zhang, R.L. Brown, Y. Wei, P. Zhao, S. Liu, X. Liu, Y. Deng, X. Hu, J. Zhang, X.D. Gao, Y. Kang, A.M. Mercurio, H.L. Goel, C. Cheng, *Genes Dev.* **2019**, *33*(*3-4*): p. 166-179, DOI: 10.1101/gad.319889.118.
[30] E. Olsson, G. Honeth, P.-O. Bendahl, L.H. Saal, S. Gruvberger-Saal, M. Ringnér, J. Vallon-Christersson, G. Jönsson, K. Holm, K. Lövgren, M. Fernö, D. Grabau, Å. Borg, C. Hegardt, *BMC Cancer* **2011**, *11*(*1*): p. 418, DOI: 10.1186/1471-2407-11-418.
[31] R.A. Weinberg, *The Biology of Cancer*, **2014**.
[32] S.E. Leggett, A.M. Hruska, M. Guo, I.Y. Wong, *Cell Communication and Signaling* **2021**, *19*(*1*): p. 32, DOI: 10.1186/s12964-021-00713-2.
[33] W. Zhong, L. Pang, H. Feng, H. Dong, S. Wang, H. Cong, Y. Shen, Y. Bing, *Carbohydrate Polymers* **2020**, *238*: p. 116204, DOI: https://doi.org/10.1016/j.carbpol.2020.116204.
[34] Y.R. Zhang, R. Lin, H.J. Li, W.L. He, J.Z. Du, J. Wang, *Wiley interdisciplinary reviews. Nanomedicine and nanobiotechnology* **2019**, *11*(*1*): p. e1519, DOI: 10.1002/wnan.1519.
[35] G. Nabil, R. Alzhrani, **2021**, *13*(*4*), DOI: 10.3390/cancers13040898.
[36] V. Hintze, M. Schnabelrauch, S. Rother, *Frontiers in chemistry* **2022**, *10*: p. 830671, DOI: 10.3389/fchem.2022.830671.
[37] X. Chen, D. Iliopoulos, Q. Zhang, Q. Tang, M.B. Greenblatt, M. Hatziapostolou, E. Lim, W.L. Tam, M. Ni, Y. Chen, J. Mai, H. Shen, D.Z. Hu, S. Adoro, B. Hu, M. Song, C. Tan, M.D. Landis, M. Ferrari, S.J. Shin, M. Brown, J.C. Chang, X.S. Liu, L.H. Glimcher, *Nature* **2014**, *508*(*7494*): p. 103-107, DOI: 10.1038/nature13119.
[38] L. Isert, A. Mehta, F. Adams, O.M. Merkel, G.R. Rosania and G.M. Thurber, Editors. **2021**, Springer US: New York, NY. p. 383-396, DOI: 10.1007/978-1-0716-1250-7_17.
[39] J. Hendrix, V. Baumgärtel, W. Schrimpf, S. Ivanchenko, M.A. Digman, E. Gratton, H.G. Kräusslich, B. Müller, D.C. Lamb, *J. Cell Biol.* **2015**, *210*(*4*): p. 629-46, DOI: 10.1083/jcb.201504006.
[40] W. Schrimpf, A. Barth, J. Hendrix, D.C. Lamb, *Biophys. J.* **2018**, *114*(*7*): p. 1518-1528, DOI: 10.1016/j.bpj.2018.02.035.
[41] S. Ivanchenko, D.C. Lamb. in *Supramolecular Structure and Function 10*. **2011**. Dordrecht: Springer Netherlands.
[42] J. Schindelin, I. Arganda-Carreras, E. Frise, V. Kaynig, M. Longair, T. Pietzsch, S. Preibisch, C. Rueden, S. Saalfeld, B. Schmid, J.-Y. Tinevez, D.J. White, V. Hartenstein, K. Eliceiri, P. Tomancak, A. Cardona, *Nat. Methods* **2012**, *9*(*7*): p. 676-682, DOI: 10.1038/nmeth.2019.
[43] S. Park, U. Han, D. Choi, J. Hong, *Biomaterials Research* **2018**, *22*(*1*): p. 29, DOI: 10.1186/s40824-018-0139-5.
[44] H. Wang, S. Zhang, J. Lv, Y. Cheng, *VIEW* **2021**, *2*(*3*): p. 20200026, DOI: https://doi.org/10.1002/VIW.20200026.
[45] C.T. Greco, J.C. Andrechak, T.H. Epps, M.O. Sullivan, *Biomacromolecules* **2017**, *18*(*6*): p. 1814-1824, DOI: 10.1021/acs.biomac.7b00265.
[46] A. Tirella, K. Kloc-Muniak, L. Good, J. Ridden, M. Ashford, S. Puri, N. Tirelli, *Int. J. Pharm.* **2019**, *561*: p. 114-123, DOI: https://doi.org/10.1016/j.ijpharm.2019.02.032.

[47] Y. Yamada, M. Hashida, H. Harashima, *Biomaterials* **2015**, *52*: p. 189-198, DOI: https://doi.org/10.1016/j.biomaterials.2015.02.027.
[48] A.R. Petosa, D.P. Jaisi, I.R. Quevedo, M. Elimelech, N. Tufenkji, *Environ. Sci. Technol.* **2010**, *44*(*17*): p. 6532-6549, DOI: 10.1021/es100598h.
[49] P. Snetkov, K. Zakharova, **2020**, *12*(*8*), DOI: 10.3390/polym12081800.
[50] A. Almalik, R. Donno, C.J. Cadman, F. Cellesi, P.J. Day, N. Tirelli, *J. Control. Release* **2013**, *172*(*3*): p. 1142-50, DOI: 10.1016/j.jconrel.2013.09.032.
[51] A. Almalik, I. Alradwan, M.A. Kalam, A. Alshamsan, *Saudi Pharmaceutical Journal* **2017**, *25*(*6*): p. 861-867, DOI: https://doi.org/10.1016/j.jsps.2016.12.008.
[52] M. Zhu, S. Perrett, G. Nie, *Small* **2013**, *9*(*9-10*): p. 1619-1634, DOI: https://doi.org/10.1002/smll.201201630.
[53] D. Docter, U. Distler, W. Storck, J. Kuharev, D. Wünsch, A. Hahlbrock, S.K. Knauer, S. Tenzer, R.H. Stauber, *Nat. Protoc.* **2014**, *9*(*9*): p. 2030-2044, DOI: 10.1038/nprot.2014.139.
[54] W. Richtering, I. Alberg, R. Zentel, *Small* **2020**, *16*(*39*): p. 2002162, DOI: https://doi.org/10.1002/smll.202002162.
[55] S. Khan, A. Gupta, C.K. Nandi, *The Journal of Physical Chemistry Letters* **2013**, *4*(*21*): p. 3747-3752, DOI: 10.1021/jz401874u.
[56] F.S.M. Tekie, M. Hajiramezanali, P. Geramifar, M. Raoufi, R. Dinarvand, M. Soleimani, F. Atyabi, *Sci. Rep.* **2020**, *10*(*1*): p. 9664, DOI: 10.1038/s41598-020-66572-y.
[57] N.M. Zaki, A. Nasti, N. Tirelli, *Macromol. Biosci.* **2011**, *11*(*12*): p. 1747-1760, DOI: https://doi.org/10.1002/mabi.201100156.
[58] A. Almalik, S. Karimi, S. Ouasti, R. Donno, C. Wandrey, P.J. Day, N. Tirelli, *Biomaterials* **2013**, *34*(*21*): p. 5369-5380, DOI: https://doi.org/10.1016/j.biomaterials.2013.03.065.
[59] M. Bros, L. Nuhn, J. Simon, L. Moll, V. Mailänder, K. Landfester, S. Grabbe, *Front. Immunol.* **2018**, *9*, DOI: 10.3389/fimmu.2018.01760.
[60] M. Suvarna, S. Dyawanapelly, B. Kansara, P. Dandekar, R. Jain, *ACS Applied Nano Materials* **2018**, *1*(*10*): p. 5524-5535, DOI: 10.1021/acsanm.8b01019.
[61] J.J. Green, E. Chiu, E.S. Leshchiner, J. Shi, R. Langer, D.G. Anderson, *Nano Lett.* **2007**, *7*(*4*): p. 874-879, DOI: 10.1021/nl062395b.
[62] L. Nuhn, M. Hirsch, B. Krieg, K. Koynov, K. Fischer, M. Schmidt, M. Helm, R. Zentel, *ACS nano* **2012**, *6*(*3*): p. 2198-2214, DOI: 10.1021/nn204116u.
[63] O.M. Merkel, D. Librizzi, A. Pfestroff, T. Schurrat, K. Buyens, N.N. Sanders, S.C. De Smedt, M. Behe, T. Kissel, *J Control Release* **2009**, *138*(*2*): p. 148-59, DOI: S0168-3659(09)00305-8 [pii] 10.1016/j.jconrel.2009.05.016.
[64] B.M. Cooper, D. Putnam, *ACS Biomaterials Science & Engineering* **2016**, *2*(*11*): p. 1837-1850, DOI: 10.1021/acsbiomaterials.6b00363.
[65] B. Naeye, H. Deschout, V. Caveliers, B. Descamps, K. Braeckmans, C. Vanhove, J. Demeester, T. Lahoutte, S.C. De Smedt, K. Raemdonck, *Biomaterials* **2013**, *34*(*9*): p. 2350-2358, DOI: https://doi.org/10.1016/j.biomaterials.2012.11.058.
[66] M. Zheng, D. Librizzi, A. Kılıç, Y. Liu, H. Renz, O.M. Merkel, T. Kissel, *Biomaterials* **2012**, *33*(*27*): p. 6551-6558, DOI: https://doi.org/10.1016/j.biomaterials.2012.05.055.
[67] I.S. Bayer, *Molecules (Basel, Switzerland)* **2020**, *25*(*11*), DOI: 10.3390/molecules25112649.
[68] L. Zhong, L. Xu, Y. Liu, Q. Li, D. Zhao, Z. Li, H. Zhang, H. Zhang, Q. Kan, Y. Wang, J. Sun, Z. He, *Acta Pharmaceutica Sinica B* **2019**, *9*(*2*): p. 397-409, DOI: https://doi.org/10.1016/j.apsb.2018.11.006.
[69] M.B. Parmar, D.N. Meenakshi Sundaram, R.B. K.C, R. Maranchuk, H. Montazeri Aliabadi, J.C. Hugh, R. Löbenberg, H. Uludağ, *Acta Biomater.* **2018**, *66*: p. 294-309, DOI: https://doi.org/10.1016/j.actbio.2017.11.036.
[70] A. Almalik, H. Benabdelkamel, A. Masood, I.O. Alanazi, I. Alradwan, M.A. Majrashi, A.A. Alfadda, W.M. Alghamdi, H. Alrabiah, N. Tirelli, A.H. Alhasan, *Sci. Rep.* **2017**, *7*(*1*): p. 10542, DOI: 10.1038/s41598-017-10836-7.

[71] P. Kesharwani, R. Chadar, A. Sheikh, W.Y. Rizg, A.Y. Safhi*, Front. Pharmacol.* **2022**, *12*, DOI: 10.3389/fphar.2021.800481.
[72] J.A. Hinneh, J.L. Gillis, N.L. Moore, L.M. Butler, M.M. Centenera*, Front. Oncol.* **2022**, *12*, DOI: 10.3389/fonc.2022.982231.
[73] M. Veiseh, S.J. Leith, C. Tolg, S.S. Elhayek, S.B. Bahrami, L. Collis, S. Hamilton, J.B. McCarthy, M.J. Bissell, E. Turley*, Front. Cell Dev. Biol.* **2015**, *3*, DOI: 10.3389/fcell.2015.00063.
[74] C.C. Warzecha, R.P. Carstens*, Semin. Cancer Biol.* **2012**, *22*(*5-6*): p. 417-27, DOI: 10.1016/j.semcancer.2012.04.003.
[75] K.J.F. Carnevale, G.F. Strouse*, Bioconjug. Chem.* **2018**, *29*(*10*): p. 3429-3440, DOI: 10.1021/acs.bioconjchem.8b00575.
[76] M. Li, X. Jin, T. Liu, F. Fan, F. Gao, S. Chai, L. Yang*, Nat. Commun.* **2022**, *13*(*1*): p. 4137, DOI: 10.1038/s41467-022-31882-4.
[77] B. Steensel, E. Binnendijk, C. Hornsby, H. van der Voort, Z. Krozowski, E. de Kloet, R. Driel*, J. Cell Sci.* **1996**, *109 (Pt 4)*: p. 787-92, DOI: 10.1242/jcs.109.4.787.
[78] S. BOLTE, F.P. CORDELIÈRES*, J. Microsc.* **2006**, *224*(*3*): p. 213-232, DOI: https://doi.org/10.1111/j.1365-2818.2006.01706.x.
[79] A.M. Moreno-Echeverri, E. Susnik, D. Vanhecke, P. Taladriz-Blanco, S. Balog, A. Petri-Fink, B. Rothen-Rutishauser*, Journal of nanobiotechnology* **2022**, *20*(*1*): p. 464, DOI: 10.1186/s12951-022-01670-9.
[80] P. Banerjee, G.Y. Xiao, X. Tan, V.J. Zheng, L. Shi, M.N.B. Rabassedas*,* **2021**, *12*(*1*): p. 6354, DOI: 10.1038/s41467-021-26677-y.
[81] E.A. Pérez-Yépez, J.-T. Ayala-Sumuano, A.M. Reveles-Espinoza, I. Meza*, Int. J. Breast Cancer* **2012**, *2012*: p. 609148, DOI: 10.1155/2012/609148.
[82] L. Li, Y. Zhang, J. Wang*,* **2017**, *4*(*5*): p. 170063, DOI: 10.1098/rsos.170063.
[83] A. Albanese, W.C. Chan*, ACS nano* **2011**, *5*(*7*): p. 5478-89, DOI: 10.1021/nn2007496.
[84] A. Bandyopadhyay, R.L. Fine, S. Demento, L.K. Bockenstedt, T.M. Fahmy*, Biomaterials* **2011**, *32*(*11*): p. 3094-105, DOI: 10.1016/j.biomaterials.2010.12.054.
[85] S. Ouasti, P.J. Kingham, G. Terenghi, N. Tirelli*, Biomaterials* **2012**, *33*(*4*): p. 1120-1134, DOI: https://doi.org/10.1016/j.biomaterials.2011.10.009.
[86] H. Li, X. Chen, Y. Gao, J. Wu, F. Zeng, F. Song*, Cell. Signal.* **2015**, *27*(*1*): p. 82-89, DOI: https://doi.org/10.1016/j.cellsig.2014.09.018.
[87] W. Shi, Z. Chen, L. Li, H. Liu, R. Zhang, Q. Cheng, D. Xu, L. Wu*, J. Cancer* **2019**, *10*(*9*): p. 2035-2046, DOI: 10.7150/jca.29421.
[88] S. Chen, J. Chen, X. Hua, Y. Sun, R. Cui, J. Sha, X. Zhu*, Biomed. Pharmacother.* **2020**, *127*: p. 110069, DOI: 10.1016/j.biopha.2020.110069.

6 Supplementary data

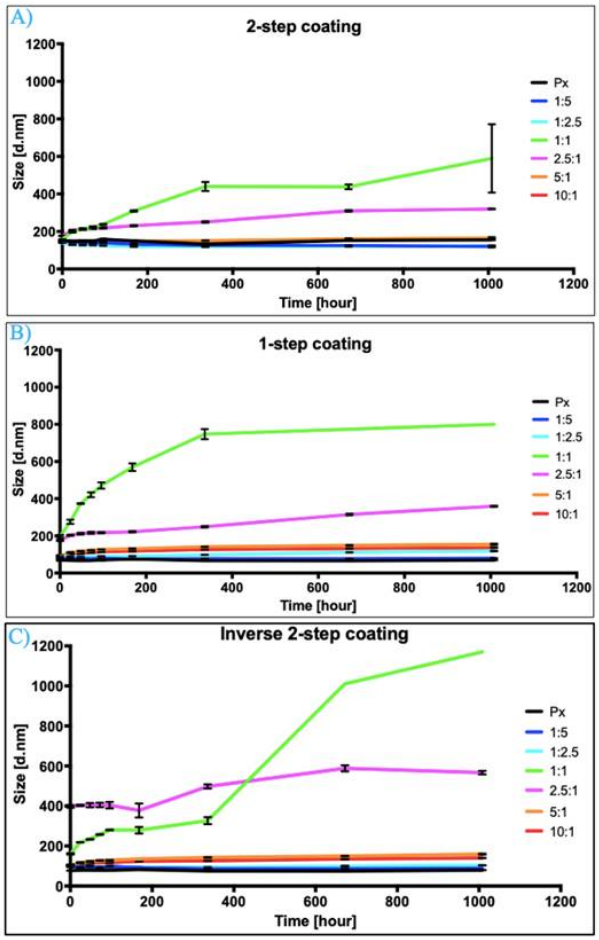

Figure S1. *Course of hydrodynamic diameter during 6-weeks of storage at room temperature of differently HA-coated polyplexes (A-C).*

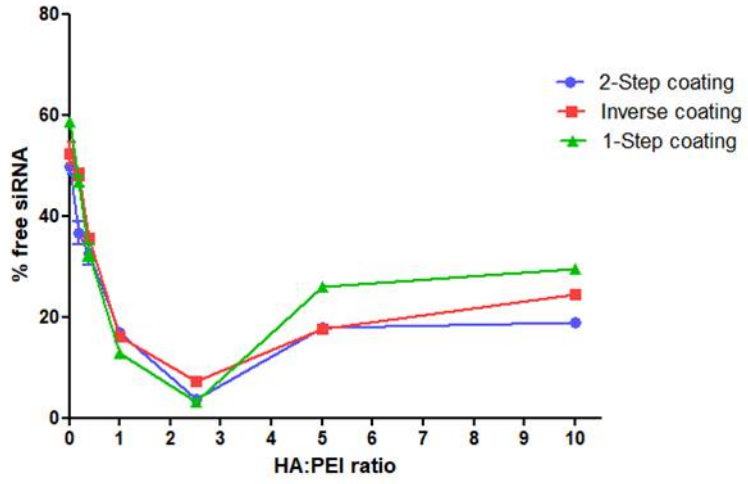

Figure S2. *Mean percentage release of siRNA at 1 IU heparin of differently coated polyplexes as indicated in the legend at distinct HA:PEI-ratios.*

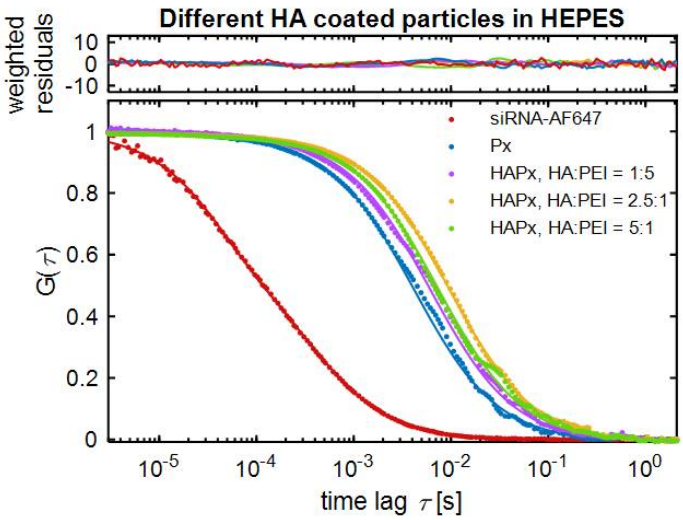

	Px	HAPx 1:5	HAPx 2.5:1	HAPx 5:1
Mean size DLS	120 nm	129 nm	168 nm	142 nm
Size FCS	78 nm	118 nm	182 nm	140 nm

Figure S3. *Autocorrelation functions (ACFs) of uncoated Px particles and coated HAPx particles, prepared with different HA:PEI ratios, in HEPES. The particles are prepared with 30% non-coding siRNA labeled with Alexa Fluor 647 (AF647), whose ACF in HEPES is shown as a reference (siRNA-AF647), and 70% unlabeled siRNA against eGFP. The HA:PEI ratio used for each preparation is indicated in the legend. The table highlights comparable sizes of the respective HAPx polyplexes obtained with either FCS or DLS.*

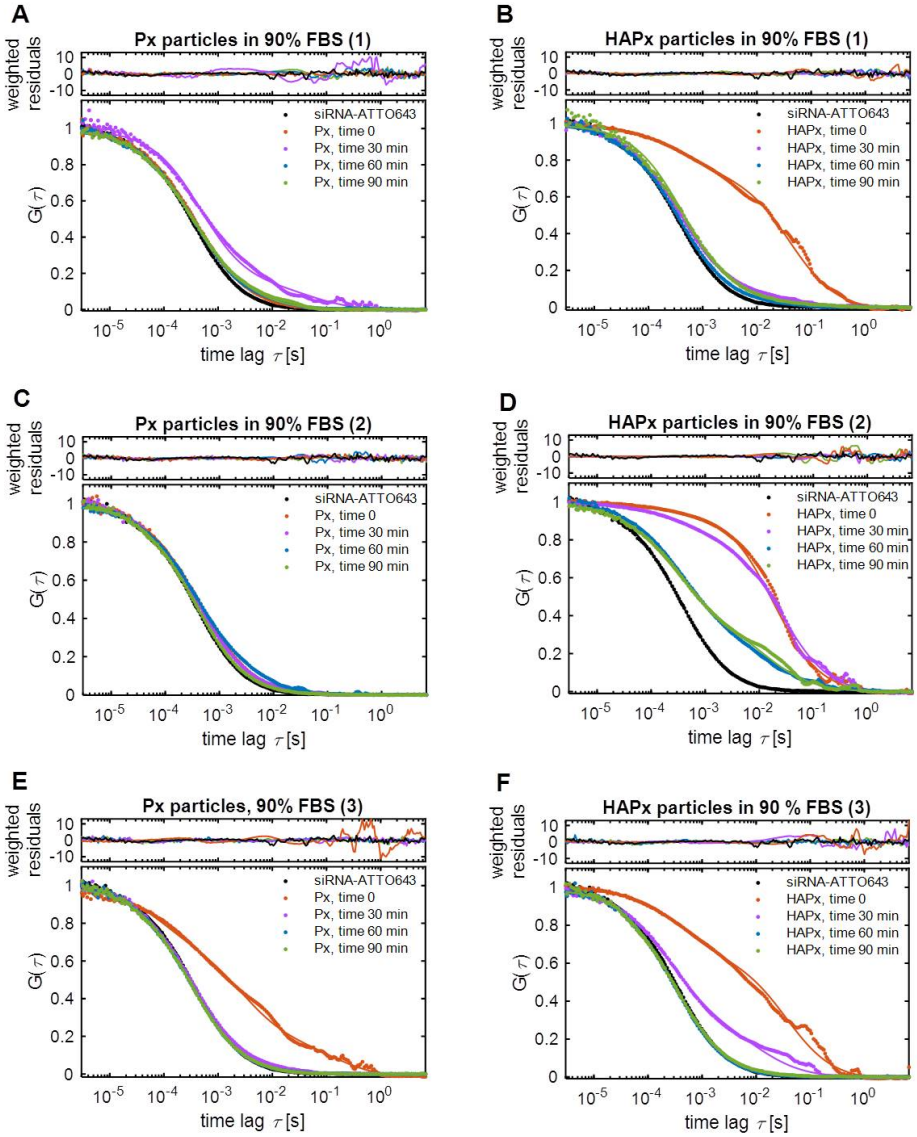

Figure S4. *Additional independent replicates of Hyaluronic Acid (HA) coated nanoparticles (HAPx) and uncoated polyplexes (Px) in 90% FBS.*

(A, C, E) ACFs of naked Px particles at different time points of incubation in 90% FBS obtained from three independent experiments as indicated in the brackets. The ACF of siRNA-ATTO643 in 90% FBS is shown as a reference. It should be noted that for the replicate (1), in panel A, the particles were prepared with 15% non-coding siRNA labeled with ATTO643, as usual, but the remaining unlabeled 85% was constituted by a 25/27mer siRNA against eGFP.

(B, D, F) ACFs of HA coated particles at different time points of incubation in 90% FBS obtained from three independent experiments as indicated in the brackets. The ACF of siRNA-ATTO643 in 90% FBS is shown as a reference. HAPx particles are formulated with a HA: PEI ratio of 2.5: 1. It should be noted that for the replicate (1), in panel B, the particles were prepared with 15% non-coding siRNA labeled with ATTO643, as usual, but the remaining unlabeled 85% was constituted by a 25/27mer siRNA against eGFP.

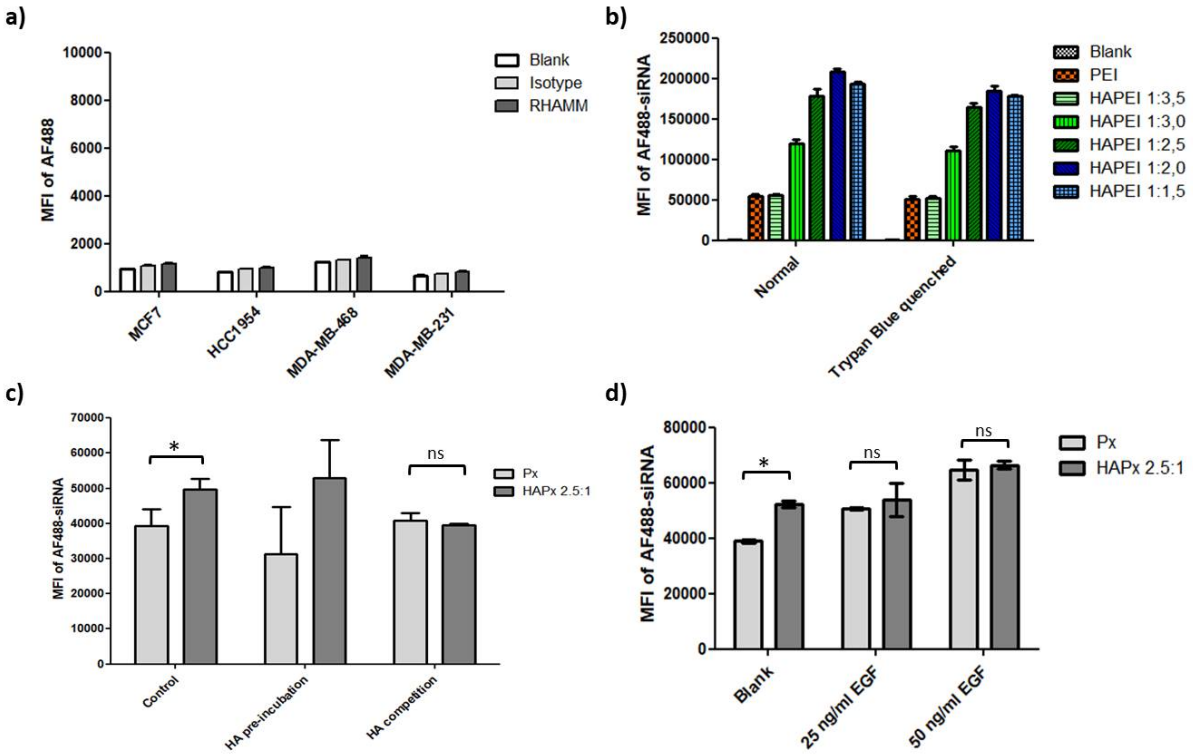

Figure S5. ***(a)*** *RHAMM surface expression in the four breast cancer cell lines quantified by flow cytometry.* ***(b)*** *HA:PEI ratio dependent particle uptake after 24 h in MDA-MB-468 cells using a higher molecular weight hyaluronic acid (140 kDa) upon 2-step coating. Cell membrane/surface bound particles were quenched using trypan blue.* ***(c)*** *24h-uptake of (HA)Px in MDA-MB-468 cells with HA-containing medium. Cells were either incubated with excess amounts of HA in priori to transfection (pre-incubation) or excess amounts of HA was maintained during transfection (competition).* ***(d)*** *24h-uptake of (HA)Px in MDA-MB-468 cells stimulated with different concentrations of EGF to stimulate EMT for 48 h prior to transfection.*

Chapter VI

Introducing the TACS-like in-vitro model as biomimetic cell culture platform for drug delivery applications

1. Introduction

The use of engineered three-dimensional (3-D) *in vitro* models for cancer research is expected to allow for superior analytical outcome as compared to conventional two-dimensional (2-D) monolayer cultures due to a more biomimetic environment.[1, 2] To study processes such as cancer invasion and metastasis, considerations of the structural and chemical peculiarities stemming from the extracellular matrix (ECM) of the tumor microenvironment need to be included for the *in vitro* evaluation of new drug candidates. As discussed in **Chapter II**, the ECM components, which breast cancer cells experience during tumor progression, are spatio-temporarily fluctuating. Hence, likewise their influence on essential biological processes including cell-division, cellular differentiation, migration and morphology differs over time and space.[3-6] Therefore, the *in vitro* efficacy of anti-cancer therapeutics is expected to vary between simple, conventional 2-D culture and 3-D culture, as the latter set-ups partially respect the dimension and unique properties of a tissue. For instance, within the tumor, the dense fiber matrix, which consists of collagen and interacting molecules, may hinder the process of diffusion of nanoparticle-based delivery vehicles. For successful tissue penetration and drug release of therapeutic nanoparticles, many factors have to be considered including particle size, shape and surface modification as well as tissue-relevant factors such as temperature, pH, matrix composition, porosity, and pore size. By using engineered tissue models, the impact of each of these factors can be quantitatively studied.

In this chapter, the electrospun TACS-like *in vitro* model presented in **Chapter IV** is shortly introduced as biomimetic cell culture platform for drug delivery applications. Additionally, the PEI-based polyplex delivery system which was optimized in **Chapter V**, coated and non-coated, was applied to cells grown on the scaffold. Lastly, the therapeutic effect of RNAi of the transcription factor XBP1 on cancer cell migration by inducing the Mesenchymal-to-Epithelial Transition (MET) was investigated.

2. Material & Methods

For detailed information on material and methods used in this chapter the reader is referred to **Chapters II, IV** and **V**. Here, only deviations from the standard operation procedures are briefly noted.

2.1 Nanoparticle transfection

Px, HAPx 2.5:1 polyplexes and Lipofectamine® lipoplexes were prepared as described in **Chapter V**.

In 24-well pates, 35.000 MDA-MB-468 cells were seeded on the TACS-like scaffolds. After 24 h of culture, cells were washed 1x with PBS and transfected with 100 µL of freshly prepared polyplexes

(uptake) or lipoplexes (knockdown) comprising the siRNA of interest (labeled, targeted, non-targeted). Per well, 400 µL of medium was added per well, which were filled up to 1 mL after 4 h of incubation.

After 24 h, medium of cells transfected with fluorescently-labeled AF488 siRNA was removed, and cells were subsequently washed 2-times with PBS. To fix the cells, 4 % PFA was added for 10 min.

For gene silencing experiments, cells were either subjected to RNA isolation and RT-qPCR or monitored with live cell imaging, 72 h after transfection with lipoplexes containing XBP1-siRNA, SNAI1-siRNA (On Target plus human SNAI1 (6615) SiRNA-Smartpool, Horizon Discovery, Waterbeach, UK) or negative control (NC) siRNA. Cells were transfected with 100 pmol (RT-qPCR) or 50 pmol and 100 pmol (live cell imaging) of siRNA, respectively. Untreated (Blank) cells grown for 72 h, served as additional reference.

2.2 Confocal imaging – Particle internalization

To stain the actin cytoskeleton, fixed cells on the scaffolds were incubated with 8.25 µM rhodamine-phalloidin solution for 40 min. Hereinafter, cells were washed another 3 times with PBS. Nuclei were stained with a 0.5 µg/mL DAPI solution for 10 min. Finally, after an additional washing step, samples were mounted on glass slides using FluorSave and stored at 4°C until the next day. Fluorescence images were acquired using a laser scanning microscope (Leica SP8 inverted, Software: LAS X, Leica microsystems GmbH, Wetzlar, Germany). Diode laser (405 nm) and semiconductor lasers OPSL 488 and OPSL 552 were chosen for excitation, and emission was displayed in blue (PMT1: 410–520 nm), green (HyD3: 493 – 569 nm) and yellow (PMT2: 560 nm – 760nm), respectively.

To quantify the corrected total cell fluorescence (CTCF) of the green channel of the imaged samples, Fiji software was used with the following correction:

CTFC = Integrated Density – ((Area of selected cell) x (mean fluorescence of background))

2.3 RNA isolation and RT-qPCR

Cells were washed 3-times with PBS after 72 h post transfection before 300 µL of ethanol-containing lysis buffer was added for 15 min. In order to maximize the amount of RNA per sample, triplicates were pooled prior to the RNA isolation step. Total RNA was isolated using the PureLink RNA mini kit according to the manufacturer's protocol with additional DNAse I digestion. Subsequently, 500 ng of RNA was used to synthesize cDNA using the High capacity cDNA synthesis kit. Gene-specific primers were used in the amplification step using Power SYBR™ Green PCR Master Mix and the qTOWER real-time PCR thermal cycler (Analytik Jena, Jena, Germany). C_t values were normalized to GAPDH expression, and delta C_t values were calculated for the comparison.

2.4 Live cell imaging and Trackmate analysis

Live cell imaging was performed using the Eclipse Ti inverted microscope (Nikon, Dusseldorf, Germany) with a 4/10 phase contrast objective and a charge-coupled camera (DS-Qi1Mc; Nikon). Nuclei of cancer cells were stained with Hoechst 33342 dye (Invitrogen™) according the manufacturer's protocol 72 h after transfection. Briefly, cells were washed once with PBS and subsequently incubated for 20 min in the cell culture incubator in 300 µL of 0.5 µg/mL dye in PBS. Afterwards, the dye-containing medium was removed and cells were washed another 2 times with PBS before 1 mL of fresh medium was replenished. The 24-well plates were inserted into a 37°C heating and incubation system, and the humidity was kept at 80% to prevent cellular dehydration. The cells were imaged in bright-field, and the nuclei were detected at 405 nm using the integrated fluorescence LED. Time-lapse videos were taken with a time interval of 5 min between images over a total time span of 12 h.

For single-cell trajectories, the position of nuclei was analyzed using the TrackMate plugin within the Fiji software [7]. Values of "Track displacement" and "Mean migration speed" were extracted.

3. Results & Discussion

3.1 TACS5-mimicking in vitro model allows for endocytosis of nanoparticles

A long term goal within this thesis project is to use the tissue-relevant *in vitro* model as drug screening platform for cancer therapeutics. Promising strategies to tackle cancer include the delivery of nucleic acids such as siRNA and mRNA formulated as nanoparticulate medicine. However, nanoparticle endocytosis in 3D environments is distinct from 2D cell culture, and cellular tolerability of particles can be affected [8, 9]. In a proof-of-concept experiment, it was tested whether PEI-based polyplexes (Px) as standard vehicles for nucleic acid delivery are efficiently endocytosed by the MDA-MB-468 cancer cells growing on the TACS-like *in-vitro* model. Hyaluronic acid-coated Px particles at a HA:PEI-ratio of 2.5:1, were additionally included as CD44-receptor-targeted nanocarrier system since they were the most promising candidates evaluated in the uptake study described in **Chapter V**.

Initially, to visualize uptake of nanoparticles on TACS5-mimics, fluorescently labeled non-coding siRNA was encapsulated and MDA-MB-468 cells were transfected for 24 h. Based on the blue (nuclei) and red (cytoskeleton) fluorescence signals assessed by confocal imaging of low magnification (10x, **Figure 1a**), cells widely settled on the scaffold. Both particle systems were well distributed over cells indicated by a broadly scattered green (siRNA) fluorescence signal. The signals of the red and green channel spatially overlapped, implying engagement of polyplexes with cells (data not shown).

Images at higher magnification (40x) confirmed spatial overlap of siRNA molecules with cellular elements (**Figure 1b**). Indeed, imaging suggested successful uptake of nanoparticles as both particle systems accumulated in juxtanuclear regions, which is characteristic for the spatial organization of endosomes/lysosomes. Further, particles seemed to preferentially engage with cells but spared the fibrous matrix as only a few green fluorescence signals were detected on the nanofibers. To estimate differences in cellular uptake between Px and HAPx particles, a series of confocal images (n = 3, respectively) was analyzed for the mean corrected total cell fluorescence (CTCF) of the green/siRNA channel. As shown in **Figure 1c**, mean CTCF of cells transfected with HAPx species was significantly higher (33.0%, $P < 0.05$) than the one of Px particles. Notably, this increase of HAPx uptake is similar to the elevation of 44.3 % observed in conventional 2-D cell culture presented in **Chapter V**. Therefore, the HA-coated delivery system exhibited improved uptake in both 2-D and 3-D set-ups. Based on these findings, it is more likely for HAPx polyplexes to efficiently deliver siRNA *in vivo*. However, a comparison of *in vitro* particle internalization with an appropriate animal model would be required to robustly determine the predictive value of the TACS-like matrix.

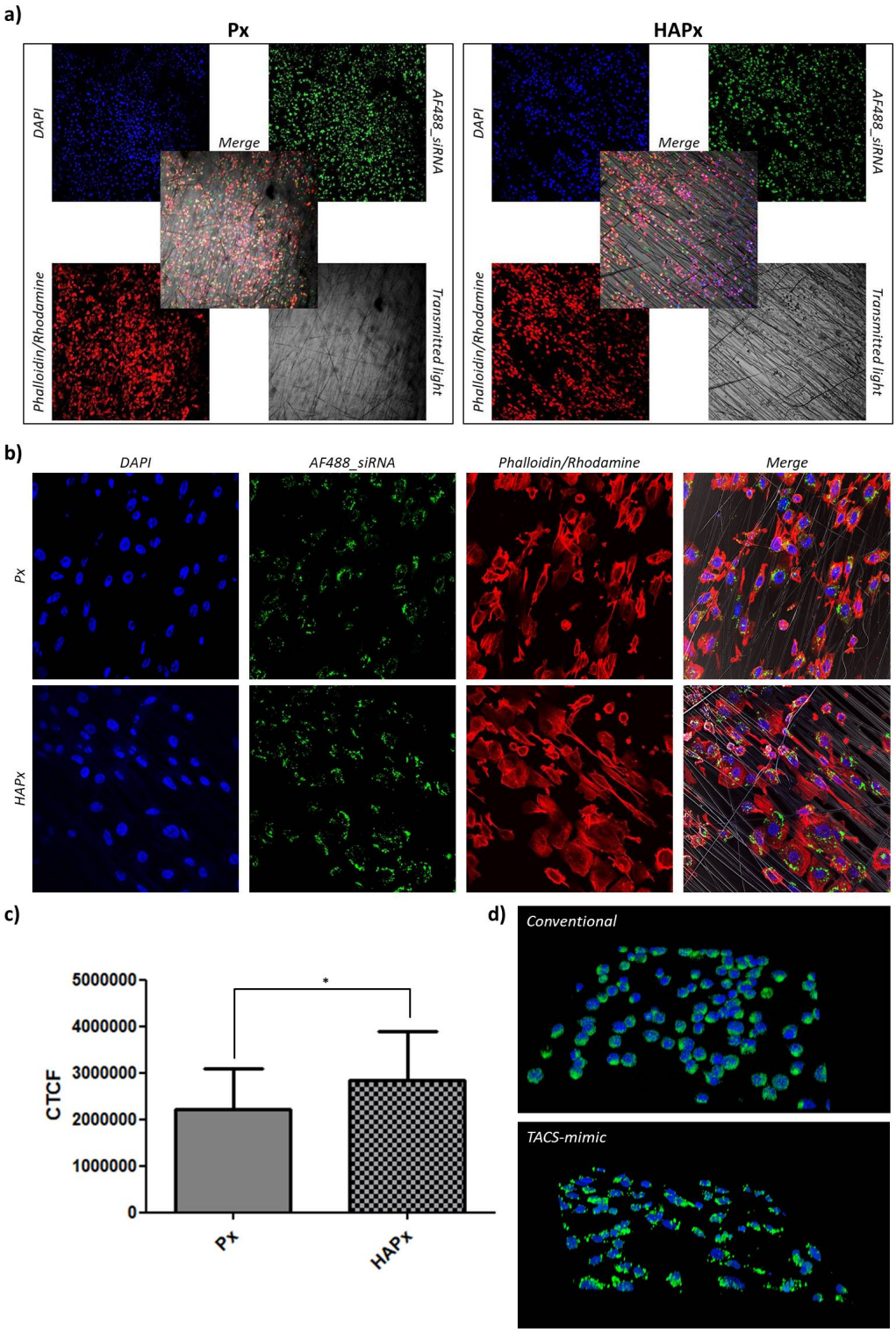

Figure 1. *Confocal images of cells growing on the fibrous in vitro model transfected with AF488-siRNA containing polyplexes (green) shown at 10x (**a**) and 40x (**b**) magnification. Nuclei are shown in blue (DAPI) and the cytoskeleton in red (rhodamine). The scaffold itself was recorded as bright-field image. (**c**) Differences between uptake of Px and HAPx particles was analyzed based on the corrected total cell fluorescence (CTCF) with n(cells) = 20. Error bars indicate SD. Statistical significance was assessed with a t-test (**d**) Z-stacks of transfected cells growing on conventional 2-D cell culture substrates (upper panel) or TACS-like mimics (lower panel).*

Furthermore, the differences between uptake of nanoparticles on conventional culture dishes and TACS5-mimics were investigated performing z-stacks, respectively. As shown in **Figure 1d**, juxtanuclear accumulation indicated effective particle uptake in both set-ups. However, polyplexes were found to have a broadly scattered distribution on the 2D-substrate but a rather packed positioning on the 3D scaffold, implying fundamental differences in cellular uptake. Indeed, the former distribution profile is thought to correlate with low transfection efficiencies [10] which underscores the importance to use 3-D models for drug screening purposes. Moreover, the nuclei on conventional 2-D dishes displayed a homogenously distributed rather disk-like morphology. This flattened morphology is phenotypic for 2-D monolayers [11]. Instead, nuclear morphologies were more heterogeneous on the TACS-like scaffolds, and nuclei displayed voluminous shapes.

3.2 siRNA-mediated knockdown of XBP1 impairs cellular displacement on the TACS-like scaffold without affecting the EMT-phenotype

Based on our finding in **Chapter IV** and **V**, the transcription factor XBP1 may play an important role during EMT as well as for cellular adaption to the fibrous scaffold. On the one hand, we found enriched XBP1 protein levels in the EMT-positive cell line MDA-MB-231. On the other hand, we showed that it is upregulated in breast cancer cells growing on the fiber matrix. Here, it was investigated whether cellular motility on the TACS5-like scaffold is affected by siRNA-mediated knockdown of XBP1. The IRE1 – XBP1 pathway was shown to function as direct transcriptional activator of central transcriptions factors of the EMT machinery including SNAIL1.[12] Thus, downregulation of XBP1 can concomitantly reduce the EMT-driving activity of SNAIL1. siRNA against SNAIL1 was additionally included as positive control. In the past, it was shown that SNAI1 knockdown can effectively impair cellular migration of breast cancer cells.[13] Here, lipofectamine® transfection reagent was used to treat mesenchymal MDA-MB-231 cells with either negative control (NC) siRNA or siRNA directed against XBP1 and SNAIL1.

Initially, mRNA knockdown was estimated using RT-qPCR. Further, EMT-markers E-cadherin (CDH1) and vimentin (VIM) were assessed to monitor a possible reversal of the EMT-phenotype (MET) as result of the RNA interference (RNAi) effect. According to the data shown in **Figure 2a**, transfection with 100 pmol siRNA significantly reduced mRNA expression of XBP1. However, neither SNAIL1, nor CDH1 and VIM expression were significantly changed 72 h post-transfection. Unfortunately, RNAi using SNAIL1-siRNA was not effective. Two other commercially available siRNA sequences against SNAIL1 were subsequently tested, confirming ineffectiveness, too (data not shown).

Nevertheless, cellular motility on the TACS5-scaffold was subsequently studied in a timeframe of 12 h, 72 h after the transfection with two different amounts of siRNA. Cellular displacement (**Figure 2b**) and mean migration speed (**Figure 2c**) were calculated based on live cell imaging combined with

image analysis using the Trackmate plug-in of ImageJ software.[7] Both parameters are described in detail in **Chapter IV** and were found to be solid descriptive parameters of cellular motility as well as affected by the EMT-phenotype and EMT-like changes. Therefore, they were expected to be reduced once EMT is inhibited or reversed. As predicted by the previous knockdown experiment, SNAIL1-siRNA treatment did not alter either of the two parameters. Likewise, cellular motility of cells transfected with 50 pmol of XBP1-siRNA remained unchanged. However, XBP1 transfection at 100 pmol significantly reduced cellular mean displacement by 38.9 % ($P < 0.01$) in comparison to transfection with negative control siRNA. Even tough not reaching statistical significance, mean displacement in comparison to untreated cells was also impaired, as cells displaced 14.6 % less far. Instead, mean migration speed remained constant irrespective of the type and amount of siRNA transfected.

In summary, the treatment with XBP1-siRNA efficiently induced mRNA knockdown in mesenchymal MDA-MB-231 cells. However, other than expected, the expression of downstream transcription factor SNAIL1 remained unaffected. Since XBP1's indirect action on EMT is mediated by its regulatory role on SNAI1 expression, it appeared conclusive that neither CDH1 nor VIM expression levels were altered. Because both half-lives of XBP1 as well as SNAIL1 protein have to be considered, it is plausible that the time window of 72 h for the transfection was too short to record significant changes of SNAI1 mRNA levels, consequently to monitor MET-like changes.

Unfortunately, it was not possible to conclusively evaluate the effect nanoparticle-triggered SNAI1 knockdown would exert on cellular motility of breast cancer cells growing in the TACS5-like *in vitro* model, as RNAi was ineffective. Nevertheless, in case of effective RNAi, we can assume reduced migratory behavior as was shown for miR200c induction in MDA-MB-231 cells in **Chapter IV**. In congruence with mRNA expression levels of CDH1 and VIM, transfection with siRNA targeting SNAIL1 and XBP1 did not alter the migration speed of the MDA-MB-231 cell line growing on the *in vitro* scaffold. However, cellular displacement was impaired by XBP1 knockdown implying a non-EMT-related effect of XBP1 on cellular motility. Indeed, it was recently shown that activation of the IRE1 – XBP1 axis in the MDA-MB-231 cell line invokes a loss of desmoplakin via Zinc finger E-box-binding homeobox (ZEB) activation without affecting EMT-phenotypic markers E-cadherin and vimentin.[12] Desmoplakin, as part of desomosomes, participates in cell-cell adhesion and its loss is known to promote cancer cell migration and malignancy. According to this scenario, it is plausible that XBP1 knockdown entailed upregulation of desmoplakin, which subsequently altered cell-cell junctions, impairing cellular displacement along the nanofibers.

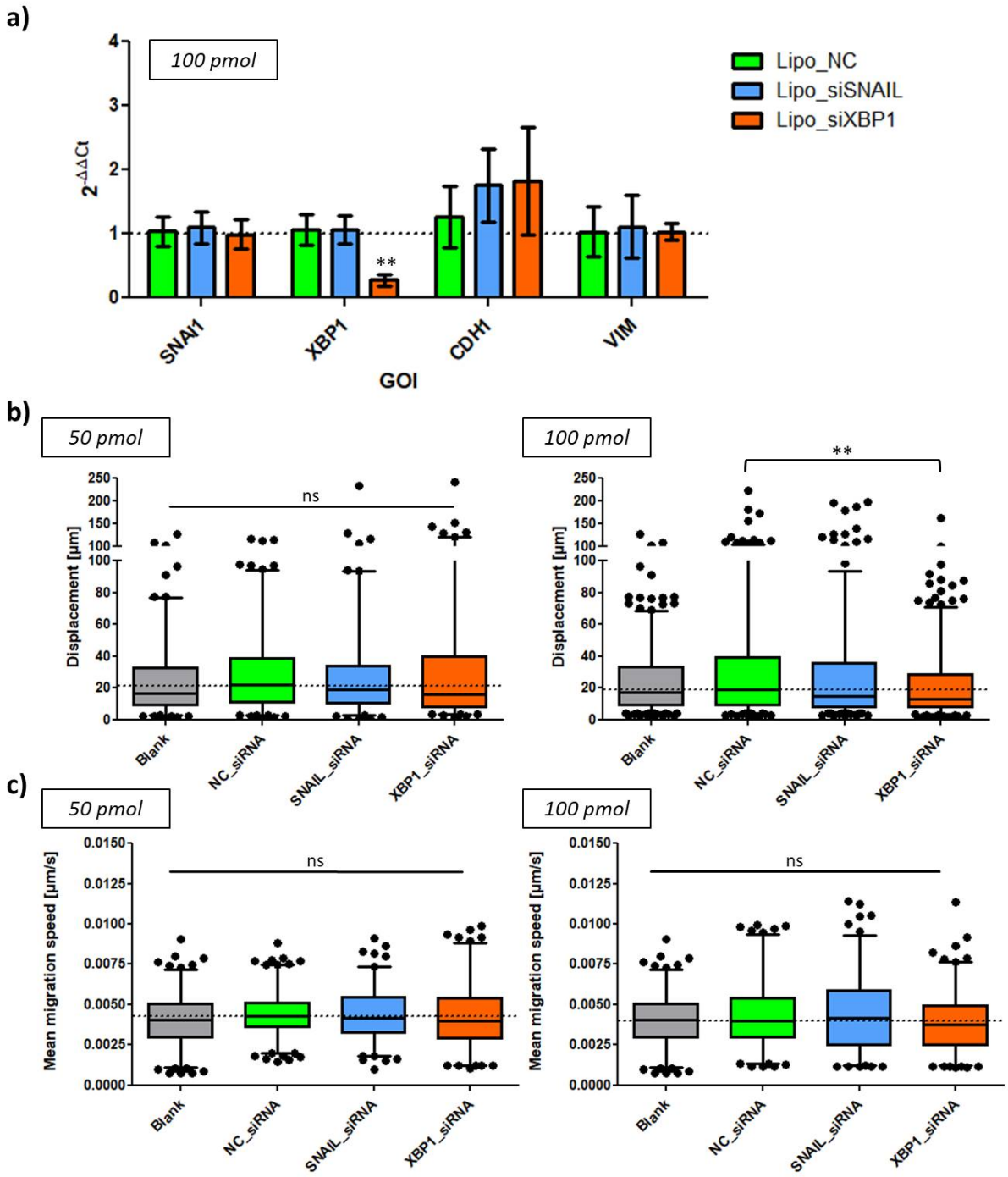

Figure 2. *(**a**) relative mRNA levels of SNAI1, XBP1, CDH1 and VIM shown as $2^{-\Delta\Delta Ct}$-value after 72 h transfection with siRNA containing lipoplexes. Error bars indicate SD (n = 2). (**b-c**) Migration analysis of transfected cells (with 50 or 100 pmol siRNA) growing on the matrix. Track displacement (**b**) and mean migration speed (**c**) were plotted as whiskers plot (5-95 percentiles). The dotted line indicates the mean-values of the negative control samples, respectively. One-way ANOVA with Bonferroni multiple comparison test was performed in GraphPad Prism software (Graph Pad Software, La Jolla, CA, USA) to calculate P-values at a 95% confidence interval*

4. Conclusion

This chapter demonstrated how the TACS-mimicking *in vitro* model may be introduced as advanced transfection platform for nanoparticulate delivery systems. We provided methodological and analytical knowledge on how to apply the TACS-like scaffold for the daily lab-work. Once again, the presented data confirmed the biological performance and functionality of the *in vitro* model. Cells within the scaffold were able to internalize important amounts of nanoparticles as was shown for (HA)Px polyplexes. However, the intracellular arrangement of endocytosed particles seemed to be distinct from conventional 2-D culture. Finally, we found RNAi of XBP1 to impair cellular displacement within the fibrous scaffold without affecting EMT-related markers. Longer transfection times may be required to elucidate EMT-related effects of siRNA-mediated knockdown of transcriptional activator XBP1.

5. References

[1] E.P. Carter, R. Roozitalab, S.V. Gibson, R.P. Grose, *Trends in cancer* **2021**, *7*(*11*): p. 1033-1046, DOI: 10.1016/j.trecan.2021.06.009.

[2] S.A. Langhans, *Front. Pharmacol.* **2018**, *9*, DOI: 10.3389/fphar.2018.00006.

[3] M.W. Conklin, P.J. Keely, *Cell Adhes. Migr.* **2012**, *6*(*3*): p. 249-260, DOI: 10.4161/cam.20567.

[4] G. Rauner, C. Kuperwasser, *Dev. Cell* **2021**, *56*(*13*): p. 1875-1883, DOI: https://doi.org/10.1016/j.devcel.2021.06.016.

[5] A. Ray, Z.M. Slama, R.K. Morford, S.A. Madden, P.P. Provenzano, *Biophys. J.* **2017**, *112*(*5*): p. 1023-1036, DOI: https://doi.org/10.1016/j.bpj.2017.01.007.

[6] K. Unnikrishnan, L.V. Thomas, R.M. Ram Kumar, *Front. Oncol.* **2021**, *11*, DOI: 10.3389/fonc.2021.733652.

[7] J.-Y. Tinevez, N. Perry, J. Schindelin, G.M. Hoopes, G.D. Reynolds, E. Laplantine, S.Y. Bednarek, S.L. Shorte, K.W. Eliceiri, *Methods* **2017**, *115*: p. 80-90, DOI: https://doi.org/10.1016/j.ymeth.2016.09.016.

[8] V. Belli, D. Guarnieri, M. Biondi, F. Della Sala, P.A. Netti, *Colloids Surf. B. Biointerfaces* **2017**, *149*: p. 7-15, DOI: 10.1016/j.colsurfb.2016.09.046.

[9] F. Farvadi, M.H. Ghahremani, F. Hashemi, M. Reza Hormozi-Nezhad, M. Raoufi, S. Zanganeh, F. Atyabi, R. Dinarvand, M. Mahmoudi, *J. Colloid Interface Sci.* **2018**, *531*: p. 245-252, DOI: https://doi.org/10.1016/j.jcis.2018.07.013.

[10] E.J. Sayers, S.E. Peel, A. Schantz, R.M. England, M. Beano, S.M. Bates, A.S. Desai, S. Puri, M.B. Ashford, A.T. Jones, *Mol. Ther.* **2019**, *27*(*11*): p. 1950-1962, DOI: https://doi.org/10.1016/j.ymthe.2019.07.018.

[11] M. Kapałczyńska, T. Kolenda, W. Przybyła, M. Zajączkowska, A. Teresiak, V. Filas, M. Ibbs, R. Bliźniak, Ł. Łuczewski, K. Lamperska, *Arch. Med. Sci.* **2018**, *14*(*4*): p. 910-919, DOI: 10.5114/aoms.2016.63743.

[12] A. Nath, A. Oak, K.Y. Chen, I. Li, R.C. Splichal, J. Portis, S. Foster, S.P. Walton, C. Chan, *Mol. Cancer Res.* **2021**, *19*(*2*): p. 240-248, DOI: 10.1158/1541-7786.mcr-19-0480.

[13] B.N. Smith, L.J. Burton, V. Henderson, D.D. Randle, D.J. Morton, B.A. Smith, L. Taliaferro-Smith, P. Nagappan, C. Yates, M. Zayzafoon, L.W. Chung, V.A. Odero-Marah*, PLoS One* **2014**, *9*(*8*): p. e104987, DOI: 10.1371/journal.pone.0104987.

Chapter VII

Tracking siRNA-nanocarrier assembly and disassembly using FRET

Parts of this chapter were published as book chapter in "*Methods in Pharmacology and Toxicology 2021 - Quantitative Analysis of Cellular Drug Transport, Disposition and Delivery*" as:

Lorenz Isert, Aditi Mehta, Friederike Adams and Olivia M. Merkel; "Tracking siRNA-nanocarrier assembly and disassembly using FRET"

1. Abstract

The success of cellular nucleic acid delivery, such as siRNA, mRNA or plasmid DNA strongly depends on the selected carrier system. Its attributes must guarantee the incorporation of the nucleic acid into nano-sized particles, followed by efficient cellular uptake, resistance to the changing physico-chemical environment during endo-lysosomal trafficking and finally the adequate release of its payload in the cytosol of the cell. While the outcome of the last step can easily be evaluated in case of siRNA delivery via knockdown of a reporter gene, the kinetics experienced by particles on their cellular journey remain mostly unknown.

Fluorescence/Förster resonance energy transfer (FRET) is a versatile tool in nanocarrier- based theranostics and encompasses the transfer of excitation energy from a donor molecule in an excited state to an acceptor molecule in close proximity. To understand the kinetics of cellular nucleic acid delivery, we use the multifunctional PEG-PCL-PEI (PPP) triblock copolymers in combination with a FRET-based nanocarrier reporting system consisting of hydrophobic Quantum Dots 605 (Qdots605) and Alexa Fluor 647 (AF647) labelled siRNA.

FRET based monitoring of both distinct entities allows us on the one hand to monitor the necessary compaction (= assembly of polymer vehicle and cargo) and decompaction (= disassembly and release of cargo) of the nano-carrier and on the other hand enables tracking the cellular trafficking of both molecules individually subsequent to the carrier-siRNA dissociation.

2. Introduction

It was in the 1990s when Yasuhiro Matsumura and Hiroshi Maeda discovered a significant accumulation of i.v. administered proteins within the tumour tissue. They explained this phenomenon by enhanced permeability and retention (EPR) for nano-sized macromolecules as a result of neovascularisation and defects in the lymphatic drainage system during carcinogenesis.[1] Even though this EPR-effect is controversial among scientists, strenuous effort was ever since invested in nanotechnology-based therapeutics for all kinds of diseases.

One approach spawn from this technology is nucleic acid delivery via polymeric carrier systems. The incorporation of negatively charged nucleic acids in “polyplexes” (= polyelectrolyte complexes) via electrostatic interactions with cationic polymers generates nano-sized particles. Whereas biocompatibility and biodegradability of recent formulations could overcome the initial problems of toxicity, the uncertainties about cellular kinetics remain the major obstacle for its clinical translation.

FRET-based approaches have been extensively used to study communication between different molecular species on a cellular level in examples such as protein-protein interaction. The capability of nanometer resolution providing both quantitative and qualitative information has allowed FRET to become a versatile method for microscopy, flow cytometry and spectrofluorimetric applications.[2] The choice of FRET partners is crucial for the success of this approach. The emission spectrum of the donor fluorophore has to overlap with the excitation spectrum of the acceptor molecule, allowing for radiation-less energy transfer via long range dipole-dipole interaction.[2] The merits of an extensive overlap (e.g. higher FRET efficiency) are often counterbalanced by cross talk and cross excitation between both molecules necessitating further compensation steps for accurate results. A prerequisite for FRET is that FRET-donor and acceptor fluorophores are within a range of 1 – 10 nm. Hence, FRET efficiency is highly impacted by distances depicted in the formula:

$$E_{FRET} = \frac{1}{1+(\frac{r}{R_0})^6}$$

, where the FRET efficiency ($\mathbf{E_{FRET}}$) is proportional to the inverse sixth power of the distance (**r**) between the two molecules. The Förster Radius (R_0) is the distance at which energy transfer is 50% efficient and characterizes distinct FRET pairs.

In this chapter we demonstrate, how these circumstances in the context of nucleic acid delivery can be exploited.

As mentioned above, polyplex assembly encompasses electrostatic interactions between polymers and nucleic acids. By fluorescently labelling both components with distinct fluorophores, which together generate a FRET-capable system, it is possible to gain information about assembly and disassembly kinetics at high resolution. Its usage is not restricted to particle formation but may also be introduced for *in vitro* and *in vivo* applications.

The PEG-PCL-PEI (PPP) triblock copolymer offers a multifunctional drug delivery platform. It self-assembles to micelle-like particles with a core-corona structure where the hydrophilic PEG shell surrounds and shields the hydrophobic poly-ε-caprolactone (PCL) core.[3] The poly(ethylenimine) (PEI) segment builds a cationic interface due to amine groups that are protonated under physiological conditions. This enables the incorporation of negatively charged nucleic acids, such as siRNA. Fluorescence-labelling of siRNA can readily be produced via click chemistry or other conjugation chemistry. Here, we use succinimidyl ester (NHS) modified Alexa Fluor 647 as labelling dye that functions as FRET-acceptor in our system. As FRET-donor we chose Quantum Dots (Qdots). Qdots are luminescent semiconductor inorganic nanoparticles with unique spectral properties. Wideband excitation and narrow emission spectra paired with a high quantum yield and photo-stability are explaining the substantial use of Qdots as biosensors. The ease of modifying the physical properties (e.g. hydrophobicity) has popularized their use for theranostic approaches in nanomedicine.[4, 5] The

Organic Quantum dots 605 that are used here are of hydrophobic nature. Before polyplex assembly, the PCL segment can be exploited as hydrophobic reservoir for the Qdots and once condensed with siRNA the FRET-system is completed.

3. Materials

The PPP polymer used throughout the experiments was synthesized as described elsewhere.[6] For longterm storage, an aqueous solution of the polymer was lyophilized. NMR analysis revealed: (4 kDa mPEG – 2 kDa PCL)$_{3.2}$ – 10 kDa PEI.

3.1 Polymer synthesis

a) Polyethylenimine (PEI) M_n ~ 10.000 (Sigma-Aldrich).
b) Polyethylene Glycol Monomethyl Ether (mPEG) 4000 (TCI).
c) Caprolactone (PCL monomer) (Sigma-Aldrich).
d) Acryloyl chloride, 96% (Thermo Fischer Scientific).
e) Tin(II) 2 – ethylhexanoat salt (Sigma-Aldrich).

3.2 Particle formation

a) Qdot® 605 ITK™ organic quantum dot (Thermo Fischer Scientific).
b) Disposable Syringes HSW NORM-JECT®, 2-part, sterile (TH Geyer).
c) Needles for single use FINE-JECT®, 0.7 x 50 mm (VWR).
d) 10 mM HEPES buffer pH 7.4.

3.3 Polyplex assembly

Fluorescently labeled siRNA (here: amine modified siRNA (Integrated DNA Technologies) was labeled with succinimidyl ester (NHS) modified AlexaFluor 647 (Life Technologies) according to the manufacturer's protocol) and diluted in 10 mM HEPES buffer pH 7.4

3.4 Fluorescence spectroscopy

a) FluoroNunc 96-well white plate (Thermo Fisher Scientific).
b) 4x SYBR® Gold Nucleic Acid Gel Stain (Thermo Fisher Scientific).
c) 10 mM HEPES buffer pH 7.4
d) Sodium chloride (Sigma Aldrich)

3.5 Heparin competition assay

a) Heparin sodium salt from porcine intestinal mucosa (Sigma Aldrich)
b) 10 mM HEPES buffer pH 7.4

4. Methods

For all experiments we suggest:

- Avoid light exposure during and after the sample preparation to prevent photobleaching.
- Thaw siRNA on ice and try to avoid RNase contamination (RNaseZap®).
- For *in vitro* assays work under sterile conditions and sterilize all equipment and reagents using appropriate methods.
- All buffers should to be filtered through a filter with 0.22 µm pore size to eliminate potential sample contamination.

4.1 Particle formation – solvent displacement

To obtain nano-sized polyplexes we use a solvent displacement technique as described elsewhere.[5] Briefly, the polymer (together with the Qdots) is dissolved in an amphiphilic organic solvent (here acetone) that is entirely miscible with water. Injection of the organic solution into the aqueous phase under stirring leads to the formation of micelle-like particles driven by the "ouzo effect".[7]

Importantly, to guarantee the loading of the PCL segment with Qdots during this step, the Qdots have to be dispersed in the same organic solvent that is used during the solvent-displacement. Here, we first describe solvent exchange of Quantum dot stock solution and consequently the particle formation procedure.

a) 1 part of Qdot stock solution (1µM; decane) is added to 20 parts of magnetically stirred acetone.
b) Stir at 300 – 400 rpm.
c) Decane is evaporated under reduced pressure for at least 2 h.
d) The evaporated amount of solvent is replenished every 10 – 15 min (depending on the applied reduced pressure) by filling up with acetone. (see Note 1)
e) 1 mL of 10 mM HEPES buffer at pH 7.4 is added in a 20 mL vial.
f) A stir bar is added and the level of liquid is marked on the glass wall (see Note 2).
g) The vial is placed under the hood and stirred at 300 – 400 rpm.
h) In a 0.5 mL tube, 20 µL of PPP stock solution (c(PEI) = 10 mg/mL; concentration of PEI within PPP polymer can be accessed via Copper or TNBS assay) is mixed with 25 µL of the

Qdot stock and filled up to 200 µl with acetone to obtain a final concentration of 1 mg/mL PEI (see Note 3).

i) In another tube, 1 mg/mL PEI is prepared without adding Qdots (serves as blank control later on).
j) A 1 mL single-use syringe with a 22-G needle is loaded with the polymeric solutions (see Note 4).
k) The polymer solution is slowly injected into the vial containing buffer. Assure that the tip of the needle remains underneath the surface of the buffer during the whole injection process (see Note 5).
l) The evaporated amount of solvent is replenished every 20 – 30 min by filling up with buffer to the marked volume level.
m) Sample is kept stirring for at least 3 h.
n) The final PEI concertation is 0.2 mg/mL and particles (P) are ready for use or may be stored at 8°C in the fridge for several days.

4.2 Polyplex assembly

To manufacture the FRET-based reporting system, PPP nanoparticles have to be condensed with fluorescently labelled siRNA. The nitrogen to phosphate groups ratio (N/P – ratio) serves as physicochemical characteristic for the assembly process. The ratio should be optimized for every polymer prior to experiments ensuring entirely incorporated siRNA. To do so, the percentage of free siRNA (siRNA, which has not been condensed with the PEI) can easily be assessed via SYBR – Gold assay (for explanation of SYBR – Gold assay, see below).

The N/P – ratio calculation is based on the amount of siRNA (pmol per assembly) and generates the mass (m) of PEI needed for polyplex formation. Knowledge about the molecular weight (MW) of the protonable unit of PEI and amount of phosphate groups/molecule siRNA (52 nucleotides in 25/27mer siRNA used here) is needed.

$$\frac{N}{P} = \frac{n(PEI) \times \ amount\ of\ \frac{amines}{molecule}(x_a)}{n(siRNA) \times \ amount\ of\ \frac{phosphate}{molecule}(x_p)}$$

$$n(PEI) = \frac{N}{P} \times n(siRNA) \ \times \frac{x_p}{x_a} \qquad with\ n = \frac{m}{M_W}$$

$$m(PEI) = \frac{N}{P} \times n(siRNA) \times M_W(PEI) \ \times \frac{x_p}{x_a}$$

a) V(P) needed for a N/P–ratio of 10 at 100 pmol siRNA-AF647 is calculated.

$$m(PEI) = c(PEI) \times V(P) = \frac{N}{P} \times n(siRNA) \times M_W(PEI) \times \frac{x_p}{x_a}$$

$$\mathrm{V(P)} = \frac{\frac{N}{P} \times n(siRNA) \times M_W(PEI) \times \frac{x_p}{x_a}}{c(PEI)} = \frac{10 \times 100 \times 10^{-12} mol \times 43.04 \frac{g}{mol} \times \frac{52}{1}}{0.2 \frac{g}{L}}$$

$$\mathrm{V(P)} = 11.2 \times 10^{-6} l = 11.2 \mu L$$

b) 11.2 µL of prepared particles (P) is pipetted in a 0.5 mL tube and filled up to 50 µL with buffer.
c) 100 pmol of (AF647-labeled) siRNA is pipetted in another tube and filled up to 50 µL with buffer. In the following experiments the molar ratio of labeled to unlabeled siRNA is varied (see l/ul – ratio).
d) P are added to siRNA and carefully mixed by pipetting up and down.
e) Sample is incubated for 20 min.
f) Polyplexes (Px) are now ready for use or may be stored at 8°C in the fridge for one day.

4.3 Fluorescence spectroscopy – Proof of FRET capability

Whether FRET is taking place or not can be demonstrated by fluorescence intensity based approaches, either by donor – quenching, where only the decline in donor emission intensity is monitored or by recording a fluorescence emission spectrum of the FRET pair. The latter approach (chosen here) enables a deeper insight in particle kinetics, as both entities are monitored at the same time.

To confirm that the system undergoes FRET, we suggest the preparation of particles P as described above. By varying the molar ratio of labeled to unlabeled (**l/ul – ratio**) siRNA for the subsequent polyplex assembly Px (keeping the total amount of siRNA in pmol constant), a decrease in donor signal intensity can be monitored. Simultaneously an increase in FRET signal intensity (acceptor dye) occurs (**Figure 1a**). By keeping the N/P – ratio constant, the physicochemical properties of Px are kept constant and the most efficient FRET system can be evaluated (**Figure 1b**).

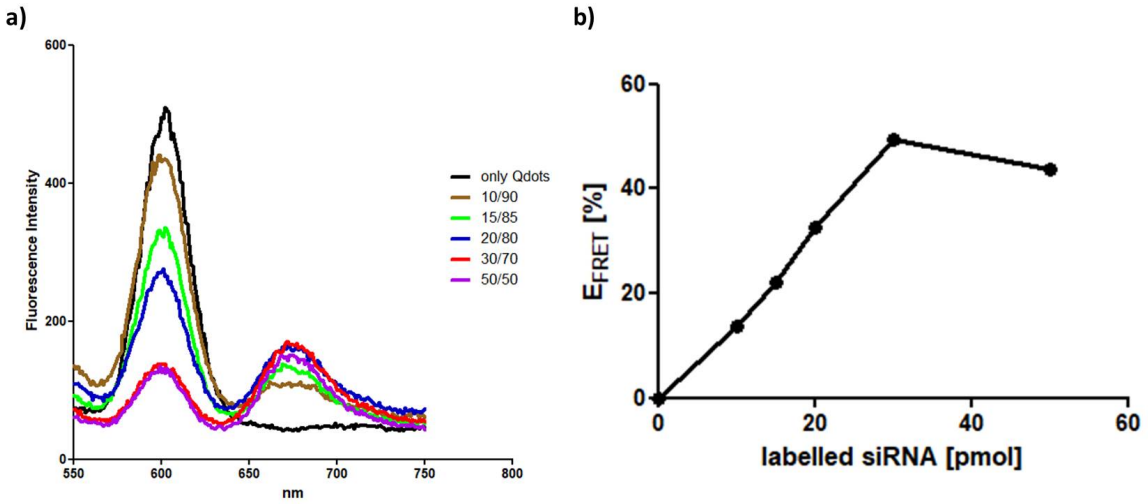

Figure 1. *Demonstrating FRET – capability of a nanocarrier system: Fluorescence spectra of polyplexes equipped with Qdots 605 (Emission maximum at 605 nm) and AF647 – labeled siRNA (Emission maximum at 671 nm) shows FRET (**a**).The black line represents the maximum fluorescence of Qdot loaded nanoparticles (without siRNA condensation). The colored lines depict the fluorescence spectra of polyplexes prepared at different l/ul – ratios. Increasing the l/ul – ratio improves FRET efficiency, but it stagnates upon a ratio of 30/70 (**a, b**). The FRET efficiency E_{FRET} was calculated based on the formula shown in chapter 3.5 and was plotted against the amount (pmol) of AF647 labeled siRNA. I_A = fluorescence intensity at 671 nm. I_D = fluorescence intensity at 605 nm (**b**).*

a) Polyplexes (Px) are prepared as described above with different l/ul – ratio of siRNA (e.g. the ratio 30/70 consists of 30 pmol AF647 – labeled siRNA and 70 pmol non – labeled siRNA).
b) For 1 sample, the condensation step (3.2.3) with the siRNA is spared. Instead, P is pipetted into a tube filled with 50µl buffer. This sample represents the maximum donor intensity.
c) As blank sample, Qdot-free particles ($P_{w/o}$) are prepared and condensed with siRNA at the same l/ul – ratios as for the Px. For the quantification, the emission spectra of $P_{w/o}$ are subtracted from the ones of Px.
d) The quartz cuvette is rinsed with HELLMANEX® III (Hellma Analytics) buffer 2% before and after each measurement (see **Note 6**).
e) Cuvette is rinsed once with buffer before sample is filled in
f) Samples are measured with the excitation wavelength being set to 405 nm and the emission spectrum from 550 nm – 800 nm (Fluoreszenz Photometer "Cary Eclipse 50", Varian Inc.).

4.4 Fluorescence spectroscopy – Assessing polyplex stability

Withstanding physiological stressors (e.g. high electrolyte concentrations, serum proteins) after systemic administration plays a crucial role for effective drug delivery of polyplexes.[8] Combining a FRET – based carrier system with fluorescence spectroscopy can be a powerful tool to predict particle stability for *in vitro* and *in vivo* applications.

In the following section, we describe an experiment addressing the impact of a high electrolyte containing buffer system on polyplex stability. Particle aggregation, disassembly and swelling are possible events occurring under these conditions. This FRET-based stability assay is a modification of the assay presented before, as we only monitor the donors' emission intensity (**Figure 2**).

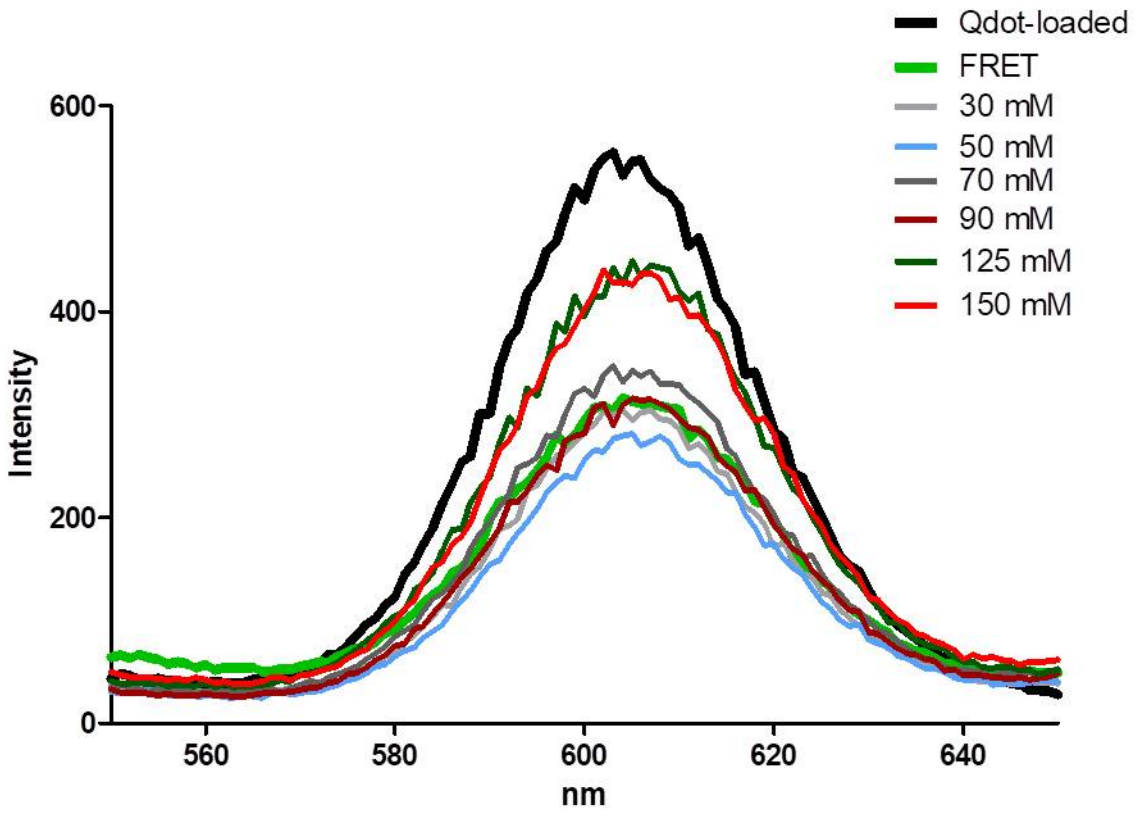

Figure 2. *Fluorescence intensity of Qdots at different electrolyte concentrations:. The black line represents the maximum fluorescence of Qdot loaded nanoparticles (without siRNA condensation) and the lime green line shows FRET, indicated by donor quenching for nanoparticles at a l/ul – ratio of 30/70. Increasing the NaCl concentration from 0 mM to 150 mM reduced the quenching of Qdot fluorescence intensity. This increase in donor emission intensity can be indicative for particle swelling or particle rupture.*

a) Preparation of polyplexes differs from 2.2
b) NaCl stock solution (900 mM NaCl), that allows to adjust the samples' electrolyte concentration is prepared:

n = 5	**0 mM NaCl**	**30 mM NaCl**	**50 mM NaCl**	**70 mM NaCl**	**90 mM NaCl**	**125 mM NaCl**	**150 mM NaCl**
V(stock) [µl]	0	3.33	5.56	7.78	10	13.89	16.67
V(buffer)[µl]	100	96.67	94.44	92.32	90	86.11	83.33

c) 11.2 µL of prepared particles (P) is pipetted in a 0.5 mL tube and filled up to 40 µL with buffer.
d) 100 pmol siRNA of a 30/70 l/ul – ratio is pipetted in another tube and filled up to 40 µL with buffer.
e) P and siRNA are combined to a total volume of 80 µL and carefully mixed by pipetting up and down.
f) Sample is incubated for 20 min to obtain polyplexes Px (**Figure 3a**).
g) Px are gently mixed with 20 µL of the respective NaCl solution for each condition by pipetting up and down and incubated for 10 min.
h) Excitation wavelength is set to 405 nm and the emission spectrum from 550 nm – 650 nm.
i) The quartz cuvette is rinsed with HELLMANEX buffer 2% before and after each measurement. (See **Note 6**)
j) Cuvette is rinsed once with buffer.
k) As blank sample, HEPES buffer is used.
l) Once Px are filled in quartz cuvette they are equilibrated for 2 min before measurement.

To better interpret data from fluorescence spectroscopy we suggest combining this FRET – assay with the SYBR – Gold assay. The SYBR – Gold dye intercalates with siRNA resulting in a fluorescing molecule. siRNA that is condensed with the polymer is not accessible for intercalation. Thus it can be evaluated whether the observed decrease in donor quenching results from siRNA release through polyplex rupture (**Figure 3c**) or from the high electrolyte content attenuating polymer – siRNA interaction. The latter can cause particle swelling (**Figure 3b**) and divergence of the FRET – pair but will not generate a fluorescence signal in the SYBR Gold assay. Dynamic Light Scattering can also be helpful to detect potential particle swelling which is within its resolution.

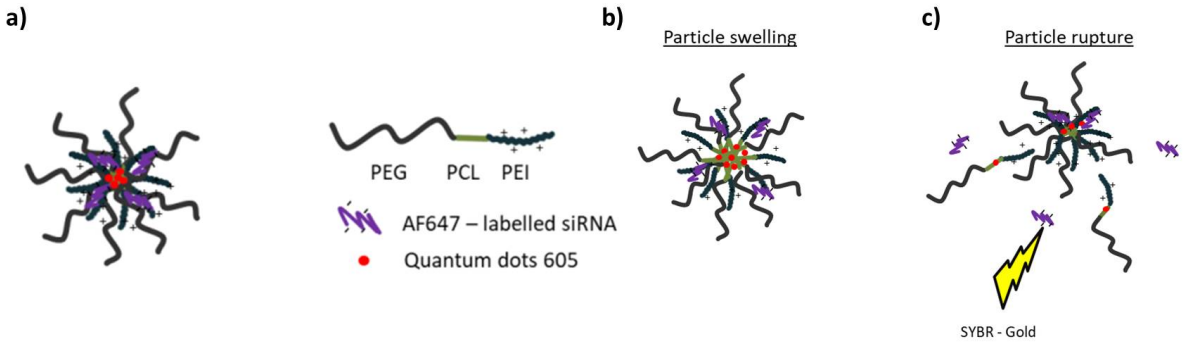

***Figure .**: Polyplex stability: Schematic illustration of PPP polyplexes (**a**). High electrolyte concentrations alter the electrostatic interaction between polymer and siRNA. Decreased condensation at high ionic strength may induce particle swelling (**b**) or even particle rupture (**c**). Both events will cause a decrease in FRET coupling, leading to an increase in donor emission intensity.*

m) Repeat step 2. – 8. for $P_{w/o}$ condensed with non – labelled siRNA (prepare all samples in triplicates).
n) SYBR – Gold dye is diluted 2500x with buffer. Calculate for 30 µL reagent/sample.
o) 100 µL of each sample is placed in a well of a 96 – well plate.
p) As positive control sample, bare non – labeled siRNA (= 100 % free siRNA) is used in equivalent amounts as for Px formation As blank sample, buffer is used.
q) 30 µL SYBR –Gold reagent is added per well and incubated for 10 min.
r) Fluorescence is measured with plate reader (BMG FLUOstar Omega). Set the excitation filter to 485 nm and the emission filter to 520 nm.

4.5 Heparin competition assay

Anionic macromolecules e.g. proteoglycans, glycosaminoglycans and phospholipids, pose a momentous challenge to polyplex stability during systemic circulation and interaction with cells. . Polyanionic species may not only electrostatically bind to the polyplexes but even replace siRNA molecules (**Figure 4a**) leading to physicochemically altered nanoparticles with lower transfection efficiency.[8] Heparin, a polyanionic glycosaminoglycan, is regularly used for stability assays, because of its high anionic charge density.[9] It competes with siRNA for the cationic amine groups in the polymer and at a distinct concentration it releases the siRNA from the particles leading to an increase of donor dye but a reduced acceptor dye fluorescence intensity (**Figure 4b**).

Here we describe an assay that is an easy variant of the assay presented above. To study the release kinetics, it is helpful to calculate the FRET efficiency (E_{FRET}) and plot it against the amount of heparin added (**Figure 4c**).

$$E_{FRET} = \frac{I_A}{I_A + I_D} \times 100\ \%$$

$\mathbf{I_A}$: Fluorescence intensity of acceptor dye

$\mathbf{I_D}$: Fluorescence intensity of donor dye

Again, we suggest the combination with the SYBR –Gold assay.

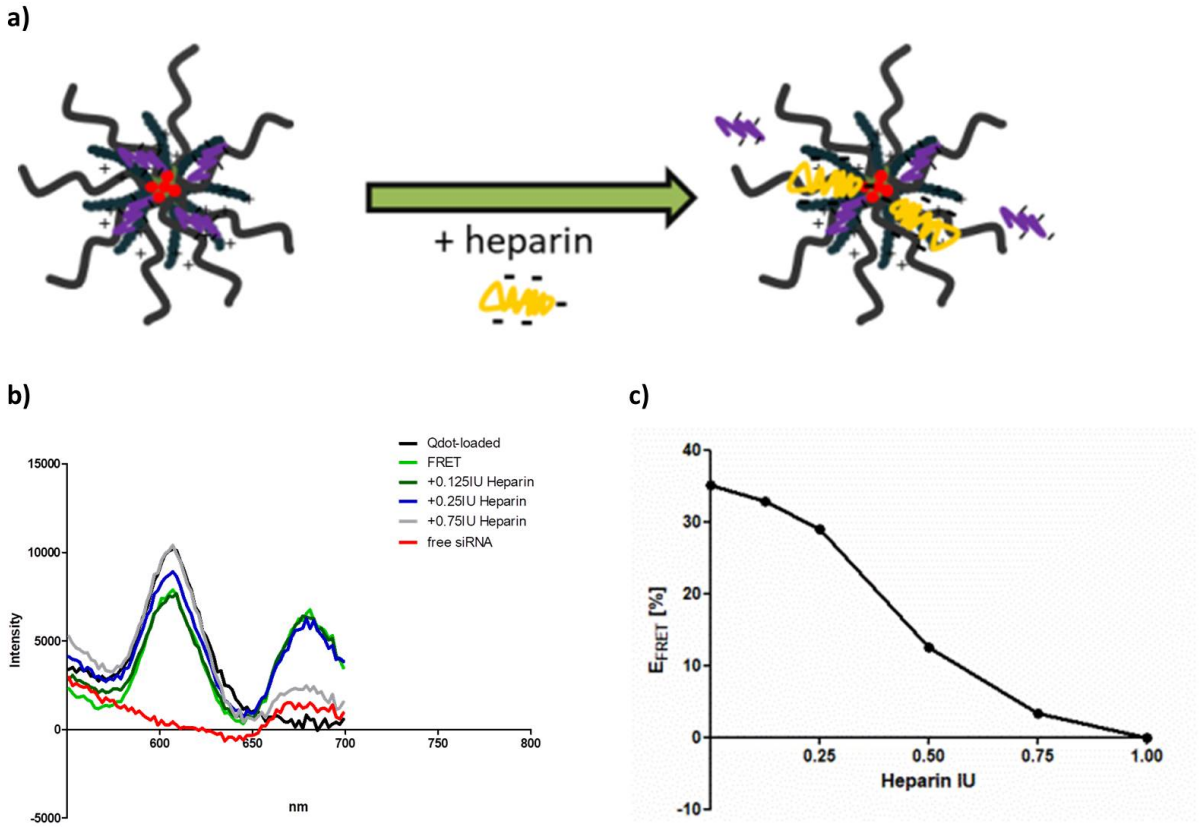

Figure 4. *Striking out siRNA from the polyplex will reduce FRET, which can be monitored by an attenuation of donor signal quenching and a concomitant decrease of acceptor fluorescence intensity (Figure 4b). . The black line represents the maximum fluorescence of Qdot loaded nanoparticles (without siRNA condensation) and the lime green line shows FRET, indicated by donor quenching for nanoparticles at a l/ul – ratio of 30/70. Addition of 0.25 IU heparin already restores some of the donor fluorescence intensity. At 0.75 IU heparin the maximum donor intensity is monitored. FRET efficiency is reduced by siRNA replacement and is dependend on the amount of heparin added. Kinetics of replacement can indirectly be assessed by plotting* E_{FRET} *against the applied amount of heparin (Figure 4c). Quantification is again based on equation of chapter 3.5.*

a) Polyplexes Px for one l/ul - ratio are prepared as explained in section 2.2.
b) A dilution series of heparin in the used buffer system (10mM HEPES pH 7.4) is prepared by starting from 2 IU/10 µL till 0.0625 IU/10 µL.
c) 10 µL of each heparin dilution is added per 100 µL of Px sample
d) Samples are incubated for 30 min.
e) Heparin is included in the blank sample (It may alter the background).
f) The quartz cuvette is rinsed with HELLMANEX buffer before and after each measurement. (See **Note 6**)
g) Cuvette is rinsed once with your buffer.
h) Excitation wavelength is set to 405 nm and the emission spectrum from 550 nm – 800 nm.

4.6 Translation of FRET – approach and difficulties of quantitative analysis

One major hurdle for the implementation of this approach to other nano – carrier systems is, that polymer systems (ideally) have to offer the ability to incorporate FRET donor and acceptor molecule via 2 different functionalities (here: hydrophobic Qdots via PCL and negatively charged siRNA via PEI). Even though other FRET – approaches exploiting just one functionality for both molecules have successfully been produced [5], nanoparticle assembly and disassembly kinetics can be addressed only to some extent. The herein presented PEG-PCL-PEI polymer system not only allows for the latter, but enables biodistribution study of the polymer and tracing of nucleic acid delivery (for *in – vitro* and *in – vivo* applications) at the same time.

Quantitative analysis of *in – vitro* and *in – vivo* experiments (e.g. molecules Qdots/siRNA per cell) with methods like flow cytometry and confocal laser scanning microscopy is quite challenging, and requires further compensation and calibrations steps. [10] Additionally, quenching and/or self – quenching phenomena complicate quantitative analysis. Regarding our nano – carrier system, overreaching QDot loading of the PCL core, excessive use of fluorescently – labeled siRNA or complexation/condensation of polymer with labeled siRNA (**Figure 5**) can cause such processes and thereby impede quantitative analysis.

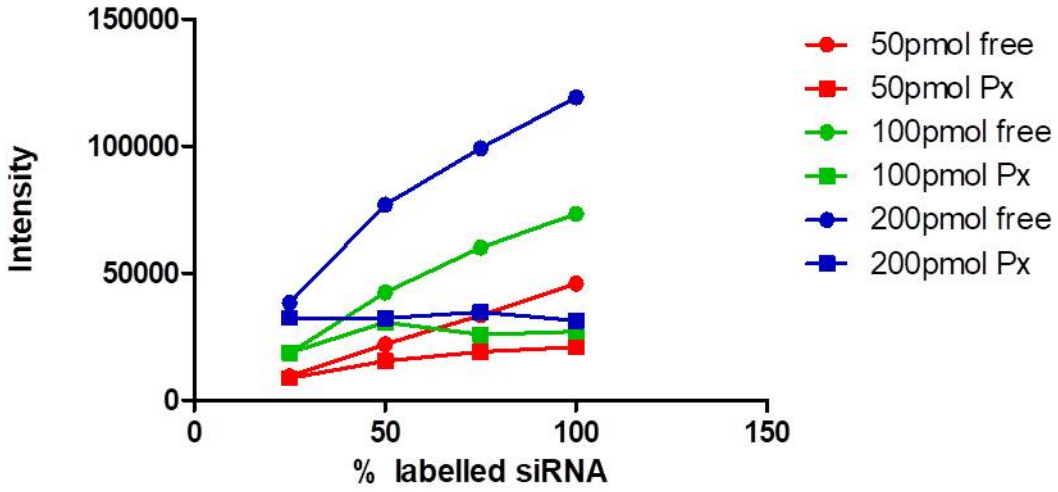

Figure 5. *l/ul – ratio depended quenching (here shown in % labeled siRNA) of AF647 during polyplex assembly: PPP polyplexes (Px) with 50, 100 and 200 pmol siRNA at l/ul ratio of 25/75, 50/50, 75/25 and 100/0 were formed and fluorescence intensity (λEx: 605 nm) was compared to non – complexed (free) siRNA of respective ratios. Dots show linear increase in fluorescence intensity for free siRNA. Squares indicate AF647 quenching when complexed with PPP polymer.*

4.7 Analysing the data

For the quantification of the data all samples were produced in triplicates. GraphPad Prism software was used for analysis, If not mentioned differently 10 mM HEPES pH 7.4 was used as blank sample.

5. Notes

1. Alternatively use “Flocculation” protocol provided by ThermoFischer.
2. Use an appropriate stir bar size that guarantees uniform mixing and won’t collide with the glas wall. Uneven stirring would most certainly worsen the sample quality. Also thoroughly rinse the glass vial with highly purified water to remove any undesired particles (e.g. dust).
3. To facilitate the injection and to assure a final concentration of 1 mg/mL we suggest to prepare sample in excess. n = 1.3 should suffice.
4. The diameter of the needle may alter the physical properties of the polyplexes. In the described experiments we saw decreasing sizes for smaller diameters.
5. For even better size distribution of particles and a higher reproducibility use a syringe pump.
6. We generally recommend to use a 96 – well plate for higher sample throughput.

6. References

[1] J. Fang, H. Nakamura, H. Maeda, *Adv Drug Deliv Rev* **2011**, *63*(*3*): p. 136-51, DOI: 10.1016/j.addr.2010.04.009.

[2] D. Shrestha, A. Jenei, P. Nagy, G. Vereb, J. Szöllősi, *International journal of molecular sciences* **2015**, *16*(*4*): p. 6718-6756, DOI: 10.3390/ijms16046718.

[3] T.K. Endres, M. Beck-Broichsitter, O. Samsonova, T. Renette, T.H. Kissel, *Biomaterials* **2011**, *32*(*30*): p. 7721-7731, DOI: https://doi.org/10.1016/j.biomaterials.2011.06.064.

[4] T. Endres, M. Zheng, A. Kılıç, A. Turowska, M. Beck-Broichsitter, H. Renz, O.M. Merkel, T. Kissel, *Mol. Pharm.* **2014**, *11*(*4*): p. 1273-1281, DOI: 10.1021/mp400744a.

[5] C.T. Greco, J.C. Andrechak, T.H. Epps, M.O. Sullivan, *Biomacromolecules* **2017**, *18*(*6*): p. 1814-1824, DOI: 10.1021/acs.biomac.7b00265.

[6] Y. Liu, J. Nguyen, T. Steele, O. Merkel, T. Kissel, *Polymer* **2009**, *50*(*16*): p. 3895-3904, DOI: https://doi.org/10.1016/j.polymer.2009.06.043.

[7] M. Beck-Broichsitter, E. Rytting, T. Lebhardt, X. Wang, T. Kissel, *Eur. J. Pharm. Sci.* **2010**, *41*(*2*): p. 244-53, DOI: 10.1016/j.ejps.2010.06.007.

[8] S. Behzadi, V. Serpooshan, W. Tao, M.A. Hamaly, M.Y. Alkawareek, E.C. Dreaden, D. Brown, A.M. Alkilany, O.C. Farokhzad, M. Mahmoudi, *Chem. Soc. Rev.* **2017**, *46*(*14*): p. 4218-4244, DOI: 10.1039/C6CS00636A.

[9] H. Debus, P. Baumhof, J. Probst, T. Kissel, *J. Control. Release* **2010**, *148*(*3*): p. 334-343, DOI: https://doi.org/10.1016/j.jconrel.2010.09.007.

[10] R. Mittal, M.P. Bruchez, *Current Protocols in Cytometry* **2009**, *49*(*1*): p. 6.26.1-6.26.7, DOI: 10.1002/0471142956.cy0626s49.

Chapter VIII

Final summary and concluding remarks

This work may be understood as an approach to improving the modeling of EMT *in vitro* by successively increasing the complexity of a cell culture system. During the development of the model, new insights into cell-ECM interactions were gathered ranging from 2-D to 3-D perspectives. The interdisciplinary character of this thesis revealed biological, biophysical and biotechnological novelties which comprise basic research on EMT as well as specific technological and methodological aspects concerning the design of advanced *in* vitro-models and nanoparticulate drug delivery for therapeutic and theranonstic applications.

Initially, a 2-D cell culture model was introduced. The phenotype of the selected breast cancer cell lines was integrated into EMT-phenotypic nomenclature. According to EMT-marker expression, cellular motility and morphology, the so-called "EMT-triad", the "EMT-status" was defined which related mesenchymal-like attributes to cells. Hence, a high EMT-status was descriptive for accumulation of mesenchymal characteristics and *vice versa*. The EMT-phenotyping model ranking cell lines into epithelial (E), epithelial-mesenchymal intermediate (E/M) and mesenchymal (M) states, should ideally be considered as toolbox for upcoming studies. In particular, researches that do not necessarily aim to intensively engage with the biology behind EMT but instead require a robust model system for EMT-related research in the context of breast cancer could make use of the here presented EMT-model. Notably, the data implies that solely analyzing morphological parameters, such as the nuclear circularity or the aspect ratio has predictive relevance regarding the present EMT-phenotype. Therefore, imaging methods for diagnostic or research-related purposes that are able to dissolve cellular or sub-cellular morphologies may benefit from the input of this work. The actual utility of the phenotyping model was simulated by inducing miR200c in a cell line with high EMT-status. This resembled a therapeutic intervention targeting EMT, *i.e.* induction of MET. It was found that therapeutically relevant factors such as reduced motility and re-differentiation, matched with morphological parameters comprised within the model. Overall, the phenotypic alterations as part of the EMT-MET cycle were well represented by this model.

While cellular signaling pathways are highly conserved across species and cell types, their functional outcomes are specified by the context in which they are activated. The concept of "contextuality of signaling" appears to apply well for EMT, since EMT is also defined for cellular events during embryogenesis as well as differentiation processes that occur as part of wound healing. We tried to reflect and study the contextual character of EMT by introducing several aspects of the tumor microenvironment to the aforementioned cell culture system. On the basis of the epithelial-stromal compartmentalization within the breast tissue, collagen types comprised within either epithelial or stromal compartment were tested for their EMT-inducing capacity alone, or in combination with soluble factors. Surface coatings of cell culture dishes with each collagen type (IV/I) were chosen to model the ECM of *in situ* carcinoma or invasive carcinomas, respectively. Remarkably, cells that were neither affected by the collagen substrate, nor by stimulation with growth factors, underwent EMT as

result of a combinatorial treatment (collagen I/IV + TGF-β1). This included increased levels of vimentin, elongated morphologies and elevated motility. These findings, to the best of our knowledge, have not yet been described *in vitro* and may relate to the *in vivo* scenario where cells at the invasive front of a tumor experience stromal ECM together with inflammatory responses from the tumor microenvironment. However, we observed this phenomenon to be independent of collagen type but depending on the cell line. Therefore, the specific context may not only include the co-action of ECM and growth factors but also necessitates a genetic context which enables cells to perceive the contextual signals in a way that results in EMT. Thus, our findings should encourage subsequent studies on EMT to investigate the mechanistical causality behind this contextual EMT-induction. Understanding the underlying biology may help to identify new molecular targets for the treatment of progressive ductal carcinoma *in situ (*DCIS) and breast cancer in general.

During tumor progression, the topographical landscape within the breast cancer tissue is changing due to inflammatory remodeling processes. Only recently, a variety of tumor-associated collagen signatures (TACS) i.e., stromal collagen bundles that surround primary tumors of the mammary gland, were identified to contribute to tumor progression. In order to put TACS into *in vitro* practice, poly(ε-caprolactone)-nanofibers were electrospun on cell-culture substrates. The spinning process and contemplated analytical methods were optimized and standardized to ensure the reproducibility of the model. The resulting fiber mats were analyzed regarding their physical, chemical and toxicological characteristics. Introducing the fibrous TACS-mimics as cell culture substrates allowed to investigate the *in vivo* scenario during which malignant breast cancer cells have overcome epithelial barriers and start to invade the adjacent, fibrous stroma. This step is of particular interest as it represents an early event of the metastatic cascade which is partially promoted by EMT. Spatial confinements and topographical pattern (*e.g.* TACS) represent external mechanical stimuli that may trigger mechano-signaling events intracellularly and thereby induce or sustain an invasive phenotype. Interestingly, the TACS-like *in vitro* model initiated altered transcription of EMT-related genes. Among them, the transcriptional activator XBP1 as relatively new EMT-marker was significantly increased. However, the EMT-induction strongly depended on the EMT-status of the respective cell line. Cell lines with low EMT-status were less affected than cell lines with high EMT-status, implying a certain degree of already existing cellular plasticity to be required to efficiently integrate into and engage with the scaffold. Correspondingly, E/M hybrid cells showed accelerated and more directed migration in comparison to 2-D substrates while cellular motility of fully epithelial cells was compromised. Indeed, growth factor mediated EMT in the latter cells significantly improved cellular motility along the fibers. In conclusion, the EMT-status appeared to govern the contact guidance cells experienced within the TACS-like scaffold. Transferring this to a therapeutic context, drugs that interfere with the EMT machinery may inhibit the acquisition of cellular plasticity and impair cellular motility. As a consequence of disturbed interactions between invasive cancer cells and collagen fibers *in vivo*, such

therapeutic interventions may prevent tumor progression by restricting migration on TACS, *i.e.* inducing traffic jam on this migratory highway towards metastasis.

Another valuable finding within this thesis is related to biophysical considerations of single cells on the scaffold. Generally, malignant cells establish a soft phenotype in order to easily navigate through pores and confinements of the ECM. However, cells that underwent EMT-like changes on the TACS-like *in vitro* model concomitantly displayed an increased elastic modulus. In fact, stimulation of the same cancer cell lines with growth factors to induce EMT in 2-D culture resulted in a comparable increase in cellular stiffness. This means, that transient stiffening of cancer cells is a descriptive marker of the EMT process, regardless of the initial trigger (*e.g.* biochemical, topographical). The actual stiffening was partially attributed to changes in the architecture of the cytoskeleton, including stress fiber formation, and increased expression of intermediate filament vimentin. We observed this stiffening phenomenon in the early phase (< 72 h) of the EMT process, and it is expected that sustained EMT induction will finally result in a softer phenotype. The initial increase in cellular stiffness may serve cancer cells to re-direct their migration and to orientate in space. Nevertheless, it is necessary to study a broader range of cell lines and cell types, including primary tissue cultures to validate our findings. Again, it would be interesting to study, how cellular mechanics are affected by drugs that interfere with EMT. If the transition is impaired, how would cells mechanically adapt to the fibrous scaffold? Would the absence of the initial stiffening imply efficacy of a therapeutic intervention? Possibly, cells can highjack the EMT-inhibition and acquire an amoeboid type of migration which is considered to be part of the Epithelial-to-Mesenchymal-to-Amoeboid-Transition (EMAT) spectrum. This phenotype is rarely detected *in vitro*, but our fibrous model was able to support amoeboidness of the MDA-MB-468 cell line under stimulation with EGF. Presumably, amoeboid-like cells are highly compliant since “amoeboidness” is a state of pronounced morphological plasticity depicting a non-ECM-degrading type of migration upon severe spatial confinement. Since research only recently started to recognize the importance of EMAT for cancer cell migration, models like the one established here are valuable options to gain new insights on the cell biology and mechanics of the EMAT spectrum.

From a drug delivery-perspective, EMT is accompanied by two circumstances that are of interest for developing appropriate drug candidates. First, the partial acquisition of mesenchymal effector proteins can potentially be exploited for targeted delivery. Surface expression of EMT-specific receptor proteins enables selective endocytosis of functionalized drugs or nanoparticles. This therapeutic option should be employed to increase selectivity and decrease off-target effects of potential drug candidates. Second, the regulatory network of EMT including its manifold signaling cascades offers a huge variety of molecular targets to engage with. Here, RNA interference (RNAi) as therapeutic strategy holds great promise as theoretically any EMT-related molecule can be selected and specifically targeted by designing an siRNA complementary to its mRNA. The approach chosen in this work was

based on the cationic polymer poly(ethylenimine) (PEI) which is a common polymeric nano-carrier for siRNA delivery. The functionality of the delivery system was refined by coating the pre-formed PEI-siRNA polyplexes (Px) with hyaluronic acid (HA). HA-coated nanoparticles (HAPx) were well suited to target CD44 receptor (CD44-R) overexpressing breast cancer cells. Simultaneously, the HA-moiety introduced a hydrophilic, anionic shell that provided stealth properties with improved stability in high protein-content environments. An in-house fluorescence quenching-based assay (FQbA) conducted with a common fluorescence plate-reader was developed in order to predict the stability of nanoparticles in protein-rich, *in vivo*-like environments. The data obtained was compared to results from Fluorescence Correlation Spectroscopy (FCS). Indeed, FCS confirmed the predictive relevance of the assay. Thus, the FQbA depicts a novel analytical tool to estimate polyplex stability in a high-throughput fashion. It can be potentially used in order to sort and select the appropriate carrier design during the formulation screening phase of new drug candidates.

The HA/CD44-R ligand-receptor pair is indeed currently extensively applied and studied as targeting principle which is reflected by several clinical trials on HA-chemotherapeutic drug conjugates. However, several variant isoforms (CD44v) exist apart from the CD44 standard isoform (CD44s) which complicates HA/CD44-R targeting strategies. Notably, according to our data, it appears that the CD44-configuration, which cancer cells express on their surface, fluctuates during tumor progression and EMT. Epithelial cancer cells of low malignancy tend to express low levels of CD44s. EMT-like changes that result in E/M-hybrid phenotypes entail increased expression of CD44v isoforms, but low expression levels of CD44s. Triggers, that further induce EMT-like changes support the transition towards a fully mesenchymal phenotype, which expresses high amounts of CD44s isoform (= isotype-switching). Those cells exhibit cancer stem-like properties and, once they have reached the systemic circulation, may develop into circulating tumor cells (CTC). Our findings indicate that nanoparticles coated with medium-molecular weight HA are subjected to distinct uptake kinetics and delivery efficiency depending on the present receptor isoform and expression level. As a consequence, choosing the right time point for a clinical intervention with HA-containing drugs is imperative.

While primary carcinomas such as DCIS presumably do not significantly overexpress CD44v/s, cells that start to invade the stroma parallelly develop a partial-EMT phenotype, which can be targeted with HA-bound drug or nanoparticles. Indeed, based on our data, CD44v-isoforms which are the prevailing receptor type at this stage, internalized HA-coated nanoparticles more slowly but to a higher extent as compared to cells with enriched CD44s protein. Therefore, HA-modified medicine can be particularly selective and efficient at this step of the disease. Additionally, HAPx particles spared non-CD44v/s overexpressing cells implying less off-target accumulation. Hence, HA-coated nanoparticles that are loaded with siRNA against molecules of the EMT machinery are suitable candidates to decelerate the progression of an invasive carcinoma. Ideally, such approaches can shrink the size of the tumor mass to render it accessible for surgical intervention.

Finally, metastatic tumors adapt stem-like properties and are accompanied by CTCs that persist within the blood circulation. CTCs are of particular threat to patients, as they may initiate secondary tumors at any distant organ and therefore determine years of progression-free survival. These cells enter a quiescent state and often develop resistance to conventional chemotherapy. Likewise, triple-negative breast cancer cells (TNBCs) are enriched in stem-like properties and frequently lack conventional treatment options due to acquired drug resistance. Consequently, HA-furnished nanoparticles are particular useful as they specifically target those CD44s overexpressing cells. We designed HAPx particles that showed fast, selective and increased uptake as well as efficient mRNA knockdown in CD44s-high triple-negative breast cancer cells. Anti-cancer molecules as cargo of such carriers may therefore allow to selectively strike those key processes of the metastatic cascade. However, a fundamental question remains regarding the treatment of EMT. Theoretically, therapeutic interference with EMT at the metastasizing stage of the disease may induce MET, *i.e.* the trans-differentiation of mesenchymal-like cells towards an epithelial phenotype. Therefore, it is of utmost importance to reveal, whether MET-stimulating drugs will be detrimental to patients as they promote an epithelial phenotype being capable of subsequently leaving the vasculature to colonize and proliferate at a secondary site in the body. Still, identifying targets for RNAi that re-sensitizes EMT-undergone cells towards conventional chemotherapy remains to be a promising strategy to defeat metastatic cancer diseases in the future. This highlights nanocarriers as multi-functional delivery vehicle to co-deliver chemotherapeutic agents together with siRNA molecules directed against EMT.

This thesis described progressive improvements of an EMT *in vitro* model in order to approach *in vivo* requirements. Starting two dimensionally, we included growth factors and collagen types which reflected the compartmentalization within the tissue of the mammary gland. The TACS-like matrix introduced an additional dimension including topographical peculiarities of the diseased tissue. In a proof-of-concept experiment we finally tested the performance of the most promising nanoparticle-candidate, characterized and tested before, within a more bio-mimetic and bio-relevant context. However, formulation screenings were not yet conducted. Thus the project should now focus on different molecular targets that are related to EMT. The optimal HAPx formulation should then be applied to systematically study the effect RNAi of chosen targets exerts on cancer cell motility and migratory behavior within the fibrous scaffold. Nevertheless, both, the nanoparticulate delivery vehicle and the *in vitro* model can be further optimized. Fine-tuning the HA:PEI-ratio as well as testing different molecular weight species of hyaluronic acid can still modulate physico-chemical characteristics in a way that may ultimately improve the biological performance and *in vivo* stability of the drug delivery system. Interchanging PEI with more biocompatible and biodegradable cationic polymers, such as oligospermines, should definitely be considered in order to achieve clinical relevance of the delivery system on the long-term. Regarding the scaffold, incorporation of the fibers into a hydrogel-based matrix would improve tissue-mimicry. As a potential next step, thicker fiber mats could be produced. After punching out a little hole in the center of a fiber mat, cancer spheroids

can be placed in this pit and submerged with an ECM-mimicking hydrogel. The depth and width of the pit should ideally be adjusted to the size of the studied spheroids embedding only the lower moiety of the spheroid. Thereby, dissemination of cancer cells from a primary tumor and the subsequent migration along TACS could be efficiently modeled in 3-D. It may as well be possible to establish this model in a well-plate format to facilitate and accelerate *in vitro* culture. The co-culture with stromal or myoepithelial cells would further improve the organotypic cancer 3-D model and allow for studying their reciprocal communication as well as their impact on cellular migration along the fibers. Overall, the high-throughput character and cost-effectiveness of such advanced 3-D *in vitro* models may partially replace intricate animal models in the future. The recently adjusted legal aspects of animal testing regarding the approval of new drug candidates by the FDA will further push industry and research to develop new technologies that will more and more succeed in approaching *in vivo*-like conditions.

Chapter IX

Appendix

1. List of Abbreviations

ACF	Autocorrelation Function
AFM	Atomic Force Microscopy
A_R	Aspect Ratio
ATP	Adenosintriphosphate
BC	Female Breast Cancer
BCA	Bicinchoninic Acid
BM	Basement Membrane
BRCA	Breast Cancer gene
BSA	Bovine Serum Albumin
CA	California
CAF	Cancer-Associated Fibroblast
cDNA	Complementary DNA
CD	Cluster of Differentiation
CDH1	Cadherin 1gene
C_N	Nuclear Circularity
CSC	Cancer Stem Cell
CSR	Cellular Stress Response
CTC	Circulating Tumor Cell
CTCF	Corrected Total Cell Fluorescence
DAPI	4′, 6-Diamidino-2-Phenylindole
DCE	1,2-Dichloroethane
DCIS	Ductal Carcinoma In-Situ
DCM	Dichloromethane
DDR	Discoidin-Domain Receptor
DLS	Dynamic Light Scattering
DMEM	Dulbecco's Modified Eagle's Medium
DMF	*N,N*-Dimethylformamide
DMSO	Dimethylsulphoxide
DNA	Deoxyribonucleic Acid
DOX	Doxycycline hydrochloride
dsRNA	Double-stranded RNA
E	Epithelial
ECM	Extracellular Matrix
EDTA	Ethylenediaminetetraacetic Acid

EGF	Epidermal Growth Factor
EGFR	Epidermal Growth Factor Receptor
EMEM	Eagle's Minimum Essential Medium
EMP	Epithelial-to-Mesenchymal Plasticity
EMT	Epithelial-to-Mesenchymal Transition
EMAT	Epithelial-to-Mesenchymal-to-Amoeboid Transition
EPR	Enhance Permeability and Retention
ER	Estrogen Receptor
FBS	Fetal Bovine Serum
FCC	Fiber-Coated Coverslip
FCS	Fluorescence Correlation Spectroscopy
FDA	Food and Drug Administration
FI	Fluorescence Intensity
FQbA	Fluorescence Quenching-based Assay
FRET	Fluorescence Resonance Energy Transfer
GASC1	Gene Amplified in Squamous cell Carcinoma 1
HS-GC-MS	Headspace Gas Chromatography-Mass Spectrometry
GF	Growth Factor
HA	Hyaluronic Acid
HAPx	Hyaluronic Acid-coated Polyplexes
HARE	Hyaluronan Receptor for Endocytosis
HAT	Histone Acetyltransferase
HDAC	Histone Deacetylase
HEPES	4-(2-Hydroxyethyl)-1-piperazineethanesulfonic acid
HER2	Human Epidermal Growth Factor Receptor 2
HPW	Highly Purified Water
HRP	Horseradish Peroxidase
HSP	Heat Shock Protein
IBC	Invasive Breast Cancer
IF	Intermediate Filament
IL	Interleukin
JP	Japan
kDa	kilo Dalton
KDM6b	Lysin (K) Demethylase 6b
LDA	Laser-Doppler-Anemometry
LNP	Lipid Nanoparticles

LOX	Lysyl Oxidase
LYVE1	Lymphatic Vessel Endothelial Hyaluronan Receptor 1
M	Mesenchymal
MA	Massachusetts
MAT	Mesenchymal-to-Amoeboid Transition
MET	Mesenchymal-to-Epithelial Transition
MMP	Matrix Metalloproteinase
mRNA	Messenger RNA
miRNA	Micro RNA
MSC	Mesenchymal Stem Cell
MaSC	Mammary Stem Cell
MTT	3-(4,5-Dimethylthiazol-2-yl)-2,5-diphenyltetrazolium bromide
MW	Molecular Weight
NC	Negative Control
NMR	Nuclear Magnetic Resonance
NF-κB	Nuclear Factor kappa-light-chain-enhancer of activated B cells
NH	New Hampshire
NHS	*N*-Hydroxysuccinimide
N/P-ratio	Nitrogen-to-Phosphate-ratio
NY	New York
PA	Pennsylvania
PAA	Polyacrylic Acid
PAGE	Polyacrylamide Gel Electrophoresis
PBS	Phosphate Buffered Saline
PCL	Poly (ε-caprolactone)
PCR	Polymerase Chain Reaction
PDI	Polydispersity Index
PD-L1	Programmed Death-Ligand 1
PEG	Polyethylene Glycol
PEI	Poly(ethylenimine)
PDGF	Platelet-Derived Growth Factor
PFA	Paraformaldehyde
PMT	Photomultiplier
PPP	PEG-PCL-PEI
PR	Progesterone Receptor
PTEN	Phosphatase and Tensin homolog

Px	Polyplexes
Qdots	Quantum dots
RGD	Arginylglycylaspartic acid
RHAMM	Receptor for Hyaluronan-Mediated Motility
RIPA	Radioimmunoprecipitation Assay
RNA	Ribonucleic acid
ROS	Reactive Oxygen Species
RP-HPLC	Reversed Phase-HPLC
RT	Room Temperature
RT-qPCR	Reverse transcription quantitative real-time PCR
SD	Standard Deviation
SDS	Sodium Dodecyl Sulphate
SEM	Scanning Electron Microscopy
ssRNA	Single-stranded RNA
siRNA	Short interfering RNA
TACS	Tumor-Associated Collagen Signatures
TBA	tert- Butanol
TBST	Tris Buffered Saline with 0.1% Polysorbate 20 (Tween 20)
TF	Transcription Factor
TGF-β	Transforming Growth Factor-beta
TGF-βR	Transforming Growth Factor-beta Receptor
TLP	Transmitted Light Photography
TME	Tumor Microenvironment
TNBC	Triple-Negative Breast Cancer
TP53	Tumor Protein 53
TRITC	Tetramethylrhodamine
TX	Texas
UPR	Unfolded Protein Response
VEGF	Vascular Endothelial Growth Factor
VIM	Vimentin gene
VIPER	Virus-Inspired Polymers for Endosomal Release
XBP1	X-box Binding Protein 1
ZEB	Zinc Finger E-box-binding Homeobox

2. List of publications and presentations associated with this thesis

2.1 Publications

- **L. Isert, A. Mehta, F. Adams, O. M. Merkel:** "Tracking siRNA–Nanocarrier Assembly and Disassembly Using FRET" Methods in Pharmacology and Toxicology 2021, DOI: 10.1007/978-1-0716-1250-7_17
- **B. Freystetter, M. Grab, L. Grefen, L. Bischof, L. Isert, Petra M. D. Bezuidenhout, C. Hagl, N. Thierfelder:** "Combining 3D-Printing and Electrospinning to Manufacture Biomimetic Heart Valve Leaflets". J Vis Exp. 2022 Mar 23;(181). DOI: 10.3791/63604-v
- **A. Mehta, E. D. Vedove, L. Isert, O. M. Merkel:** "Targeting KRAS mutant lung cancer cells with siRNA-loaded Bovine Serum Albumin nanoparticles" Pharmaceutical Research 2019, 36, (9), 133. DOI: 10.1007/s11095-019-2665-9
- **R. Kandil, Y. Xie, R. Heermann, L. Isert, K. Jung, A. Mehta, O. M. Merkel:** "Coming in and Finding Out: Blending Receptor-Targeted Delivery and Efficient Endosomal Escape in a Novel Bio-Responsive siRNA Delivery System for Gene Knockdown in Pulmonary T Cells". Advanced Therapeutics 2019. DOI: 10.1002/adtp.201900047
- **N. Hartl, F. Adams, G. Costabile, L. Isert, M. Döblinger, X. Xiano, R. Liu, O. M. Merkel:** "The Impact of Nylon-3 Copolymer Composition on the Efficiency of siRNA Delivery to Glioblastoma Cells". Nanomaterials 2019, 9, (7), pii: E986. DOI: 10.3390/nano9070986
- **M. Andima, G. Costabile, L. Isert, A. J. Ndakala, S. Derese, O. M. Merkel:** "Evaluation of β-Sitosterol Loaded PLGA and PEG-PLA Nanoparticles for Effective Treatment of Breast Cancer: Preparation, Physicochemical Characterization, and Antitumor Activity". Pharmaceutics 2018, 10 (4), pii E232. DOI: 10.3390/pharmaceutics10040232

2.2 Poster Presentations

- **L. Isert, A. Mehta, O. M. Merkel:** „Tracing the Delivery of Nanocarrier-siRNA Polyplexes Aiming to Monitor Intracellular Trafficking Using FRET"; 15th European Symposium on Controlled Drug Delivery, Egmond aan Zee, The Netherlands 10th-13th April 2018
- **L. Isert, A. Mehta, O. M. Merkel:** „Assessing the Impact of Extracellular Matrix Components on Epithelial-Mesenchymal-Transition in Breast Cancer via Electrospun Fiber Mats"; 3rd EACR Goodbye Flat Biology conference, Berlin, Germany 9th-12th September 2018
- **L. Isert, A. Mehta, O. M. Merkel:** „Interplay of Mutation Load and Tumour Microenvironment Determines Phenotype in Breast Cancer"; EACR Seed and Soil conference, Berlin, Germany 7th-9th October 2019